

The role of climate in Hardpan formation in mine tailings and its environmental effect

Von der Naturwissenschaftlichen Fakultät
der Gottfried Wilhelm Leibniz Universität Hannover
zur Erlangung des Grades

Doktor der Naturwissenschaften

Dr. rer. nat.

genehmigte Dissertation

von

M.Sc. Mostafa Gamal Eldeen Taha Redwan

geboren am 07.12.1978 in Sohag, Ägypten

2011

Referent: Prof. Dr. Francois Holtz
Korreferent: Prof. Dr. Axel Schippers
Drittprüfer: PD. Dr. Torsten Graupner
Tag der Disputation: 29. September 2011

ERKLÄRUNG ZUR DISSERTATION

Hierdurch erkläre ich, dass ich meine Dissertation mit dem Titel, *The role of climate in Hardpan formation in mine tailings and its environmental effect* selbständig verfasst und die benutzten Hilfsmittel und Quellen sowie gegebenenfalls die zu Hilfeleistungen herangezogenen Institutionen vollständig angegeben habe.

Die Dissertation wurde nicht schon als Masterarbeit, Diplomarbeit oder andere Prüfungsarbeit verwendet.

Hannover, den 16.06.2011

Mostafa Redwan

LIST OF PAPERS RESULTING FROM THIS RESEARCH

Redwan M, Rammlmair D. Simultaneous Monitoring of Water Saturation and Fluid Conductivity in Unconsolidated Sand Columns. *Soil Sci. Soc. Am. J.* 2010; 74: 1457-1468.

Redwan M, Rammlmair D. Understanding micro-environment development in mine tailings using MLA and image analysis. 10th International Congress for Applied Mineralogy (ICAM2011), 1-5 August 2011, Trondheim, Norway.

Redwan M, Rammlmair D, Meima JA. Application of Mineral Liberation Analysis in studying micro-sedimentological structures within sulfide mine tailings and its effect on hardpan formation. Resubmitted to the *Science of the Total Environment*.

Redwan M, Rammlmair D. Influence of climate, mineralogy and mineral processing on hardpan formation in two, low-sulfide, high- carbonate, gold mine tailings in the Eastern Desert of Egypt. Submitted to *Environmental Earth Sciences*.

To my Parents

To my children, Jody & Cady

To my wife, Marwa

To all people who helped me,

I dedicate this work with

all love and respect

"The ruins of an older world are visible in the present structure of our planet, and the strata which now compose our continents have been once beneath the sea, and were formed out of the waste of pre-existing continents. The same forces are still destroying, by chemical decomposition or mechanical violence, even the hardest rocks, and transporting these materials to the sea, where they are spread out, and form strata analogous to those of more ancient date."---- James Hutton, 1788.



TABLE OF CONTENTS

Abstract	i
Kurzfassung	iii
GENERAL INTRODUCTION	1
1.1. Mine wastes production	2
1.2. Weathering reactions and contaminations by AMD	4
1.3. Natural attenuations reactions	6
1.4. Thesis Objectives	10
CHAPTER 1: HARDPAN FORMATION IN DAVIDSCHACHT MINE TAILINGS IMPOUNDMENT, FREIBERG, AND ITS EFFECT ON METALS ATTENUATION ...	12
PART I. Characteristic features of the hardpans along the whole tailings impoundment.	13
I.1. Abstract.....	13
I.2. Introduction.....	13
I.3. Site Description and history of the impoundment	16
I.3.1. Climate.....	18
I.4. Methods.....	18
I.4.1. Physical properties	19
I.4.2. Geochemical properties	19
I.4.3. Mineralogical properties	22
I.5. Results and discussions.....	23
I.5.1. Physical properties	23
I.5.1.1. Moisture content	23
I.5.1.2. Particle size distribution.....	23
I.5.1.3. Specific surface area (BET).....	24
I.5.2. Geochemical properties	25
I.5.2.1. Bulk rock chemistry	25
I.5.2.2. Acid Neutralization	25
I.5.2.3. Paste-water extractions	26
I.5.3. Mineralogical properties	33
I.5.3.1. Bulk rock mineralogy	33
I.5.3.2. Detailed mineralogy using SEM and MLA	33
I.6. Summary and conclusions	46
PART II. Detailed investigations on the upper surface layers of the impoundment.....	54
II.1. Abstract.....	54
II.2. Objectives	54
II.3. Materials and methods.....	55
II.4. Results and discussions	55
II.4.1. Bulk physical properties	56
II.4.1.1. Moisture content	56

II.4.1.2. Particle density	57
II.4.1.3. Specific surface area (BET).....	58
II.4.1.4. Particle size distribution	58
II.4.2. Geochemical properties	59
II.4.2.1. Bulk rock chemistry.....	59
II.4.2.2. Paste-extraction results	59
II.4.3. Mineralogical properties.....	62
II.4.3.1. Bulk /detailed rock mineralogy	62
II.5. Conclusions	73

CHAPTER 2: HARDPAN FORMATION IN EGYPT: POSSIBILITY AND ENVIRONMENTAL RISKS

2.1. Abstract	75
2.2. Introduction	75
2.3. Study area.....	78
2.3.1. Climate	83
2.4. Material and methods	83
2.5. Results and discussions	85
2.5.1. Geochemical properties.....	85
2.5.1.1. Bulk rock chemistry	85
2.5.1.2. Paste-water extraction	89
2.5.2. Physical and mineralogical properties.....	90
2.5.2. 1. Particle size distribution	90
2.5.2. 2. Specific surface area (BET)	91
2.5.2. 3. Bulk mineralogy (XRD).....	92
2.5.2. 4. Detailed mineralogy by mineral liberation analysis (MLA)	93
2.6. Conclusions and environmental concerns	100

CHAPTER 3: NEW COLUMNS DESIGN FOR THE INVESTIGATION OF IONS ACCUMULATION IN THE CAPILLARY HEAD IN UNCONSOLIDATED SANDS ...

3.1. Abstract	106
3.2. Introduction	106
3.3. Methodology and Experimental Set-up.....	109
3.3.1. Theory of X-ray Absorption.....	109
3.3.2. Columns	110
3.3.3. Materials Characterization	111
3.3.4. Instrumentation.....	112
3.3.4.1. X-Ray Absorption	112
3.3.4.2. Electrical Conductivity.....	113
3.4. Measurement and Data Processing	113
3.4.1. X-Ray Absorption	113
3.4.1.1. Measurement	113
3.4.1.2. Data Processing.....	114
3.4.2. Electrical Conductivity.....	115
3.4.2.1. Measurements.....	115
3.4.2.2. Data Processing	116
3.5. Results and Discussion.....	116
3.6. Conclusions	128

CHAPTER 4: EFFECT OF TEMPERATURE AND WATER CONTENT ON HARDPAN FORMATION IN MINE TAILINGS: COLUMN EXPERIMENTS	130
4.1. Introduction	131
4.2. Methodology and Experimental Set-up.....	131
4.2.1. Columns & Instrumentations	131
4.2.2. Materials Characterization	138
4.3. Measurement and Data Processing	141
4.4. Results and discussion.....	143
4.4.1. Water loss.....	143
4.4.2. Electrical/fluid conductivities	144
4.4.3. Oxygen and temperature measurements	145
4.4.4. pH measurements	145
4.4.5. Efflorescence sulfates composition.....	146
4.4.6. Pore-water extractions.....	148
4.4.7. Paste-water extractions and solid samples analysis	148
4.5. Conclusions	162
CHAPTER 5: SUMMARY AND CONCLUSIONS	172
5.1. Synthesis of the results	173
5.1.1. General conclusions	173
5.1.2. Specific conclusions	177
5.2. Outlook.....	178
REFERENCES CITED	179
ACKNOWLEDGMENTS	197
LEBENS LAUF	199



Mine tailings discharge is one of the most important environmental aspects to be taken into consideration for most mines before, during and after operations. To prevent environmental problems resulting from the weathering of sulfide minerals within the tailings impoundments and the subsequent generation of acid mine waters rich in SO_4^{2-} , Fe^{2+} and some toxic metals, or through erosion and spreading out to e.g agricultural areas, a detailed investigation of a number of aspects including the mineralogical, geochemical and sedimentological status quo are required. In this study, mine tailings located in completely different climatic regions (Germany, sulfide mine tailings and Egypt, gold mine tailings) were studied for their mineralogical, geochemical and physical properties, in addition to, the tailings disposal techniques used, in order to understand the processes affecting hardpan formation. This was combined with column experiments for monitoring the transport/precipitation processes in small scale. Mineral Liberation Analysis (MLA) was applied, especially for the samples from Germany in order to quantify the textural, mineralogical and chemical changes in a μm - and mm scale for better understanding mineral alteration, and precipitation of secondary phases and gels, and last but not least the processes leading to the formation of hardpans.

From the following study it was concluded, that thickened tailings disposal in Egypt, did not lead to grain size and mineral fractionations, and therefore the critical amount of reactive phases cannot be achieved within the lamina required for hardpan formation. This is in sharp contrast to the tailings disposal in Germany where deposition of the slurry by spigot points caused mineral/grain size segregations and therefore different lamina with contrasting physical, mineralogical and chemical pattern enhancing hardpan formation. The amounts of acid producing sulfides and acid buffering compounds such as carbonates and e.g plagioclase, biotite in these lamina are critical for the very local acid/neutralization potentials. The higher amount of carbonates compared to reactive sulfides in a homogeneous environment (Egypt case, Barramiya site) doesn't favour hardpan formation compared to slightly higher sulfides in a highly heterogeneous sequence (Germany case). The availability of water, oxygen, and temperature, besides the basic premises such as microbiology, mineralogy, grain size etc., drive reactions within the tailings. During the rarely rain fall events in Egypt, water mainly runs off, little is soaked by the material and driven out quickly by capillary

transport generating scattered efflorescence, since reaction times are minimized. Alteration of the few sulfides generates rims of Fe-sulfates around the sulfide grains and disseminated gypsum spots close to the upper surface and in the immediate vicinity of desiccation cracks. The tailings in Germany are characterized by a comparable humid climate which favours periods of raining events (mobilization directions downward) and periods of drying (mobilization upward under capillary forces) which are very important for oxidation, transport and precipitation processes within and between the lamina. The increased electrical/fluid conductivities especially in the critical zone above the water table depend mainly on the fast rising capillary head fluids which accumulate all the available ions around the particles and moved upward. Efflorescent sulfate crusts were recognized as first alteration products in the course of element mobilization combined with evaporation in column experiments, especially with high temperatures. Within these crusts toxic elements like As and Pb can be fixed through co-precipitation processes. However, their attenuation depends on the stability of the hosting secondary phases in the new environment over time even under climatic changes. The development of hard crusts capable of inhibiting rain and oxygen infiltrations is highly enhanced in areas with high temperature and water contents but their formation requires definitely an elevated potential of reactive compounds in the accessible zone of alteration and a multiple repetition of drying and wetting cycles, and eventually long reaction time, dependent on the primary mineral and grain size distribution.

Keywords: *Hardpan formation . Mine tailings . climate .*



Die Deponierung von Rückständen der Aufbereitung von Erzen als s.g. Mine Tailings, ist ein sehr wichtigster Umwelt relevanter Aspekt, den es während und nach der Ablagerung zu betrachten gilt. Um Umweltprobleme, die aus der Verwitterung von Sulphiden in Tailingsablagerungen erwachsen und zur Generierung von sauren Minenwässern, reich an SO_4^{2-} , Fe^{2+} und einigen toxischen Metallen, bzw. zur Ausbreitung durch Erosion und z.B. auf Landwirtschaftflächen führen, zu vermeiden sind detaillierte Untersuchungen u.a. zum mineralogischen, geochemischen und sedimentologischen „status quo“ erforderlich. In dieser Untersuchung wurden Mine Tailings aus gänzlich unterschiedlichen klimatischen Regionen (Deutschland, Sulphidbergbau Tailings; Ägypten, Goldbergbau Tailings) auf mineralogische, geochemische und physikalische Eigenschaften hin, unter Einbeziehung der Ablagerungsbedingungen untersucht, um die Prozesse, die zur Entstehung von Krusten (hardpans) führen zu verstehen. Diese Untersuchungen wurden mit Säulenexperimenten zur Beobachtung der kleinmaßstäblichen Transport-/Fällungsprozesse verknüpft. Automatisierte Mineral Analyse (Mineral Liberation Analysis; MLA) wurde angewandt, speziell für die Proben aus Deutschland, um eine Quantifizierung textueller, mineralogischer und chemischer Veränderungen im μm und mm Maßstab vorzunehmen, um Mineralalteration, Fällung von sekundären Phasen und Gelen und nicht zuletzt die Prozesse, die zur Krustenbildung selbst führen, besser zu verstehen.

In der folgenden Untersuchung wurde erkannt, dass die eingedickten Tailingsablagerungen in Ägypten nicht zur Korngrößen- und Mineralfraktionierung führten und so die zur Krustenbildung nötigen kritischen Mengen an reaktiven Phasen in den Lagen nicht erreicht wurden. Dies steht in scharfen Kontrast zur Tailingsablagerung in Deutschland, wo die Einbringung der Suspension über Spülstationen zu einer Mineral/Korngrößenfraktionierung führte und dadurch verschiedene Lamina mit kontrastierenden physikalischen, mineralogischen und chemischen Merkmalen, welche Krustenbildung unterstützen, erzeugten. Die Anteile der Säure produzierenden Sulphide und der Säure puffernden Phasen wie z.B. Karbonate und Biotit in diesen Lamina sind kritisch für das sehr lokale Säure-/Neutralisierungspotential. Der höhere Gehalt an Karbonaten bezogen auf reaktive

Sulfide in einem homogenen Umfeld (Barramiya, Ägypten) wirkt sich ungünstig auf Krustenbildung aus, wohingegen eine sehr heterogenen Abfolge mit leicht höheren Sulphidgehalten (Deutschland) dieselbe begünstigt. Die Verfügbarkeit von Wasser, Sauerstoff und Temperatur kontrollieren neben den Grundvoraussetzungen wie Mikrobiologie, Mineralogie, Korngröße etc. die Reaktionen in den Tailingsablagerungen. Während der seltenen Regenereignisse in Ägypten fließt der Großteil des Wassers oberflächlich ab, nur ein geringer wird vom Material aufgesogen und rasch wieder durch Kapillartransport ausgetrieben und verursacht nur vereinzelt Ausblühung, da die Reaktionszeiten minimiert sind. Die Alteration der wenigen Sulphide generiert einen Eisensulfatrand um die Sulphidkörner und disseminierte Gipskristalle nahe der Oberfläche und in unmittelbarer Nähe zu Trocknungsrissen. Die Tailingsablagerung in Deutschland ist charakterisiert durch ein vergleichbar humides Klima, gekennzeichnet durch periodische Regenfälle (Mobilisationsrichtung gravitativ) und Schönwetterperioden (Aufwärtsbewegung durch Kapillartransport). Dies ist wichtig für die Oxidations-, Transport- und Fällungsprozesse innerhalb und zwischen den Lamina. Die erhöhten elektrische/Fluidleitfähigkeiten speziell innerhalb der kritischen Zone oberhalb des Wasserspiegels sind hauptsächlich abhängig von schnell migrierenden Kapillarkopf wo die Erstfluide alle verfügbaren Ionen um die Partikel herum einsammeln und akkumulieren und nach oben transportieren.

Krusten aus ausblühenden Sulphaten bilden sich speziell bei erhöhten Temperaturen als erste Alterationsprodukte aus mobilisierten Elementen im Zuge der Verdunstung in Säulenversuchen. In diesen Krusten können toxische Elemente wie As und Pb durch Co-Präzipitation fixiert werden. Allerdings hängt deren dauerhafte Fixierung von der Stabilität der Wirtsphase über die Zeit in der neuen Umgebung unter den gegebenen klimatischen Bedingungen ab. Die Entstehung von Krusten, welche in der Lage sind Regenwasser- und Sauerstoffinfiltration zu unterbinden, tritt verstärkt in Zonen erhöhter Temperatur und höherer Wassergehalte auf. Sie ist jedoch definitiv auf ein erhöhtes Potential reaktiver Bestandteile in der für die Alteration zugänglichen Zone sowie auf eine multiple Wiederholung von Benetzungs- und Trocknungszyklen und eventuell langen Reaktionsperioden, abhängig von Primärmineralen und Korngrößenverteilung, angewiesen.

Schlagworte: *Krustenbildung . Mine Tailings . Klima .*

GENERAL INTRODUCTION



1.1. Mine wastes production

After the exploration stage of ore minerals (which contain valuable elements like Au, Cu, Pb, Zn) or industrial minerals (like bauxite and phosphate) has been finished, the exploitation begins through open pit and underground mining. Then the ore is transported in blocks to the milling processes to reduce it from larger than one meter to a few millimetres through crushing and milling (Fig.1). The size reduction processes are very important to easily liberate the ore from the gangue (less valuable, waste) minerals. Crushing is carried out in a dry phase, whereas grinding is carried out for the suspended particles in water. The separation of the ore from gangue minerals is done through a series of methods including magnetic, gravimetric, electric separations. This depends on the type and the physical and chemical properties of the ore and the gangue minerals. Flotation circuits are systems of cells and auxiliary equipment arranged to yield maximum results from an ore in creating a concentrate following the grinding and reagent treatment (Dold, 2000). After the valuable minerals have been extracted by flotation, the residual materials (which reach sometimes 95-99% of the treated material especially in case of low grade ores) are transported in the form of suspension (fine grained sediment-water slurry) to its final deposition in the tailings impoundments.

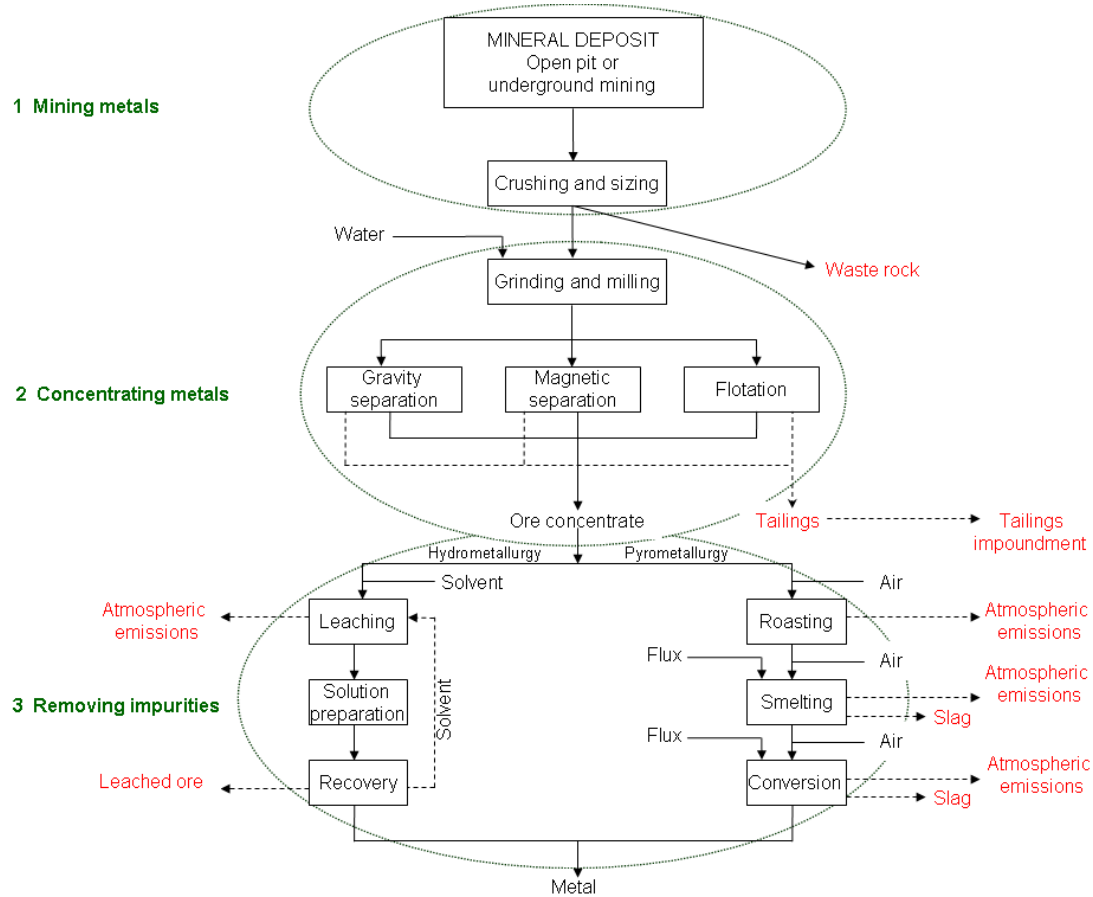


Fig.1. Simplified flow-charts of the mineral processing operation steps to form the final metals and waste (modified after Ripely et al., 1996 and Lottermoser, 2003). Red fonts referring to the waste formed within each step.

Tailings dams found in these impoundments may be constructed upstream (towards the tailings), downstream (away from the tailings) or centreline (Davies and Martin, 2000). The final grain size of the tailings ranges from sand to clay, and deposition takes place in an aqueous environment similar to sediments. Therefore, sedimentary structures like graded bedding, stratification, lateral pinchout textures are common. Due to the continuous changes of the spigot point (discharge point) with time, the depositional environment changes with time along the vertical profile (Robertson, 1994). Therefore, each tailing has its characteristic internal sedimentary structures different from other tailings which affect the hydraulic properties of it.

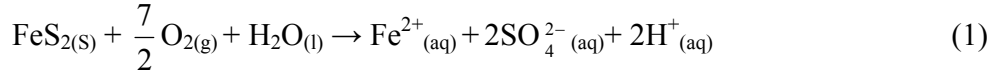
1.2. Weathering reactions and contaminations by ARD/AMD

Weathering processes in mine tailings are very complicated in the field scale and reactions can't be fully predicted. This is related to the material itself due to changes in mineral assemblages, variation of mineral ratios and variations within the composition of individual mineral, as well as the accessibility of the reactive surfaces to fluids and gases during the oxidation and buffering reactions. Furthermore due to the depositional process influencing grain size distribution, distance from surface, type of lamina and its inclination. All of this has to be seen in context to the seasonal fluctuation of climatic conditions of the region.

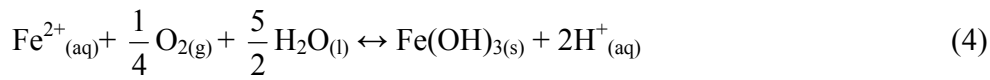
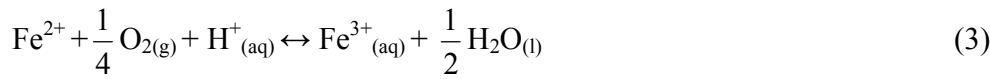
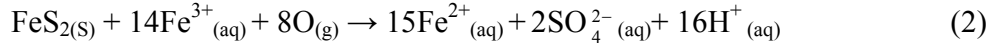
The main environmental problems related to mine wastes is the formation of acid rock drainage (ARD) generated from mine waste rock or tailings, and acid mine drainage (AMD) generated from mine structures such as pits and underground workings. These acid drainage waters originated by pyrite and other highly reactive sulfides oxidation and are characterized by pH values below 4, high concentration of Fe^{2+} , Fe^{3+} and SO_4^{2-} , high conductivity and high concentration of potentially toxic and trace elements such as As, Cd, Pb, Zn, Cu, Hg, Sb, Se, etc.. The formations of this ARD/AMD are primarily related to the mineralogy of the waste material. As some wastes contain larger amounts of highly reactive sulfides minerals compared to the neutralizing minerals in the system, the formation of acid drainage waters is increased. Also, oxygen and water are the main important factors in the oxidation processes, this in addition to, particle size and available surface area, distribution of minerals in the system, permeability and the climate. These are site-specific factors and can't be used to predict the formation of acid drainage at other sites, and even not at another area of the same site.

Looking at a pyrite crystal, its oxidation is carried out in three main steps (Nordstrom, 1982; Wiersma and Rimstidt, 1984; Evangelou and Zhang, 1995; Nordstrom and Alpers, 1999; Blowes et al., 2003), from sulfur oxidation, to Fe^{2+} oxidation and then hydrolysis and precipitation of Fe^{3+} complexes. Oxygen is the main oxidant of pyrite at neutral pH, in which the presence of bacteria is very important to catalyze the reaction, whereas ferric iron is the major oxidant at low pH due to its high solubility (Singer and Stumm, 1970). Fe^{3+} increases the reaction rate from ten to hundred times faster than oxygen (Ritchie, 1994) and oxidation rates due to presence of bacteria (e.g. *Acidithiobacillus ferrooxidans* and *Thiobacillus ferrooxidans*) are up to factor 10^5 faster than in the

absence of it (Singer and Stumm, 1970; Morin and Calas, 2006). The oxidation of Fe^{2+} to Fe^{3+} in sulfides is the energy source of some of the bacteria.



The presence of bacteria (e.g., *A. ferrooxidans*) increase the rate of reaction



Actually, the ARD/AMD is not a sudden phenomenon, but it formed in graded stages. Broughton and Robertson, 1992 showed that the pH decreased in stages over time (Fig.2) controlled by the buffering mineral assemblages. Stage I has a near neutral pH range, the oxidation is carried out by oxygen and the released acidity is controlled quickly by the alkalinity within the rock (carbonate minerals). This stage can last for weeks, months or even years depending on the acid/neutralization potentials of the waste. Then the pH drops in stages as the alkalinity consumed (Stage II) depending on the nature of the neutralizing minerals. Here the sulfate, acidity and trace metal concentrations are increased. Buffering may be provided by metal hydroxides. Bacteria which catalyzed the oxidation predominated at pH around 4.5 to increase the rate of acid generation. In Stage III, the Fe^{3+} is the main oxidant and the pH buffering depends on silicate minerals dissolution (Broughton and Robertson, 1992).

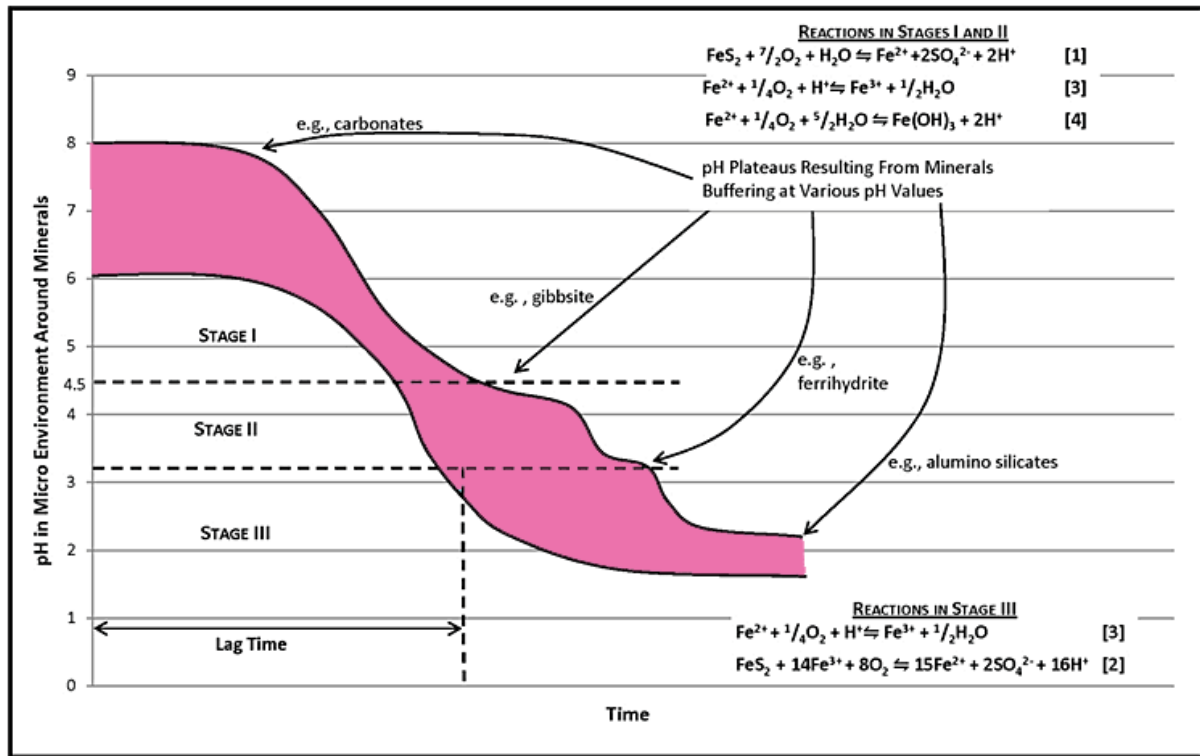
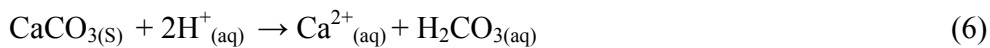
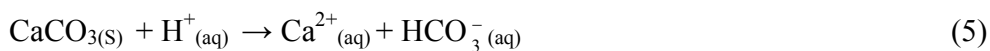


Fig.2. Acid rock drainage formation stages (after Broughton and Robertson, 1992).

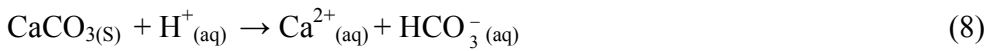
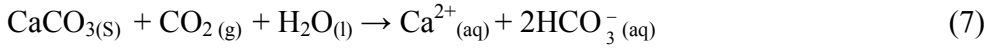
1.3. Natural attenuations reactions

Natural attenuation processes here include a variety of physical, chemical and biological processes that help to minimize the mass, mobility, volume and concentration of contaminants in the ground water. These processes include pH buffering and acid neutralization, adsorption at the mineral-water interface, mineral dispersion, and dilution/dispersion (Wilkin, 2007).

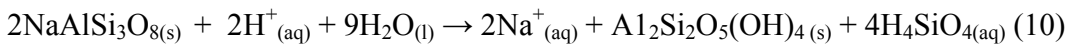
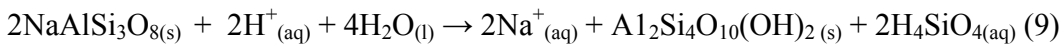
After the high acid waters formed due the sulfides oxidation, the gangue minerals are forced to react with the solution. Carbonate minerals (eg. calcite CaCO_3 , dolomite $\text{CaMg}(\text{CO}_3)_2$, ankerite $\text{Ca}(\text{Fe,Mg})(\text{CO}_3)_2$) play the key role in the buffering reactions, trying to stabilize the pH at near neutral conditions. For example, the end product of calcite dissolution is depending on the pH, producing either bicarbonate (HCO_3^-) in high pH medium or carbonic acid (H_2CO_3) in low pH medium.



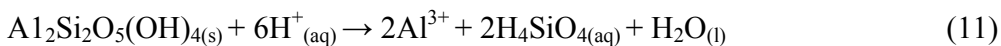
However, calcite solubility depends on the presence (open system, reaction 8) or absence (closed system, reaction, 9) of carbon dioxide (Stum and Morgan, 1981). In open systems like the unsaturated part of the waste rock piles, calcite solubility is very high, compared to low calcite solubility in the tailings due to the absence of CO₂ gas (Lottermoser, 2003).



Silicates and aluminosilicates participate to a lesser extent in buffering reactions due to their low solubilities compared to carbonates. This is governed by the acidity of the medium. Their dissolution rates are very slow (10^{-11} - 10^{-13} mol m⁻² s⁻¹; Banwart and Malmström, 2001) compared to those of carbonates (10^{-5} - 10^{-6} mol m⁻² s⁻¹). Lasaga and Berner (1998) showed that the lifetime for one mm crystal of calcite would take 0.43 years, compared to 575,000 years for albite, 921,000 years for microcline and 2,600,000 for muscovite, at pH 5 and 25°C. Also, the dissolution rates vary at different pH conditions. Reactions of silicates and aluminosilicates with acids will result in the transformation of some constituents to more acid-stable and less reactive minerals in addition to the release of other constituents into solution (Plumlee, 1999). Olivine and wollastonite have a high neutralization potential, larger than highly calcic members of the plagioclase feldspars, whereas sodic members have a much lower neutralization potential (Jambor et al., 2002). For example, dissolution of albite (NaAlSi₃O₈) can produce montmorillonite (Al₂Si₄O₁₀(OH)₂) or kaolinite (Al₂Si₂O₅(OH)₄), depending on the pH:.

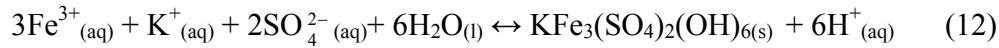


Silicates and aluminosilicates are responsible for the enrichment of elements like K⁺, Si⁴⁺, Al³⁺, Ca²⁺, and F⁻ in the pore-water (Acker and Bricker, 1992; Blum and Stillings, 1995). Also, clay minerals and aluminosilicates may dissolve and consume hydrogen ions in the reaction. For example, kaolinite may dissolve to form gibbsite:



Hydrolysis and precipitation of Fe³⁺ in the form of Fe³⁺ oxyhydroxides or Fe³⁺ sulfate is controlled by the pH-Eh conditions and the presence of elements such as potassium and sulfur (Nordstrom et al., 1979; Bigam et al., 1996). Three possible precipitates might result from this

hydrolysis (McGregor et al., 1998), namely; amorphous Fe hydroxide (Fe(OH)₃), goethite (αFeOOH) and K-jarosite (KFe₃(SO₄)₂(OH)₆).



Normally, these secondary crystalline and amorphous phases precipitate below the oxidation zone or even within it. With drying these precipitates, hardpans or cemented layers form (Thornber et al., 1987; Blowes et al., 1991; McGregor and Blowes, 2002; Rammlmair, 2002; Lee and Gilkes, 2005; Lottermoser and Ashley, 2006; Graupner et al., 2007; Rammlmair et al., 2008). The term hardpan/cemented layer generally is used in agriculture science in the description of a soil profile which acts as a barrier for root plat growth (Raper et al., 2005). It is formed by dissolution of the reactive materials due to the contact with rainwater, producing porewater with high concentration of dissolved components that move upward due to capillary transport under the effect of evaporation. At the capillary fringe, the water evaporates and the dissolved components precipitate as secondary minerals and gels, agglutinating the surrounding particles, locking pores (porosity decrease) and building up the hardpan (Rammlmair, 2002). Its formation is very important not only in coating the reactive sulfide minerals and preventing them from further reactions, but also in removing the contaminant from the water by adsorption/co-precipitation reactions (Blowes et. al. 1991; McGregor et al., 1998; McGregor and Blowes, 2002; Rammlmair, 2002; Zänker et al., 2002; Sánchez-España et al., 2005; Sidenko and Sherriff, 2005; Alakangas and Öhlander, 2006; Wang and Mulligan, 2006; Haffert and Craw, 2008; Carmona et al., 2009; Romero et al., 2010). These layers act as barrier protecting the heaps horizontally from further alterations by reducing or inhibiting water and even oxygen infiltration due to particle agglutination and pore filling (Rammlmair, 2002) and therefore reduce the acid drainage formation.

There are many factors controlling the process of hardpan/ cemented layer formation; some relate to the material itself according to its chemical, mineralogical and sedimentological premises, others relate to the climatic influence, in addition to other parameters like the density, surface area, pore size and shape, water saturation, capillary size, solution chemistry, evaporation/precipitation level, re-dissolution, viabilities, etc. (Rammlmair and Meyer, 2000).

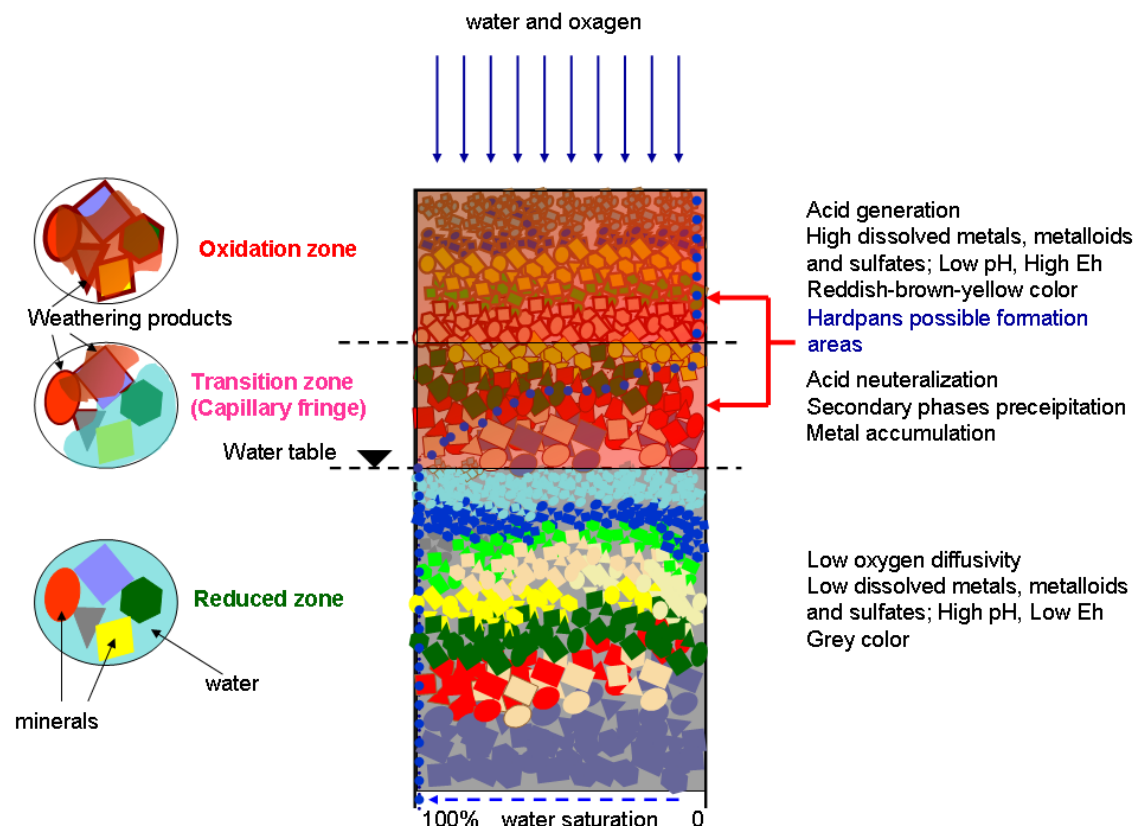


Fig.3. Simplified diagram showing the formation of hardpan layer within the transition zone (modified after Blowes et al., 1994).

Graupner et al. (2007) differentiated between the hardpans and cemented layers, as hardpans are produced at the capillary fringe due to agglutination of particles under the action of capillary transport within an oxygen dominated environment. Precipitation of secondary phases and gels happen due to supersaturation, around the grains, and reduces porosity. Whereas cemented layer formation, occurs at the transition between oxidized (unsaturated) and reduced (saturated) zones, due to variations in master geochemical variables, such as pH and Eh. The heterogeneous distribution of grain sizes and reactive materials, and the occurrence of sulphide-rich layers on top of low permeability layers in tailings (Graupner et al., 2007), the production of micro-porosity and micro-channels due to selective leaching of reactive phases (Rammlmair, 2002), as well as the addition of carbonate-rich buffering material during the late stages of tailings deposition (Blowes et al., 1991) would enhance the formation of hardpan and cemented layers.

Hardpan formation is known from semi arid to arid climates and has also been detected in humid climates (Rammlmair, 2002). An increase in temperature seems to increase its formation rate and

continuous rain precipitation seems to reduce the chance of hardpan formation because of the downwards-directed water flow (Jung, 2003). As the seasonal variations of climate determines the evaporation conditions and the water availability, consequently controls the succession of precipitation-dissolution cycles (Dold and Fontboté, 2001; Valente and Leal Gomes, 2009). Also, topography and erosion diversify the microclimate conditions that behave as thermodynamic microenvironments for precipitation at the waste-dumps (Valente and Leal Gomes, 2009).

1.4. Thesis Objectives

The main focus of this study is to investigate the formation of hardpans/cemented layers in different environments (climatologic influences on its formation) in relation to the mineralogical and geochemical composition of the tailings and its potential to reduce the contaminant distribution in the area as a natural phenomenon. Therefore, tailor-made columns for kinetically interdisciplinary investigations in combination with non-invasive measuring techniques will be developed. Since hardpans/cemented layers may play an important role in the natural attenuation of potentially toxic elements, the newly formed secondary phases will be studied for their mineralogical composition, their crystallinity, and for the amount of accumulated metals in phases of different crystallinity. Particular attention is paid to the neutralization and acid potentials of these tailings material and its possibility for acid production.

The thesis is divided into four main parts:

The first two chapters related to the investigation on the possibility of hardpans formation in two different climatic regions; Germany and Egypt. The other two related to investigations done on column experiments regarding the element mobility and hadpans formation. These chapters are as follows:

I- Studying one mine tailings impoundment from south-eastern Germany (Freiberg, Davidschacht mine tailings), representing a moist continental climate environment. This chapter was named '**Hardpan formation in Davidschacht mine tailings impoundment, Freiberg, and its affect on metals attenuation**'. This chapter was divided into two parts, the first part is general information about the distribution of hardpans within the tailings impoundments and the other part focuses on the upper surface layers of the area.

II- Studying two mine tailings impoundments from two gold mine tailings in the Eastern Desert of Egypt which represents a dry tropical (desert) climate environment. This chapter is named '**Hardpan formation in Egypt: Possibility and environmental risks**'.

III- Laboratory work – method development: Design of columns for kinetic interdisciplinary investigation. This chapter is named '**New columns design for the investigation of ions accumulation in the capillary head in unconsolidated sands**' in which a combination of non-destructive methods of water saturation (Hopmans et al., 1992; Garnier et al., 1998; Bayer et al., 2004) and conductivity (Furche et al., 2007) measurements of some soil columns of varied grain sizes using x-ray absorption and multi-level electrical conductivity was utilized. Additionally sampling ports were installed at different levels, for temperature, oxygen, rhizons (for water sampling) and pH, in addition to a set of balances to monitor water evaporation.

IV- Laboratory work – climatologic experiments. This chapter is named '**Effect of temperature and water content on hardpan formation in mine tailings: column experiments**'. The columns were filled with material of defined composition (from polymetallic sulphide tailings brought from Freiberg mine site). Firstly, the material was physically, mineralogically and chemically characterized. The columns were subjected to the influence of varying climatic premises such as changing amount of water input and variable temperature. The experiments were run for 6 months.

Here, water and ion transport phenomena were monitored using Geoscanner (EDXRF) in addition to multilevel conductivity measurement. Minimal impact was applied to investigate oxygen, temperature, and pH/Eh changes with time by using several ports distributed along the depth of the column. At the end of the experiment, the columns were subject to different analysis to investigate alteration, mineral changes, secondary phases developed, as well as the attenuation of different metals in relation to the climatic conditions prevailed.

V- Summary and conclusions. This chapter include a detailed discussion and summary and of the different results carried out in this study.



**Hardpan formation in Davidschacht
mine tailings impoundment, Freiberg
and its effect on metals attenuation**

PART I. Characteristic features of the hardpan along the whole tailings impoundment.

I.1. Abstract

The Davidschacht mine tailings impoundment was investigated to show the extend of the hardpan layers and the grain size variations along four surface profiles at the flat top and five detailed sections laterally displaced along a discontinuous profile at the western flank. Each quasi horizontal profile has its unique properties due to the spilling process itself and changing of the type of discharged mine tailings. Regarding grain size distribution, fine silt and clays are concentrated in the centre of the impoundment and toward the east, while medium-fine grained sands are localized in west-nord direction. Alteration of sulfides and silicates after deposition was not homogeneous. Besides completely unaltered lamina, all stages of replacement and alteration were observed, ranging from incipient to total alteration, with the formation of sulfates and gels of different compositions. In highly altered zones, all the arsenopyrite was consumed during the oxidation, leaving pyrite and other sulfides behind. The distribution and percentage of secondary crystalline and amorphous phases depend mainly on the percentage of sulfides, carbonates and other silicates at definite horizons. Attenuation of toxic elements especially As takes place in the amorphous gels and to a lesser percent in the crystalline phases. From microprobe analysis, amorphous gels contain the highest concentration of As with max. of 39.4% As_2O_3 , 6.8% PbO, and 6.2% ZnO; jarosite contains max. 15.6% As_2O_3 , 1.8% ZnO, and 1.5% PbO; and the max. content of As_2O_3 in gypsum is 1.4%. Scorodite nodules adsorbed some trace elements like In and Bi, Cu and Pb, as measured by microprobe analysis, in the range of 0.11 up to 0.16%. The sulfide content, as well as gel, gypsum and other secondary phases were higher in the lower sections compared to the upper sections of the profile at the flank. This relates either to amelioration of mineral extraction, but more probably to the longer transport pathways, as the sampling of the upper level was performed about 10 m off the edge due to excavation.

I.2. Introduction

Mining, mineral treatment, metallurgical activities, and subsequent deposition of mining wastes, have a major impact on the environment, which is due to rock drainage, exhalations as well as wind transport of aerosols, dust and fines, and sometimes dam failure. After extraction of the economically important minerals from the sulfide ores by flotation, a large volume of finely ground

sand- to silt-size waste material is usually transported in the form of a suspension to tailings impoundments for final deposition (Blowes et al. 1991; Robertson, 1994). After deposition, these materials are affected by various alteration and diagenesis processes. The interaction of sulfide-bearing tailings with water and oxygen causes the formation and release of Acid Rock Drainage (ARD), which is strongly enriched in sulfate, ferrous iron and other metals and metalloids, into ground water or rivers (Blowes et al., 1995, Johnson et al., 2000; Nieto et al., 2007; Courtin-Nomade et al., 2009). In addition, the finest particles of the wastes may spread out by wind or by exhalation of volatile products (Rammlmair and Grisseemann, 2000).

In some sulfide bearing mine tailings, an interesting feature can be observed as a result of oxidation/cementation processes, namely the formation of hardpans or cemented layers (Thornber et al., 1987; Blowes et al., 1991; McGregor and Blowes, 2002; Rammlmair, 2002; Lee and Gilkes, 2005; Lottermoser and Ashley, 2006; Graupner et al., 2007; Rammlmair et al., 2008). Hardpans and cemented layers refer to regions of reduced porosity due to a local accumulation of weathering products. Blowes et al. 1991 considered that cemented layers represent primitive stages in hardpan development. Graupner et al. (2007) differentiated between them, using the term hardpan for the formation of crusts at the capillary fringe due to the agglutination of particles under the action of capillary transport. They used the term cemented layers for the crusts formed at the transition between oxidized (unsaturated) and reduced (saturated) zones, which is due to variations in master geochemical variables such as Eh and pH. The heterogeneous distribution of grain sizes and highly reactive mineral phases, and the occurrence of sulfide-rich layers on top of low permeability layers in tailings favour the formation of cemented layers (Graupner et al., 2007). In the present study, we applied the term hardpan to layers where secondary phases clogged pores and agglutinated fragments, either detected at the tailings top surface or at the boundary between the oxidized and unoxidized tailings, which were consolidated as these zones dried out.

Hardpan formation involves the dissolution of reactive materials due to contact with oxygen and rain water; usually mediated by microbiological activity, which generates pore water with a high concentration of dissolved components. This pore water may move upward due to evaporation driven capillary transport. At the capillary fringe, the water evaporates and the dissolved components precipitate as secondary minerals and gels, agglutinating the surrounding particles, locking pores and building up the hardpan (Rammlmair, 2002). The main environmental and economic implications of hardpan formation involve the accumulation of dissolved metals in certain zones (Blowes et. al. 1991, McGregor and Blowes, 2002; Rammlmair, 2002; Sánchez España, et al.,

2007) due to sorption/co-precipitation (Alakangas and Öhlander, 2006). Furthermore, hardpans may protect the heaps from further alterations by reducing or inhibiting water and even oxygen infiltration due to particle agglutination and pore filling (Rammlmair, 2002).

Hardpans will only be formed under certain circumstances as a result of a coincidence of a number of key parameters. For hardpan formation these key parameters include the critical amount of reactive minerals and their accessible surface areas, heterogeneity regarding grain size distribution, as well as the occurrence of sulfide-rich layers on top of impervious layers near the reactive phases (Graupner et al., 2007), and in some cases the addition of carbonate-rich buffering material during the late stages of tailings deposition (Blowes et al., 1990). For hardpan formation at the capillary fringe, key parameters include the critical amount of reactive minerals and their accessible surface areas, pore shape, pore size, water saturation, capillary size, solution chemistry, evaporation/precipitation level, re-dissolution, and viabilities (Rammlmair and Meyer, 2000). Redwan and Rammlmair (2010) documented in column tests the effect of extreme ion accumulation in the rising capillary head with the effect of “first come, first serve” and a strong depletion of ions in the slower moving fluids in the deeper parts. These supersaturated fluids feed hardpan formation at the capillary fringe. Besides the depositional environment, the overall climate of the area as well as the microclimate at the site is important. Continuous rainfall at the capillary fringe may prohibit hardpan formation due to slow wash out and downward movement of the water flow. Very dry climates will not allow a storage of enough water for reaction times long enough to substantially promote the oxidation of sulfides in the tailings. Therefore, episodes of intense rain fall (winter times) with surface parallel run off, followed by dry periods promoting evaporation (summer times) may be ideal for hardpans formation at both the capillary fringe and at transition zones (Jung, 2003). However, investigations of the development of the hardpan formation process at the micro-scale are not substantiated in the literature.

Modern SEM-based mineral liberation analysis is fundamentally used for optimizing process plant design and for detailed characterization, quantification and evaluation of the ore during mineral processing operations. MLA is used to increase the speed and the accuracy of the liberation analysis compared to the costly and time consuming traditional tools of using an optical microscope and/or a semi-automated SEM, which give semi –quantitative results (Fandrich et al., 2007). MLA gives information about a wide variety of mineral properties such as grain sizes, mineral abundances, mineral texture and degree of liberation for the ore. However, MLA has not been applied to study mine dumps and tailings. The application of MLA on thin sections of tailings

materials may be very useful, because information about the mineral assemblages in the μm to mm scale can easily be obtained. Additionally, variations in chemistry of amorphous gel phases, which can hardly be identified using normal optical microscopy, can be mapped for better understanding of the fluid behaviour within the pores. The focus of this part is to characterize the the mineralogical, geochemical and physical properties of the hardpan layers in Davidschacht mine tailings.

I.3. Site Description and history of the impoundment

For more than 800 years, the polymetallic sulfide deposits of Freiberg have been mined for silver, lead, copper and zinc. The Late Variscan polymetallic sulfide mineralizations are characterized by two ore paragenesis. The mineralizations are structurally controlled (orientation NNE–SSW to N–S and E–W to ENE–WSW) and were generated by multi-stage hydrothermal activity in the vein and shear zone systems. The host rock in the Freiberg district includes gneisses, mica-schists, and amphibolites. The first ore paragenesis includes sulfides and quartz with some carbonates formed during hydrothermal reactivation, the later one contains re-deposition of sulfides, carbonates and/or barite (Baumann et al. 2000; Tichomirowa, 2002).

The Davidschacht mine shaft is the main shaft of the Himmelfahrt Fundgrube mine (north-east of the town of Freiberg). The flotation process was conducted in three successive steps: First -flotation of PbS, then of ZnS and finally of arsenic bearing FeS_2 . Flotation was done at pH 7-8. Starting from 1952, NaCN was added to the processing for technological reasons. The entrance of free cyanide into the drained waters (Freiberger Mulde) was prevented by adding calcium chlorite in the final stage as a bleaching agent (GEOS report, 1993).

The Davidschacht mine tailings impoundment is located to the north of its shaft (Fig. 1.1) and has an artificial dam downslope to the N and E (Fig. 1.2). The tailings deposited from 1951 to 1964. Most of the materials came to the impoundment due to mining from the first ore paragenesis (pyritic lead formation ‘Kb’, which is a quartz-bearing $\text{As}(-\text{Au})-\text{Zn}-\text{Cu}(-\text{In}-\text{Cd})-\text{Sn}-\text{Pb}-\text{Ag}-\text{Bi}-\text{Sb}$, polymetallic sulfide vein-type mineralization with arsenopyrite, pyrite/marcasite, pyrrhotite, Fe-rich sphalerite, stannite, chalcopyrite, cassiterite, tetrahedrite, bornite, and galena. Quartz is the main gangue mineral, with rare carbonates (eg. calcite, dolomite, siderite and rhodochrosite (Seifert and Sandmann, 2006). Limestone was added to the impoundment from Hermsdorf (GEOS report, 1993). The feed was done mainly from the dam, also from the west using pre-separated coarser material as wall. During the spilling processes, the spigot point developed grain sizes and mineral

fractionations along and across the spilling direction. Lamina developed, each one is different in grain size and composition.

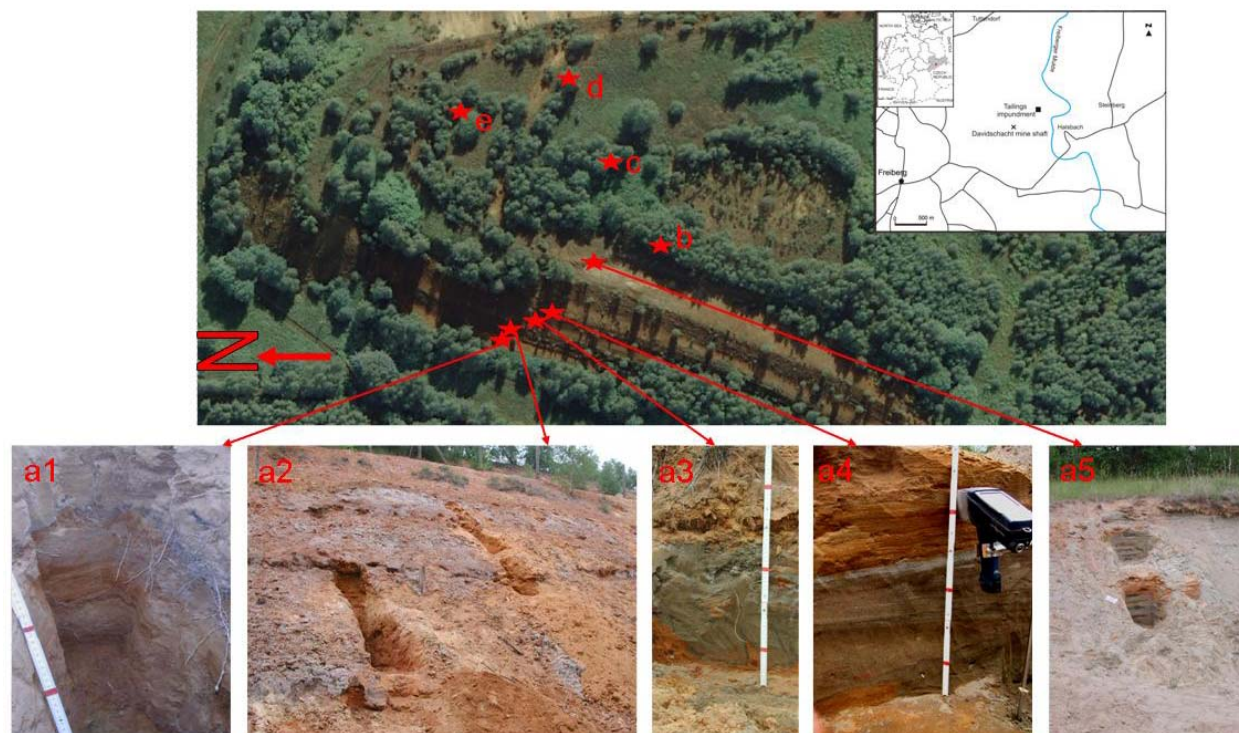


Fig. 1.1. Location map of the study area with sampling locations indicated on an aerial photograph taken on 2007 of Davidschacht tailings impoundment, with profiles position taken on the western side and on the top surface (ATKIS[®]-DOP, © Staatsbetrieb Geobasisinformation und Vermessung Sachsen 2008).

The height of the impoundment reaches 60 m, ranging from 360 m to 420 m in elevation, and covers a surface area of 7.5 ha. The volume of the waste material stored at this site was estimated to be approx. 1.3 Mt (GEOS report, 1993). The average metal content of the heap material was determined to be 0.25 wt. % Pb, 0.24 wt. % Zn and 5.57 wt. % S (GEOS report, 1993). The tailings impoundment was partly covered with coarse sand, topsoil (thickness of cover: 0-0.2 m) and plants. The tailings impoundment contains oxidized layers and hardpans at the western flank, and generally also at the top of the impoundment below the plant covers, which indicate that the plant cover was added recently after oxidation began. The hardness of the hardpan layers varies, depending on the percentage and distribution of secondary crystalline and amorphous phases in it. The colours range from dark orange to dark brownish, and range from violet, whitish grey to dark grey.

Detailed investigations of the hardpans have been studied along the western flank of Davidschacht tailings impoundments. The lower sections of the slope profile are fully oxidized down to 50 cm below slope surface, and most of them consist of thick hardpan layers interrupted by unoxidized-oxidized layers and some clay lenses of few centimetres in distribution. The profiles studied are one along the western side of the tailings impoundment (Fig.1.1, a1-a5), and four surface profiles (Fig. 1.1 b, c, d and e).

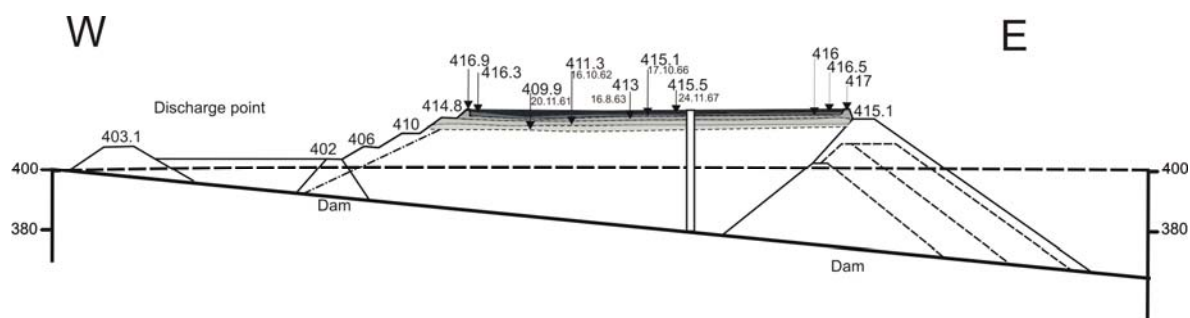


Fig. 1.2. Davidschacht tailings dam construction sequence (All numbers refer to the elevation above sea level), simplified after GEOS report, 1993.

I.3.1. Climate

The area around Freiberg is mainly influenced by a continental climate, by hot summers and cold winters. In 2008 a total rain precipitation of 945 mm/y was reported with an average temperature of 21.3°C. The sampling was done at the first of June 2008. Total rain precipitation in May 2008 was 42 mm and the average temperature was 13.9°C (Data were taken from the Eppendorf, Saxonia weather station, <http://wetterarchiv.wetter.com/station/2864/>). According to Hänsel and Matschullat (2006), the years 1953/54, 1959, 1962/63, 1972, 1976, 1982/83, 1990/91, 1996 and 2003 are considered as the major Saxon dry periods, which relate to relatively high evaporation rates in these periods.

I.4. Methods

The physical, geochemical and mineralogical characteristics have been studied for each of these layers. First the unoxidized tailings samples were homogenized, whereas hardpan and oxidized samples were crushed before homogenization. Then both types were split into a number of aliquots using a sample splitter. One aliquot was used for the determination of the gravimetric moisture content. Two other aliquots were dried at 30°C, one was used to measure the particle size distribution, particle density and BET. The other was ground to grain sizes less than 5µm with a RS

200 instrument with an agate milling set (Retsch GmbH), in order to measure particle density and perform X-ray fluorescence (XRF), X-ray diffraction (XRD), and LECO analyses. The fourth aliquot was used for a paste water extraction experiment. Polished sections and polished thin sections were done for the hardpan blocks and for the unoxidized samples on a dry basis regarding, cutting and polishing. The different analysis techniques are described in detail below.

I.4.1. Physical properties

Gravimetric moisture content, particle density, and BET were determined for the unoxidized and oxidized samples, whereas particle size distribution was done only for the unoxidized samples.

Moisture content (wt.%) was estimated using the gravimetric difference between wet and oven dried samples for one day at 105°C. The particle density of the tailings and hardpan layers was measured twice using an AccuPyc 1330 Helium pycnometer instrument (Micromeritics Instrument Corporation), for the normal sandy samples and for the powdered samples after grinding, respectively. The particle size distribution was measured in two steps. For grain sizes larger than 63 µm, a CAMSIZER instrument (Retsch GmbH) was applied, whereas for grain sizes less than 63µm a SediGraph 5100 instrument (Micromeritics Instrument Corporation) was applied. This particle size analysis method was not used for hardpan samples as already consolidated. The specific surface area was determined by nitrogen gas adsorption measurements with a Gemini III 2375 Analyzer instrument (Micromeritics Instrument Corporation). Samples were degassed overnight prior to analysis and the specific surface area was calculated using the BET (Brunauer, Emmett and Teller, 1938) equation.

I.4.2. Geochemical properties

X-ray Fluorescence spectroscopy (Philips PW1480 and PW2400) was applied to measure the bulk chemical composition of all the samples. A LECO furnace instrument (LECO Corporation, model CS-200) was used to measure total sulfur (S-total), total carbon (C-total), and organic carbon (C-org) concentrations. Carbonate carbon (C-carb) was calculated as the difference between C-total and C-org.. S-sulfate was measured by attacking the sample with 0.2 M NH₄-oxalate for 2 hours at pH 3.0 (controlled by adding 0.2 M oxalic acid) in a water bath at 80°C. The dissolved sulfur content was measured by ICP-OES, which represents S-sulfate (Dold, 2003). Then sulfide sulfur (S-sulfide) content was derived from the difference between S-total, after subtracting the sulfur equivalent for Ba in barite measured by XRF, and sulfate sulfur (S-sulfate).

A paste extraction on all the samples was performed at distilled water to solid ratio of 1:1. With a Heidolph Reax Overhead Shaker (Heidolph Instrument Corporation) the mixture was continuously

shaken for 24 h at room temperature. The extractant was then filtered using a 0.45 µm filter (type FP30, Whatman International Ltd.). The pH and conductivity measurements were performed on the extractant using a Pocker-size precision pH meter CG 837 (Schott Instruments GmbH), and a microprocessor conductivity meter type LF 323-B/set, model TetraCon 325 (Juergens &Co GmbH, Germany), respectively). The pH electrode was calibrated using pH 4 and 7 buffers before and between a series of measurements.

Samples with a pH lower than ~ 5 were acidified to preserve metals in solution by adding a few drops of HNO₃ (69% concentration) until the pH was lower than 2 (controlled by pH paper), then the extractant was analysed by ICP-QMS (Agilent 7500ce) for trace elements and by ICP-OES (SPECTRO Analytical Instruments GmbH, model Ciros Vision CCD) for major cations and S. Samples with a pH higher than 5 were divided into two aliquots, then one was subjected to HCO₃ titration, the other one was acidified and analysed by ICP-QMS and ICP-OES.

The ITRAX X-ray Microscope (Cox Analytical Systems, Sweden) (Fig. 1.3) is used for multi-elemental mapping of vertical or horizontal polished slices of sizes up to 20x30 cm, which mounted on an xyz-stage. It is based on a Rich. Seifert & Co. ISO-DEBEYEFLEX 3003 HV-Generator and a 3 kW, 60kV long fine focus Philips XRD Mo tube Type PW 2275/20. However, the beam is focused by a glass mono-capillary to 100 µm diameter. The energy dispersive RÖNTEC XFlash Si(Li) detector of 139 eV resolution with an evacuated nozzle mounted in 45° between detector and sample (Rammlmair et al., 2001). Analyses can be performed in three different modes, points and profiles, where the complete obtained spectra are saved for further matrix correction, and areas, where the count rates for selected channels attributed to individual elements are stored. A number of individual points, profiles or areas for analysis can be selected via the optical camera. First the elements of interest selected, then the time for each analysis (min 0.5 sec), and the individual step size (100 µm standard) chosen. The measuring spot and the lateral analytical resolution can be selected in the 1000-10 micrometers range.

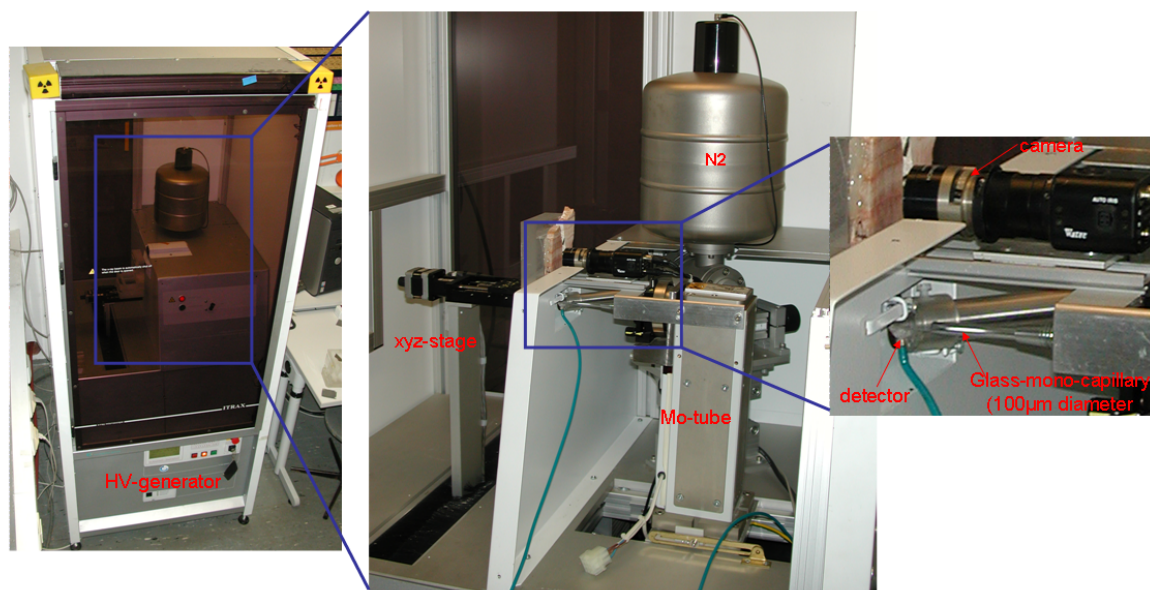


Fig. 1.3. ITRAX microscope with its different components.

Disadvantages of the system are that light elements can hardly be detected at short exposure times. Even if the geometry for each sample point is similar, points at the sample edges show shadow and edge effects for certain elements. Since the diameter of the beam sometimes is in the range of individual grains, X-ray diffraction patterns of certain minerals might cause overlap with other element channels. Also, variable sample thickness at different points, pore size or changing matrix density might influence the count rate.

The electron microprobe (EM; CAMECA SX-100 microprobe) analysis was applied to study the alteration stages within the sulfides especially the amorphous gels and poorly crystalline phases, jarosite- group minerals and gypsum from the hardpan layers as well the compositions of some unoxidized minerals like the carbonates, sulfides and silicates. Operating conditions were a 15 kV accelerating voltage and a 20 nA beam current and reduced to 12 kV for carbonates. Mineral standards were used for the quantifications and element data for the altered materials were obtained using a TAP crystal for Si $K\alpha$ Al $K\alpha$, Mg $K\alpha$, Na $K\alpha$ and As $L\alpha$ analysis; a PET crystal for K $K\alpha$, Ca $K\alpha$, Ti $K\alpha$, Ba $L\alpha$, Sb $L\alpha$, Bi $M\alpha$, Tl $M\alpha$, Cl $K\alpha$, P $K\alpha$, Sn $L\alpha$, In $L\alpha$, Ag $L\alpha$, Pb $M\alpha$ and S $K\alpha$; and a LiF crystal for Fe $K\alpha$, Mn $K\alpha$, Cr $K\alpha$, V $K\alpha$, Cu $K\alpha$, Ce $L\alpha$, Co $K\alpha$, Ni $K\alpha$ and Zn $K\alpha$. Detection limits under the applied measurement conditions for most the elements are lower than 700 ppm.

Geochemical speciation calculations have been performed to investigate solubility controlling processes for major and minor elements in the tailings samples. Thereto, the PHREEQC code

version 2.16.03 (Parkhurst and Appelo, 1999) was applied, using the minteq database (Allison et al., 1990). This database was modified by adding additional equilibrium constants for As(V) aqueous species as well as a solubility constant for scorodite ($\text{FeAsO}_4 \cdot 2\text{H}_2\text{O}$) based on data by Langmuir et al. (2006), and by taking the K-jarosite solubility constant from the PHREEQC database.

I.4.3. Mineralogical properties

The bulk mineralogy of all the samples was analyzed by powder X-ray diffraction (XRD), using a Philips PW 3710 series automated powder diffractometer, with monochromated $\text{CuK}\alpha$ (mean wavelength of 1.542 Å) radiation. It was operated at 40 kV and 30 mA, with glancing angles 2θ between 2° and 65° , in addition to using a secondary graphite crystal monochromator. For evaluation of the data the software package Galaxy linked with a PDF2 database was employed.

Polished sections and polished thin sections were investigated with an optical microscope and subsequently with an Environmental Scanning Electron Microscope (ESEM, type FEI Quanta 600 FEG) coupled with an energy dispersive X-ray (EDX) detector (Apollo XL from Ametek Inc.) for detailed characterization, identification, and quantification of primary and secondary crystalline and amorphous phases as well as for textural relationships using MLA software package (Mineral Liberation Analyzer, JKTech).

Although MLA is generally operated in the high vacuum mode of the SEM, the low vacuum mode was used to be able to investigate the samples without enhanced desiccation of the pore filling gels. The first step in the application of MLA is the generation of an adequate mineral standard database. This is done by collecting EDX spectra for each phase of interest. The BSE images obtained from the SEM allow a differentiation of individual phases according to their grey values. These phases can subsequently be identified using single x-ray analysis collected within the centre of each grain or by using x-ray mapping. The best but unfortunately most time consuming method to be applied for the investigated material was x-ray mapping with the GXMAP (Ford analysis or grain-based X-ray mapping) method. A grid was created over each grain and X-ray data were collected at each point of the grid as described by Fandrich et al. (2007) and Dobbe et al. (2009). This method was used to overcome the drawback of the XBSE (Extended BSE liberation analysis) method, which collects one spectrum in the centre of each particle after de-agglomeration, and cannot discriminate between minerals with the same atomic numbers. Because the investigated material shows very distinct changes in the micrometric scale, the de-agglomeration process, which deletes the connection between particles, had to be de-activated during the measurements. In our investigations, we used the XBSE method in areas with low mineral grains accumulations, and the

GXMAP method in areas with dense mineral accumulations. From the collected EDX spectra for each mineral and the measured spectra for the regions of interest, we obtain the classified MLA image.

MLA results were used to calculate the particle (by cancelling the porosity) and bulk densities for the unoxidized and hardpan layers in the top surface layers, by multiplying the percentage of each primary or secondary mineral by its density value got from other publications (e.g. Smyth and McCormick, 1995).

I.5. Results and discussions

I.5.1. Physical properties

I.5.1.1. Moisture content

The moisture contents of the samples were quite variable; depending on grain size distribution, degree of alteration and percentage of gel phases. Generally, samples in the upper part of the profile (a4-a-5) contained lower percentage of water compared to the lower part of the profile (a1-a3). The LOI values for the hardpan layers were higher than those for uncemented layers (Fig. 1.7).

I.5.1.2. Particle size distribution

Particle size analyses for the unoxidized samples showed that they were mainly well sorted, medium grain to fine sands with very little silt and clay (Fig. 1.4). Profile (a5) is about 10 m off edge and showed therefore smaller grain sizes than expected at the edge. For the rest of profile (a), the silt percentage increased in the lower parts with several layers enriched in the clay fraction. The surface profile (b) showed similar pattern to profile (a), but at the lower parts the silt to sand pattern reached 1:1 with increased percentage of clay (20%). Profile (c) showed in the upper parts higher percentage of silt and its lower part it dominated by silt with lower percentage of clay (it has the lowest values of geometric mean grain size, Fig. 1.4). Profile (d) showed higher percentage of silt at the middle depths and decreased at the lower depths. Profile (e) showed higher percentage of sand almost along the whole profile with some silt and little clays. For the hardpan layers, the grain sizes were in the range of medium to fine grained sizes as concluded from scanning the polished sections and polished thin sections with MLA.

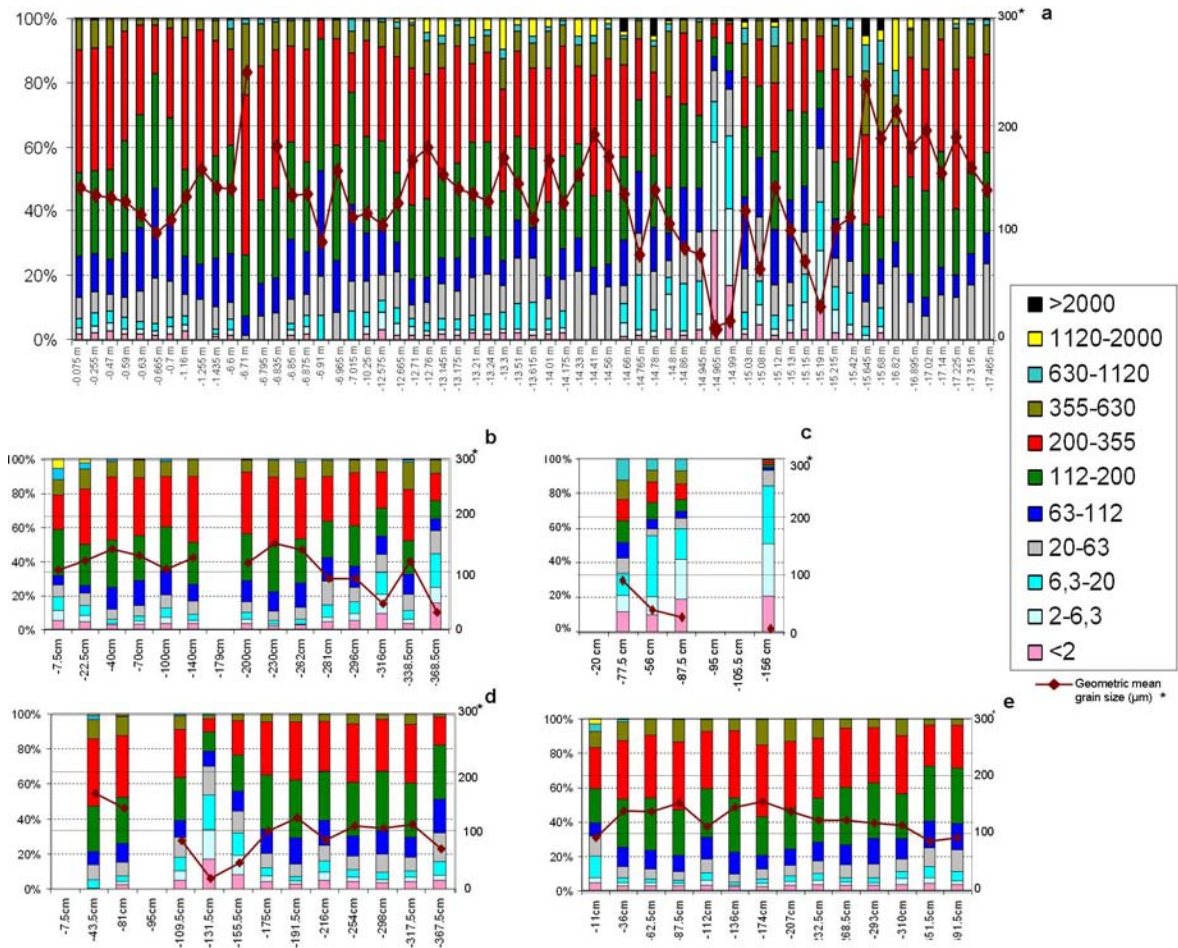


Fig. 1.4. Grain size distribution (weight percent) and geometric mean grain sizes (μm) of the samples in the measured profiles. Grain sizes (legend) are in micrometers.

1.5.1.3. Specific surface area (BET)

The specific surface areas are in part related to the grain sizes, for example for clay layers it reached max $42.5 \text{ m}^2 \text{ g}^{-1}$. Values for the hardpan layers were usually increased whilst unoxidized layers showed a decrease (Fig. 1.7). The increase in the surface area in the hardpan layers is related to selective dissolution of phases or particles or to precipitation of secondary products which might enhance the surface area up to a factor of 10,000 for individual mineral sponges (Rammlmair, 2002). He postulated a significant role in increasing water retention, and therefore prolonged reaction times, in transport, and capillary transport capacity at an oscillating capillary fringe zone, where precipitation of the dissolved materials and colloids takes place as gels or secondary phases.

I.5.2. Geochemical properties

I.5.2.1. Bulk rock chemistry

The samples investigated show distinct differences in composition. Comparing oxidized hardpans with almost unoxidized samples on a dry basis. Fe₂O₃ appeared enriched, whereas MnO, MgO, CaO, SO₃ are low in the upper part of profile (a) and enriched in the lower parts. For profile (b), it showed enrichment of Fe₂O₃, MgO, Al₂O₃, NaO and K₂O in the hardpan layers, but low values in profiles c, d and e. As become higher in the upper surface layers in profile b, d and e, and increased in the lower parts of profile c. Zn increased in the lower parts of profile b, c, e and Pb higher in the upper parts of profiles c, d and e, and decreased in b (Figures 1.7 and 1.8, Table 1.2).

I.5.2.2. Acid Neutralization

The potential of the unweathered layers in the upper profile (a5) to form AMD was estimated on the basis of the acid potential (AP) and neutralization potential (NP) of the material after Lawrence and Wang (1997). The NP provides a measure of the ability of waste materials to consume the acidity produced when sulfide minerals oxidize, and AP is a measure of the ability of waste materials to produce acidity.

Carbonate NP was calculated on the basis of C-carb and AP on the basis of S-sulfide, using Eq. 1 and 2, respectively (Lawrence and Wang, 1997).

$$\text{Carbonate NP (kg CaCO}_3\text{/t)} = \frac{\text{mg C in sample} \times 8.34}{\text{weight of sample (g)}} \quad (1)$$

$$\text{AP (kg CaCO}_3\text{/t equivalent)} = \text{S-sulfide (\%)} \times 31.35 \quad (2)$$

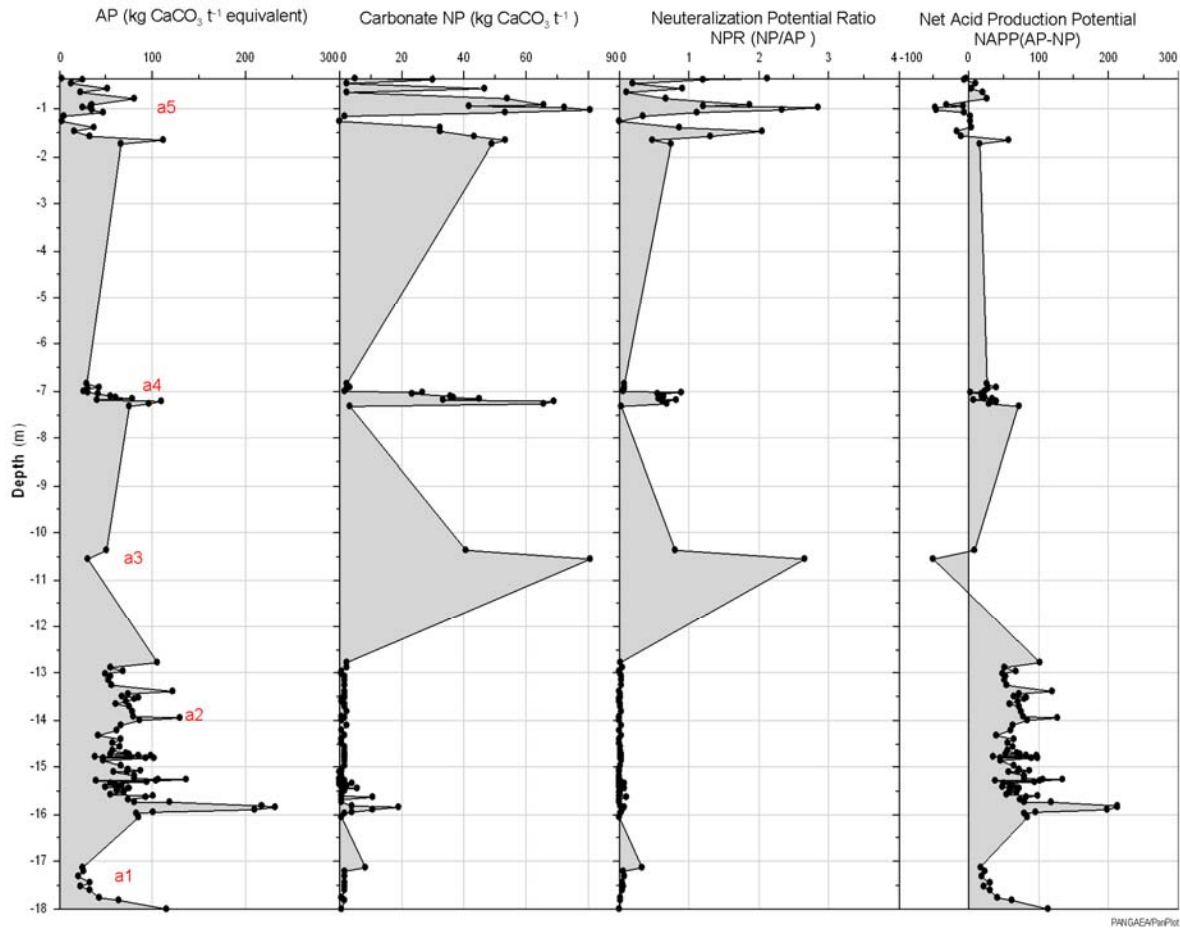


Fig.1.5. Changes of acid potential (AP), Carbonate neutralization potential (NP), neutralization potential ratio (NPR) and net acid production potential (NAPP) with depth.

The potential of the samples to form AMD was then evaluated on the basis of the net acid production potential (NAPP), which equals to AP-NP, and the neutralization potential ratio (NPR), which equals to NP/AP. According to Fig. 1. 5, the NPR is generally less than 1.0, the sulfide sulfur percent of the samples reached 7.4% (Fig. 1.7, Table 1.2), and the NAPP generally more than 20 kg CaCO₃ t⁻¹, indicating that these samples have a potential for producing acids. The NAPP shows a slight increase from top downward for both altered and unaltered samples.

1.5.2.3. Paste-water extractions

i-Carbonate dissolution and source of Ca, Mg and Mn

Increasing of the pore-water pH to values near 6.0 is an indication of carbonate minerals dissolution (Gunsinger et al., 2006). The paste pH for the unoxidized grey layers were around 7

(max. 7.78), however for hardpan layers it decreased sharply to values from 2 to 3, only for the top layer (below the soil cover) it reached 4.76 (Fig. 1.7). The increase within the unoxidized zones is due to pH buffering reactions, where the generated acid is completely neutralized by carbonate minerals. It also coincided with a carbonate carbon content increased in the unoxidized layers to 0.6% (average), compared to 0.04% (average) in the hardpan and oxidized layers and total alkalinity in the unoxidized layers reaching an average of 27.9 mg L⁻¹. Concerning conductivity, values for hardpan and oxidized layers (average 3.51 mS cm⁻¹) were higher compared to unoxidized layers (2.1 mS cm⁻¹), due to highly dissolvable metals and sulfate in these zones (Fig. 1.7). Note that these high values might relate to the enhanced accessibility due to crushing of the hardpans, where formerly protected areas are exposed to the fluid.

The average concentrations of Ca²⁺ and Mg²⁺ in the extracted water samples from hardpan layers are 527 mg L⁻¹ and 32 mg L⁻¹, respectively. The high concentration of Ca²⁺ may be due to the addition of limestone from Hermsdorf (GEOS report, 1993) to the tailings. Whereas the average concentrations of Ca²⁺ and Mg²⁺ in the extracted water samples from the unoxidized layers are 515 mg L⁻¹ and 29.4 mg L⁻¹, respectively (Fig. 1.7, Table 1.2). The Mg²⁺ content in the upper part of profile (a) is quite higher than that in its lower parts. The sources of high Ca²⁺ and Mg²⁺ concentrations in the oxidized zones, are from the dissolution of the calcite, ankerite (Ca (Fe Mg Mn) (CO₃)₂), dolomite (Ca Mg (CO₃)₂) and Ca-Mn, Ca-Mg-Mn siderite identified by XRD and SEM, in addition to Ca²⁺ and Mg²⁺ rich aluminosilicate minerals such as plagioclase and biotite. Ca²⁺ re-precipitated in the hardpan zone as well as in the unoxidized layers as gypsum, in the hardpan layers often associated to K-jarosite and some amorphous gels of variable composition.

The concentration of Mn²⁺ in solution is increased due to the dissolution of Mn-bearing biotite as measured by microprobe for the altered/unaltered grains, and probably also from amphibole and carbonates. The average concentration is 31 mg L⁻¹ within the hardpan and oxidized layers probably due to its desorption from amorphous gels (max. 0.41% using microprobe analysis). The average concentration decreased to 0.9 mg L⁻¹ in the unoxidized layers (Fig. 1.7).

ii-Silicate and aluminosilicate dissolution

The average concentrations of Si⁴⁺ and Al³⁺ in hardpan and oxidized layers are 156 and 169.4 mg L⁻¹, significantly higher than the concentration of both element in the unoxidized layers (25.6 and 0.28 mg L⁻¹, respectively) (Fig. 1.7). Potassium average concentration in the hardpan layers is 1.2 mg L⁻¹, this concentration increased in the unoxidized layers to 4.7 mg L⁻¹. The lower values of K in

the hardpan layers, probably due to its fixation in K-jarosite, which is less soluble in the applied extraction procedure.

The source of Si^{4+} , Al^{3+} and K^+ ions in the hardpan layers is basically the dissolution of aluminosilicate minerals, mainly biotite, amphibole, with probably minor contribution of muscovite, phengite, chlorite, illite and feldspars, all of them identified by XRD and SEM.

iii-Mobility and stability of sulfide oxidation products

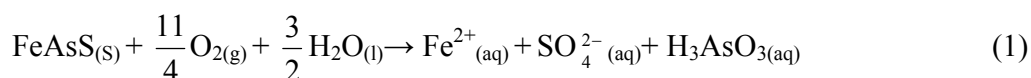
Iron

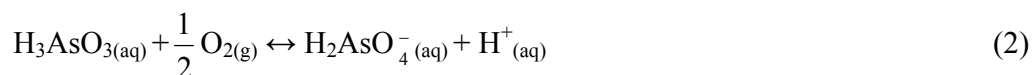
The main sources of iron in the extracted solution are due to the oxidation of sulfides, mainly pyrite and arsenopyrite and to a lesser extent the breakdown of the mafic minerals such as biotite and amphiboles at pH lower than 3. The average concentration of iron is 318 mg L^{-1} within the hardpan layers and 0.08 mg L^{-1} in the unoxidized layers (Fig. 1.7, Table 1.2). As we discussed before, the hydrolysis and precipitation of Fe^{3+} in the form of Fe^{3+} oxyhydroxides or Fe^{3+} sulfate depend on the pH-Eh conditions and the availability of elements like K and S (Bigham et al., 1996). Three possible precipitates, amorphous Fe hydroxide ($\text{Fe}(\text{OH})_3$), goethite (αFeOOH) and K-jarosite ($\text{KFe}_3(\text{SO}_4)_2(\text{OH})_6$) can be produced from the hydrolysis (McGregor et al., 1998). These secondary phases occurred as replacement of some primary phases or as cements filling the pores between the quartz and other silicates which resist the alterations.

Arsenic, Copper, Lead and Zinc

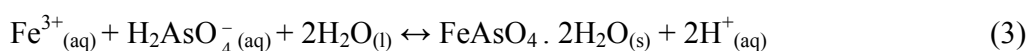
The primary source of arsenic is the oxidation and subsequent dissolution of arsenopyrite and arsenian pyrite. Oxidation of arsenopyrite (FeAsS) results in the release of sulfur and arsenic. Rimstidt et al. (1994) found that arsenopyrite is more reactive than pyrite, chalcopyrite, galena, and sphalerite in acid mine-drainage environments. Nesbitt et al. (1995) found that arsenopyrite reacted with air-saturated distilled water and gave Fe^{3+} oxyhydroxides as the main iron surface species, and As^{5+} , As^{3+} , and As^+ were as abundant as As^- surface species, with some amount of sulfate on the mineral surface.

Like pyrite, arsenopyrite oxidation involves many individual reaction steps. The following reactions are usually bacterially mediated (e.g. Tuovinen et al., 1994; Plumlee, 1999; Morin and Calas, 2006).



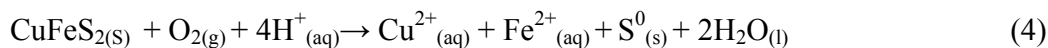


The average concentration of dissolved As in the hardpan layers with 9.9 mg L⁻¹ was found to be significantly higher than in the unoxidized layers with 0.18 mg L⁻¹ (Fig. 1.6, 1.7), i.e the concentration decreases with increasing pH. Some of the arsenic is attenuated by precipitation of scorodite (Dove and Rimstidt, 1985) by the reaction of Fe³⁺ with arsenate, which is more stable at low pH conditions (below pH 5, Haffert and Craw, 2008). However, other forms of ferric arsenates may be formed (Paktunc et al., 2004).



Also some arsenic can be incorporated in the jarosite structure, but its highest concentrations were found in the gel (amorphous) phases as identified by SEM-EDS analyses with a percent reached 39% as identified by microprobe analysis (Fig. 1.13 and Fig. 1.14, Table 1.1).

The main source of Cu³⁺ is the oxidation and dissolution of chalcopyrite. The dissolution rate of chalcopyrite depends on the associated sulfide minerals, that the presence of molybdenite or pyrite accelerated its dissolution (Dutrizac and MacDonald, 1973) and the presence of galena or iron rich sphalerite decrease its dissolution.



The average dissolved concentration of copper in the hardpan and oxidized layers is 22.4 mg L⁻¹, and 0.01 mg L⁻¹ in the unoxidized layers.

As galena (PbS) and sphalerite (ZnS) are considered as non-acid producing sulfides, but if iron, partially replaces zinc in the sphalerite structure (Pring et al., 2008) it will be considered as an acid generator like pyrrhotite (Walder and Schuster, 1998). The Pb concentration was very low in the extracted water samples compared to sphalerite. Sphalerite oxidation depends on some factors like the temperature, pH and the type of oxidant (O₂ or Fe³⁺) (Rimstidt et al., 1994; Olanipekun, 1999).

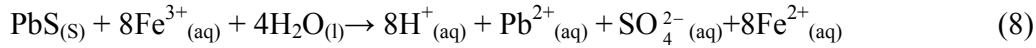


The average concentrations of dissolved Zn²⁺ in the hardpan layers is 8.4 mg L⁻¹, whereas the average value in the unoxidized zones reaches 0.75 mg L⁻¹ (Figs. 1.6, 1.7, Table 1.2).

Galena oxidation as a main source of Pb²⁺ in the tailings has been studied by a lot of authors (eg. Tossell and Vaughan 1987; Basilio et al. 1996; Shapter et al. 2000). By weathering galena in natural oxygenated environments, anglesite will form as alteration product, which is weakly soluble below pH 6 (Shapter et al., 2000).



under acidic conditions, galena can be oxidized by Fe^{3+} (Rimstidt et al. 1994)



The concentrations of dissolved Pb^{2+} were very low in the unoxidized layers (average 0.003 mg L^{-1}), whereas the concentration in the hardpan layers reaches an average of 0.07 mg L^{-1} (Figs. 1.6, 1.7, Table 1.2).

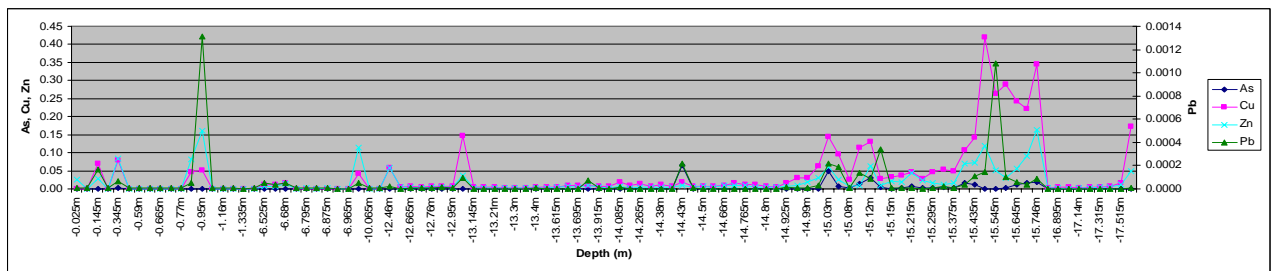


Fig. 1.6. Solid/dissolved ratios of As, Cu, Zn and Pb.

Sulfate

Sulfate has a very high mobility compared to the other elements. The water soluble fraction of the samples showed a higher concentration of SO_4^{2-} (average 3390 mg L^{-1}) in the oxidized zones (hardpan layers) compared to 1389 mg L^{-1} in the unoxidized layers (Fig. 1.7, Table 1.2). This relates to the oxidation of sulfide minerals especially pyrite, and arsenopyrite, and precipitation of gypsum ($\text{CaSO}_4 \cdot 2\text{H}_2\text{O}$) and K-jarosite ($\text{KFe}_3(\text{SO}_4)_2(\text{OH})_6$) which are most abundant in these zones, in addition to some amorphous gels. K-jarosite and gypsum are frequently found as oxidation products of mine wastes and they limit the concentration of SO_4^{2-} in the pore water (Blowes and Jambor, 1990; Johnson et al., 2000; Moncur et al., 2005).

The low concentration of SO_4^{2-} near the impoundment surface and in the hardpan layers in profile (a4) probably related to the dissolution of gypsum by infiltrated rain water (McGregor et al., 1998). This is supported by the disappearance of this mineral in the XRD identification.

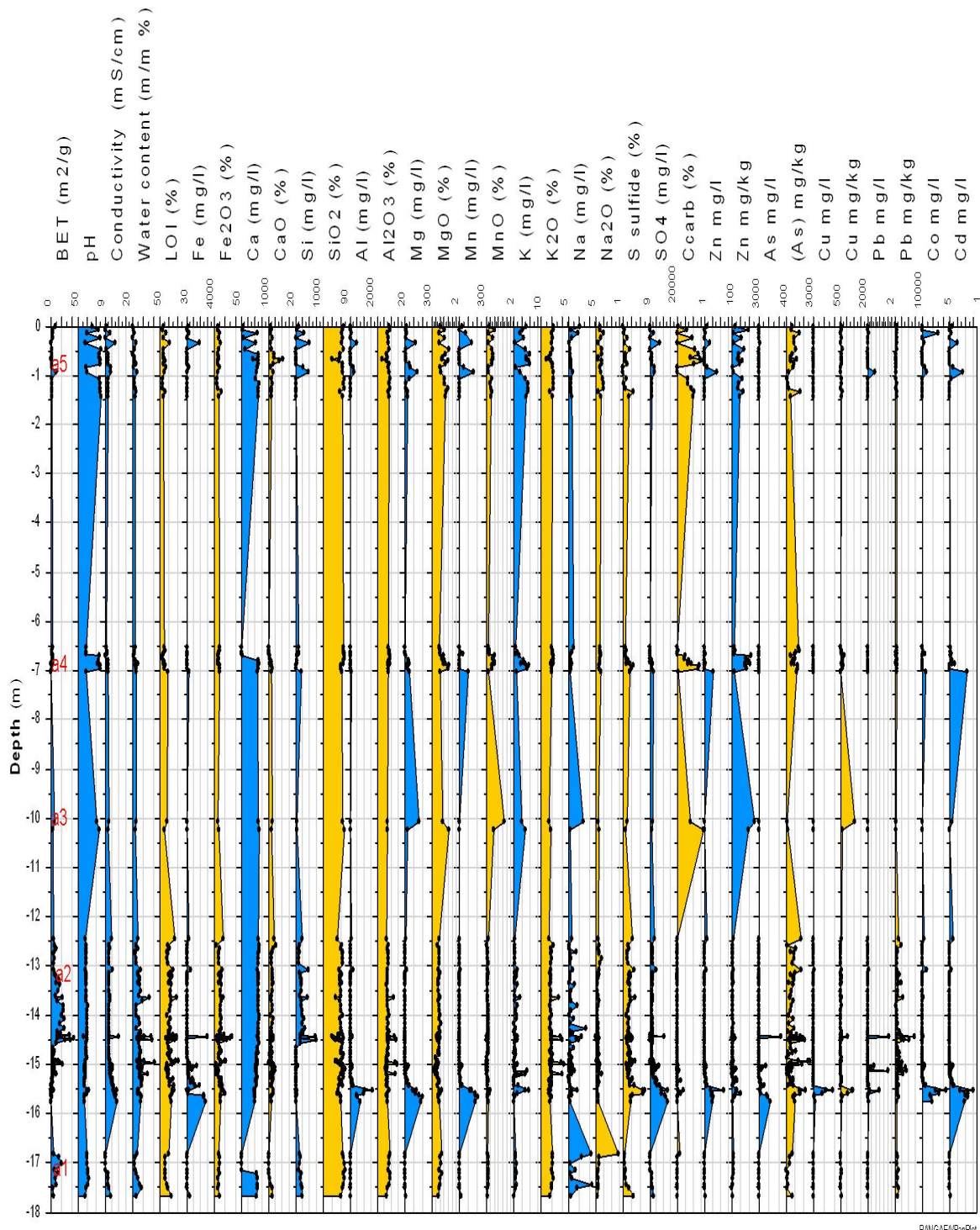


Fig. 1.7. Depth profiles showing BET and the geochemical properties of the pore-water extraction (■) and of the solid samples (■) for profile a on the western side of the tailings impoundment.

(Alderton et al., 1980; Zuoping and Chuanxian, 1996). The unoxidized layers show a similar pattern at very low values (up to 6 orders of magnitude).

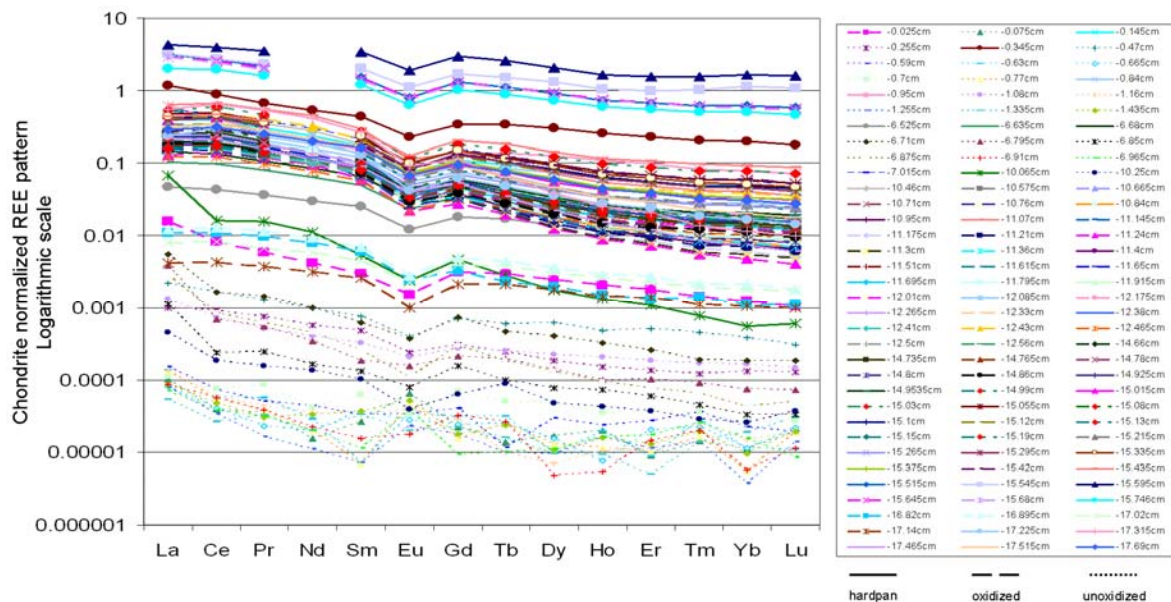


Fig. 1.9. Chondrite-normalized REE patterns for the paste water extractions (based on mg L^{-1}) (thick lines refer to the hardpan layers, dotted lines refers to the unoxidized layers).

1.5.3. Mineralogical properties

1.5.3.1. Bulk rock mineralogy

The XRD-analysis has shown that the unoxidized layers are generally characterized by the presence of quartz, muscovite-illite, and chlorite, as the dominant phases. This in addition to the following less dominant phases: pyrite, arsenopyrite, siderite, ankerite, dolomite, calcite, fluorite and barite. The hardpan layers are characterized by the presence of partly large amounts of amorphous gels (identified only by microscopy and SEM), gypsum and K-jarosite, besides quartz, feldspars, barite and fluorite, in addition to some pre deposition altered phases such as chlorite, and illite which were recognized in the unoxidized layers, too.

1.5.3.2. Detailed mineralogy using SEM and MLA

A number of thin sections from hardpans were obtained along profile (a). By EDXRF ITRAX element mapping regions of interest were chosen for MLA method. Detailed mineralogy was done by optical microscopy, SEM, in addition to MLA. The statistical data on the MLA images was done

using image analysis software (analysis, Olympus Soft Imaging Solutions GmbH). A detailed description of the MLA method has been presented in Chapter one.

Within the different lamina, grain sizes showed variations as a result of fractionation during the spilling processes which is important for water retention capacities and oxidation reactions (Fig. 1.10). Under the SEM, pyrite crystals showed different stages of alterations at different depths not only according to their position along the profile but even regarding individual lamina in the same thin section. This depends on the availability of oxygen, water, grain sizes and accessible reactive surface area at each position. Sometimes pyrite crystals were not attacked since surrounded completely by gels, or were partially altered along cracks or in zones of elevated As content, and again surrounded by gels (Figs. 1.11A; 1.13 A-B, 1.15). K-jarosite pseudomorphs after pyrite and arsenian pyrite are frequently distributed along the whole profile (Fig. 1.11B), which indicates that the pore water already contained sufficient K^+ , which probably derived from the dissolution of aluminosilicates by low pH water due to sulfides oxidation, to produce jarosite. This is consistent with the results from Gorbach et al., 1967 and Dutrizac and Jambor, 2000.

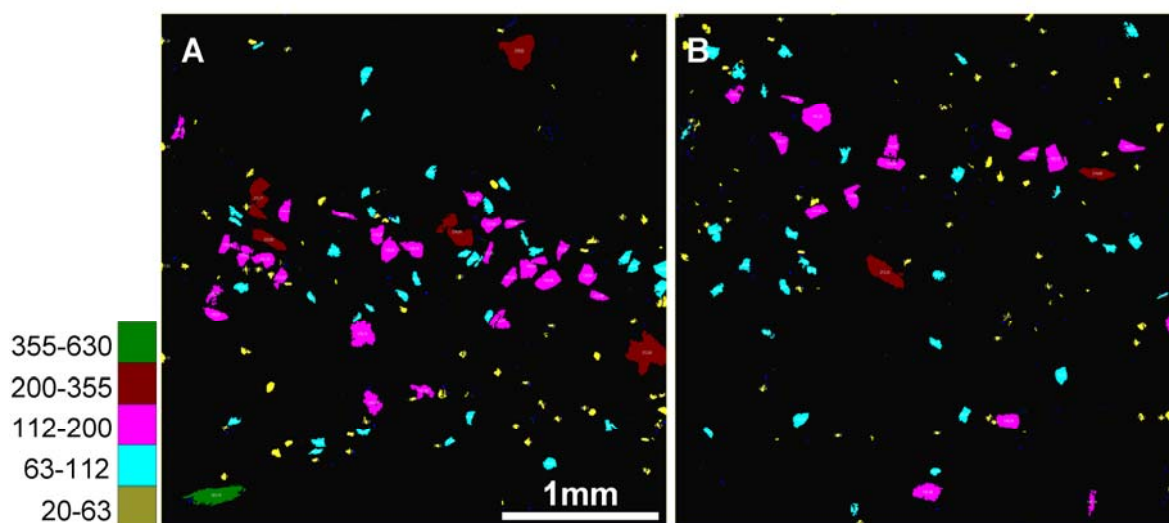


Fig. 1.10. Grain size fractionations of sulfides (A) and carbonates (B) within an unoxidized layer (depth -0.84m).

Relatively stable amorphous As-Fe hydroxides/oxides precipitated in an early stage of dissolution of arsenopyrite at grain outlines and within cracks (Rammlmair, 1996) (Figs. 1.11 A; 1.13 C-D; 1.14A), additionally, colloform textured gels might occur within grain interstitials (Figs. 1.12 C-D; 1.15). Each lamina might display different chemical pattern. Generally, in case of zoned gels, the

outer rims close to the pores, have elevated water content, as well as arsenic and some iron, whilst the inner zones show elevated silica, potassium and sulphur contents. These phenomena are in part related to the Liesegang ring phenomenon well described for agate formation (Landmesser, 1995), where an originally homogeneous gel due to unmixing and diffusion controlled dissolution precipitation reactions might show pronounced chemical layering. Alternatively a repetitive process due to the periodic interaction of pore water with rain water at contrasting physicochemical conditions could cause As co-precipitation with Fe and/or adsorbed onto, iron oxides resulting in the formation of colloform textured cements with varying levels of As. These phenomena were also recorded by Courtin-Nomade et al., 2003 at the surface of metalliferous mine tailings in France and by Ahn et al., 2005 at the tailings pile of the Nakdong mine in Korea.

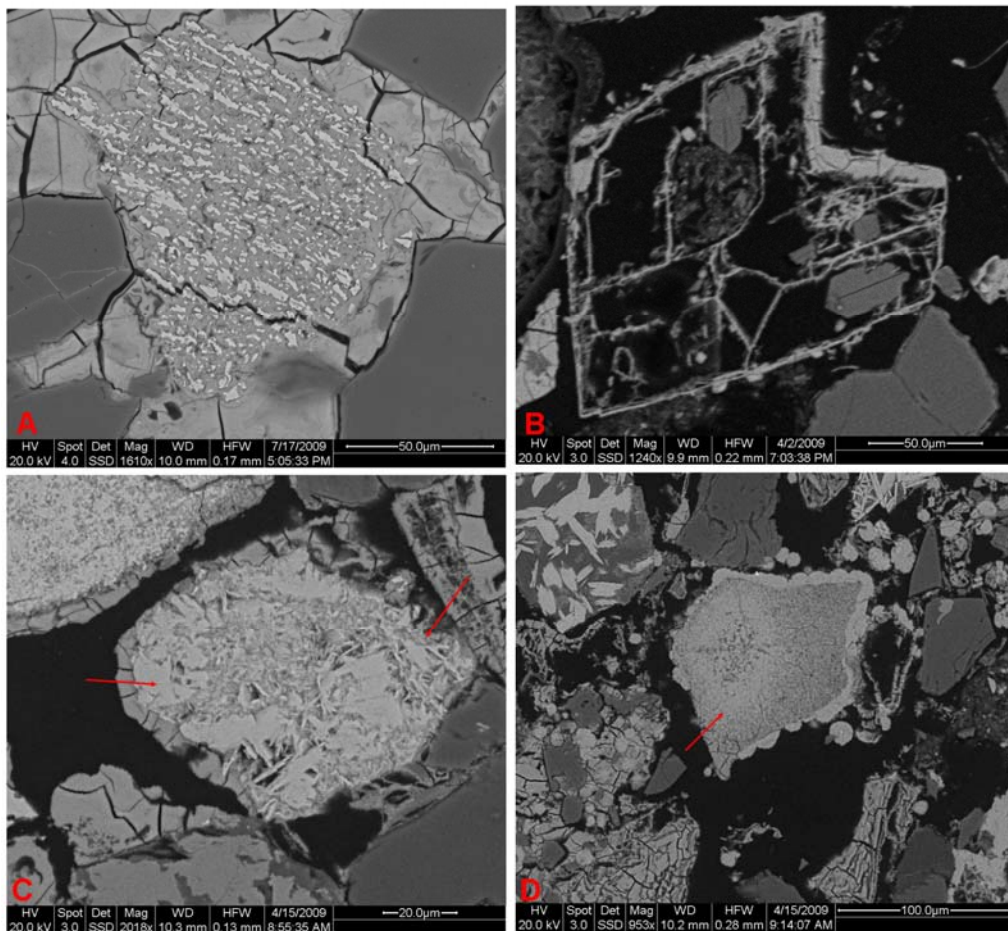


Fig. 1.11. BSE images of A) almost completely altered pyrite crystal surrounded by gel (-12.95cm), B) K-jarosite outlining an arsenopyrite with fractures and gypsum crystals in the voids (-12.95m), C) iron oxide laths overgrowth surrounded by gels, as indicated by arrows (-12.95m), D) FeAs sulfate surrounded by scorodite (-12.95m).

Scorodite is a very common secondary product from arsenopyrite oxidation (Dove and Rimstidt, 1985), which formed under low pH environment (Haffert and Craw, 2008). It is very stable under strong acidic conditions (Vink, 1996), and become unstable under higher pH values (neutral or alkaline), releasing the arsenate and break down to goethite or iron hydroxides (Dove and Rimstidt, 1985). In our thin sections, most scorodite grains characterized by dispersed spherules (Figs. 1.12 A-B; 1.14D), found in areas where a higher porosity is available, in the vicinity of the amorphous gel layers (i.e. in the transition zone between amorphous gel layers and the underlain high porous areas). The pH within this zone is below pH 4.

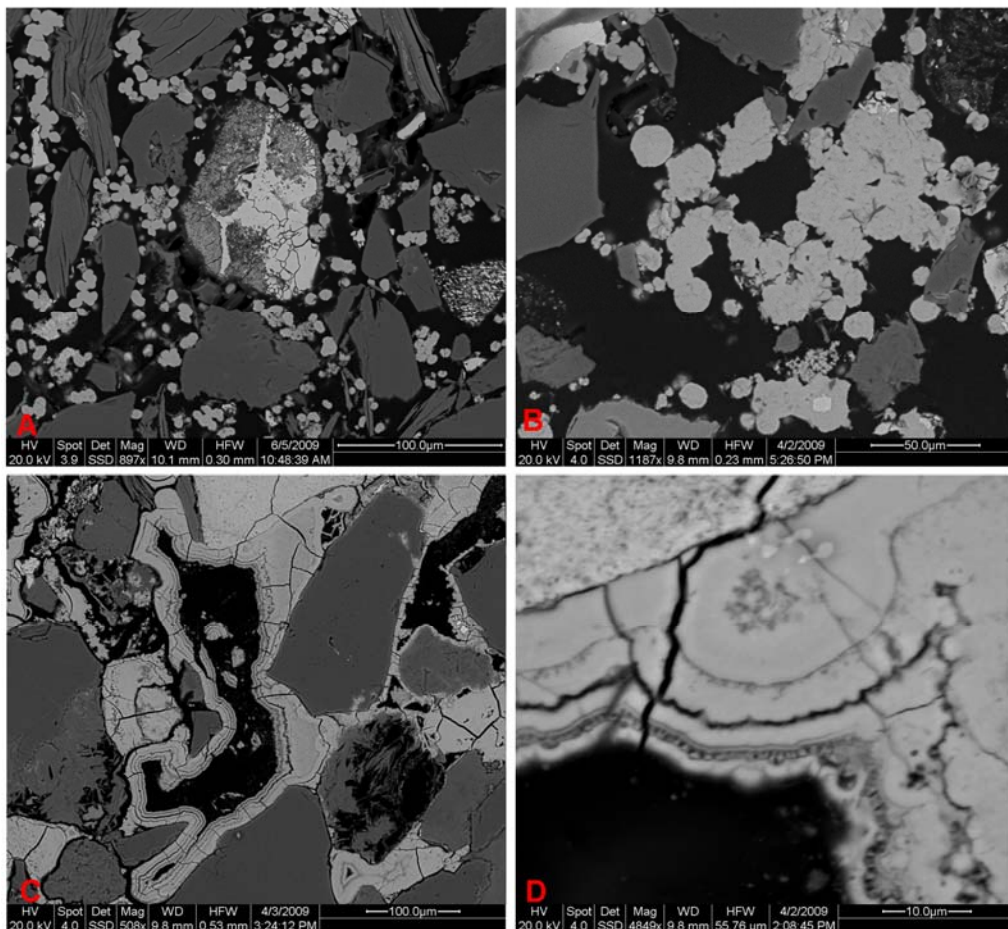


Fig. 1.12. BSE images of A) partially altered pyrite crystal surrounded by scorodite (-17.69m), B) large scorodite spherules (-12.95m), C-D) typical colloform texture in gels, with enlarged part of it (-12.95m).

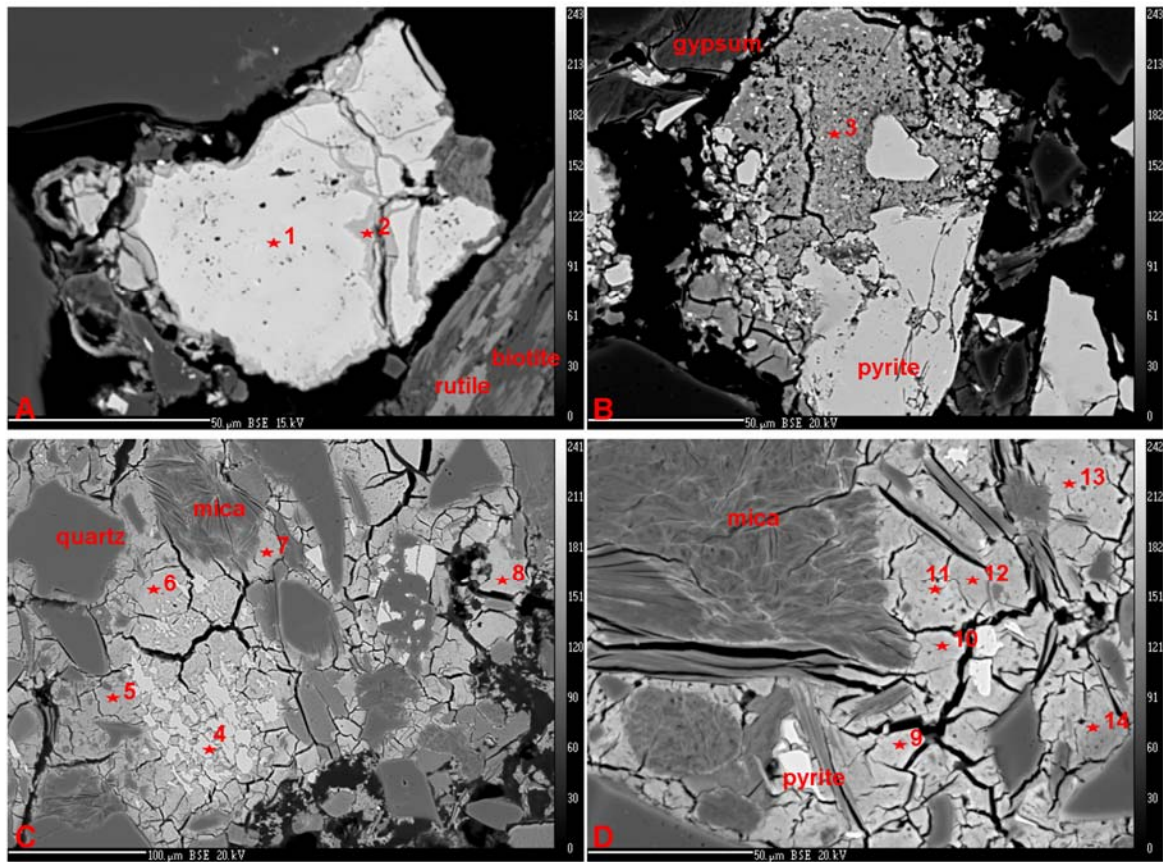


Fig. 1.13. BSE images with microprobe analysis of A) partially altered As-pyrite crystal surrounded with alteration products (-0.84m), B) advanced alteration within pyrite crystal (-17.69m), C-D) relics of pyrite surrounded by gels of varied compositions (17.69m).

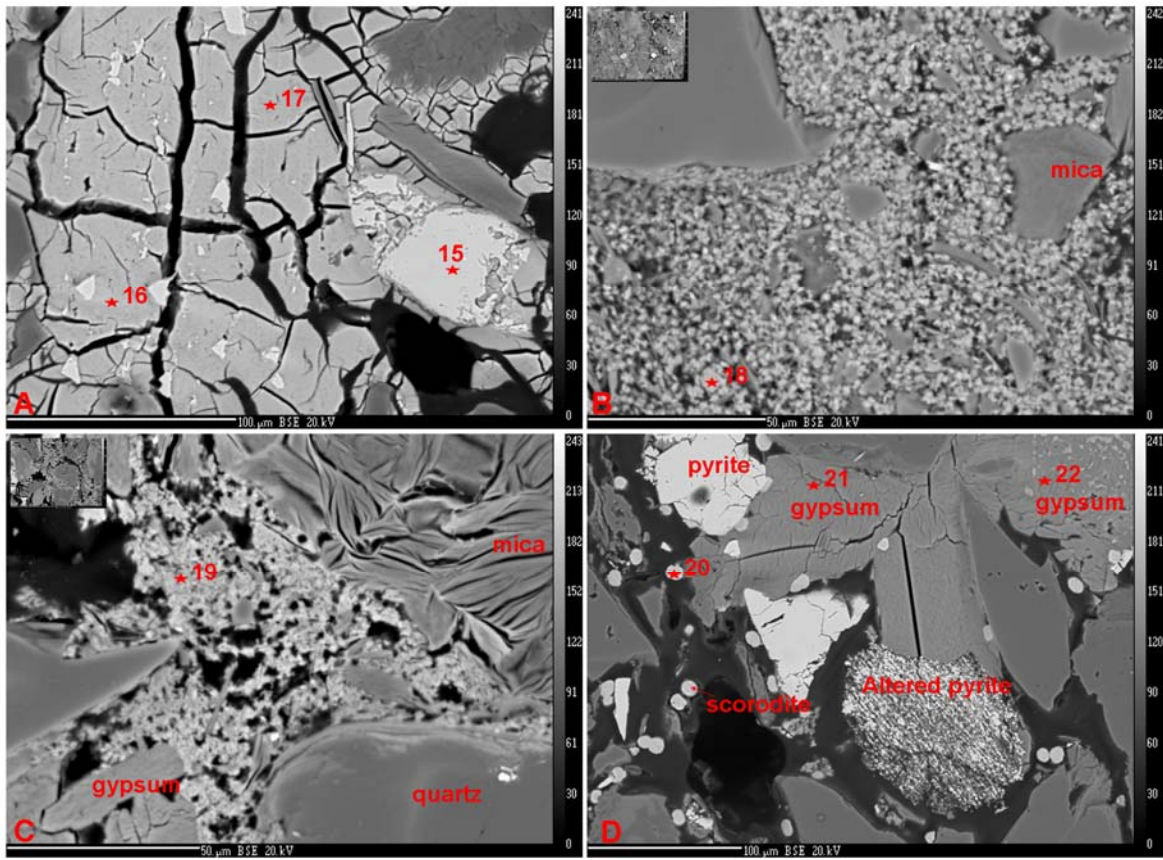


Fig. 1.14. BSE images with microprobe analysis of A) relics of Co-pyrite surrounded by gels of varied compositions (17.69m), B-C) jarosite intergrowth (-17.69m), and D) scorodite spherules with gypsum (17.69m).

	3	5	6	7	8	9	10	11	12	13	14	16	17	18	19	20	21	22		1	2	4	15
F	0.3	0.2	0.1	0.2	0.2	0.1	0.2	0.2	0.2	0.2	0.5	0.1	0.2	0.2	0.2	0.1	0.3	1.7	Na	0.0	0.0	0.1	0.0
Na2O	0.1	0.1	0.0	0.0	0.0	0.0	0.0	0.0	0.0	0.0	0.0	0.0	0.0	0.2	0.0	0.0	0.0	0.0	Mg	0.0	0.2	0.0	0.0
MgO	0.0	0.0	0.0	0.0	0.0	0.0	0.0	0.0	0.0	0.0	0.0	0.0	0.0	0.1	0.1	0.0	0.0	0.0	Al	0.0	0.2	0.0	0.0
Al2O3	0.2	2.9	0.2	0.0	0.1	0.2	0.2	0.6	3.1	0.3	0.1	0.2	0.1	3.1	3.9	0.5	0.0	0.0	Si	0.0	0.0	0.0	0.0
SiO2	2.0	5.9	0.7	0.3	0.7	4.5	0.3	1.0	5.3	0.8	0.4	0.3	0.3	4.4	5.8	0.3	0.2	0.5	P	0.0	1.3	0.0	0.0
P2O5	0.3	0.8	1.2	0.7	1.5	0.9	1.1	1.0	1.2	1.0	0.6	1.2	1.1	0.3	0.2	1.0	0.0	0.0	S	53.1	0.0	53.3	53.6
SO3	24.2	9.3	6.8	16.3	7.5	3.5	11.1	10.8	6.0	14.6	16.8	5.7	7.9	15.9	16.7	1.0	55.6	51.4	Cl	0.0	22.0	0.0	0.0
Cl	0.0	0.0	0.0	0.0	0.0	0.0	0.0	0.0	0.0	0.0	0.0	0.0	0.0	0.0	0.1	0.0	0.0	0.1	Ca	0.0	1.5	0.0	0.0
K2O	0.0	1.2	0.2	1.7	0.0	0.1	1.0	1.2	0.6	1.6	1.8	0.0	0.1	0.5	2.6	0.0	0.0	0.0	V	0.0	1.3	0.0	0.0
CaO	0.1	0.0	0.1	0.1	0.1	0.0	0.0	0.1	0.0	0.1	0.1	0.0	0.1	0.1	0.2	0.0	41.7	41.2	Fe	45.6	0.0	44.4	45.1
TiO2	0.0	0.0	0.0	0.0	0.0	0.0	0.0	0.0	0.0	0.0	0.0	0.0	0.0	1.9	0.0	0.1	0.0	0.0	Co	0.1	0.0	0.1	0.1
MnO	0.1	0.0	0.0	0.0	0.0	0.0	0.0	0.0	0.0	0.0	0.0	0.0	0.0	0.0	0.1	0.0	0.0	0.0	Ni	0.0	0.3	0.0	0.0
Fe2O3	58.3	34.4	36.9	40.4	35.9	28.8	39.1	37.9	35.4	39.6	42.3	36.2	37.9	45.1	32.7	34.2	0.2	1.2	As	0.1	69.9	0.0	0.0
CuO	0.1	0.0	0.0	0.0	0.0	0.0	0.0	0.0	0.0	0.0	0.0	0.0	0.0	0.1	0.0	0.1	0.0	0.0	Sn	0.0	4.6	0.0	0.0
ZnO	1.3	0.0	0.0	0.0	0.0	0.0	0.0	0.0	0.0	0.0	0.0	0.0	0.0	0.2	0.1	0.0	0.0	0.0	Sb	0.0	0.2	0.0	0.0
As2O3	9.3	19.9	35.0	22.8	35.1	26.0	30.1	29.1	29.5	24.1	0.3	39.4	32.2	15.6	9.4	43.2	0.0	0.6	Total	98.8	101.4	97.9	98.8
In2O3	0.0	0.0	0.0	0.0	0.0	0.0	0.0	0.0	0.0	0.0	0.0	0.0	0.0	0.0	0.0	0.2	0.0	0.0					
SnO2	0.0	0.0	0.0	0.0	0.0	0.0	0.0	0.0	0.0	0.0	0.0	0.0	0.0	0.0	0.1	0.0	0.0	0.0					
Sb2O3	0.1	0.0	0.0	0.0	0.0	0.0	0.0	0.0	0.0	0.0	0.0	0.0	0.0	0.0	0.0	0.0	0.0	0.0					
PbO	0.0	0.4	0.1	0.7	0.0	0.0	0.3	0.2	0.1	0.6	0.8	0.1	0.1	0.1	0.5	0.1	0.0	0.0					
Bi2O3	0.1	0.0	0.0	0.0	0.0	0.0	0.0	0.0	0.0	0.0	0.0	0.0	0.0	0.0	0.1	0.0	0.0						
Total	96.4	75.2	81.3	83.2	81.0	64.4	83.4	82.0	81.5	82.8	63.7	83.2	79.9	87.8	72.6	80.9	98.0	96.6					

Table. 1.1. Microprobe analysis of the data on figures 1.13 and 1.14.

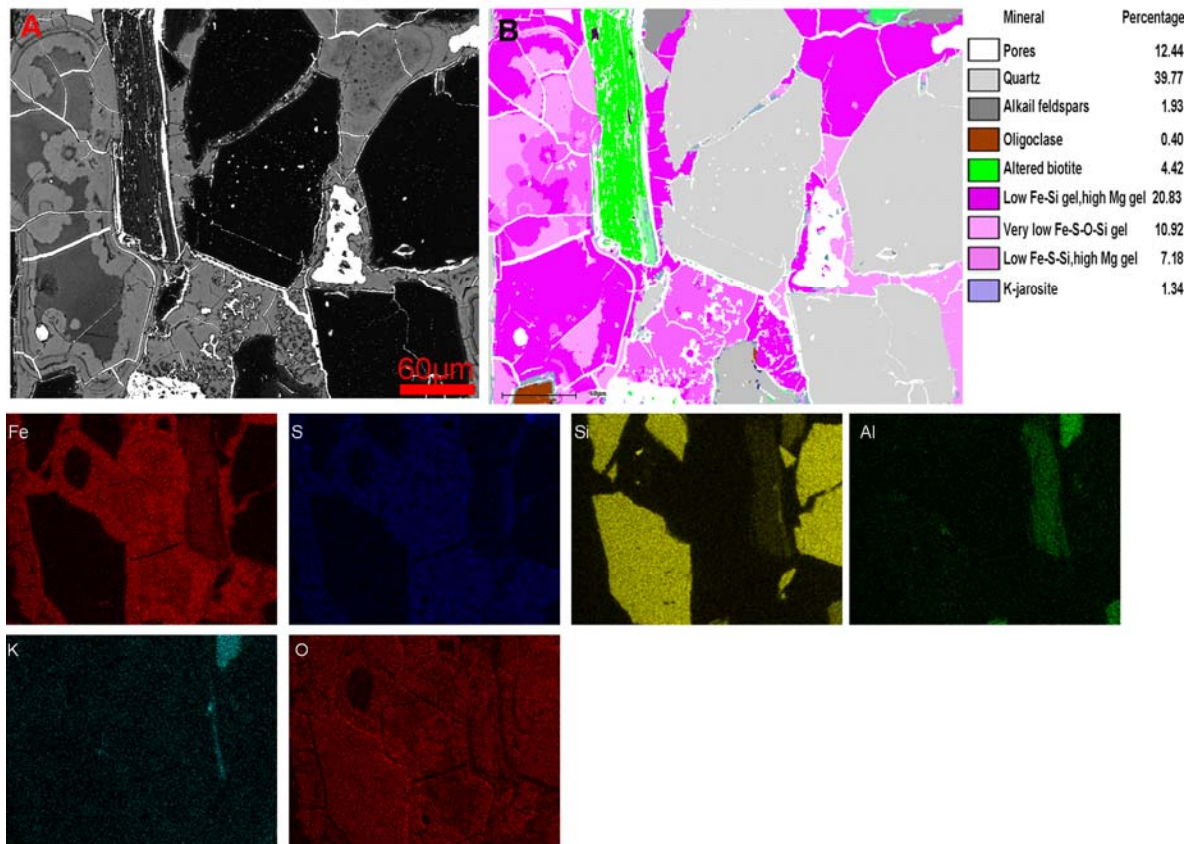


Fig. 1.15. BSE (A) and classified MLA (B) images of a pyrite crystal surrounded by Fe-Si-S-As-Mg gel of varying percentages, in addition to single element maps (-12.95cm depth).

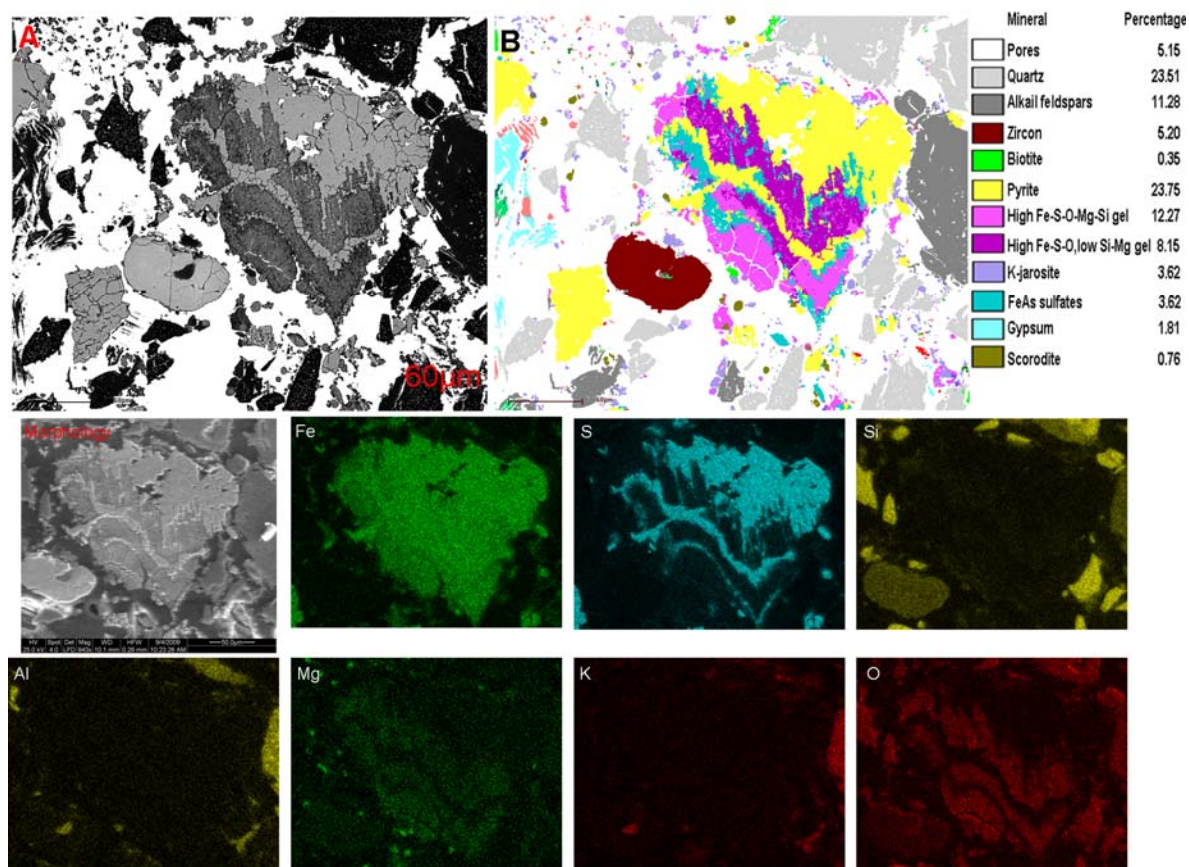


Fig. 1.16. BSE (A) and classified MLA (B) images of a pyrite crystal surrounded by Fe-Si-S-As-Mg gel of varying percentages, in addition to SE image and single element maps (-17.69m depth).

A number of hardpan layers were investigated in detail by MLA and by EDXRF-microscopy. Within these layers, Fe, As, and S showed a strong enrichment in distinct lamina, related to the secondary precipitations of amorphous gels and secondary phases. Whereas, Si, K, and Ca on the other hand, showed homogeneous distributions due to its availability in different primary minerals. For the hardpan sample at -0.15m depth (profile a5) (Fig. 1.17), the average porosity was about 43.5 area-%, with lower percentage of sulfides (0.06 area-%), gels (3.2 area-%) and gypsum and other secondary phases (0.7area-%). The phase distribution along the MLA map has been quantified along a cumulative profile (Fig 1.18). The gels concentrate at two narrow zones, at -0.4 to -0.6 cm. and at -0.85 to -1.3 cm with average concentrations of 6.4 and 4.7 area-%, respectively. The porosity reached lowest values of 38 area-% at the second gel rich layer. Gypsum and other sulfates show a scattered distribution along the whole thin section with a little higher concentration in areas of high sulfide contents. Clays increased toward the top of the profile to -0.5 cm depth with average content

of 7.6 area-%. Quartz showed homogeneous distribution along the whole thin section, while mica and chlorite decreased in zones of higher gel content.

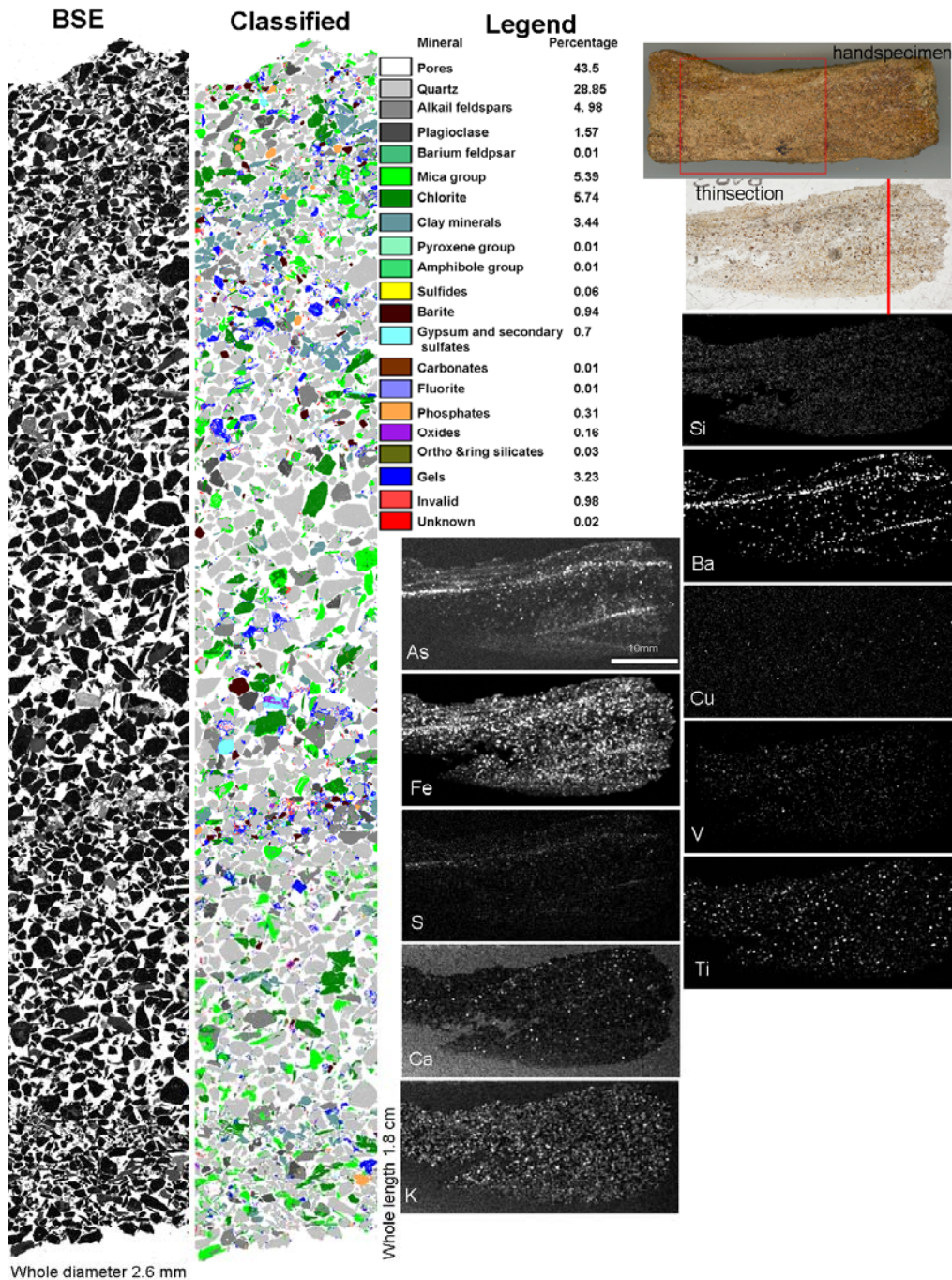


Fig. 1.17. BSE (A) and classified MLA (B) images of hardpan layer, with optical flat bed scanned hand specimen, the obtained thinsection with a line referring to the position of MLA measurement and EDXRF-microscopy derived element distribution maps (-0.15m depth).

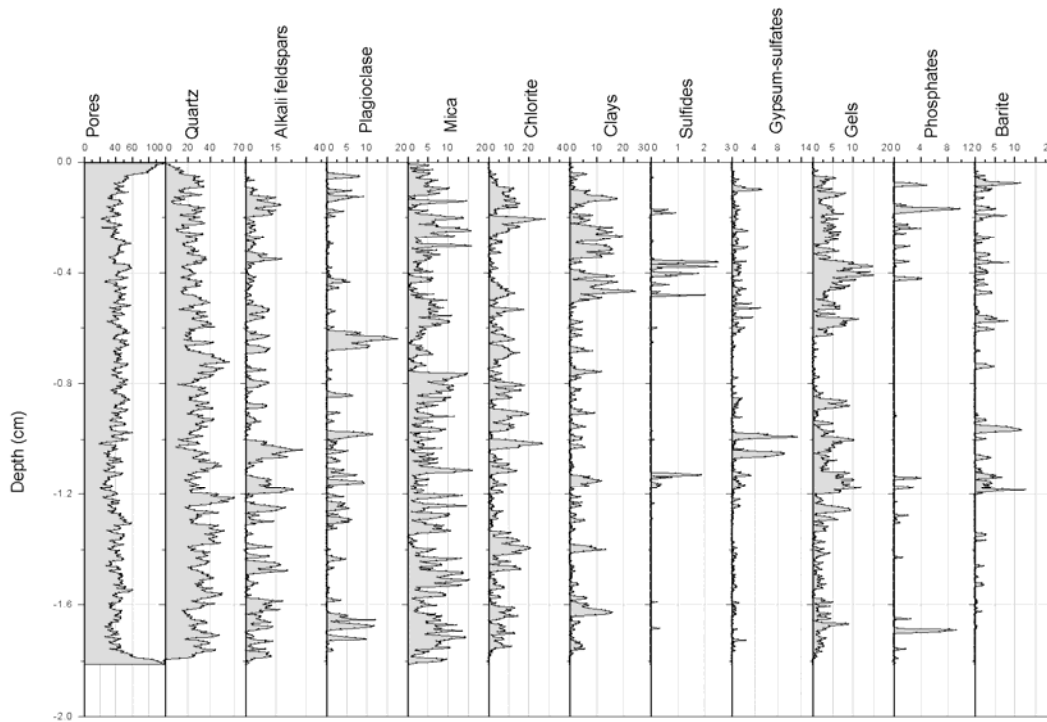


Fig. 1.18. The area-% distribution of some phases along a MLA based vertical profile of the above hardpan layer. Data derived from figure 1.17.

For the hardpan layer at -12.95m depth (profile a2; Fig. 1.19-1.20), the porosity turns out to be quiet variable. For example, at two distinct zones, the pores are almost filled by gels, sulfates or K-jarosite. At depth from -0.56 to -0.59 cm, the porosity reached average 12.89 area-%, due to the precipitation of gels (average 47.63 area-%). At depth from -0.63 to -0.65, the porosity reached average 14.75 area-%, due to the precipitation of gels (average 39.4 area-%), gypsum and other sulfates (average 18.6 area-%) (Fig. 1.20). Also, at depth from -0.81 to -1.08, the porosity reached 22.02 area-% due to the precipitation of gels (average 28.38 area-%), gypsum and sulfates (average 11.36 area-%). Gypsum, showed a patchy distribution throughout the section. It increased with sulfides near the surface (between -0.6 to -1.0 cm.). Quartz and chlorite distributed along the whole section and decreased in areas of higher porosity.

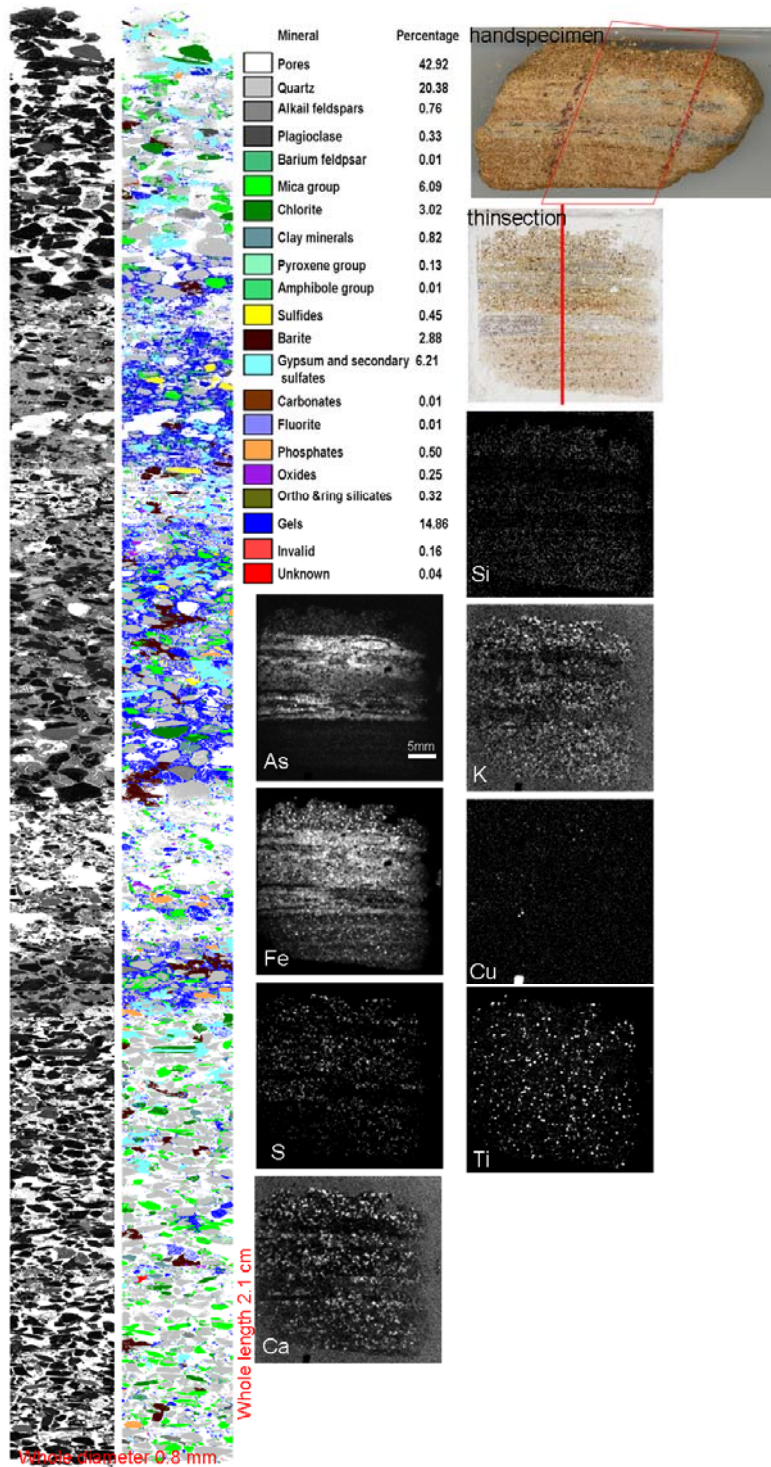


Fig. 1.19. BSE (A) and classified MLA (B) images of hardpan layer, with scanned hand specimen, the obtained thinsection with a line refers to the position of MLA measurement and element distribution maps (-12.95m depth).

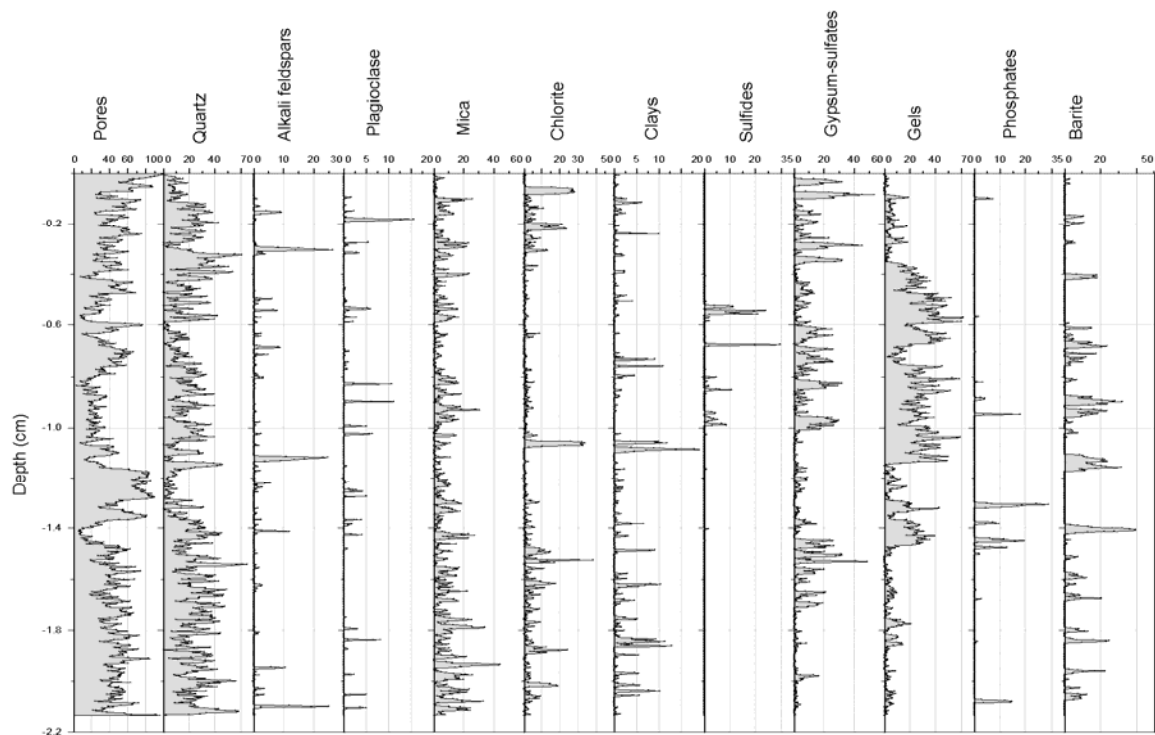


Fig. 1.20. The area-% distribution of some phases along the vertical profiles in hardpan layer. Data derived from figure 1.19.

The hardpan layer at -17.69m depth (profile a1; Fig. 1.21-1.22) again showed variable porosity, due to precipitation of gels, sulfates and K-jarosite. At depth from -1.66 to -1.79 cm, the porosity reached average 12.9 area-%, due to the precipitation of K-jarosite (average 16.3 area-%,) and gels (12.7 area-%,) and other sulfates (2.63 area-%). Also, at depth from -0.317 to -0.41, the porosity reached average 13.1 area-%, due to the precipitation of sulfates (average 3.6 area-%) and gels (average 13.48 area-%,)), (Fig. 1.22). Gypsum, showed a patchy distribution throughout the section. It increased with sulfides near the top part of the section (above -1.82 cm, average content 8.2 area-% and above -1.42 cm, average content 3.2 area-% respectively). Most scorodite was characterized as dispersed spherules, found in areas where a higher porosity is available in the upper part, accompanied with sulfides at -0.55 to -0.7 cm (average content 1.4 area-%). in the vicinity of the amorphous gel layers (i.e. in the transition zone between amorphous gel layers and the underlain high porous areas), from which the scorodite crystallized. Quartz and chlorite increased in the lower parts (below -1.8 cm (average content 42.7 area-%), and -13.6 cm (average content 2.3 area-%).),

respectively). Barite and accessory minerals show similar pattern with two distinct peaks around -0.35 and -1.7 cm.

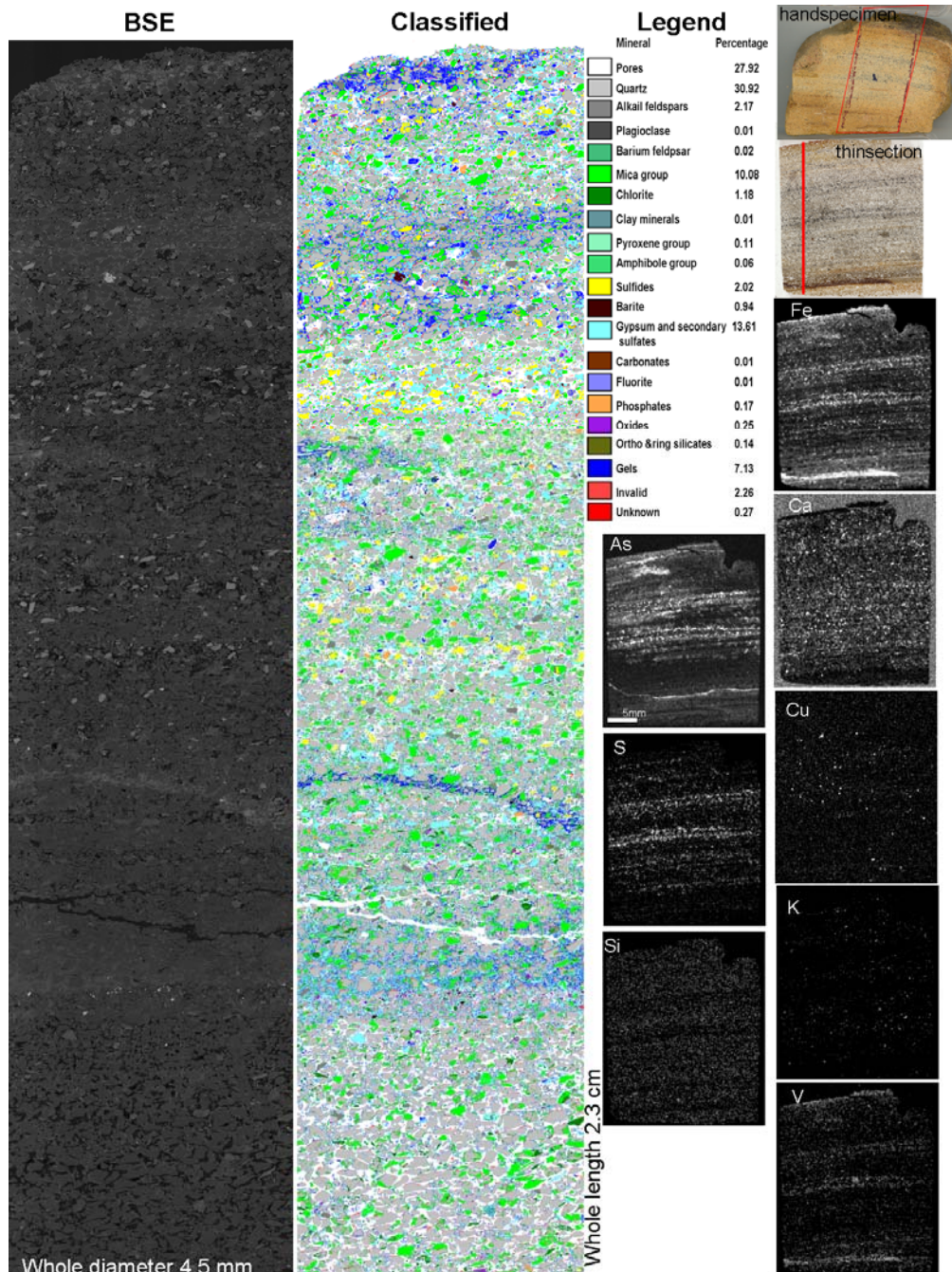


Fig. 1.21. BSE (A) and classified MLA (B) images of hardpan layer, with scanned hand specimen, the obtained thin section with a line refers to the position of MLA measurement and element distribution maps (-17.69m depth).

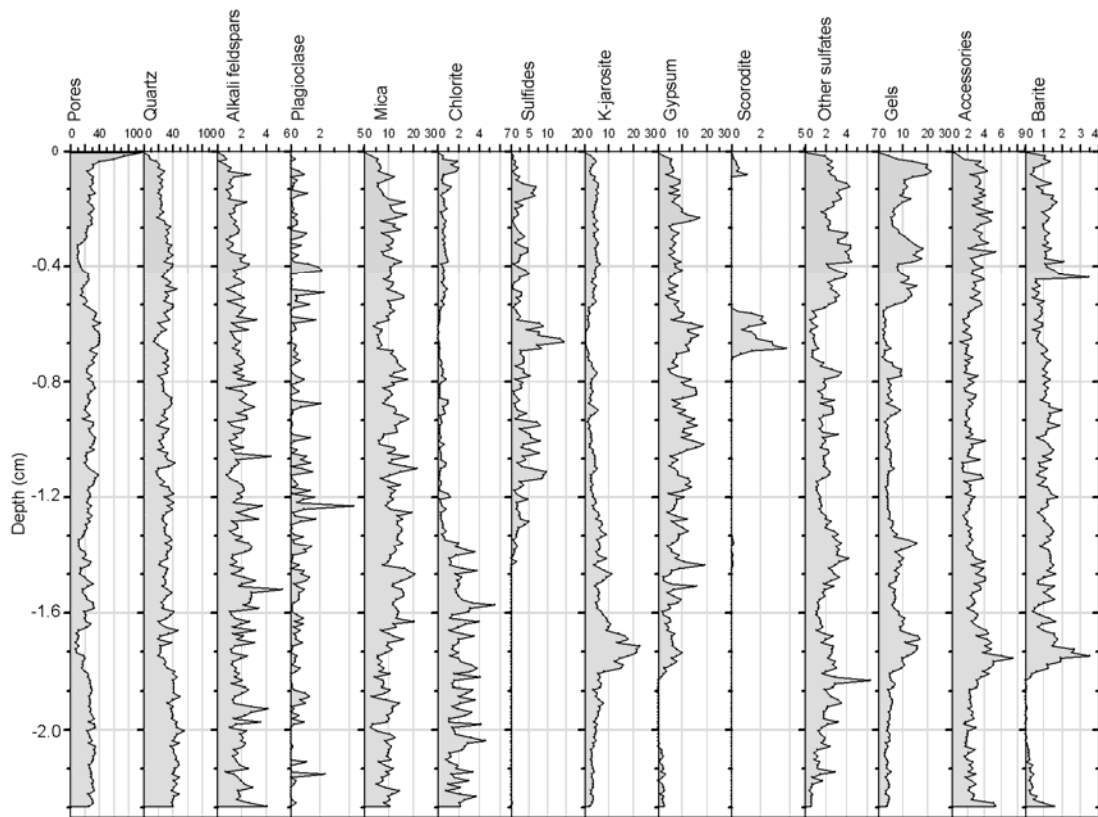


Fig. 1.22. The area-% distribution of some phases along the vertical profiles in hardpan layer. Data derived from figure 1.21.

I.6. Summary and conclusions

Different profiles from Davidschacht mine tailings impoundment in Freiberg, Germany, have been investigated in order to study the different stages of alteration and the development of hardpan layers in macro and micro-scale. The depositional dynamics is documented by alternating graded bedding for individual phases, generating characteristic transitions from fine grains toward the top to coarse-grained toward the bottom with localization of sulfides and other heavy minerals in certain lamina. The setting at the lamina boundaries is crucial for the development of cemented layers within a graded bed. Such a setting is described best by the coincidence of crucial parameters such as grain size contrast, saturation/unsaturation, open pore for gas migration, pH contrast due to neighbouring micro environments governed by reactive sulfides and buffering carbonates and silicates and their grain sizes, extended wetting times, repetitive wetting/drying processes, layers arrangement and capillary flow and transport. Within the lamina succession numerous, but definitely

a small part of lamina fulfil these conditions. Within the laminas which are prospective for hardpan development all stages from almost un-oxidized to fully oxidized can be observed. This is either due to exposure time and/ or accessibility. The alteration of sulfides at different stages can be taken as a measure of the advancement due to the availability of oxygen and water as well as the progress in clogging as a slowing down or limiting parameter (Fig.1.23).

From field investigations, different thick hardpan layers distributed along the western flank of the impoundment have been detected. Each layer consists of different lamina of different degrees of alterations depending on its mineralogical content. Using MLA combined with image analyses, a huge statistical data set can be extracted even for small lamina like grain size distribution, different mineralogy and gradation between minerals, porosity, boundary conditions, alteration progress, water retention capacities. These data can be applied for modelling programs for prediction of the mine tailings behaviour with time and for better remediation strategies in the long run. The contents of sulfide gel, gypsum and secondary phases are elevated in the lower parts compared to the upper parts. This could be due to amelioration of mineral extraction and/or longer transport pathways, as the sampling in the upper level was performed about 10 m far from the edge due to recent excavation for building materials, whilst in the lower part of the profile a maximum of 1 m depth was achieved.

The necessary boundary conditions can be achieved at various times and multiple levels in the tailings depending on depositional pauses and advancing weathering due to progressive oxidation front. Hardpans might form as a result of precipitation of secondary phases, clogging pores at the capillary fringe governed by the local climate or precipitate as cemented layers at the saturated/unsaturated boundary. Whilst the first type of hardpan is somehow stationary restricted to the oscillating capillary fringe, the second one is more related to the advancing vertical and lateral progression of oxidation and water saturation. Since the vertical progression due to the formation of hardpan layers is slowed down with each newly formed cemented layer in the multiply repeated fine/coarse lamina association, the lateral progression will be favoured over time. This will result in a layer parallel runoff towards the tailings core.

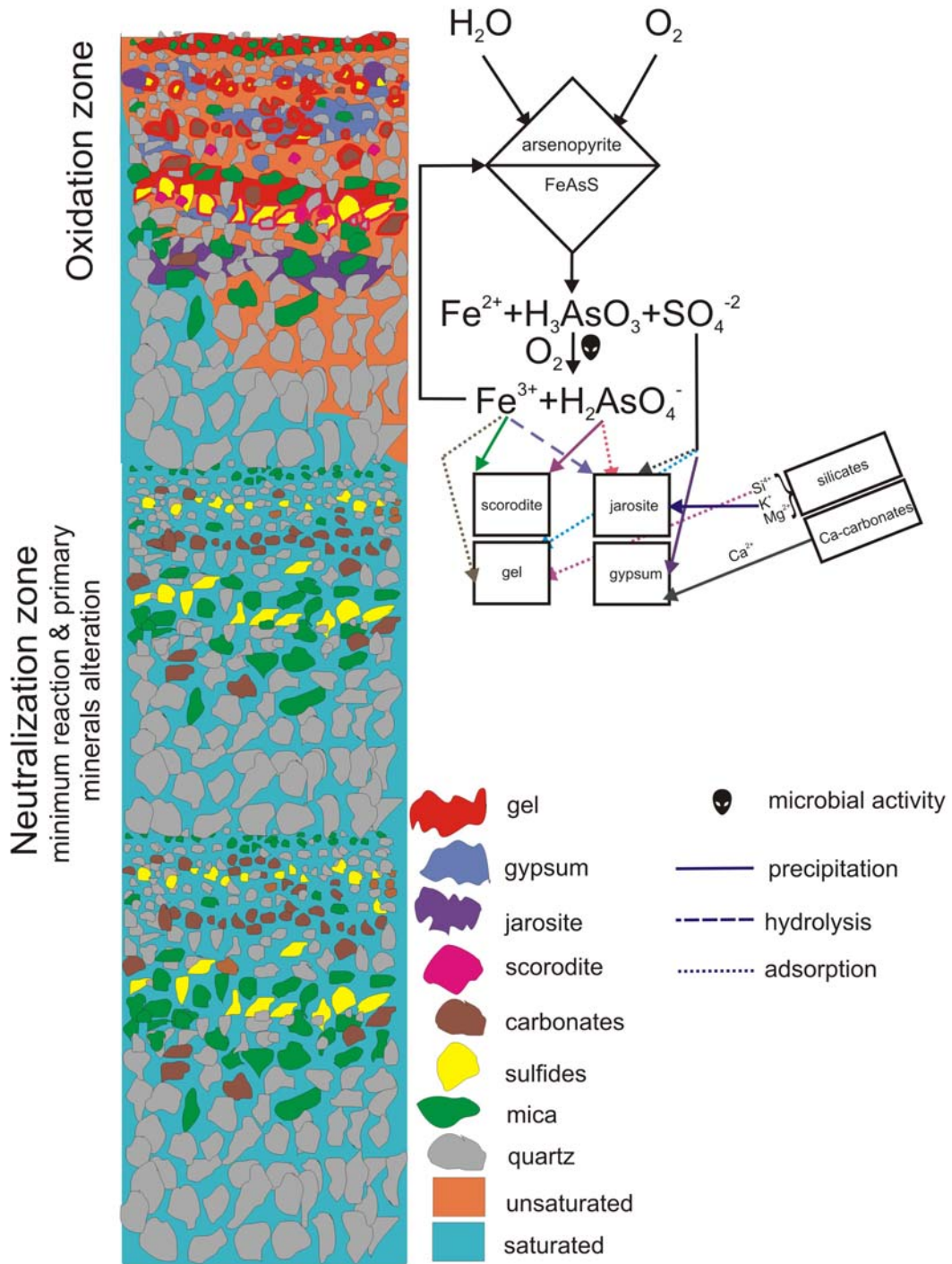


Fig. 1.23. Sketch showing the process of hardpan formation in the area.

Chapter 1-part 1: Characteristic features of the hardpans along the whole tailings impoundment

	U	U	U	U	U	U	U	U	O	H	O	H	O	O	O	O	H	H	H	O	O	O
Depth (m)	-6.71m	-6.75m	-6.795m	-6.835m	-6.85m	-6.875m	-6.91m	-6.965m	-7.015m	-10.065m	-10.25m	-12.46m	-12.575m	-12.665m	-12.71m	-12.76m	-12.84m	-12.95m	-13.07m	-13.145m	-13.175m	-13.21m
Water content (m/m %)	1.92		5.16		8.28	10.26	5.70	7.28	7.95	7.14	5.41	10.60	7.33	9.80	5.70	5.77	7.14	7.79	15.63	11.26	10.67	12.34
BET (m2/g)	3.86	3.92	3.41	4.39	4.05	1.49	2.89	3.10	1.18	7.84	3.69	6.02	6.46	10.25	8.00	5.32	6.87	6.30	6.33	7.29	7.61	10.69
pH	7.10		6.77		6.88	6.63	7.41	7.28	2.74	6.12	7.10	2.41	2.76	2.66	2.76	2.72	2.79	2.74	2.36	2.71	2.72	2.76
Conductivity (mS/cm)	0.50		2.52		2.44	2.57	2.44	2.47	2.12	3.05	2.48	4.58	3.03	3.33	3.15	3.20	3.13	3.11	5.55	3.22	3.12	3.22
HCO3 titration	15.00		24.00		15.00	15.00	24.00	21.00		24.00	18.00											
SiO2 (%)*	72.03	69.85	69.13	69.64	68.60	69.34	59.66	60.57	61.07	66.12	70.13	48.05	61.92	60.32	66.29	65.87	66.38	65.37	52.76	58.50	62.52	56.62
TiO2 (%)*	0.40	0.44	0.42	0.37	0.40	0.47	0.41	0.40	0.41	0.31	0.37	0.36	0.57	0.36	0.38	0.37	0.39	0.37	0.38	0.49	0.43	0.39
Al2O3 (%)*	9.04	9.08	8.85	8.08	8.30	9.28	8.02	7.84	8.04	7.74	7.67	6.93	8.31	7.48	7.93	7.84	8.17	8.04	7.43	7.47	7.62	7.22
Fe2O3 (%)*	6.76	8.78	7.88	7.79	9.52	7.76	10.88	10.23	10.00	7.69	8.42	16.14	4.60	10.62	8.76	9.55	8.84	9.56	14.96	12.27	9.27	13.75
MnO (%)*	0.60	0.47	0.52	0.59	0.62	0.59	0.42	0.43	0.17	1.35	0.54	0.13	0.06	0.12	0.12	0.11	0.12	0.15	0.12	0.13	0.12	0.12
MgO (%)*	0.85	0.77	0.93	0.93	0.98	0.89	1.23	1.20	0.59	0.81	1.28	0.56	0.41	0.53	0.52	0.52	0.57	0.58	0.51	0.62	0.55	0.52
CaO (%)*	1.22	0.75	1.63	2.02	1.35	1.15	2.57	2.73	2.12	2.89	2.08	4.27	5.28	3.40	2.68	2.13	2.18	2.32	3.20	2.90	3.15	2.79
Na2O (%)*	0.20	0.19	0.17	0.17	0.17	0.19	0.14	0.15	0.20	0.10	0.13	0.10	0.15	0.11	0.16	0.15	0.23	0.18	0.13	0.12	0.13	0.12
K2O (%)*	2.31	2.31	2.23	2.02	1.93	2.35	2.02	1.98	2.08	1.60	1.82	1.56	2.35	1.85	1.96	1.93	2.07	1.90	1.80	1.77	1.89	1.78
P2O5 (%)*	0.16	0.21	0.19	0.16	0.18	0.20	0.20	0.19	0.18	0.14	0.15	0.16	0.16	0.14	0.20	0.16	0.21	0.16	0.14	0.17	0.16	0.17
(SO3) (%)*	0.88	0.48	0.95	1.00	0.47	0.78	2.75	2.98	1.64	1.95	1.45	2.47	5.74	1.94	1.47	0.52	0.57	0.89	1.13	1.42	2.14	1.27
LOI (%)*	3.36	3.71	4.61	5.13	4.92	4.34	5.92	5.57	8.89	8.28	5.02	16.50	9.31	11.28	8.18	9.27	8.68	9.09	14.81	12.19	10.62	13.57
Sum *	97.84	97.02	97.53	97.91	97.48	97.33	94.20	94.30	95.40	99.05	99.05	97.23	98.89	98.14	98.70	98.40	98.43	98.63	97.37	98.07	98.60	98.34
(As) (mg/kg)*	5230	10616	8007	7376	9421	6536	13254	13067	12488	1844	2760	17363	1441	10901	5365	9026	8902	7551	17065	10487	5441	8902
Ba (mg/kg)*	8420	9880	8220	5342	5847	12081	31572	31299	23409	340	400	588	1980	746	1229	581	585	425	621	1029	1004	681
Cu (mg/kg)*	316	148	149	133	158	120	205	176	62	1053	171	83	62	52	64	46	39	52	124	54	58	66
Pb (mg/kg)*	537	655	655	613	757	571	835	772	816	494	561	1424	2465	931	1085	749	704	717	769	1185	1656	1221
Rb (mg/kg)*	176	174	168	152	135	170	154	148	161	124	136	114	171	136	146	142	154	139	125	132	139	134
Sn (mg/kg)*	358	747	667	613	740	655	763	718	734	503	673	559	1600	662	1486	765	789	745	402	1070	1593	965
Sr (mg/kg)*	168	162	133	96	106	187	600	585	443	14	17	26	48	25	30	19	25	21	22	32	27	25
Zn (mg/kg)*	2157	1553	1708	1947	2040	1516	1534	1707	308	2548	1903	210	118	157	174	141	129	132	218	158	157	154
Zr (mg/kg)*	147	229	206	175	222	227	191	190	178	98	142	151	553	123	198	138	185	135	113	153	174	153
Al (mg/l)**	1.84		0.72		0.86	1.12	0.04	0.04	82.30	0.09	0.06	86.80	11.40	17.40	14.50	14.90	13.30	12.40	250.00	15.00	10.40	13.00
Ca (mg/l)**	61.10		626.00		659.00	619.00	644.00	639.00	588.00	616.00	661.00	634.00	672.00	651.00	667.00	631.00	636.00	639.00	581.00	634.00	621.00	630.00
Fe (mg/l)**	0.13		0.04		0.04	0.01	0.02	0.02	347.00	0.13	0.12	305.00	27.20	53.20	39.40	46.40	35.10	33.40	556.00	40.20	35.30	31.20
K (mg/l)**	2.10		3.87		2.62	4.26	5.60	4.91	1.15	3.17	4.42	0.45	0.56	0.38	0.51	0.37	0.41	0.55	1.53	0.62	1.24	1.22
Mn (mg/l)**	1.49		1.92		2.38	8.00	0.03	0.02	100.00	7.64	0.02	8.03	1.18	1.67	1.64	1.35	1.50	1.60	11.20	1.94	1.39	1.76
Na (mg/l)**	0.45		0.55		0.59	0.67	0.56	0.57	0.42	2.78	0.42	0.74	0.27	0.27	1.61	0.34	0.55	0.43	0.90	0.33	0.46	0.37
SO4 (mg/l)**	195.36		1704.87		1956.56	1851.69	1701.87	1734.83	3056.18	2334.08	1779.78	3385.77	1911.61	2085.39	1953.56	1995.51	1950.56	1950.56	4823.97	2040.45	1953.56	1977.53
Mg (mg/l)**	17.90		39.60		56.70	54.50	23.10	35.10	54.60	164.00	32.20	16.50	2.56	4.20	4.36	3.48	3.64	3.60	21.30	4.39	3.05	3.38
Si (mg/l)**	55.00		53.00		63.00	58.00	9.00	11.00	195.00	37.00	35.00	233.00	149.00	128.00	131.00	119.00	113.00	114.00	468.00	146.00	164.00	175.00
As (mg/l)***	0.04		0.06		0.07	0.12	0.08	0.08	6.78	0.03	0.06	4.12	0.23	0.35	0.32	0.37	0.24	0.24	10.98	0.24	0.18	0.13
Ba (mg/l)***	0.03		0.01		0.01	0.01	0.01	0.01	0.01	0.01	0.01	0.01	0.01	0.01	0.01	0.01	0.01	0.01	0.01	0.01	0.01	0.01
Cd (mg/l)***	0.05		0.12		0.11	0.22	0.01	0.01	0.66	0.11	0.01	0.14	0.01	0.01	0.01	0.01	0.01	0.01	0.08	0.01	0.01	0.00
Ce (mg/l)***	0.00		0.00		0.00	0.00	0.00	0.00	0.29	0.01	0.00	0.26	0.14	0.14	0.12	0.13	0.12	0.12	0.41	0.11	0.09	0.10
Co (mg/l)***	0.00		0.00		0.00	0.00	0.00	0.00	0.75	0.00	0.00	0.40	0.01	0.01	0.01	0.01	0.01	0.05	0.90	0.01	0.01	0.01
Cu (mg/l)***	0.03		0.01		0.01	0.01	0.02	0.01	2.59	0.05	0.01	4.83	0.26	0.32	0.29	0.31	0.29	0.35	18.13	0.31	0.21	0.24
La (mg/l)***	0.00		0.00		0.00	0.00	0.00	0.00	0.13	0.02	0.00	0.10	0.05	0.06	0.05	0.05	0.04	0.04	0.15	0.04	0.03	0.04
Li (mg/l)***	0.04		0.05		0.06	0.06	0.02	0.02	0.24	0.06	0.02	0.17	0.03	0.04	0.03	0.04	0.04	0.04	0.35	0.07	0.06	0.06
Nd (mg/l)***	0.00		0.00		0.00	0.00	0.00	0.00	0.14	0.01	0.00	0.13	0.07	0.07	0.06	0.06	0.06	0.06	0.21	0.05	0.04	0.05
Ni (mg/l)***	0.02		0.02		0.02	0.04	0.00	0.00	0.34	0.02	0.00	0.08	0.01	0.02	0.03	0.02	0.02	0.02	0.20	0.02	0.01	0.01
Pb (mg/l)***	0.00		0.00		0.00	0.00	0.00	0.00	0.04	0.00	0.00	0.03	0.00	0.01	0.01	0.01	0.01	0.00	0.07	0.00	0.00	0.00
Sr (mg/l)***	0.03		0.09		0.10	0.11	0.21	0.19	0.09	0.16	0.12	0.18	0.09	0.15	0.08	0.10	0.08	0.09	0.12	0.12	0.09	0.11
U (mg/l)***	0.00		0.00		0.00	0.00	0.00	0.00	0.05	0.00	0.00	0.20	0.01	0.02	0.02	0.02	0.02	0.01	0.88	0.02	0.01	0.02
Y (mg/l)***	0.00		0.00		0.00	0.00	0.00	0.00	0.14	0.00	0.00	0.04	0.02	0.03	0.02	0.02	0.01	0.01	0.06	0.01	0.01	0.01
Zn (mg/l)***	1.99		2.64		2.10	3.51	0.17	0.42	34.87	2.37	0.38	12.18	0.52	0.65	0.59	0.52	0.51	0.54				

PART II. Detailed investigations on the upper surface layers of the impoundment.

II.1. Abstract

In this paper, Mineral Liberation Analysis (MLA) was applied as a new approach to elucidate and quantify textural, mineralogical, and chemical changes in a μm - and mm scale to promote the understanding of processes relevant for mineral alteration, precipitation of secondary phases and gels, and especially guiding to hardpan formation at Davidschacht mine tailings, Freiberg. In addition, the bulk mineralogical, geochemical, and physical properties have been investigated in detail. Within the upper 1.5 meter of this impoundment, a repetition of oxidized sediments with pH values between 2 and 3, and unoxidized sulfide-bearing and carbonate-rich sediments with pH values around 7.0 was observed. Each layer and even each lamina inside the layer had its unique properties. The alteration process was not homogeneous, even within the same lamina, different stages of oxidation were observed. According to the MLA measurements, the 2D pore area decreased from about 43 area-% in the investigated unoxidized layer to values ranging from 24 to 10.5 area-% in the investigated hardpan layers, which is due to the accumulation of secondary precipitates. The clogging of pores in μm -sized hardpan layers by these precipitates was localized at the contact zone of graded layers. The lower part consists of a layer enriched in very fine-grained mica and chlorite fragments, which has a relatively high water retention capacity. This layer is overlain by the bottom of the next graded layer, being coarse grained, with coarse open pores, and an elevated content of primary reactive sulfides. This layer provides access to oxygen and rain water to stimulate reactions, eventually supported by microbiological activity. Since graded layers might be amputated at top or bottom, the above described assemblage was not ubiquitous, but nevertheless multiply encountered even on thin section level.

The application of MLA has opened up new opportunities to study the sedimentological and mineralogical setup in relation to oxidation, transport and precipitation processes in a μm scale, and can be used also for calculating the acid base accounting for the individual lamina within the tailings which might provide a more accurate prediction of its behavior in the long run.

II.2. Objectives

The main objective of this work was to study the effect of fine sedimentological structures on the alteration processes in the upper surface layers of a sulfide-containing tailings impoundment, which is composed of a succession of unaltered/oxidized packages of lamina/layers. Thereto, MLA

combined with image analysis software was used as a new technique to obtain information on porosity, density, and grain size distributions, the degree of mineral alteration, and the distribution of the primary and secondary minerals within individual lamina on a μm scale. Additionally, the bulk mineralogical, geochemical, and physical characteristics were determined. This information is very important for a better understanding of the processes controlling the development of micro-/macro-hardpans within the tailings material on the long run.

II.3. Materials and methods

The investigation here focussed on the uppermost 150 cm below the top on the western side, about 10 m east of the edge of the impoundment, which was set free due to excavation of sands used as building materials by the locals (Fig. 1.1, a5). A total of 18 samples were collected in excavation pits of about 50-60 cm depth to remove the outer part of the exposure (Fig.1.1, a5). Four hardpan layers separated by unoxidized grey layers have been recognized in this profile. At each horizon, the hardpans were broken and stored as blocks in self-sealed plastic bags, whereas the unoxidized tailings samples were collected using stainless trowel and preserved in self-sealed plastic bags, to decrease possible contaminations during transport to the laboratory. Unoxidized samples used for making polished thin sections were taken in position using small plexiglass boxes in order not to deform the lamina arrangement. The physical, geochemical and mineralogical characteristics have been studied for each of these layers. The methods used were described in details in the first part of this chapter.

II.4. Results and discussions

From the distribution of the oxidized and hardpan layers along the investigated profile it can be concluded that the deposition of the material was done in three cycles, separated by non-deposition periods (Fig.1.24). Each unoxidized layer has its unique physical and mineralogical properties which relate to pulses of the spilling process itself and to the movement of the discharge points. The layers are composed of series of packages of fine graded lamina of variable grain sizes, partly amputated at top due to erosion by the following pulses or at bottom due to variable distance from the discharge point and probably pulse intensity, showing locally criss-cross bedding. Graded bedding favours contrasting water saturation and oxidation. This is reflected in the field by the undulated surface of the oxidation front and by lateral lamina parallel extension of the oxidation.

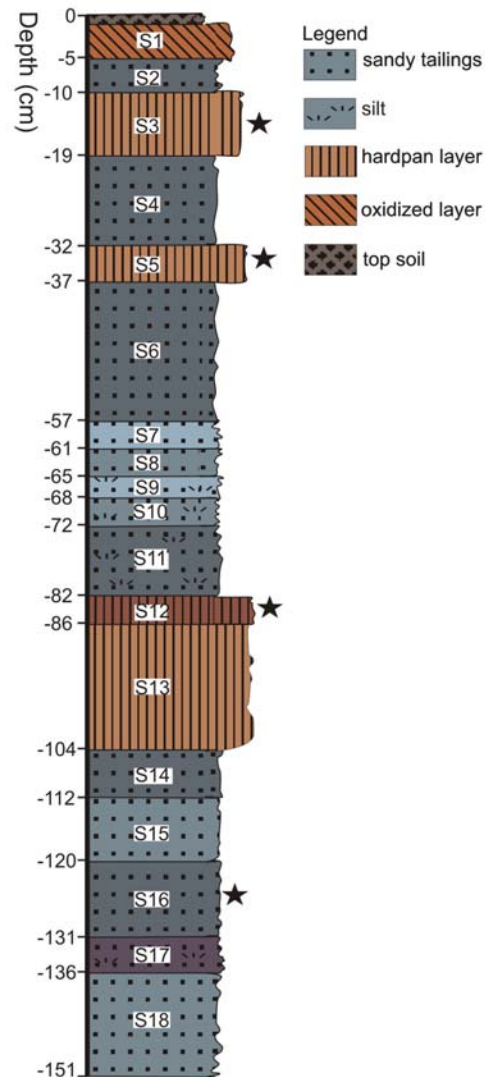


Fig.1.24. Sketch showing depth distribution of the unoxidized/oxidized layers. Colour changes resembles to the real colour in the field. ★ Refers to the sample used for detailed mineralogical investigations.

II.4.1. Bulk physical properties

II.4.1.1. Moisture content

Moisture content (wt.%) is dependent on the period of sampling. The samples were taken at the end of a dry period. Most of the hardpan layers showed elevated moisture content in relation to the directly underlying unoxidized layers (Fig. 1.25), which may be due to the presence of high amounts of water fixed by the amorphous phases and the reduced porosity.

II.4.1.2. Particle density

For all the investigated samples, the particle densities of the hardpan layers appeared to be lower than for the unoxidized layers (Fig. 1.25). The particle density of hardpan layers varies between 2.71 g cm^{-3} and 2.82 g cm^{-3} and of unoxidized layers between 2.78 g cm^{-3} and 3.0 g cm^{-3} (Fig. 1.25). The particle density correlates with the S-sulfide content of the samples, which is decreased to very low values in the hardpan layers. Similar particle densities were obtained with MLA, being 2.84 g cm^{-3} for the investigated unoxidized layer and 2.69 g cm^{-3} for the investigated hardpan layer. However, the bulk density of the unoxidized layer (1.6 g cm^{-3}) was calculated to be lower than of the hardpan layer (2.02 g cm^{-3}) (MLA-analysis, data extracted from Fig. 1.30). McGregor and Blowes (2002) have observed hardpans with higher bulk and particle densities compared to the unoxidized material, which they have attributed to the decreasing porosity within the hardpan layers as a result of an accumulation of secondary precipitates filling the pores. In the present study, however, it remains unclear to which extent possible differences in original primary mineralogy between the different layers explain the observed differences in particle density.

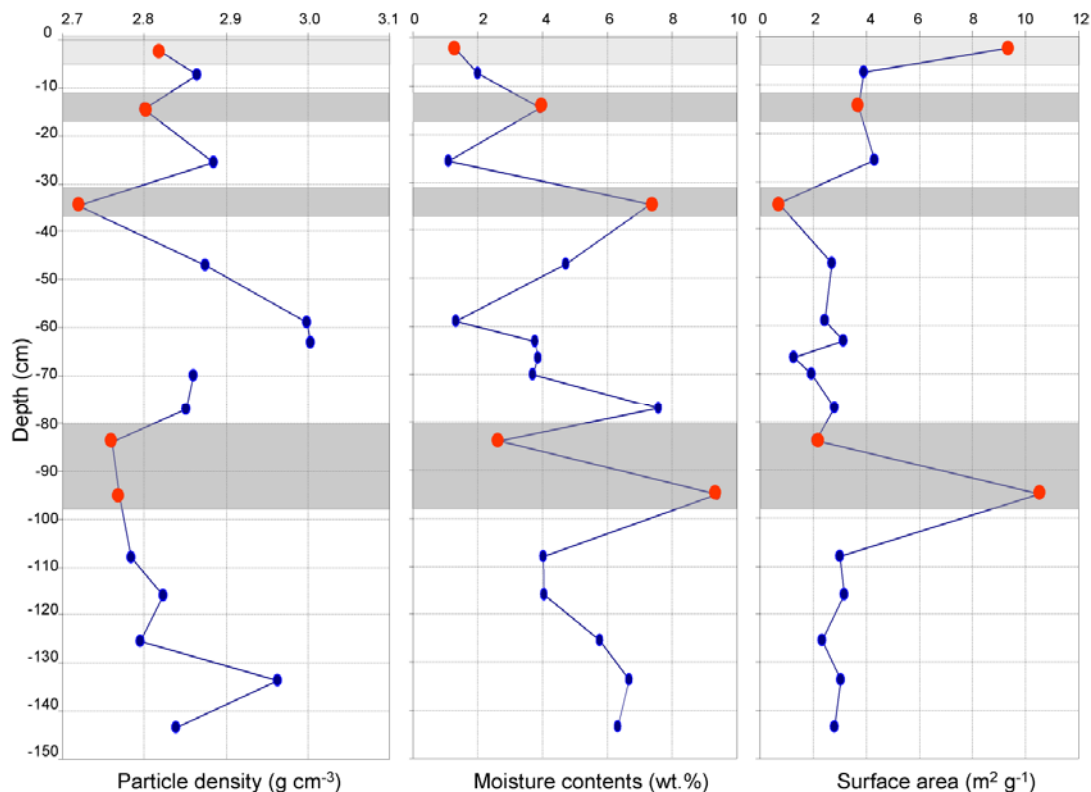


Fig.1.25. The distribution of particle density, moisture content and surface area with depth. Hardpan and oxidized layers are indicated by dark and light grey rectangles respectively.

II.4.1.3. Specific surface area (BET)

The specific surface areas of the unoxidized layers ranged between 1.2 -4.0 m² g⁻¹, whereas the surface area for the hardpan layers was sometimes higher and sometimes lower compared to the underlying unoxidized layers, but generally between 0.7-10.5 m² g⁻¹ (Fig. 1. 25). The increased surface area within the hardpans was attributed to selective dissolution of phases or particles, and by precipitation of secondary products which might enhance the surface area up to a factor of 10,000 for individual mineral sponges (Rammlmair, 2002), which in turn increased the water retention capacities within the tailings.

II.4.1.4. Particle size distribution

Particle size analyses for bulk unoxidized samples mainly show well-sorted, medium-grained to fine sands with very little silt and clay content (Fig. 1.26). Hardpan samples were also within the range of medium to fine-grained sizes, as were concluded from scanning the polished sections and polished thin sections with MLA (Fig. 1.31). One has to note that particle sizes even from small samples (few cm³) always consist of mixtures of a number of lamina of different grain size distributions. These laminations are principally due to grain size fractionation along the spilling pass, which is mainly dependent on the distance in the spilling direction.

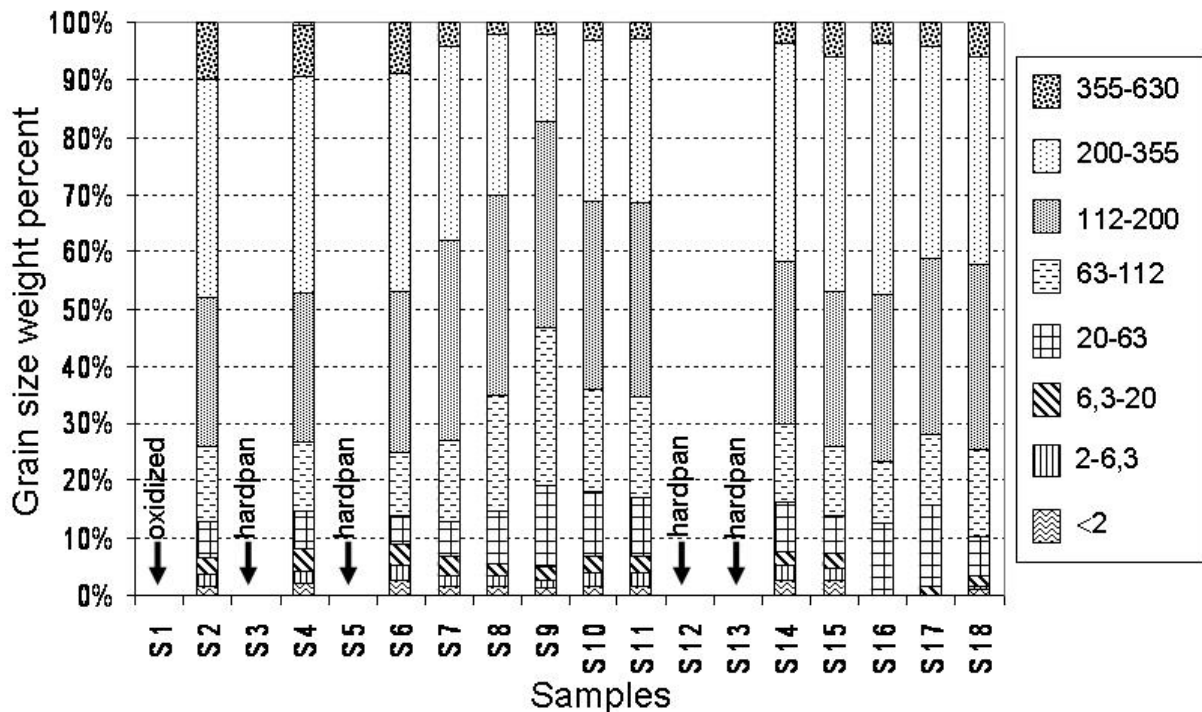


Fig.1.26. Grain size distribution of the unoxidized samples (empty lines refer to hardpans). Grain sizes (legend) are in micrometers.

II.4.2. Geochemical properties

II.4.2.1. Bulk rock chemistry

The investigated samples showed distinct differences in bulk chemical composition at different depths due to mineral fractionations during the spilling processes (Fig. 1.27). For example, the XRF data revealed an elevated LOI for hardpan samples (average 7.06%) compared to unoxidized samples (4.5 %). This is due to hydration and oxygenation reactions. At a depth of -66.5 cm, the material is highly enriched in Ba, MnO and CaO, and low in SiO₂. At a depth of -133.5 cm, the material is highly enriched in Fe₂O₃, S-sulfide, As, Sn, Cu, Co, Pb, and Zn.

II.4.2.2. Paste-extraction results

The paste pH for the unoxidized grey layers was measured to be 6.9 – 7.8, the paste pH for the hardpan layers 2.5 – 3.1, and the paste pH for the top oxidized layer below the soil cover 4.8 (Fig. 1.27). This observed pH-difference between oxidized and unoxidized layers is explained by the presence or absence of carbonated minerals (especially calcite, ankerite (Ca (Fe Mg Mn)(CO₃)₂), dolomite (Ca Mg (CO₃)₂) and Ca-Mn, Ca-Mg-Mn siderite) and sulfides oxidation products. The unoxidized layers contain an average C-carb content of 0.6 %, whereas the oxidized layers have been depleted of carbonate minerals (C-carb 0.03 %).

The solutions obtained by paste extraction were calculated to be close to equilibrium with respect to gypsum (S.I. between -0.17 and +0.07), except for the two uppermost samples and the samples beneath the first and second hardpan layers due to the lowest dissolved SO₄ concentration. Gypsum has not been detected by XRD or SEM in these layers. It might have been never precipitated or leached by infiltrating rain water from the uppermost part of the profile (consistent with observations by McGregor et al., 1998). Gypsum crystals which formed in later stages of sulfide oxidation may be related to the availability of calcium from the dissolution of slowly reacting aluminosilicate minerals after total dissolution of carbonates, or from dissolution of carbonates from an undepleted deeper source e.g. by capillary transport.

The neutral-pH solutions that were obtained by paste extraction of the unoxidized layers were calculated to be slightly undersaturated with respect to calcite (S.I. between -0.67 and -0.06). In these layers, several carbonate minerals have been identified. These solutions might also be in equilibrium with respect to ferrihydrite given the very low (<detection limit) dissolved Fe content. Solutions were not found to be in equilibrium with potential secondary phases that have relatively slow reaction kinetics, such as jarosite (S.I. between -4 and -19), amorphous silica (S.I. between -1

and +0.7), gibbsite (S.I. between -5 and +2), and kaolinite (S.I. between -4 and +7). All solutions were calculated to be undersaturated with respect to common secondary phases for arsenic (scorodite, $\text{FeAsO}_4 \cdot 2\text{H}_2\text{O}$), zinc (e.g. zincite, ZnO), copper (e.g. tenorite, CuO), and lead (e.g. anglesite, PbSO_4). Leaching of almost all elements strongly increased with decreasing pH, being except of K (fixed in jarosites) enriched in the hardpans (Fig. 1.27), which is consistent with the pH-dependent solubility of oxyhydroxides (e.g. Fe, Al, Mn, Zn, Cu, Pb) and the pH-dependent dissolution kinetics of aluminosilicates (e.g. Al, Si, Mg) (Stumm and Morgan, 1981).

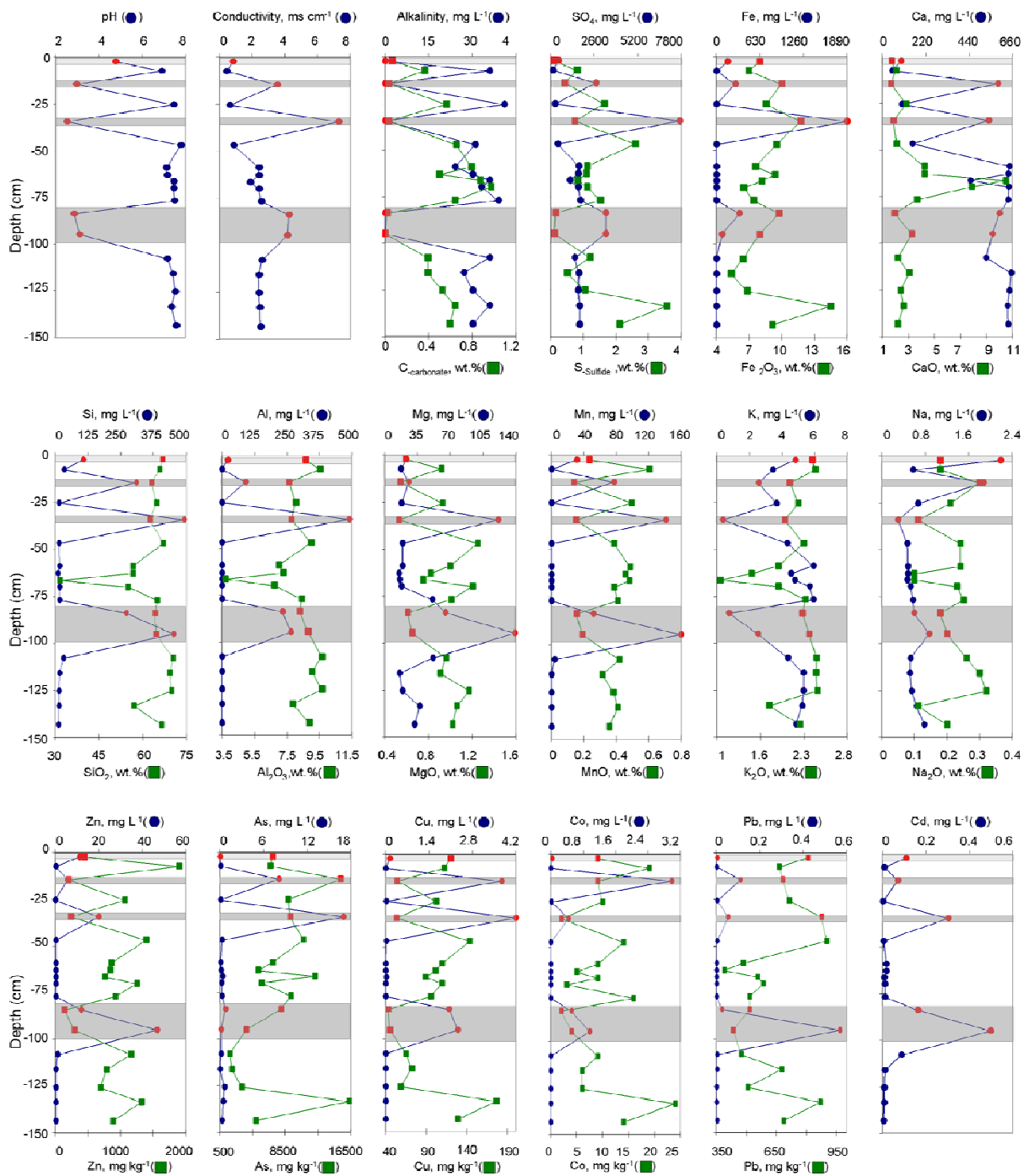


Fig.1.27. Depth profiles showing the geochemical properties of the pore-water extraction (●) and of the solid samples (■). Hardpan and oxidized layers are indicated by dark and light grey rectangles respectively.

II.4.3. Mineralogical properties

II.4.3.1. Bulk /detailed rock mineralogy

The XRD-analysis has shown that the unoxidized layers are generally characterized by the presence of quartz, chlorite, and muscovite-illite as the dominant phases. This in addition to the following less dominant phases: pyrite, arsenopyrite, siderite, ankerite, dolomite, calcite, fluorite and barite. Arsenian pyrite (more common phase), in addition to few crystals of galena, chalcopyrite and sphalerite were identified only by SEM. The hardpan layers are characterized by the presence of amorphous gels (identified only by microscopy and SEM), gypsum and K-jarosite, in addition to quartz, barite and fluorite.

Using SEM detailed aspects of the alteration processes of sulfides can be observed. In general alteration starts at the rims and focuses in cracks in the crystals as well as in zones of elevated arsenic content, and then spreads out to the rest of the grain (Fig. 1.28 A). The development of secondary coating and precipitation of gels filling pores and embedding mineral fragments as observed in hardpan layers, might protect some pyrite crystals from further oxidation (Fig. 1.28 B). Mudcrack-like texture (Fig. 1.28 B) is widespread within amorphous and poorly crystalline phases due to desiccation in the course of evaporation. This feature was also recognized by Courtin-Nomade et al. (2003). They related it to a rapid re-precipitation from As-Fe rich waters where these elements were released from the primary ore by periodic AMD and subsequently precipitated, resulting in the formation of iron cements with varying levels of As^{3+} . Figure 1.28 (C) shows a gel-like particle with changing element ratios from the centre to the rim. It begins with an Fe-As-Zn sulfate gel, which becomes enriched in silica and potassium toward the margin where a few small K-jarosite crystals have formed (indicated by an arrow). It was observed in some aluminosilicate crystals, in particularly biotite, that silica invaded and replaced the structure along the cleavage (Fig. 1.28 F). This has been addressed as a silica residuum, after deprivation of K, Mg, Fe, and Al from the crystals under very low pH conditions as shown also by Jambor, 2003. This process is important as a source for potassium for K-jarosite crystallization (Fig. 1.28 D). Therefore, its formation has been localized in areas of abundant aluminosilicates and close to zones of sulfide oxidation (Kunov and Mandova, 1997). Also, K-jarosite outlining pyrite and arsenian pyrite are frequently distributed in the samples (Fig. 1.28 E), which indicate that the pore water already contained sufficient K^+ to produce jarosite. This finding is consistent with the results by Gorbach et al., 1967 and Dutrizac and Jambor, 2000. Combined with gypsum, K-jarosite limits the concentration of SO_4^{2-} in the pore water

(Blowes and Jambor, 1990; Johnson et al., 2000; Moncur et al., 2005). Gypsum as will be shown in the MLA measurements, generally has a patchy distribution, its crystals appear quite large compared to the overall grain size and showed poikiloblastic overgrowth, filling up the pores between the primary grains. Its presence is not restricted to one particular type of lamina.

One of the altered pyrite crystals (Fig. 1.29), was measured in detail using MLA in order to get information about the chemical variations of its oxidation products embedding the crystal. Oxidation started from the rim of the crystal moving towards the center along fractures. A gel rich in Fe, As, and Al was formed. Also, in the cracks some Fe-As sulfate was encountered, in addition to a gel rich in As and a gel of very low silica content disseminated around the pyrite.

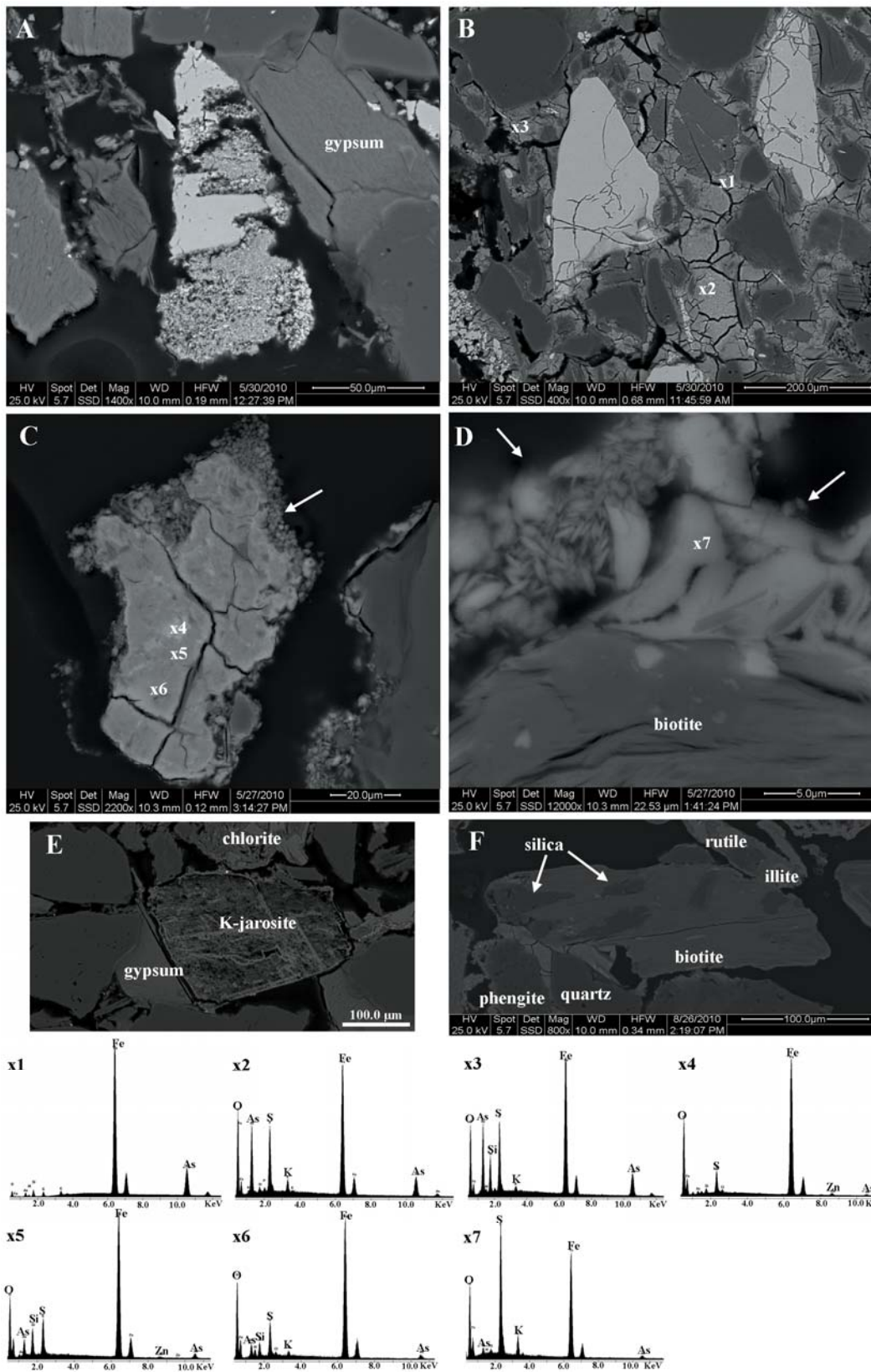


Fig.1.28. BSE images of A) advanced pyrite alteration, B) pyrite embedded in gels ranging in chemistry from almost pure iron and arsenic (x1), to low silica, but high S and K (x2) and to high silica, S, and K near the pores (x3), C) unmixed Fe-As-Zn sulfate gel (x4), being enriched in Si, S and Zn at the centre (x5), and of K and S at the rim (x6) with incipient growth of K-jarosite at the margin (indicated by an arrow), D) K-jarosite (x7) growth (indicated by arrows) around altered biotite, E) K-jarosite replacing fractures in pyrite; F) partial replacement of biotite by amorphous silica. A, C, D, and E relate to sample S12, B to sample S5 and F to sample S3.

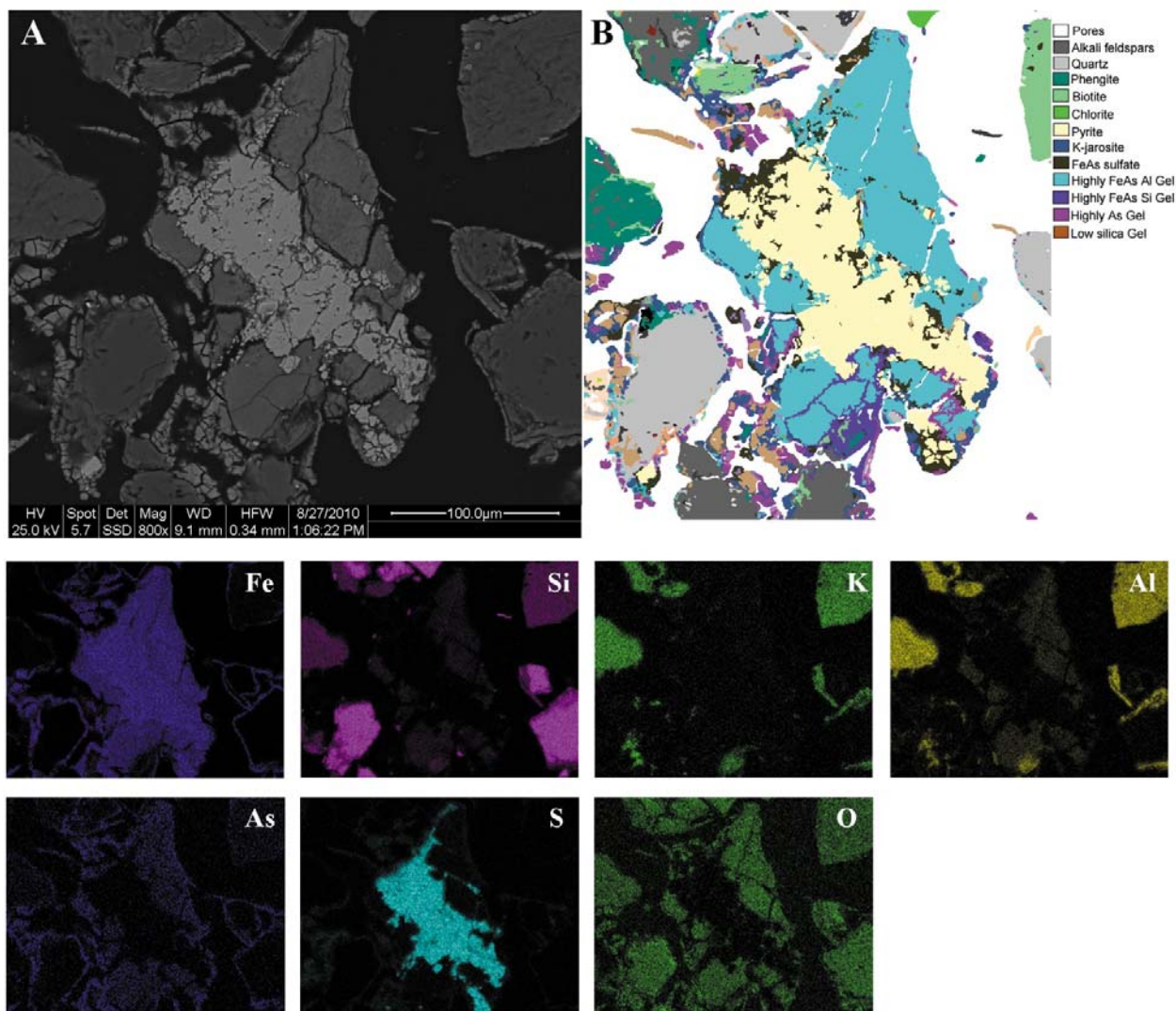


Fig.1.29. BSE (A) and classified MLA (B) images of a pyrite crystal surrounded by Fe-As-Al rich gel and its surroundings, with single element maps (sample S5).

MLA-analysis results for polished sections and polished thin sections of both, unoxidized (sample S16) and hardpan layers (samples S5 and S12) are presented in Figures 1.30, and 1.31. Small enlarged parts of Fig. 1.30 are presented in Fig. 1.32. The laminated tailings show graded bedding and sudden changes in grain size of liberated minerals and rock fragments as well as of mineral ratios. In the thin section of the unoxidized sample (Fig. 1.30 A, 1.31 A), sulfide minerals are concentrated in a few distinct layers having the higher average geometric grain sizes ($250\mu\text{m}$), whereas carbonate, chlorite and mica-group minerals can be found in many layers. Fig. 1.32 A shows in more detail, that pyrite, arsenopyrite, and most of the carbonates occur together, whereas micas and chlorites and the remaining carbonates are disseminated throughout the section. The average porosity was estimated to be 43 ± 10 area-%, by converting all background into voids. The distribution along the profile appeared to be quite homogeneous. The average sulfide mineral content is 1.9 ± 3.3 area-% (max. 23 area-%). The average carbonate content is 3.6 ± 3.7 area-% (max. 23 area-%). The average content of mica-group, chlorite and clay minerals is 11.7 ± 5.4 area-% (max. 58 area-%). Small amounts of gel-phases as well as isolated gypsum nests and secondary sulfates have also been detected, representing on average 1.1 ± 1.0 area-% (max. 7.5 area-%) and 0.9 ± 1.6 area-% (max. 15 area-%), respectively. These alteration products formed around the rims of some sulfide crystals indicating a small degree of alteration even for the so called unoxidized layers.

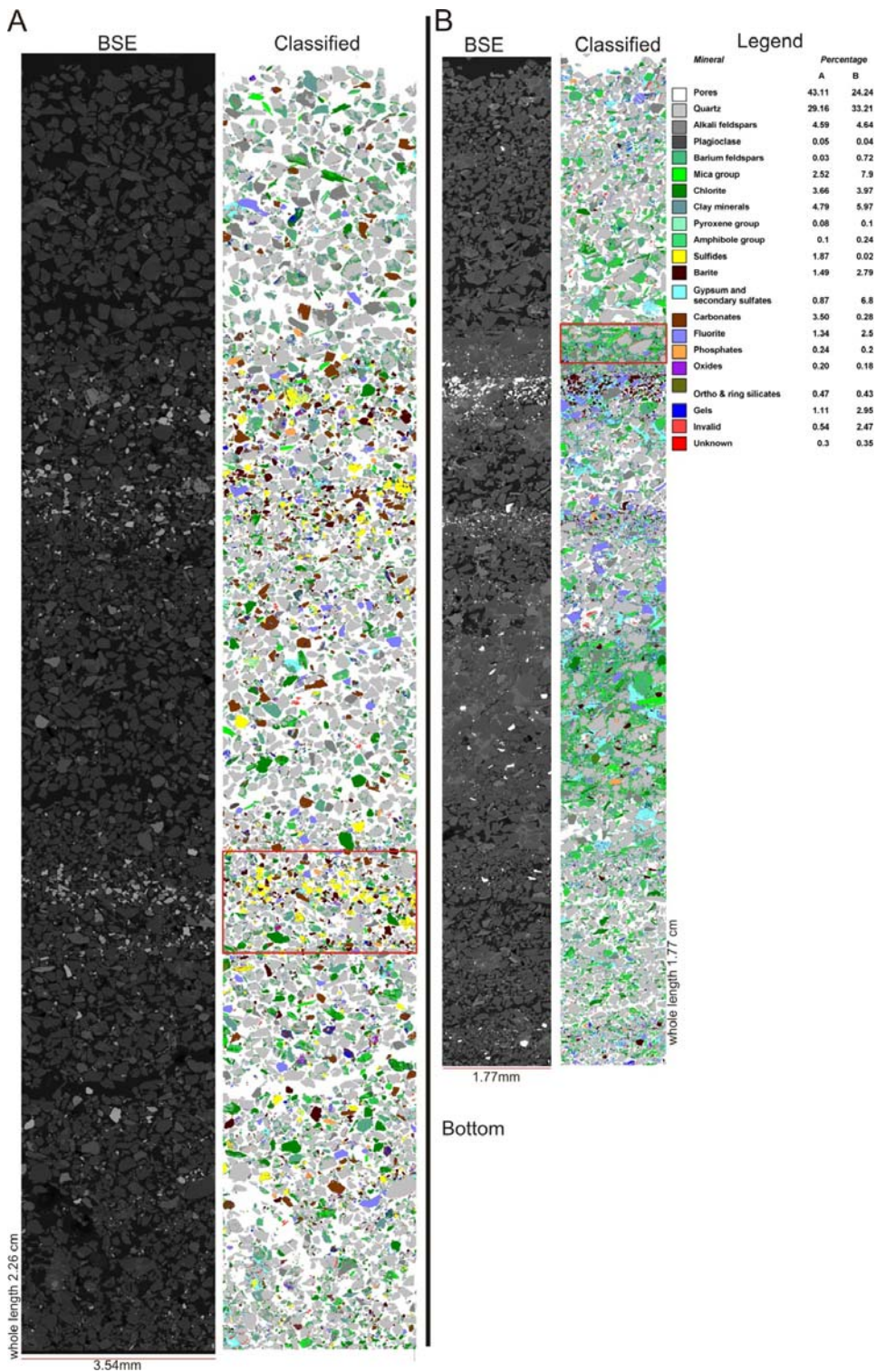


Fig.1.30. A) BSE and classified MLA images of unoxidized grey layer (sample S16). B) BSE and classified MLA images of one hardpan layer (sample S12). For colour coding see legend for mineral distribution (area-%). Rectangles refer to enlarged zones in Fig. 1.32.

The polished section and polished thin sections of the hardpan sample showed that oxidation/precipitation processes happen at certain zones, depending on the availability of reactive mineral phases (Figs. 1.30 B, 1.31 B, 32 B and C). Within the hardpan layers even unoxidized lamina can be found, but the whole block is agglutinated as a layer due to the accumulation of secondary phases. The porosity turns out to be highly variable in individual horizons. In two distinct regions (-0.44 to -0.50 cm and -0.90 to -1.05 cm), the average porosity is only 6.5 ± 3.5 area-%. In these regions, the pores are almost completely filled with very tiny chlorite and mica fragments (Fig. 1.30 B, and more detailed in Fig.1.32 C). Either the layer relates to the original spill or the tiny fragments were flushed from bottom layers at the time of deposition. This type of layer has not been observed in the unoxidized sample, however, a significantly lower amount of mica-group, chlorite and clay minerals have been found in the unoxidized sample compared to the hardpan sample (18 ± 10 and 11.7 ± 5.4 area-%, respectively). Outside these regions, the porosity is also significantly lower compared to the unoxidized sample (28 ± 10 area-%). This difference can be attributed to newly formed gypsum and other secondary sulfates (e.g. K-jarosite) and secondary gel phases. The average content of gypsum and secondary sulfates was calculated to be 7.2 ± 6.1 area-% (max. 33 area-%), and the average content of gel phases to be 3.1 ± 2.0 area-% (max. 14 area-%). In this lamina (Fig.1.32 B) most of the sulfides have been oxidized, and most of the carbonates have been dissolved, and contributed to form 25 area-% of gypsum and other secondary sulphates, and the porosity was reduced to 13 area-%. The amorphous gels contained variable amounts of Fe-Si-S-Al-Zn and sometimes K (Figs. 1.28, and 1.29).

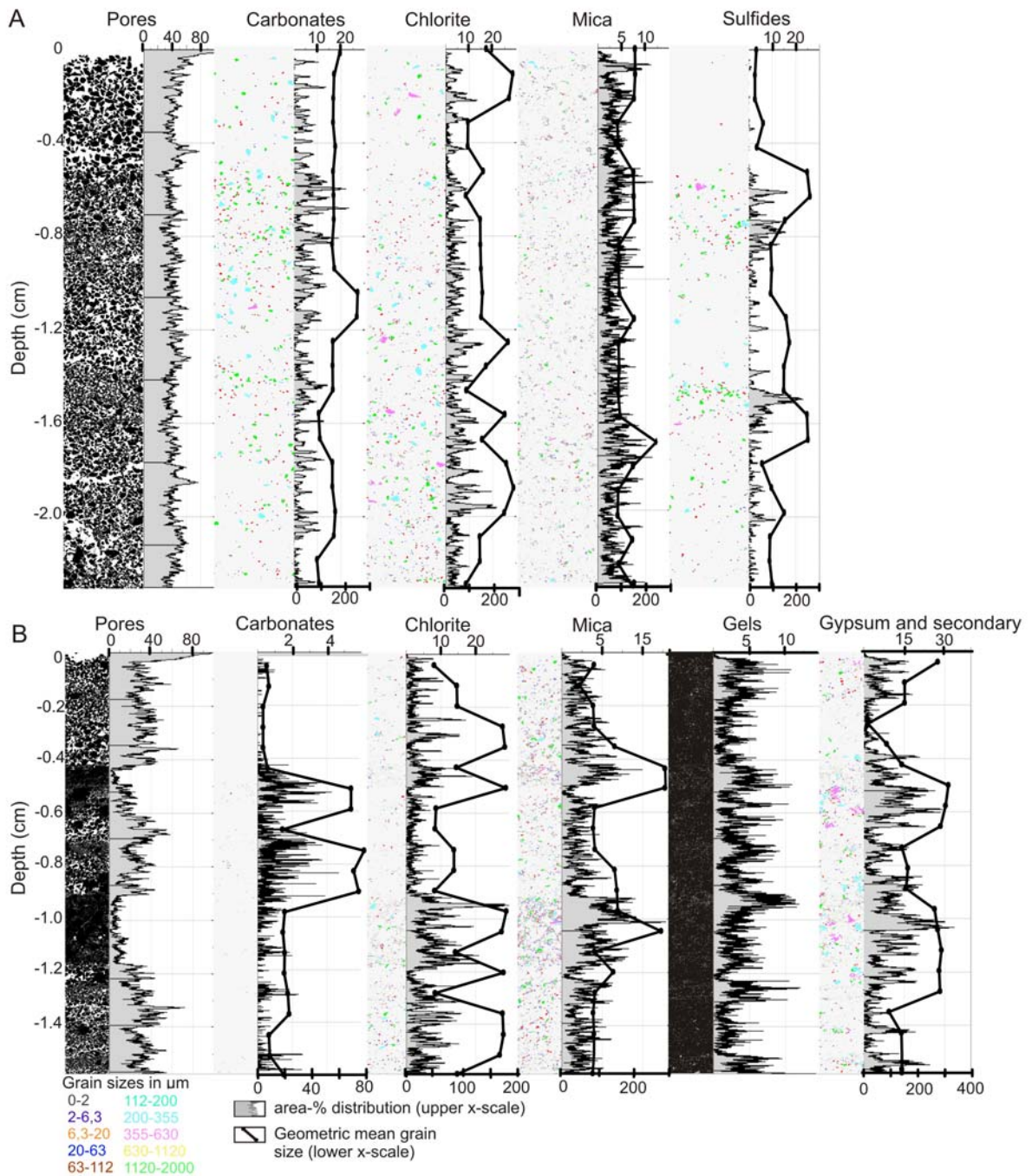


Fig.1.31. The area-%, grain size and geometric mean grain size (μm) distributions of some phases along the vertical profiles in the unoxidized (A), and hardpan (B) layers. Data derived from figure 1.30.

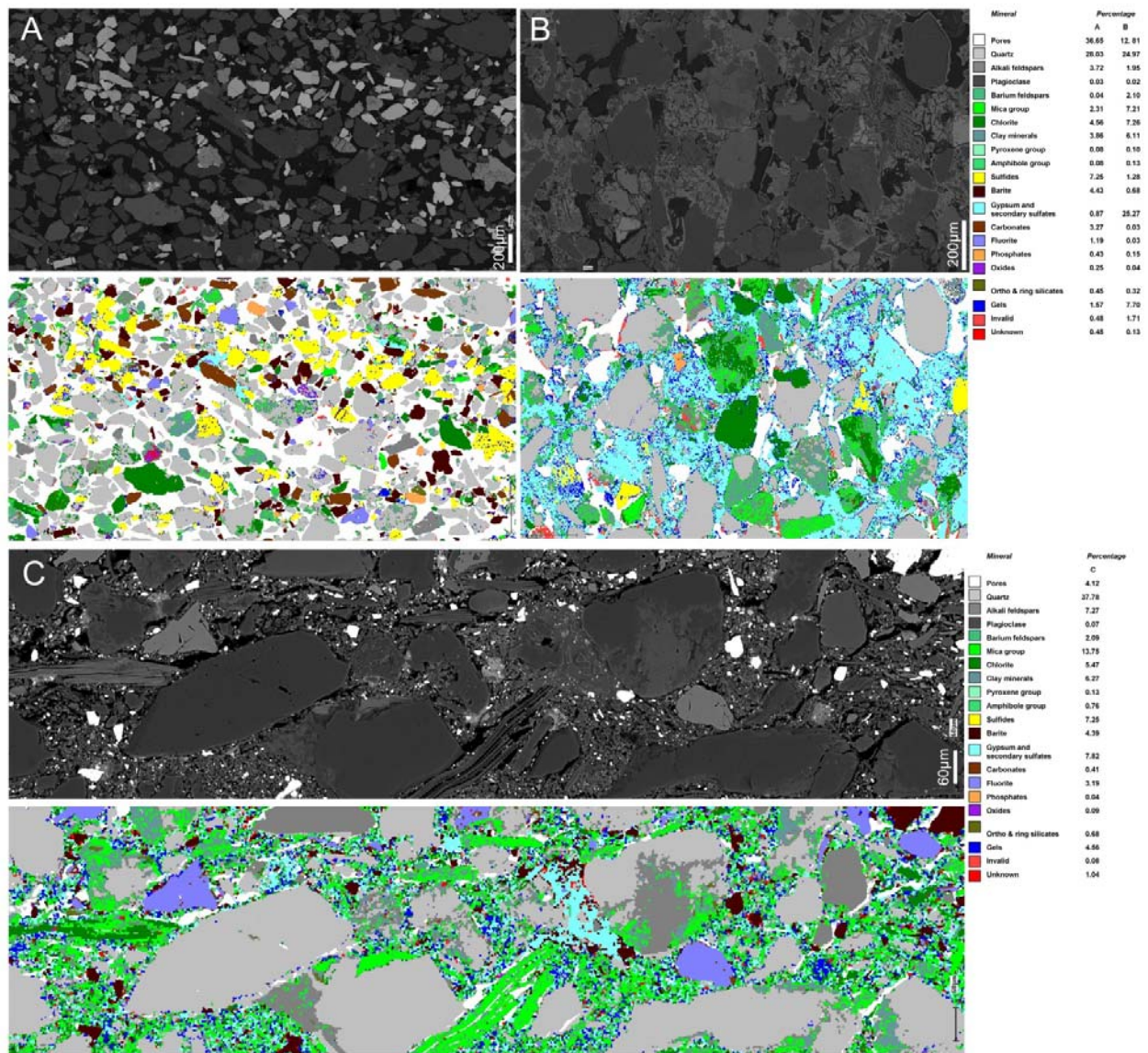


Fig.1.32. Details from the unoxidized (A) and hardpan (B, C) layers of samples S16, S5 and S12 respectively. A and C positions were indicated in Fig. 1.30.

Figure (1.33) reveals characteristic patterns for mineral volume ratios as a function of total porosity in the hardpan layer. At porosities higher than 40%, the system is dominated by quartz and elevated open pores, whilst pores below 35% show elevated partitioning of pore filling phases. This is ascribed to the availability of reactive phases. The amount of quartz decreases towards lower porosity classes. Silicates such as mica, chlorite, amphibole, and clays etc. in contrary are enriched in the low porosity domain. This is caused by the clay fraction partially filling the pores (e.g. Fig. 1.32C). Feldspars display an up and down pattern probably related to the different feldspars. Trace

and minor minerals show characteristic peaks for barite at about 30 %, for fluorite and carbonates at about 35 %, whilst phosphates, oxides and sulfides peak at around 40 % pore area. Phosphates additionally show a broad peak between 20 % and 30 % area. Most sulfides have been altered, the observed distribution, therefore, probably relates to the non accessible grain fraction (inclusions in quartz). In Fig. (1.33 D) the open porosity pattern fits well with the quartz distribution, whilst gypsum shows a strong negative correlation. The gels on the other hand follow the trend of the other silicate fractions.

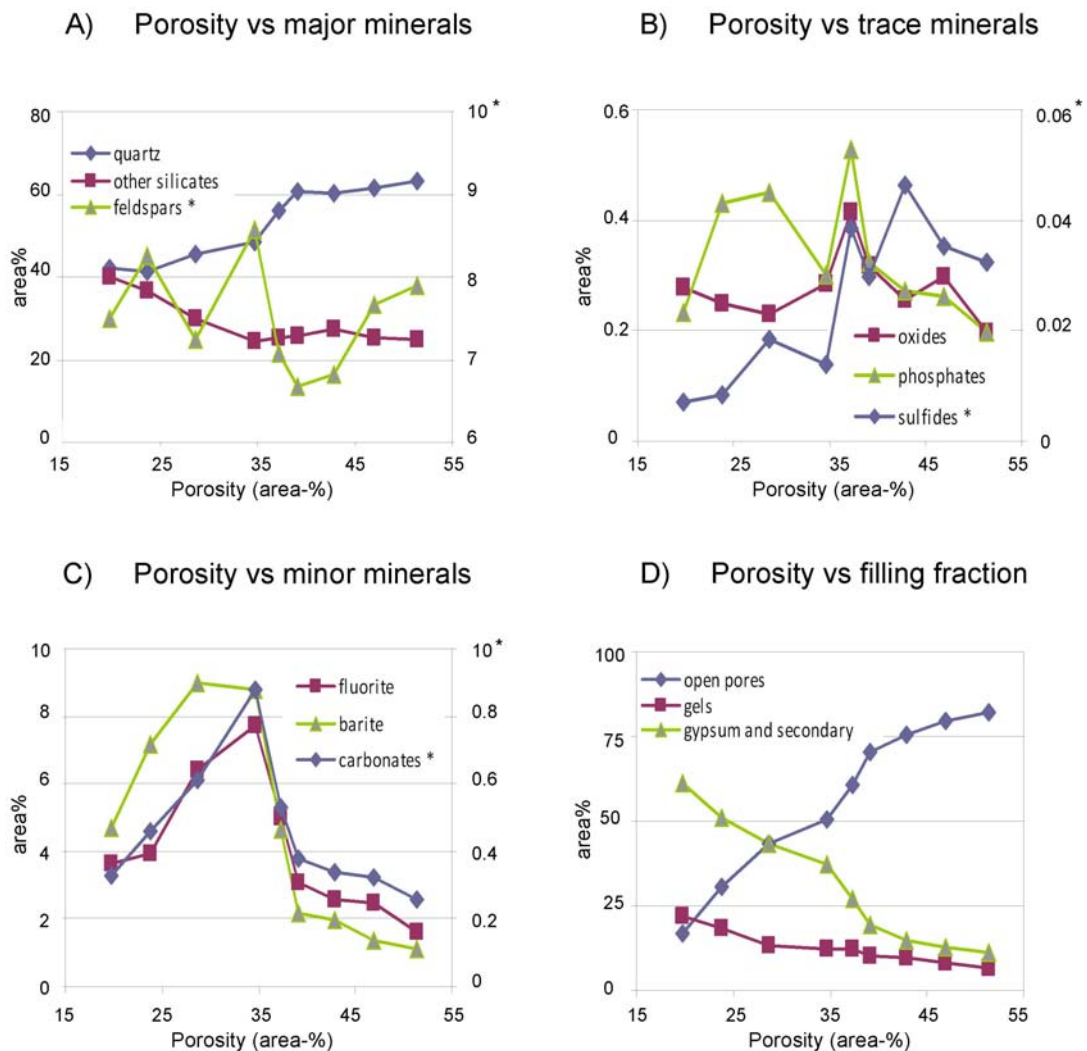


Fig.1.33. Relationship between porosity and abundance of A) major, B) trace, and C) minor minerals (in area-%) within the hardpan layer. In (D) the fraction of total porosity (set to 100%) that contributes to open pores and pores filled by gel or secondary minerals is shown. Pores related to partial or total removal of sulfides in the course of alteration could not be differentiated. The data,

which were derived from figure 1.30B, were sorted in porosity classes of 5 % steps. The right axis refers to the minerals marked with an (*). Included in “other silicates” are mica- and chlorite-group minerals, as well as clay minerals.

Due to the inhomogeneous distribution of minerals, the possibility of hardpan layer formation was increased (Graupner et al. 2007). The effect of stratification on hardpan layer formation in sulfide-bearing mine tailings was studied and modelled by Meima et al. (submitted). They found that in carbonate-free tailings the probability of hardpan layers was increased in systems where finer grained mica-enriched layers are situated immediately below relatively coarse layers enriched in arsenopyrite or pyrite, but absent in systems with a homogeneous distribution of iron-bearing sulfides. This is emphasized by the above mentioned pore to mineral relationship (Fig. 1.33), where lamina with porosities higher than 35 % contain an elevated quartz content and low amounts of accessible reactive phases. As fine grained layers retain water for a prolonged period and even might act as physical barriers elevating the water content in the overlying coarser lamina, the coarser lamina provide better access for oxygen during drying periods. The advantage of sandwich texture found in these tailings is, that even during the dry season enough humidity may be available to keep reactions going. Furthermore, the water retention capacity of the material is further increased by the observed increase in surface area upon oxidation due to selective dissolution of minerals and by precipitation of secondary products.

The stability of the observed hardpans, which act as a sink for arsenic, lead, and some other metals in the tailings environment, depends on the stability of its secondary amorphous gels and other crystalline phases at the ad hoc pH and redox conditions. Hardpans may be able to reduce the amount of water entering the heap at their positions, but since their lateral extension is limited, their protective impact may be limited in such a way that the outer rim zones of the impoundment may fall relatively dry and become stabilized. However, since the hardpans are slightly dipping towards the centre of the impoundment as shown from the different pits along the surface, this will influence the transport of water and oxygen and consequently alteration in such a way that vertical advancement is widely inhibited, but layer parallel transport of oxygen and water will promote prograding lateral alterations and may significantly contribute to the final amount of ARD. The question whether contaminants mainly concentrate due to the depositional style in the rim, or will occur eventually in elevated amounts in other areas within the impoundment needs further

investigations and drilling in zones identified by tomographic geophysical methods such as electrical resistivity and spectral induced polarisation.

II.5. Conclusions

MLA has been applied on mine tailings as a faster method to quantify and follow small μm scale changes of the primary mineral phases and the development of the secondary amorphous and crystalline phases. This information is crucial in understanding the development stages of hardpans and for the interpretation of the bulk mineralogical, physical and geochemical data obtained by other methods. For example, grain sizes showed rhythmic cycling from lamina to lamina. The density of minerals controlled the arrangement and composition of the lamina during spilling process, as we found heavy minerals rich lamina, silicates lamina and carbonates rich lamina. Bulk particle density increased in the unoxidized layers compared to the oxidized and hardpan layers. The porosity changes from homogeneous distribution in the unoxidized layers to be reduced at certain horizons in the hardpan layers due to the precipitation of gels and secondary phases. Also, the coincidence of lamina of grain size contrast, accumulation of reactive material and a relatively low primary porosity promote cementation and subsequently hardpan formation in individual lamina packages. The precipitations of the different secondary phases were related to the distribution of the primary minerals within the lamina. This study has shown that hardpans may not only form due to the accumulation of secondary phases in distinct layers, but also due to mineral fractionation as elucidated by MLA and flushing during deposition. This sandwich structure favors precipitation of secondary phases within a thin boundary layer, due to the availability of reactive compounds in immediate vicinity to each other, the extreme chemico-physical of the microenvironments gradients supported by periodical water saturation and oxygen availability, as well as microbial activity.



**Hardpan formation in Egypt:
Possibility and environmental risks**

2.1. Abstract

Despite its importance within environmental management strategies, little concern throws to sulfide oxidation and/or hardpan formation at neutral pH where dry conditions prevailed. Two gold mine tailings impoundments in Egypt, El Sid and Barramiya, were studied for their geochemical and mineralogical properties, as well as the effect of climate on hardpan formation. The two tailings impoundments are characterized by homogeneous silt sized sediments (>42%). Both have high carbonate, predominantly as calcite for El Sid and dolomite-ankerite for Barramiya, and low sulfide contents, chiefly as pyrite, galena, sphalerite, and arsenopyrite for El Sid and arsenopyrite-pyrite for Barramiya. The tailings from El Sid are characterized by high average concentration of Pb (average 2758 mg/Kg) and Zn (average 2314 mg/Kg), its lower part is dominated by mafics, whereas the upper part is dominated by granitoids. Barramiya tailings have higher As (average 2836 mg/Kg) concentration and represent a mixture of mica schists, and mafics to ultramafics. During field investigations, no hardpans have been identified, only bassanite in addition to gypsum were found at the surface of El Sid tailings impoundment, forming thin layers and desiccation crack fillings. Column experiments under normal room temperature using unmodified sediments from both locations showed that a thin but soluble hardpan layer consisting of gypsum, halite and sodium sulfate (Na_2SO_4) formed at the top of the column of El Sid tailings after two weeks, such a layer was not recognized in the column from Barramiya tailings. The homogenous thickened tailings deposition in both tailings did not favour hardpan formation, since the critical amount of reacting sulfides was never achieved in individual lamina, due to missing mineral and grain size fractionation during deposition, in addition to the high temperature and low water availability characteristic for arid desert climate regions which didn't allow significant oxidation of sulfides. As a result, both tailings may suffer from continuous erosion and spreading out of contaminants to the environment for a prolonged period of time by flash floods.

Keywords Gold mine . Thickened deposition. Tailings . Hardpan . Column experiments

2.2. Introduction

Mine tailings in semiarid and arid areas are widespread worldwide. The environmental impacts of these tailings are enormous, due to the absence of plant cover and therefore suffering from continuous water and/or wind erosions with time (Gonzalez and Gonzalez-Chavez, 2006; Mendez and Maier, 2008).

Mining activity in Egypt extends over 6,000 years. The main focus was on gold. Geologically, large areas of the Eastern Desert belong to the Precambrian basement of the Arabian–Nubian shield. More than 250 gold production sites were mined in this area during the ancient Egyptian history (Klemm et al., 2001). Mining focussed on the top parts of these sites, where the ancient miners followed the quartz veins (Fig. 2.1). At all large and economically significant gold sites, tools used for gold extraction such as stone mortars and mills, remainders of settlements along the wadis were found, dating back to Ptolemaic and Roman times (Fig. 2.1). Modern gold mining took place from 1902 to 1958 with a production of about 7 t of gold (Kochin and Bassyuni, 1968), but was stopped in 1958 due to political reasons. In the last years, big exploration projects were carried out in the Eastern Desert. In 2009 the Sukari mine was set into operation at an ancient site.

After extraction of the gold from the ore by various methods the waste materials are transported to their deposition sites e.g., the tailings impoundments (Blowes et al. 1991; Robertson, 1994). From field investigations, old mining heaps were characterized by coarser grain sizes compared to the finely ground sand to silt-size wastes of the new heaps. This is the result of a change of the mineral treatment processes from hand crushing and separation in Pharaonic and Roman times to crushing, milling, gravity separation and flotation plants of modern times (Fig. 2.1). Due to the extreme arid climate and the scarcity of water in the area, and also due to the high carbonate content of the tailings, no environmental concern has been focused on these tailings.

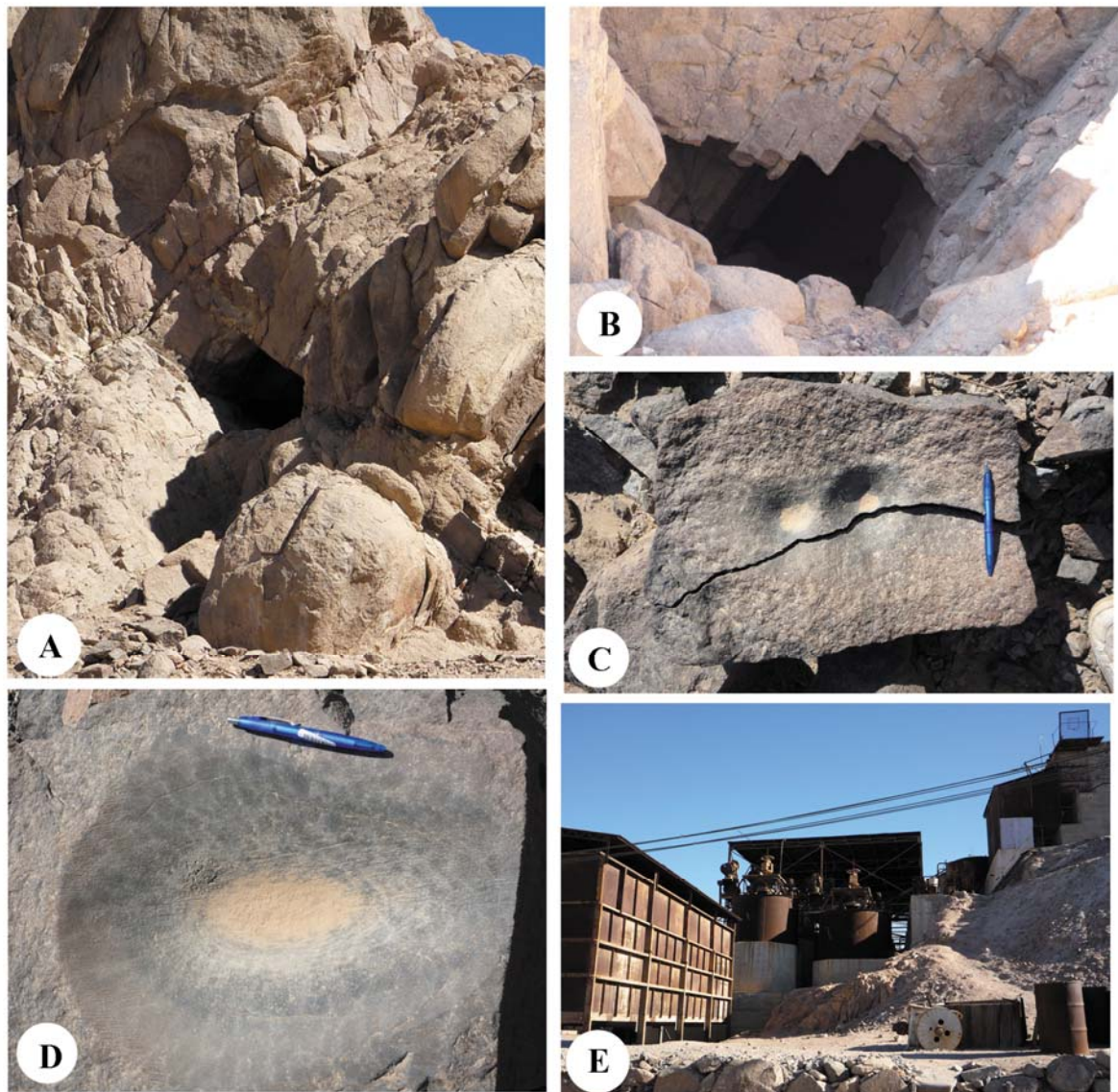


Fig. 2.1. Showing ancient Egyptian gold exploration following quartz veins and shears (A,B); stones used for ore pounding and milling (C,D); and the processing plants at El Sid mine site from the year 1958 (E).

Availability and accessibility of water, oxygen, temperature, precipitation and evaporation are important parameters for sulfide oxidation process (Henke, 2009), in addition to microbiological activity. Oxidation process involves reaction, successive dissolution of reactive minerals, transport and precipitation in definite zones. Part of the rainwater reaching the surface of a heap, will immediately run off laterally, dissolving available efflorescent phases and being responsible for so

called first flashes of Acid Rock Drainage (ARD) rich in sulfate, ferrous iron and some toxic metals. Part of the rainwater infiltrates the heap, mobilizes pore water adding more load to the AMD (Blowes et al., 1995, Nieto et al., 2007; Courtin-Nomade et al., 2009). Not all the infiltrated water contributes to AMD. A significant amount moves upward under the effect of evaporation. Then the dissolved and colloidal matter precipitates at the capillary fringe as secondary crystalline phases and amorphous gels, agglutinates grains and reduces porosity (Rammlmair, 2002), leading to the formation of hardpans (Thornber et al., 1987; Blowes et al., 1991; McGregor and Blowes, 2002; Rammlmair, 2002; Lottermoser and Ashley, 2006; Graupner et al., 2007; Rammlmair et al., 2008). Part of these phases feeds first flashes as stated above. Also, clogging of pores by secondary phases takes place in the cementation zone at the unsaturation/saturation boundary, due to physico-chemical changes in a narrow zone (Graupner et al., 2007). However, little studies have been carried out on the possibility of hardpan formation in gold (eg. DeSisto, 2008). Information was achieved basically regarding mineralogy, geochemistry and/or microbiology of gold mine tailings (Jambor and Blowes, 1991; Blowes et al., 1998; Roussel et al., 2000).

Due to the little information concerning sulfide oxidation at circum-neutral pH combined with high temperature and scarcity of water, the following work was carried out to investigate the geochemical and mineralogical characteristics of two gold mine tailings in Egypt, and study the combined effect of climate, mineralogy and tailings discharge in the weathering processes and/or hardpan formation and its influence to the surrounding environment.

2.3. Study area

In the central Eastern Desert of Egypt two tailings dams related to gold mining were selected for further investigation:

A) El Sid gold mine area and tailings, located in the halfway between Qift (at the Nile Valley) and Quseir (at the Red Sea coast) (Fig. 2.2).

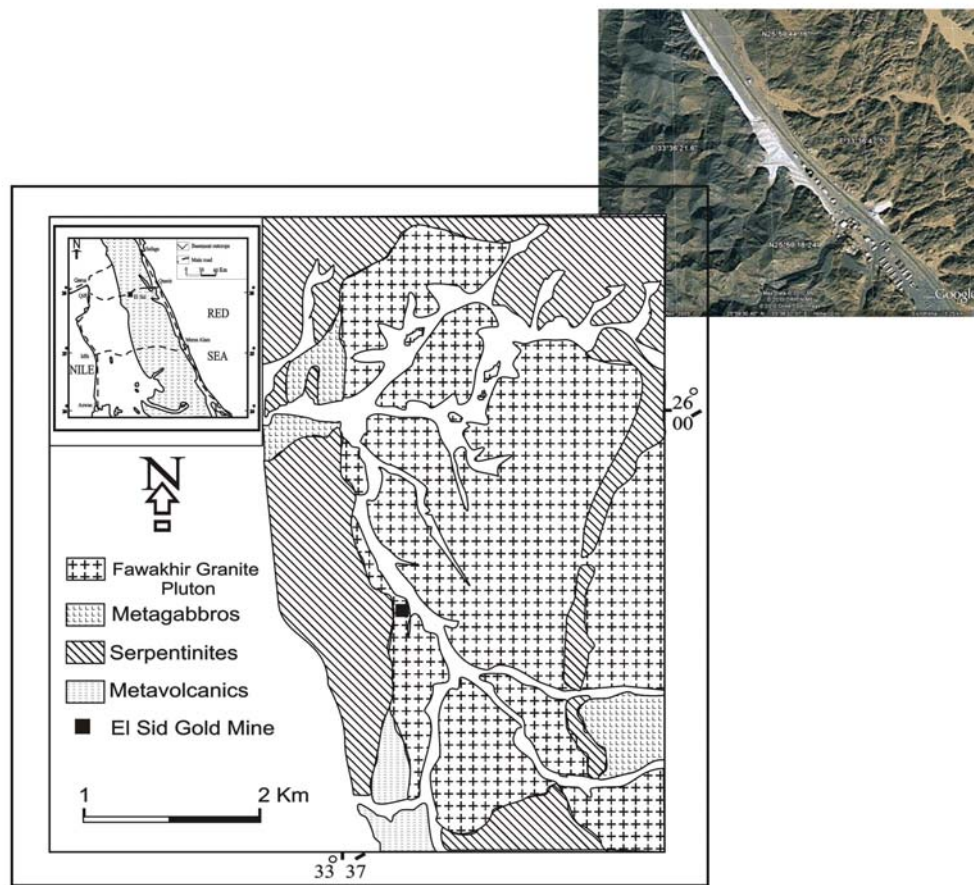


Fig. 2.2. Google earth and geological maps (after EI-Bouseily et al., 1985) of El Sid area.

El Sid is considered to represent one of the largest gold occurrences and producers in Egypt. It was mined during Pharaonic and Roman times and from 1940 until 1957. According to Kochin and Bassyuni (1968), in the last period, the mine produced 3,110 kg (100,000 oz) of gold from 120,000 tonnes of ore with an average grade of 27.9 g/t, which considered as half of the total Egyptian gold production during this time, with 330,000 tonnes of waste rock and tailings averaging about 3 g/t gold. The gold mineralization is a vein-type mineralization hosted by sheared ophiolitic ultramafic rocks. It further occurs in hydrothermal quartz veins (3-6 m thick) cutting across the granite-serpentinite contact (Botros, 2004) on the western side of Fawakhir granite pluton, and extends further west in the serpentinite through a thick zone (~15 m) of graphite schist (EI-Bouseily et al., 1985).



Fig. 2.3. El Sid gold mine tailings: Lateral (A) and surface (B) views of the profile position with a thin hardpan of gypsum (C) and gypsum crystallization on both sides of sediment refilled desiccation cracks, and close to the crack in patchy distribution (D) narrow desiccation cracks and polygons at the surface of the tailings.

Pyrite and arsenopyrite are the most common minerals throughout the deposit (El Ramly et al., 1970), in addition to sphalerite ($Zn(Cd)S$), galena (PbS), chalcopyrite ($CuFeS_2$) and minor amounts of bornite (Cu_5FeS_4) and pyrrhotite ($Fe_{1-x}S_x$) (El-Bouseily et al., 1985; Hussein, 1990), recorded in the mineralized veins.

B) Barramiya gold mine area and tailings are located in the half-way between Mersa Alam (Red Sea coast) and Idfu (Nile valley) (Fig. 2.4). Like El Sid, the gold mineralization belongs to a vein-type mineralization hosted by sheared ophiolitic ultramafic rocks (Botros, 2004).

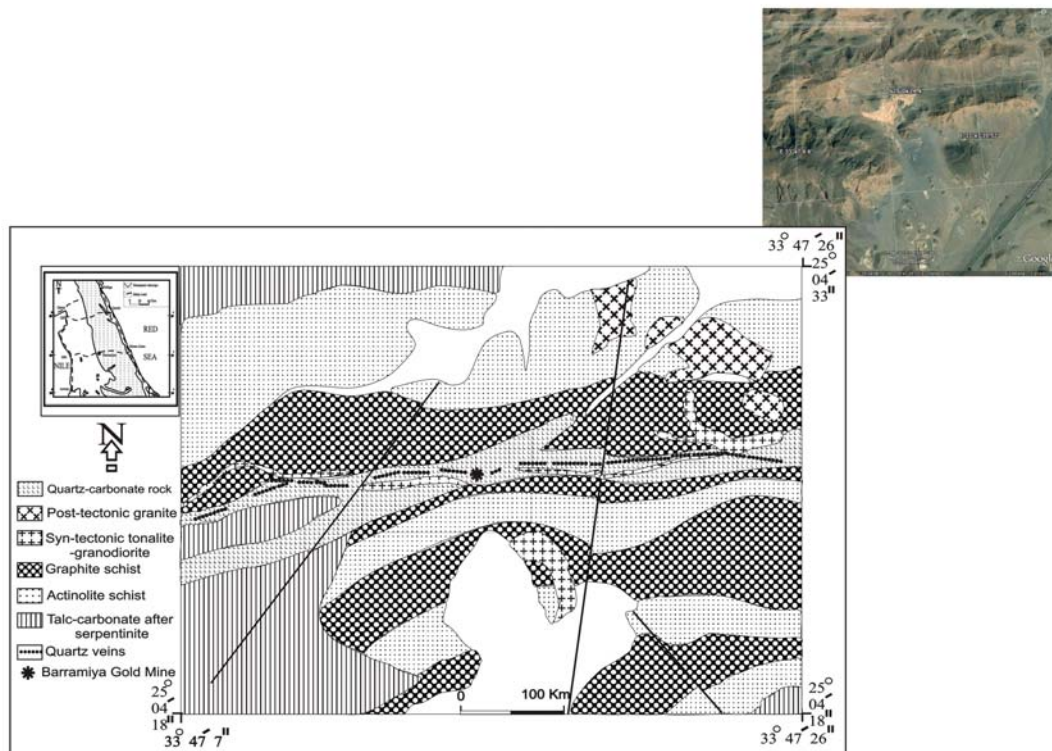


Fig. 2.4. Google earth and geological (after Botros, 2004) maps of Barramiya.

It was mined since Pharaonic times. In the 20th century from 1907- 1919, it was reopened by the “Baramia Mining and Exploration Company Ltd.”, with a total of 50211 ounces of bar gold production (Attia, 1948). Gold resources are the range of 20,000 to 27,000 tons were done by the geological survey of Egypt (EGSMA) with a gold content ranging from 2.2 to 15.5 g/t (Hussein, 1990).

The country rocks around the mine consist of an ophiolitic melange that covers about 75% of the exposed rocks. This melange is composed of allochthonous blocks and clasts of serpentinite (after dunite and harzburgite) distributed within an intensively deformed matrix of actinolite and graphite schist (Botros, 2004). The auriferous veins are restricted to several systems of fracture zones conformable with the regional schistosity and occur mainly in the graphitic schist. There are gray or dark blue gray quartzes with fine disseminations of gold and small amounts of sulfides (pyrite and chalcopyrite) (Hussein, 1990).



Fig. 2.5. Barramiya gold mine tailings: (A) Surface view, locally with wide desiccation cracks with partly intensive erosion (B); the position of the profile (C); erosion effects at deep desiccation cracks (D); and subrosion channels at the bottom (E) of the tailings caused by intensive flooding.

The gold deposit consists of four lodes, the Main Lode, Taylor's Reef, Caunter Lode and New Caunter Lode. The Main Lode is the eastern mineralized part, it is located in an intensively fractured zone in the graphitic schist with an average thickness of 1 m. The ore contains 2.2-1.5 g/t of gold content. Taylor's Reef was discovered underground north of the Main Lode, with an average thickness of 0.6m, and average assay of 16.5 g/t. Caunter Lode and New Caunter Lode represent two branches of the mineralized zone with north-south general strike and dip steeply to the southeast. The gold grade in Caunter Lode from 18.69-43.09 g/t with 0.6m average thickness, New

Caunter average thickness is 1 m with a gold grade of 8.4 g/t. The tailings consist of about 54,000 tons of auriferous sands and slimes with an average gold content of 5.67 g/t (Attia, 1948; Hussein, 1990).

2.3.1. Climate

As the area is located in the desert climate region, it is characterized by very hot and dry summers and moderate dry winters. The rain precipitation is very low and even seldom. Total precipitation reached 5.5 mm/y with max precipitation in November and December. However, intense rainfall events (often 60 mm/h) over short periods occasionally happened (Ghoneim et al., 2002) which cause flash floods, as a result of strong local convective thunderstorms created by unstable weather conditions (Greenbaum et al., 1998). The recorded maximum temperature was 36.2°C in July and minimum temperature of 11°C was recorded in January (Data were taken for the area along the Red sea from <http://www.climatetemp.info/egypt/>).

2.4. Material and methods

The tailings impoundments were deposited downstream of small wadis. During our project a total of 17 samples were collected each 10 cm-depth from El Sid tailings and 14 samples, each 20 cm-depth collected from Barramiya tailings. El Sid tailings were grey to pale yellow in colour and showed relatively small desiccation cracks compared to Barramiya which has grey-dark grey colour with beige coating and wide and deep desiccation cracks and very intensive erosion and channel washout. Before collection, the outer weathered part was removed and the tailings samples were collected using stainless trowel and preserved in self-sealed plastic bags, to decrease possible contaminations during transport to the laboratory. All samples were characterized by very fine grain sizes, and were apparently homogeneous. Aliquots were obtained using a sample splitter. The aliquots were analyzed for particle size distribution, surface area, chemistry, mineralogy, and dissolved ions after water extraction from saturated samples.

Particle size distribution was measured by two instruments, a CAMSIZER (Retsch GmbH) for grain sizes above 63µm, and a SediGraph 5100 (Micromeritics Instrument Corporation) for grain sizes below 63µm. Specific surface area was calculated using the BET equation (Brunauer, Emmett and Teller, 1938) by using nitrogen gas adsorption measurements with the Gemini III 2375 Analyzer (Micromeritics Instrument Corporation).

Chemical analysis of the samples included measurement of X-ray fluorescence (XRF, PW1480 and PW2400) on fused beads for total chemical compositions; Leco furnace instrument (LECO Corporation, model CS-200) for total sulfur, total carbon (C-total) and organic carbon (C-org) concentrations. Carbonate carbon (C-carb) was calculated as the difference between C-total and C-org. S-sulfate was measured by attacking the sample with 0.2 M NH₄-oxalate for 2 hours at pH 3.0 (controlled by adding 0.2 M oxalic acid) in a water bath at 80°C. The dissolved sulfur content was measured by ICP-OES, which represents S-sulfate (Dold, 2003). Then sulfide sulfur (S-sulfide) content was derived from the following equation:

$$\text{S-sulfide} = \text{S-total} - \text{S(barite)} - \text{S-sulfate}$$

where S(barite) equivalent to the Ba measured by XRF for barite saturation.

Sample aliquots were saturated at a sample to liquid (distilled water) ratio of 1:1. To obtain the water soluble fraction the samples were continuously shaken for 24 h at room temperature using a Heidolph Reax Overhead Shaker (Heidolph Instrument Corporation). Then the paste was filtered using a 0.45 µm filter (type FP30, Whatman International Ltd.). The pH of the extractants was measured using a Pocker-size precision pH meter CG 837 (Schott Instruments GmbH) which was calibrated before the measurements using pH 4, and 7 buffers. Conductivity measurements were performed using a microprocessor conductivity meter type LF 323-B/set, model TetraCon 325 (Juergens & Co GmbH). All the samples had a pH higher than 5, therefore, they were divided into two aliquots, one preserved unacidified for HCO₃ titration, SO₄ and Cl measurements using ion chromatography, and the other one was acidified using few drops of HNO₃ (69% concentration) until the pH become lower than 2 (controlled by pH paper), then analysed by Inductive Coupled Plasma-Optical Emission Spectrometry (ICP-OES, SPECTRO Analytical Instruments GmbH, model Ciros Vision CCD) for major cations with detection limits <0.8 mg/L and Inductive Coupled Plasma-Quadrupole Mass Spectrometry (ICP-QMS, Agilent 7500ce) for trace elements with detection limits <0.1 mg/L.

The bulk mineralogy of all the samples was analyzed by powder X-ray diffraction (XRD), using a Philips PW 3710 series automated powder diffractometer, with monochromated CuKα (mean wavelength of 1.542 Å) radiation. It was operated at 40 kV and 30 mA, with glancing angles 2θ between 2° and 65°. A secondary graphite crystal monochromator was used. For evaluation of the data the software package Galaxy linked with a PDF2 data base was employed. This, in addition to doing micro-identifications of the different phases and its textural relationships on polished sections,

made from the powder samples, using MLA (Mineral Liberation Analyzer, from University of Queensland (Australia) Julius Kruttschnitt Mineral Research Centre (JKTech)) software package which combined to FEI Quanta 600 FEG ESEM (Environmental Scanning Electron Microscope) coupled with energy dispersive X-ray (EDX) detector.

The MLA software controls the SEM hardware in order to quantitatively analyse mineral distribution within the samples. After creating a standard database for the minerals by collecting X-ray spectra for each identified mineral phase, a series of back-scattered electron (BSE) images are collected. From the differences in the grey values between the minerals, the MLA software collects spectra into the measurement file, and compared them to a standard mineral spectral database. The measurement can be done either by collecting one X-ray spectra within the centre of each phase or by making a grid of equidistant positions, or combining different methods (Gu, 2003; Fandrich et al., 2007).

In order to investigate the potential of these tailings to produce hardpans, small column experiments were carried out. The samples were water saturated, and then left to evaporate at normal room temperature.

2.5. Results and discussions

In both areas, thickened discharge and paste technologies methods were used in tailings disposal. In these methods a significant percentage of water is removed prior to its discharge (Williams and Seddon, 1999). The paste itself did not undergo fractionation, neither grain size or mineralogically nor chemically. The individual layer thickness was in the range of a few tens of centimetres close to the release from the lorry and a few centimetres after a few meters of transport. Due to the high temperature in these two areas, rapid consolidation happened to the tailings paste.

2.5.1. Geochemical properties

2.5.1.1. Bulk rock chemistry

The bulk chemical composition of the investigated tailings samples in both localities show different trends at different depth profiles (Figs. 2.6, 2.7, table 2.1). Generally, the tailings from El Sid are characterized by high average concentration of Pb (2758 mg/Kg) and Zn (average 2314 mg/Kg), whereas, Barramiya tailings have higher As concentration (2836 mg/Kg) and Al₂O₃ (11.3 %). Looking into details, the trends for El Sid tailings from 0cm to -60cm show highest values for

Al₂O₃, K₂O, Na₂O, P₂O₅, W, high Fe₂O₃, low CaO, MgO, As, Pb, Zn, Cu, and Ni pointing towards granite as the dominant host rock during mining. Between -60cm to -90cm, peaking at -80cm high values for SiO₂, Pb, Zn are recorded coinciding with a decrease in Fe₂O₃, Al₂O₃, CaO, MgO, Na₂O, K₂O, As, Ni, Sr, and Co pointing towards quartz veins as the prominent host for gold mineralization. From -90cm to -120cm, peaking at -100cm slightly elevated Fe₂O₃, Al₂O₃ elevated CaO MgO, Ni, Co and S-sulfide, favour mafic to ultramafic host, a zone from -120cm to -140cm low in CaO, MgO, Fe₂O₃, Pb, Zn, Ni, Co and S-sulfide, but very high in As and Cu which could related to a shear zone rich in arsenopyrite and chalcopyrite. The lowest part of the section (-120cm to -140cm) has highly elevated CaO, MgO, As, Pb, Zn, Ni, Cr, Co, and S-sulfide moderate Fe₂O₃, but low Al₂O₃, K₂O and Na₂O pointing to a dominant mafic host with some veining (Fig. 2.8). The chemical changes in the profile can be correlated to the progress of mining galleries from mafic host crossing the boundary to the granite (Behre Dolbear international limited technical report, 2009).

Barramiya shows small scale variation of the chemistry of the tailings (Fig. 2.8). Zones with variable Fe₂O₃, Al₂O₃, CaO, MgO, K₂O and Na₂O indicating variable amounts of mafic/ultramafic, schists, and quartz veins involved over the years. Most prominent is an enrichment of Ni and Co coinciding with high MgO, pointing towards mafic/ultramafic dominance in the upper 0cm to -140cm, and elevated K₂O and Na₂O in the lower part of the section showing a dominance of mica schists. Some layers within the two domains point towards a stronger input from other sources such as veins and/or graphite schists.

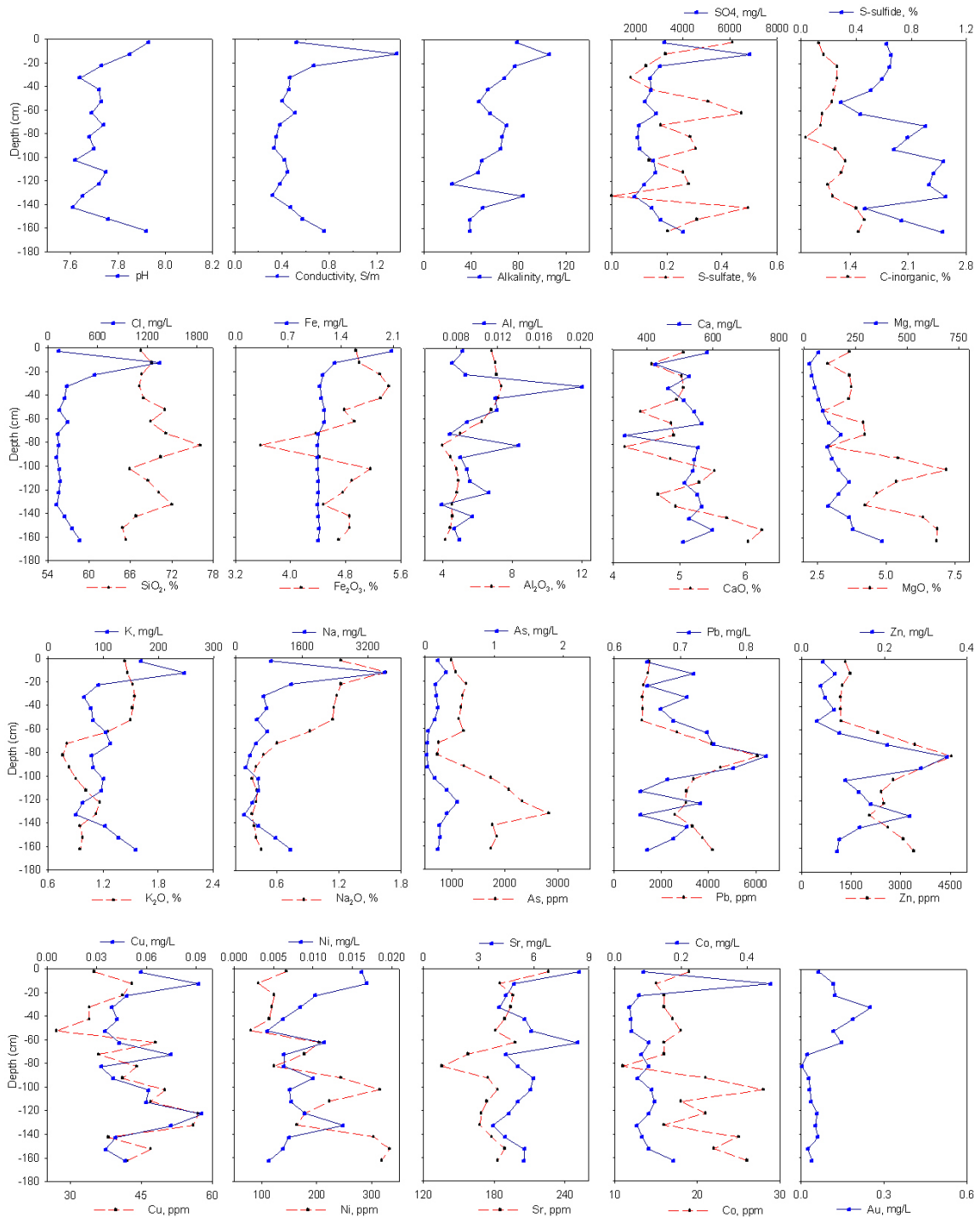


Fig. 2.6. Depth profiles showing the geochemical properties of the paste-water extraction (solid line, upper x-axis) and the solid samples (dashed line, lower x-axis, excluding S-sulfide) for El Sid tailings. Symbol (Θ) refers to scale change for the specified element between Figs. 2.6 and 2.7.

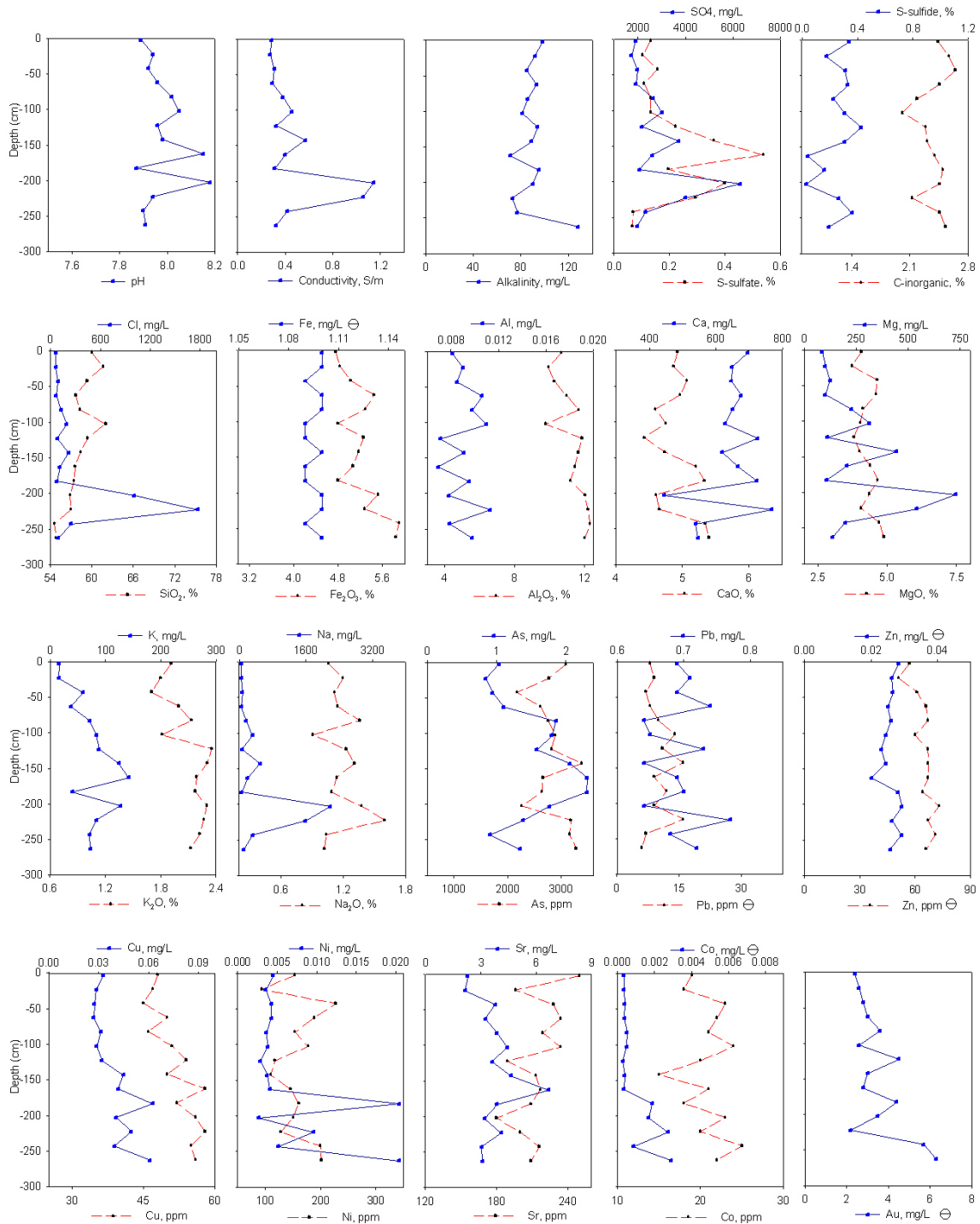


Fig. 2.7. Depth profiles showing the geochemical properties of the paste-water extraction (solid line, upper x-axis) and of the solid samples (dashed line, lower x-axis, excluding S-sulfide) for Barramiya tailings. Symbol (Θ) refers to scale change for the specified element between Figs. 2.6 and 2.7.

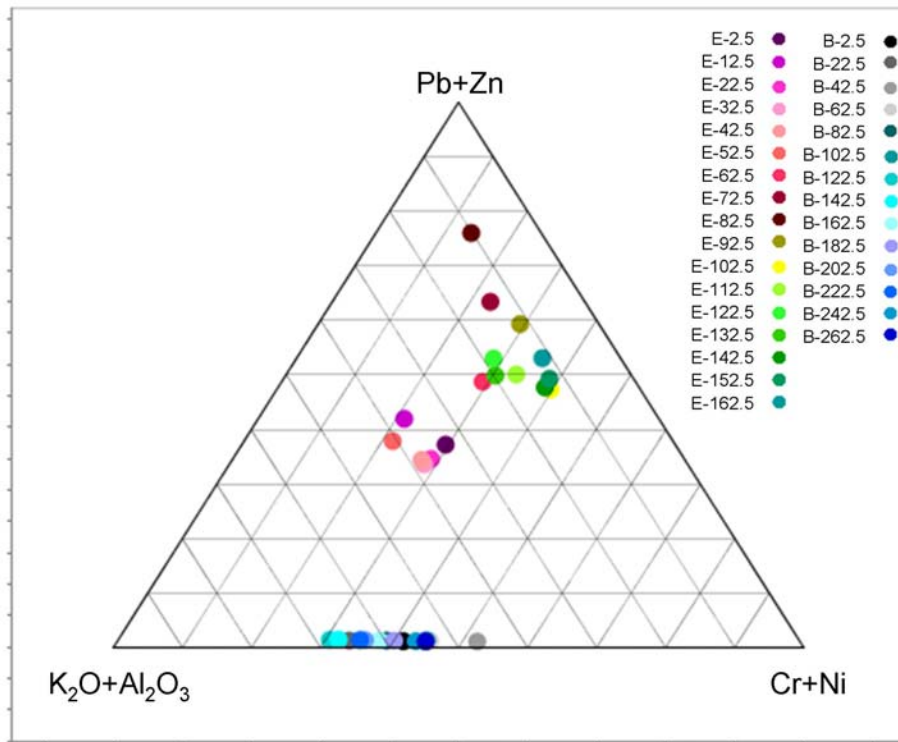


Fig. 2.8. Triangular plot of Pb+Zn, $K_2O+Al_2O_3$, and Cr+Ni, characterizing quartz vein, granite (El Sid)/mica schist (Barramiya) and mafics/ultramafics, respectively, for El Sid (E-depth [cm]) and Barramiya (B-depth [cm]) showing mixing trends related to host rocks.

2.5.1.2. Paste-water extraction

The paste pH for all samples from El Sid were in a range between 7.61 – 7.93, whereas the paste pH for all samples from Barramiya were slightly higher (pH 7.87 – 8.18) (Figs. 2.6-2.7). This is due to high carbonate, but low sulfide content in the tailings, as the average C-carb content for El Sid tailings was 1.21%, whereas for Barramiya tailings was 2.39 % and the sulfide contents were 0.72 and 0.25% respectively.

El Sid tailings showed two contrasting trends in the uppermost portion. Whilst the top 10 cm suffered a wash out of soluble salts expressed by reduced conductivity, alkalinity, SO_4 , Cl, K, Na, Cu, and Ni, other parameters such as pH, as well as Fe, Ca, Mg, and Sr were relatively elevated. The wash out did not reach the 20 cm level where precipitation related to the capillary transport was the dominant feature. The pH was slightly lower, but conductivity, alkalinity, SO_4 , Cl, K, Na, As, Pb, Zn, Cu, Ni, and Co showed highest values. The zone below 30 cm basically was dominated by the rock type and not by the alteration process. Small vertical displacement paying credit to the capillary

transport might have occurred. The high Pb and Zn values at -100cm depth coincide with elevated SiO₂ values. Mg content showed an increase towards depth, whilst other elements peak at certain depth related to the availability. Gold appears to be elevated in the upper part of the section.

Barramiya tailings showed a more complicated pattern. Whilst most elements distribution pattern related to the host rock type, the extracted water chemistry showed almost no relation to the host. This most probably relates to an intensive washout of some ions due to the much longer exposure of Barramiya to rain falls, even seldom in the desert, and to a multiple re-wetting of parts of the tailings. These will cause peak shift of ions as a result of its movement in solution either gravitatively or by capillary transport. The pH as well as conductivity were lower on the top and showed elevated values at deeper parts. Mg, SO₄, K, Na, Cu, Ni, Co somehow follows this trend.

2.5.2. Physical and mineralogical properties

2.5.2. 1. Particle size distribution

The samples are characterized by very fine grain sizes due to the method used for extraction of the gold. The materials are very poorly sorted and consist mainly of silt-size with fine to very fine sands and clay. Barramiya tailings are characterized by finer grain sizes than El Sid tailings (Fig. 2.9). This may be the reason that Barramiya has wider and deeper desiccation cracks than El Sid. Since the El Sid tailings impoundment was more than 40 years younger than Barramiya, either the number of rain fall events, a change in rain fall intensity over the years, or a regional difference could be responsible for the very intensive erosion at Barramiya compared to a moderate erosion at El Sid.

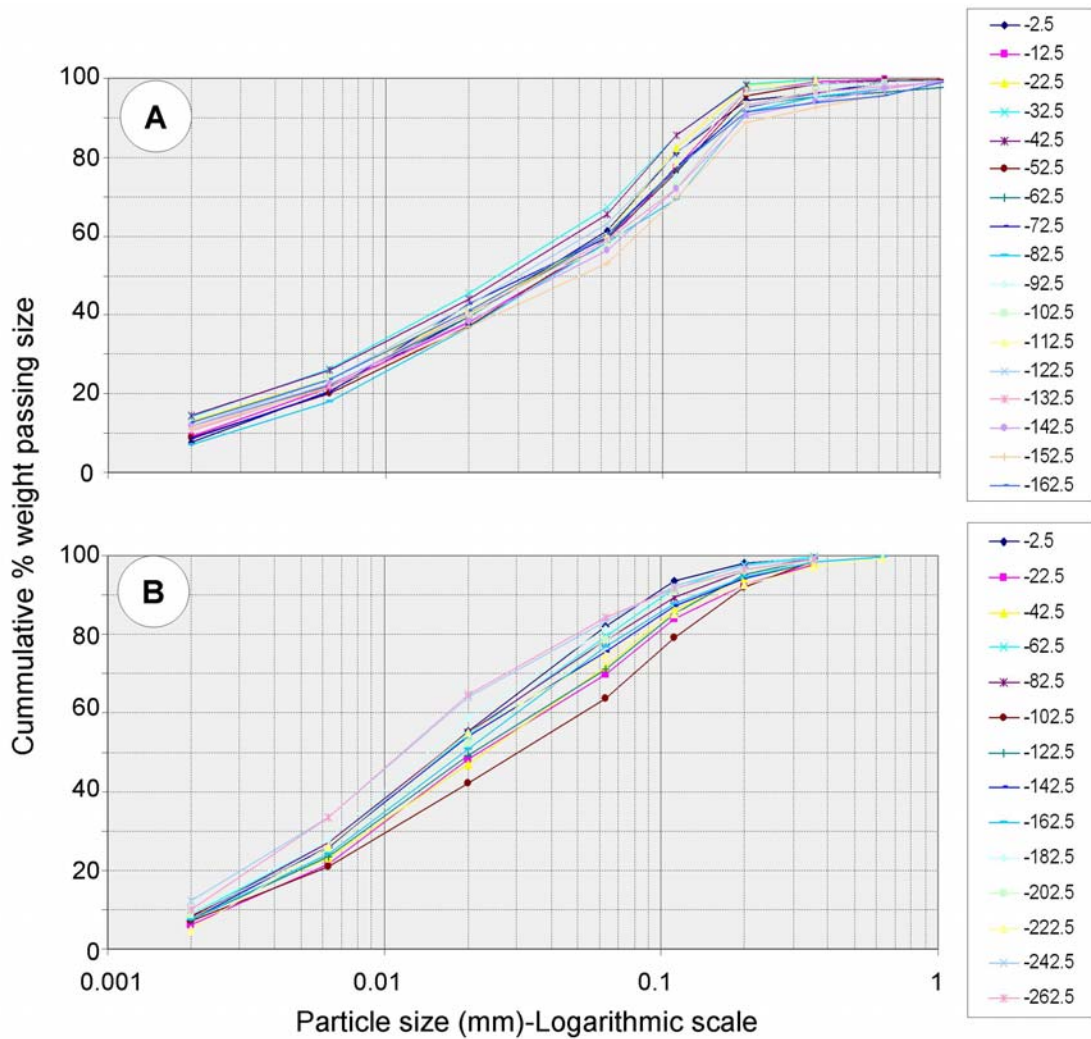


Fig. 2.9. Grain size distribution of the tailings samples from El Sid (A) and Barramiya (B) along the vertical profiles.

2.5.2. 2. Specific surface area (BET)

The specific surface areas of the samples from El Sid tailings range between, 0.4-4.2 m²/g (standard deviations 1.02) whereas the surface areas for samples from Barramiya tailings are slightly higher, ranging between 2.2-6.3 m²/g (standard deviations 1.3) with higher values toward the bottom in both cases (Fig. 2.10). The relation between the surface area and mean grain sizes (calculated using graphical statistical equation of Folk and Ward,1957) showed the expected reverse general trend with a number of excursions caused either by partial agglutination e.g. by gypsum or enhanced surface roughness due to alteration or precipitation of secondary phases and gels (Fig. 2.10).

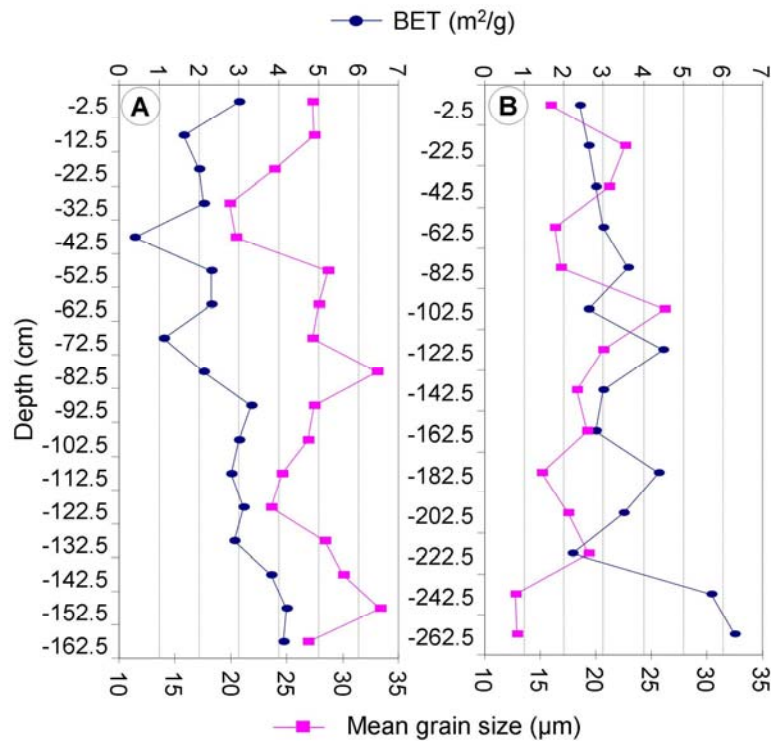


Fig. 2.10. Specific surface area (BET) and mean grain size of the tailings samples from El Sid (A) and Barramiya (B) along the vertical depth profiles.

2.5.2. 3. Bulk mineralogy (XRD)

El Sid tailings is dominated by quartz, calcite, biotite, and talc, in addition to minor phases like feldspars, chlorite, ankerite, hornblende, and gypsum as a secondary phase crystallized after deposition of the tailings. Additionally, the top layer is characterized by the presence of bassanite ($\text{CaSO}_4 \cdot 0.5\text{H}_2\text{O}$), typical for hot arid climates (Allen and Kramer, 1953; Akpokodje, 1984).

Within the profile remarkable changes in mineralogy and mineral ratios can be observed. The upper part from 0 to -70cm is characterized by an assemblage of quartz, biotite, chlorite, feldspar, calcite and ankerite. From -70cm to -100cm and from -110cm to -120cm elevated calcite, gypsum, and locally pyrite or talc, but little feldspar, biotite, and chlorite were recorded. The lower part of the section shows elevated talc and some amphibole besides biotite, chlorite, but reduced feldspar (Fig. 2.11).

Barramiya tailings on the other hand are significantly different. The whole profile is dominated by a mineral assemblage of quartz, muscovite/illite, feldspar, and greenalite with either dolomite mainly in the uppermost and lowest portion or ankerite mainly in the central part. Additionally the

lower and central portion shows talc as an additional phase. Gypsum is recorded in the lower portion. It is worthwhile to note that the samples from the lower portion were sampled at a place one meter displaced, and not covered by the upper and middle part, and close to a zone of maximum erosion and therefore repetitive wetting which promote decomposition of sulfides and precipitation of sulfates during the following dry periods.

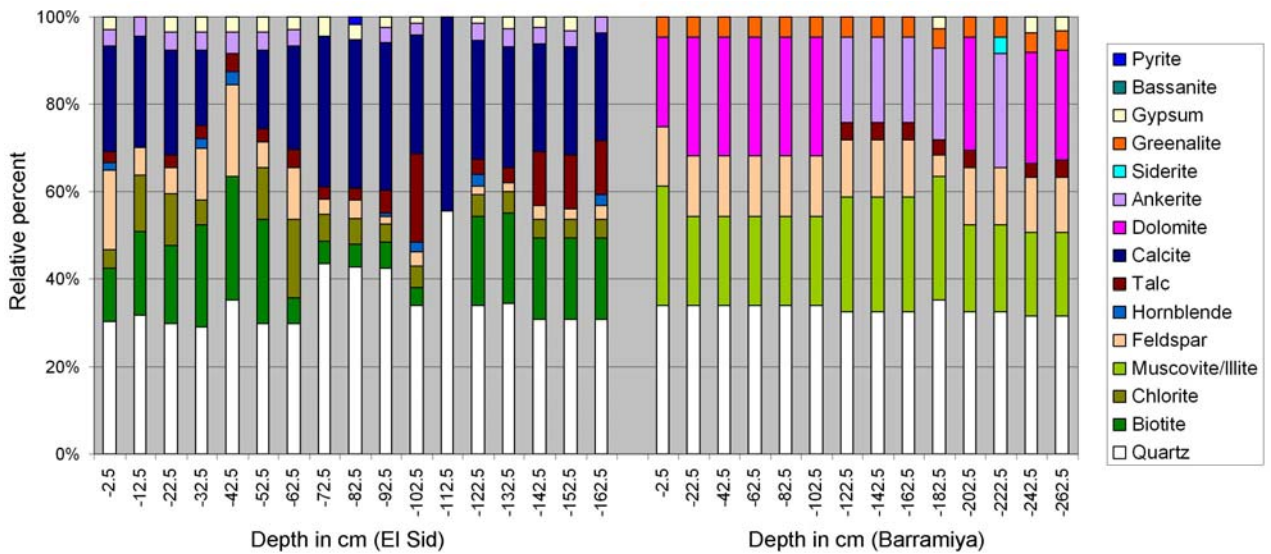


Fig. 2.11. Rough estimate of relative phase distribution based on XRD measurements coded for major phases by order of intensity from 50 to 10, and for traces from 7 to 1 and subsequently accumulated to 100% on the basis of coding.

2.5.2. 4. Detailed mineralogy by mineral liberation analyzer (MLA)

Due to the very small grain sizes and apparent homogeneity of the samples, small regions at high magnification were used to obtain the distribution and percentage of the mineral phases in the classified images using MLA. The investigated samples showed homogeneous mineral distribution and little alteration of the minerals with few secondary phases such as amorphous gels, gypsum and other sulfates (less than 1.2%). The contents of carbonate, alkali feldspar, mica and somehow amphibole group minerals, too, are higher in the samples from Barramiya whereas quartz, sulfides, and plagioclase are more abundant in samples from El Sid (Fig. 2.12). The original porosity is about 39 area-% for both locations. This was calculated by converting all background into voids. Along the profiles, porosity shows a rather homogeneous distribution.

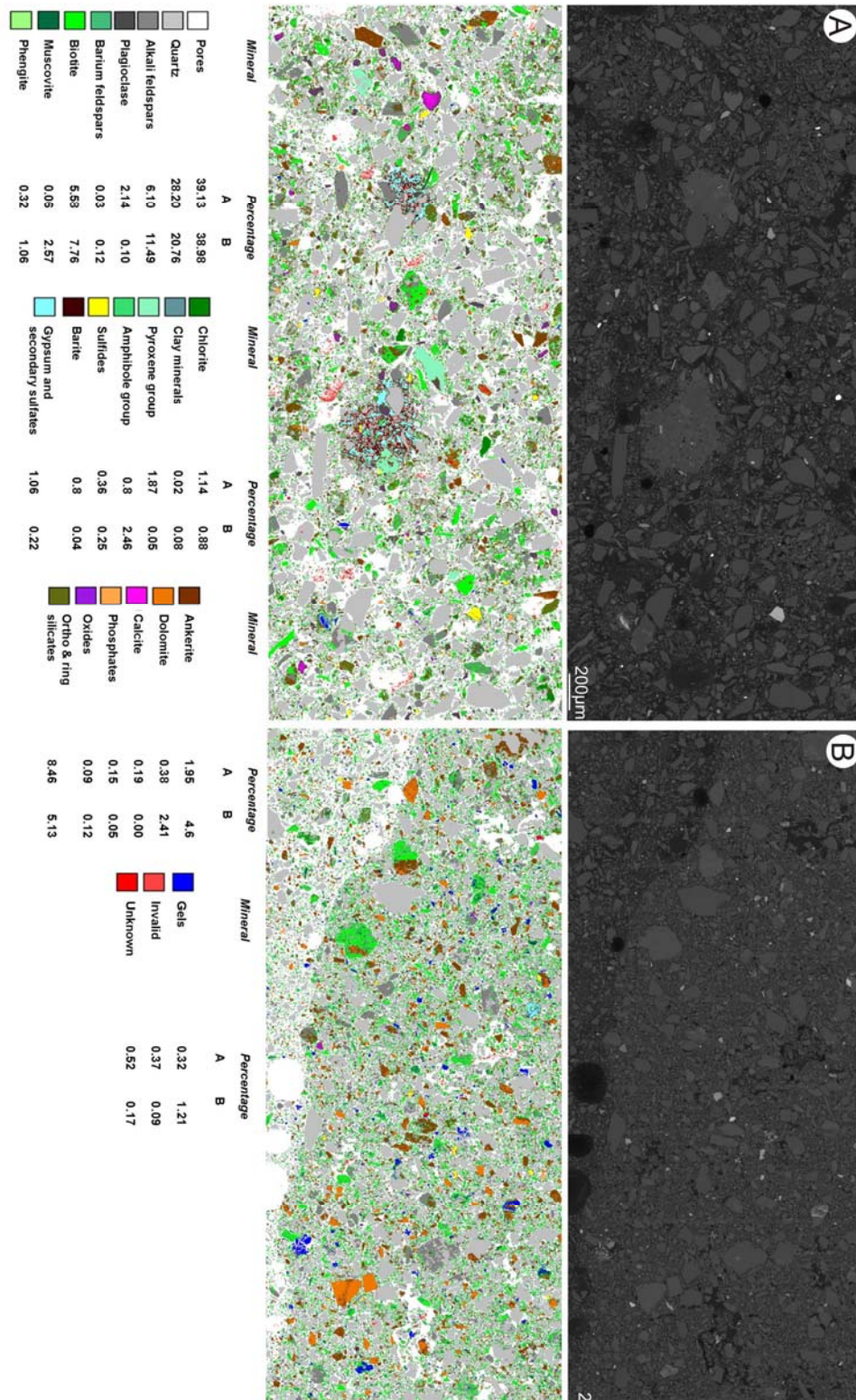


Fig. 2.12. BSE and classified MLA images of the sample from A) El Sid tailings (-12.5cm), and B) Barramiya tailings (-2.5cm). For colour coding see legend for mineral distribution (area-%).

Gypsum/ bassanite are the characteristic secondary minerals found on top of the surface layer, also Fe-Ca-Si-Al-Mg sulfates were recognized using the ESEM (Fig. 2.13E). Looking into details to the different oxidation stages in the two tailings, it can be found that due to the scarcity of water at both sites, no complete sulfide oxidation was recognized. Only incipient oxidation recognized along cracks and/or along the rims of the crystals (Fig. 2.13A-C and Fig. 2.14A-C). Gypsum is found only as small patches, a few mm in size (Fig. 2.13D and Fig. 2.14D) as a result from sulfide oxidation and neutralization reactions which release Ca and SO₄ to the pore water.

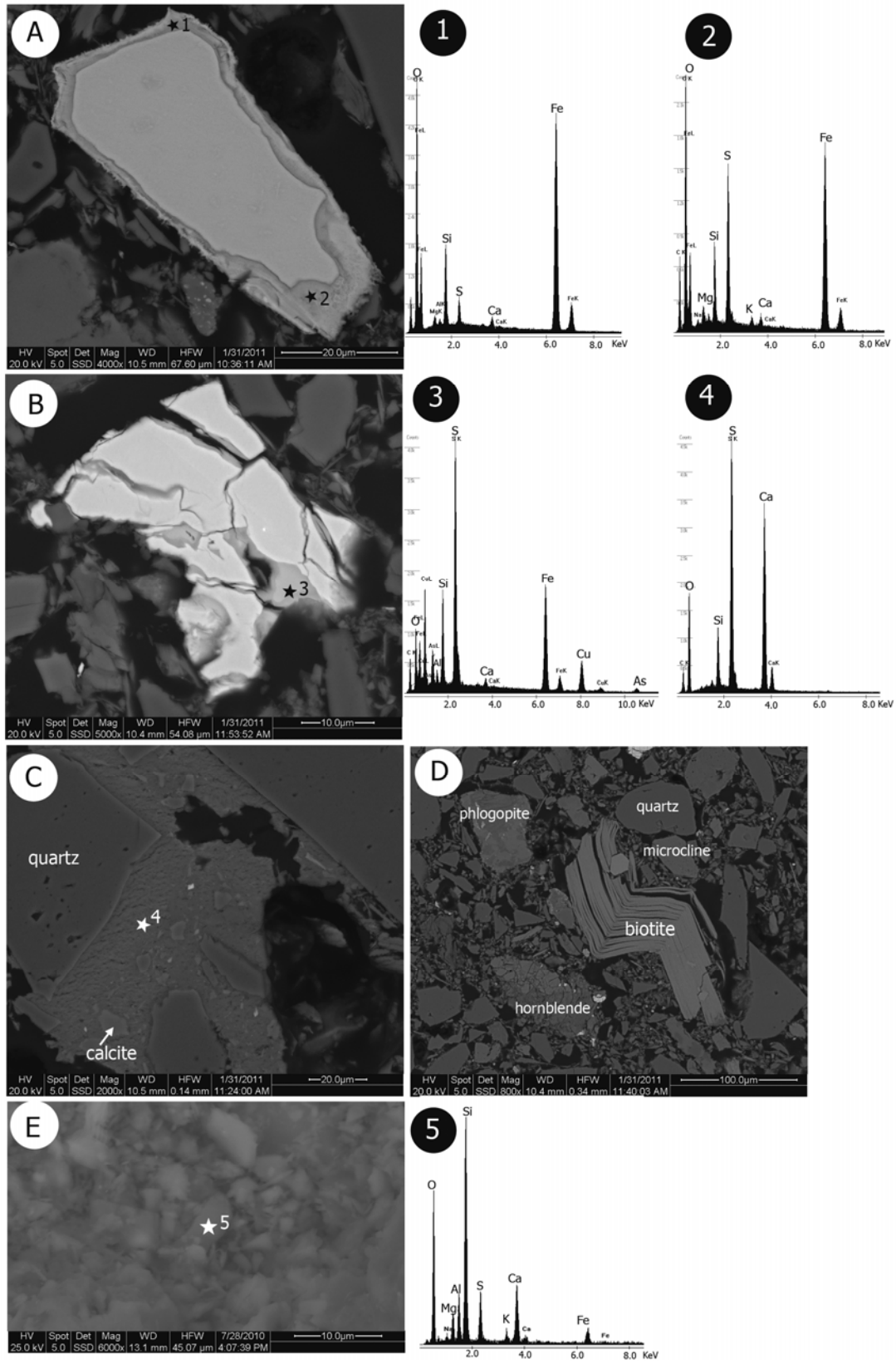


Fig. 2.13. BSE images of A) incipient pyrite alteration surrounded by sulfates of variable Si and Ca content (1,2), B) incipient arsenopyrite alteration along the cracks, filled by Fe-Cu-As-Si sulfates (3), C) gypsum agglutinating quartz and fines (4) partially filled the pores between grains, D) biotite crystal kinked during the crushing process, E) Showing the Fe-Ca-Si-Al-Mg sulfate (5) developed on the surface of El Sid tailings. Samples from El Sid tailings are at depths of -102.5 cm for A and -42.5 cm for B, C and D.

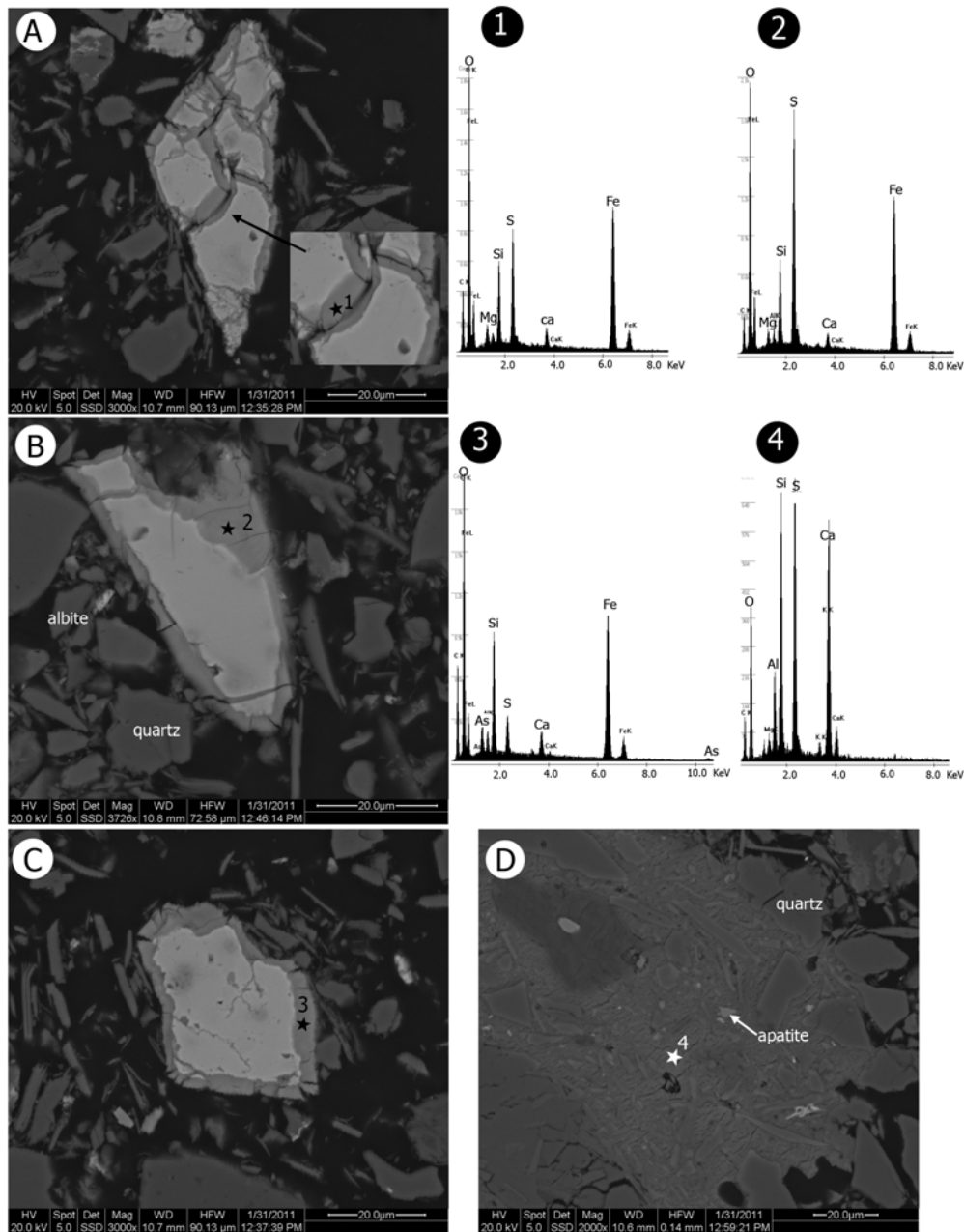


Fig. 2.14. BSE images of A-C) pyrite alteration along the rims and cracks with variable Si, Ca and Mg contents (1-3), D) partial filling of the pores by gypsum, Si Al, and Mg (4) related to embedded fine silicates. Sample from Barramiya tailings is at depth of -182.5 cm.

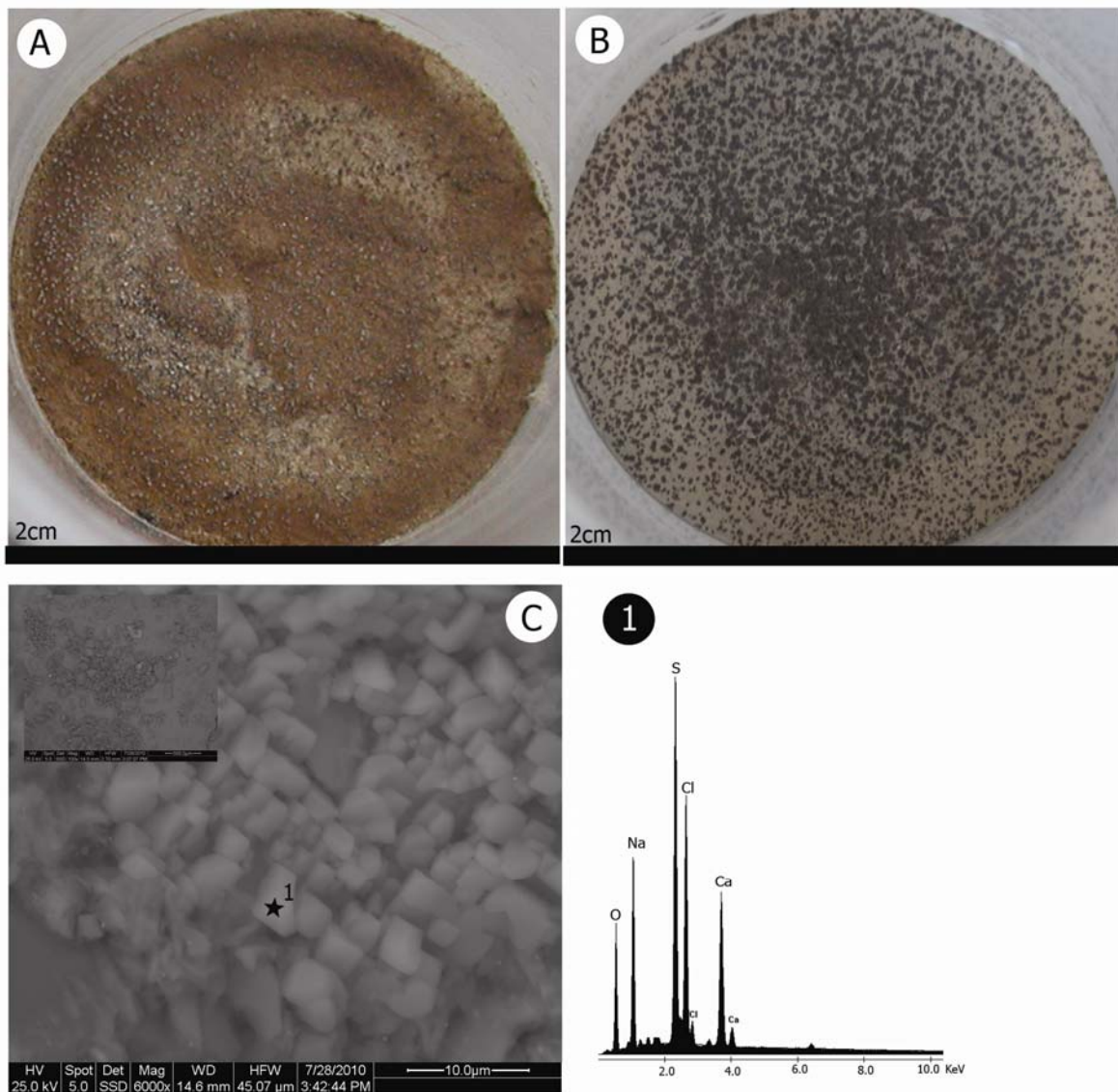


Fig. 2.15. Column experiments for El Sid (A) and Barramiya (B) tailings samples. C) Showing a well developed crust on top of El Sid tailings composed mainly of a mixture of gypsum and sodium chloride (1).

Column experiments showed that Barramiya tailings sample didn't exhibit any significant changes after one month, whereas the tailings sample from El Sid developed a crust right after two

weeks (Fig. 2.15A). The crust was composed of mixtures of gypsum, halite, sodium sulfate (based on XRD and ESEM; Fig. 2.15A,C). Since dry sample material was filled into the columns, the porosity was much higher than in the paste deposited tailings in the columns (about 51.2 volume % for Barramiya and 48.0 volume % for El Sid). The evaporation rate for both samples were similar at the beginning of the experiment, but after two weeks the rate for the El Sid tailings sample decreased due to crust formation on its top.

Thickened tailings disposal techniques were developed in humid areas because of numerous advantages including a homogeneous distribution of its mineral phases with higher water retention capacities, low hydraulic conductivity, less seepage, low downward infiltration, high surface runoff and easier reclamation (Robinsky, 1978; Robinsky et al., 1991). With the gently sloping depositional surface and the uniform grain size distribution, it will promote a shallow water table with a thick tension saturated zone above it and nearly saturated conditions to the surface, and then low oxygen infiltration and subsequent tailings oxidation. With these characteristics, the only drawback is that during the dry periods, the ions transported upward and precipitated by oxidation/dissolution reactions as soluble secondary phases which moved with the surface runoff water during raining events (Al and Blowes, 1999). From this study it can be inferred that the availability of water is the principal rate determining factor for sulfide oxidation under arid climates. Due to the using of thickened tailings disposal in both areas, no grain size fractionation happens, and the carbonate and sulfide minerals were homogeneously distributed throughout the tailings. Therefore, a limited oxidation recognized by secondary sulfates rimming the sulfides and the patchy distribution of gypsum; and further oxidation, transport and precipitations will be restricted to the upper surface layers. This oxidation can be attributed to the preservation of water during tailings disposal in the fine-grained sediments at different depths. Dold and Fontboté (2002) found during their investigations of two flotation tailings in Chile (Ojancos and P. Cerda, acharacterized by hyperarid climate with an average rainfall of 20.7mm/y) composed of Fe oxide Cu-Au deposits that at the second locality the neutralization potential was homogeneously distributed throughout the tailings and the oxidation zones were limited only to the fine-grained fractions leaving the coarse dark unoxidized layers (with higher sulfide content due to gravity separation) behind. This happen because the coarse fraction dries out first and the finer ones preserve the moisture for long period enough for further oxidation. A correlation between oxidation and grain sizes was shown by Dill et al., (2002), too. During their investigations on a pyrite deposit in Namibia (average annual rainfall

300-400mm), they found alternating layers of silt (less permeable, low oxygen diffusivity and oxidation, and therefore neutral pH) which act as aquatards, and sand (highly permeable, high oxygen diffusivity and oxidation, and therefore low pH) which behave as aquifers, with hardpans on the top surface of the impoundment.

The thin crusts, which developed at El Sid tailings (Fig. 2.3D and 2.13E), only reflect the precipitation and crystallization of secondary phases within a system where a small amount of reactive phases are involved, and contributes to the ions in solution. Solutions are composed of ions and colloids in part in equilibrium with the system and therefore mobile and of a part which reacts almost immediately within the system itself due to minute changes of physical and chemical premises such as pressure, temperature, pH, etc. (Zuddas, 2010). The mobile elements such as Ca, K, Na, SO₄, and Cl in the tailings impoundments precipitate due to capillary transport and desiccation of the system. Capillary transport precipitation focuses at the transition sediment to air at top layers as well as in desiccation cracks. Unfortunately the precipitated sulfates and chlorides are stable only under dry conditions. Sporadically occurring heavy rainfalls could therefore easily re-dissolve and mobilize the efflorescent phases and remove them completely or partially by surface runoff of the water. These heavy rainfalls further caused erosion. Part of the water infiltrated promoting again capillary transport, precipitation of easily dissolvable phases with subsequent removal. This repetitive process occurring over 40 years even at few rainfalls is the main control of the differences of the physical and chemical properties between the relatively young El Sid tailings and the much older Barramiya tailings.

2.6. Conclusions and environmental concerns

The two studied gold mine tailings impoundments in Egypt are characterized by very fine grain sizes (silty) and high surface area. Thickened discharge and paste technology methods were used in the discharge of the tailings. El Sid showed strong chemical and mineralogical variations between the upper and the lower parts of the section. Whilst the upper part is dominated by granitoids characterized by enrichment of K₂O, Na₂O, W, P₂O₅, the lower part is characterized by a mixture of Pb and Zn bearing quartz veins and mafic to ultramafic host rock enriched in Cr, Ni, MgO characterized by a talc and amphibole assemblage. The major difference between the two locations is the XRD based mineral assemblage, calcite, biotite in El Sid, dolomite, ankerite, muscovite,

greenalite in Barramiya. From MLA measurements the contents of carbonate, alkali feldspar, mica and amphibole group minerals were higher in the samples from Barramiya whereas quartz, sulfides, and plagioclase were more abundant in El Sid samples.

Regarding pH, conductivity, SO₄, Cl, and most ions from the extractant, El Sid and Barramiya showed contrasting trends. Besides the lithology based changes, El Sid showed a significant enrichment of a number of elements such as SO₄, S, Cl, Fe₂O₃, Ca, Mg, K, Na, Cu, Ni, Sr, Co towards the top, culminating at 20 cm, and being depleted for a number of elements in the top layer due to washout.

According to Graupner et al. (2007) and Meima et al. (submitted) a critical enrichment of reactive phases is crucial for hardpan formation. Critical enrichment can be understood as the necessary amount of reactive phases in a layer enabling complete or partial agglutination of particles as well as clogging of pores of the layer by volume gain of the reactive matter due to microbiologically mediated oxidation, hydration, hydrolysis and precipitation of secondary gels and crystalline phases during alteration. Such enrichment was never achieved within the investigated tailings. Therefore, no protective hardpans could be found. This is due to the homogeneous discharge, the low mean sulfide, and the elevated carbonate content, the missing mineral and grain size fractionation, the non existing lamina enriched in reactive compounds, and, the scarcity of water used during deposition and infiltration.

The tailings impoundments of El Sid and Barramiya were deposited downstream of and even within small wadis. Due to the missing physical protection by hardpans, wind and water erosion occurs and might remove all available fines and easily dissolvable efflorescent matter, such as sulfates, chlorides and some potentially toxic elements e.g. As, Pb. The paste deposited layers are well compacted and quite resistant at the present dry stage against wind and water erosion. These relatively hard tailings will become softened and severely eroded due to progressive wetting of the materials during flash flooding due to the missing protective hardpans. Therefore without suitable cover for these tailings, it will be episodically spread out to the surroundings, to the rivers feeding the Nile River, and eventually directly to the fields which may be through impact to the surrounding environment.

Chapter 2: Hardpan formation in Egypt: Possibility and environmental risks

sample name	EI SID-2.5	EI SID-12.5	EI SID-22.5	EI SID-32.5	EI SID-42.5	EI SID-52.5	EI SID-62.5	EI SID-72.5	EI SID-82.5	EI SID-92.5	EI SID-102.5	EI SID-112.5	EI SID-122.5	EI SID-132.5	EI SID-142.5	EI SID-152.5	EI SID-162.5
BET (m2/g)	3	1.6	2	2.1	0.4	2.3	2.3	1.1	2.1	3.3	3	2.8	3.1	2.9	3.8	4.2	4.1
pH	7.93	7.85	7.73	7.64	7.72	7.73	7.69	7.74	7.68	7.7	7.62	7.75	7.72	7.65	7.61	7.76	7.92
Conductivity (S/m)	0.521	1.372	0.668	0.47	0.459	0.402	0.51	0.383	0.353	0.335	0.423	0.449	0.383	0.32	0.471	0.575	0.758
HCO3 titrations	79	106	77	68	54	47	56	70	66	65	49	46	24	84	50	39	39
SiO2 (%)*	67.53	69.12	67.64	67.31	67.92	71.03	68.93	71.18	76.14	70.43	65.92	68.58	70.15	72.02	66.84	64.89	65.36
TiO2 (%)*	0.566	0.611	0.627	0.644	0.633	0.596	0.539	0.415	0.339	0.383	0.425	0.443	0.386	0.433	0.387	0.377	0.357
Al2O3 (%)*	6.82	7.03	7.11	7.38	7.2	6.81	6.26	5.03	3.98	4.46	4.8	4.92	4.83	4.54	4.58	4.44	4.17
Fe2O3 (%)*	4.95	5	5.3	5.43	5.31	4.78	4.93	4.37	3.57	4.42	5.16	4.89	4.76	4.48	4.86	4.86	4.7
MnO (%)*	0.102	0.107	0.115	0.116	0.113	0.101	0.105	0.094	0.071	0.093	0.109	0.111	0.097	0.09	0.11	0.116	0.114
MgO (%)*	3.67	2.88	3.67	3.74	3.65	2.73	4.17	4.23	2.91	5.43	7.19	5.37	4.66	4.24	6.34	6.86	6.83
CaO (%)*	5.056	4.578	5.027	5.058	4.957	4.406	4.873	4.91	4.17	4.859	5.526	5.296	4.674	4.943	5.713	6.244	6.036
Na2O (%)*	1.22	1.66	1.22	1.18	1.15	1.14	0.92	0.6	0.47	0.4	0.36	0.41	0.4	0.36	0.38	0.4	0.45
K2O (%)*	1.438	1.464	1.522	1.544	1.52	1.5	1.257	0.805	0.761	0.834	0.905	1.016	1.165	1.122	0.951	0.977	0.95
P2O5 (%)*	0.212	0.212	0.2	0.21	0.208	0.209	0.168	0.115	0.098	0.099	0.099	0.111	0.118	0.11	0.087	0.088	0.088
(SO3) (%)*	2.61	2.12	1.85	1.58	1.5	1.53	2.14	2.08	2.2	1.88	2.07	2.2	2.28	1.78	2.13	2.47	2.69
(Cl) (%)*	0.024	0.027	0.027	0.018	0.016	0.017	0.022	0.017	0.019	0.015	0.016	0.016	0.012	0.017	0.016	0.017	0.02
(F) (%)*	0.12	0.1	0.12	0.05	0.1	0.11	0.11	0.09	0.08	0.09	0.1	0.08	0.08	0.1	0.11	0.12	0.14
LOI (%)*	4.94	4.35	4.84	5.01	5.02	4.38	4.59	4.8	3.66	5.23	6.09	5.41	4.9	4.86	6.29	6.83	6.72
(As) (mg/kg)*	1000	1078	1278	1207	1181	1141	1228	760	738	1233	1744	2081	2328	2827	1771	1850	1741
Ba (mg/kg)*	330	348	333	339	327	331	265	158	135	133	122	138	169	161	121	125	125
Ce (mg/kg)*	42	57	42	26	44	60	36	27	33	38	47	31	32	38	39	36	41
Co (mg/kg)*	19	15	16	16	17	18	16	16	11	21	28	18	21	16	25	22	26
Cr (mg/kg)*	184	125	187	181	172	123	227	222	158	350	448	315	265	259	403	456	430
Cu (mg/kg)*	35	43	41	34	34	27	48	36	44	41	50	47	57	56	38	47	42
Ni (mg/kg)*	145	94	123	119	114	81	205	178	123	244	315	223	179	164	303	332	318
Pb (mg/kg)*	1490	1446	1251	1202	1210	1193	2679	4150	6084	4516	3370	3066	3052	2585	3318	3758	4179
Rb (mg/kg)*	37	38	41	38	40	38	35	21	22	24	27	28	27	29	31	33	29
Sr (mg/kg)*	226	185	196	194	189	181	198	158	136	175	183	174	169	168	178	189	183
V (mg/kg)*	64	72	77	82	82	71	71	55	37	52	69	63	63	57	68	66	58
Y (mg/kg)*	20	18	16	17	16	16	16	11	14	13	15	14	16	11	13	17	11
Zn (mg/kg)*	1331	1477	1236	1178	1185	1201	2309	3432	4541	3632	2778	2413	2492	2066	2616	3076	3393
Zr (mg/kg)*	112	113	106	110	104	104	83	57	49	49	49	53	52	47	50	48	50
Ca (mg/L)**	581	426	528	465	511	543	566	334	555	544	539	514	553	566	528	598	510
Fe (mg/L)**	2.07	1.32	1.16	1.12	1.14	1.18	1.18	1.1	1.09	1.09	1.09	1.1	1.1	1.09	1.1	1.11	1.1
K (mg/L)**	168	247	90.5	64.7	77.9	81.1	104	113	79.3	81.3	99.8	96.2	63	50.2	103	128	159
Mn (mg/L)**	0.09	0.12	0.2	0.18	0.14	0.12	0.25	0.19	0.48	0.36	0.18	0.22	0.17	0.34	0.19	0.11	0.08
Na (mg/L)**	847	3600	1340	671	749	511	763	483	346	241	541	550	404	206	553	967	1330
Mg (mg/L)**	71.1	28.3	39.9	53.2	71.7	91.2	121	180	114	138	170	218	168	120	221	239	379
Sr (mg/L)**	8.47	4.92	4.5	4.13	5.52	5.88	8.39	4.5	5.14	5.99	5.82	5.14	4.63	3.78	4.44	5.49	5.47
Cl (mg/L)**	131	1347	565	230	203	138	237	119	129	104	138	148	133	107	199	291	385
SO4 (mg/L)**	3217	6823	3030	2611	2668	2395	2886	2138	2097	2176	2754	2849	2358	1973	2690	3053	4022
As (mg/L)**	0.186	0.307	0.154	0.161	0.191	0.14	0.0504	0.0324	0.0278	0.0401	0.139	0.311	0.472	0.319	0.213	0.218	0.189
Au (mg/L)**	0.0655	0.119	0.123	0.251	0.189	0.119	0.148	0.0231	0.0043	0.0292	0.0322	0.0383	0.06	0.0527	0.0618	0.026	0.0412
B (mg/L)**	0.349	0.133	0.094	0.087	0.087	0.079	0.085	0.075	0.069	0.091	0.076	0.074	0.09	0.106	0.107	1.443	0.234
Ba (mg/L)**	0.0282	0.0252	0.0387	0.0422	0.0348	0.032	0.0322	0.0346	0.0395	0.039	0.0319	0.0294	0.0288	0.0302	0.0322	0.0313	0.0281
Cd (mg/L)**	0.00129	0.00554	0.00513	0.00448	0.00363	0.00317	0.0104	0.0369	0.0593	0.0222	0.0104	0.00983	0.00917	0.0102	0.00861	0.00582	0.00677
Co (mg/L)**	0.0875	0.47	0.0737	0.0446	0.0485	0.0493	0.103	0.0807	0.102	0.0689	0.111	0.12	0.103	0.067	0.0821	0.103	0.178
Cu (mg/L)**	0.0568	0.0913	0.048	0.0392	0.0424	0.0351	0.0438	0.0749	0.0326	0.04	0.0614	0.0598	0.0935	0.075	0.0414	0.0354	0.0473
I (mg/L)**	0.0649	0.0818	0.0282	0.013	0.0149	0.0138	0.0133	0.0098	0.0094	0.0137	0.0229	0.0203	0.0256	0.024	0.041	0.0465	0.0655
Li (mg/L)**	0.0305	0.0129	0.0107	0.0114	0.0102	0.0119	0.0128	0.0087	0.0076	0.0083	0.0082	0.008	0.0095	0.0093	0.0101	0.012	0.0119
Mo (mg/L)**	0.0465	0.0714	0.059	0.0442	0.0518	0.056	0.0245	0.00613	0.00398	0.0109	0.0333	0.0423	0.0425	0.0241	0.0323	0.0384	0.0516

Chapter 2: Hardpan formation in Egypt: Possibility and environmental risks

Ni (mg/L)***	0.0162	0.0168	0.0103	0.00842	0.00619	0.0042	0.0114	0.00629	0.00632	0.01	0.00705	0.0072	0.00897	0.0138	0.00695	0.00619	0.00441
Pb (mg/L)***	0.0257	0.0348	0.00924	0.0123	0.0121	0.0106	0.0309	0.0786	0.102	0.071	0.00937	0.00792	0.0125	0.0119	0.00628	0.00522	0.00986
Rb (mg/L)***	0.0429	0.0284	0.0196	0.0225	0.0218	0.0245	0.0442	0.0597	0.0426	0.0428	0.0369	0.0395	0.0363	0.0343	0.0374	0.0402	0.0587
(Se) (mg/L)***	0.134	1.067	0.426	0.471	0.495	0.315	0.371	0.186	0.189	0.149	0.371	0.302	0.325	0.181	0.348	0.56	1.053
C-carb (%)	1.02	1.08	1.24	1.24	1.2	1.18	1.06	1.04	0.86	1.22	1.34	1.29	1.13	1.19	1.47	1.57	1.5
S-sulfide (%)	0.620579	0.653774	0.644525	0.590523	0.506377	0.289649	0.428677	0.902319	0.775064	0.675092	1.033482	0.961032	0.929803	1.05	0.464351	0.730654	1.026182

sample name	BAR-2.5	BAR-22.5	BAR-42.5	BAR-62.5	BAR-82.5	BAR-102.5	BAR-122.5	BAR-142.5	BAR-162.5	BAR-182.5	BAR-202.5	BAR-222.5	BAR-242.5	BAR-262.5
BET (m2/g)	2.4	2.6	2.8	3	3.6	2.6	4.5	3	2.8	4.4	3.5	2.2	5.7	6.3
pH	7.89	7.94	7.92	7.96	8.02	8.05	7.96	7.98	8.15	7.87	8.18	7.94	7.9	7.91
Conductivity (S/m)	0.283	0.273	0.308	0.293	0.382	0.458	0.323	0.567	0.401	0.311	1.143	1.052	0.416	0.322
HCO3 titrations	98	92	85	93	86	81	94	89	71	95	90	73	77	128
SiO2 (%)*	60.03	61.63	59.33	57.69	58.28	62.03	59.41	58.38	57.57	57.44	56.89	56.98	54.59	54.86
TiO2 (%)*	0.54	0.532	0.541	0.625	0.64	0.539	0.633	0.613	0.601	0.534	0.661	0.594	0.691	0.675
Al2O3 (%)*	10.69	9.95	10.28	10.99	11.68	9.78	11.86	11.65	11.46	11.2	12.04	12.21	12.32	12.03
Fe2O3 (%)*	4.76	4.83	5.03	5.45	5.29	4.8	5.26	5.17	5.07	4.8	5.52	5.28	5.9	5.84
MnO (%)*	0.12	0.111	0.112	0.115	0.112	0.096	0.113	0.11	0.107	0.112	0.109	0.116	0.136	0.124
MgO (%)*	4.07	3.73	4.64	4.6	4.12	4.03	3.8	4	4.38	4.66	4.35	4.06	4.71	4.88
CaO (%)*	4.926	4.868	5.069	4.965	4.595	4.748	4.43	4.735	5.2	5.331	4.606	4.654	5.344	5.399
Na2O (%)*	1.06	1.2	1.12	1.15	1.36	0.91	1.23	1.31	1.14	1.09	1.38	1.6	1.04	1.02
K2O (%)*	1.916	1.801	1.706	1.997	2.135	1.817	2.356	2.308	2.19	2.176	2.303	2.268	2.225	2.126
P2O5 (%)*	0.064	0.056	0.068	0.081	0.094	0.077	0.092	0.077	0.084	0.078	0.101	0.074	0.081	0.075
(SO3) (%)*	0.89	0.87	0.62	0.93	0.87	0.84	1.03	1.43	1.34	1.27	1.18	0.94	0.7	0.57
(Cl) (%)*	0.011	0.008	0.02	0.011	0.019	0.026	0.019	0.022	0.018	0.011	0.023	0.028	0.016	0.012
(F) (%)*	<0.05	<0.05	<0.05	<0.05	0.06	0.06	0.05	<0.05	0.05	0.09	<0.05	<0.05	<0.05	0.06
LOI (%)*	10.17	9.73	10.8	10.71	10.04	9.55	9.04	9.39	10.13	10.58	10.18	10.4	11.45	11.55
(As) (mg/kg)*	3092	2772	2178	2617	2758	2886	2825	3384	2665	2643	2262	3183	3160	3282
Ba (mg/kg)*	297	262	253	328	380	322	391	369	365	356	404	365	336	326
Ce (mg/kg)*	41	53	60	44	57	59	46	47	37	49	55	42	57	55
Co (mg/kg)*	19	18	23	22	21	24	20	15	21	18	23	20	25	22
Cr (mg/kg)*	240	172	334	289	238	237	167	192	230	244	206	224	288	299
Cu (mg/kg)*	48	47	45	50	46	51	54	50	58	52	56	58	55	56
Ni (mg/kg)*	154	94	228	189	154	178	118	110	146	161	151	129	200	202
Pb (mg/kg)*	8	9	7	8	10	14	11	16	9	12	9	16	7	6
Rb (mg/kg)*	48	42	43	50	51	43	56	56	51	53	52	54	52	52
Sr (mg/kg)*	250	196	228	234	219	234	189	213	217	209	180	200	216	209
V (mg/kg)*	131	131	111	128	131	101	118	125	121	119	122	142	149	147
Y (mg/kg)*	26	22	27	27	29	20	28	28	28	26	27	29	25	27
Zn (mg/kg)*	57	51	61	66	67	60	67	67	67	64	73	67	71	66
Zr (mg/kg)*	87	73	96	104	113	88	117	107	105	100	114	98	105	104
Ca (mg/L)**	696	649	647	676	650	627	726	620	667	723	446	769	539	546
Fe (mg/L)**	1.1	1.1	1.09	1.1	1.1	1.09	1.09	1.1	1.09	1.09	1.1	1.1	1.09	1.1
K (mg/L)**	16.1	15.5	59.6	37.2	71.7	83.6	88.2	124	142	40	127	83.4	71.2	72.8
Mn (mg/L)**	0.07	0.08	0.08	0.08	0.08	0.08	0.08	0.08	0.07	0.08	0.07	0.08	0.07	0.08
Na (mg/L)**	46.5	41.6	71.9	42.7	165	315	66.8	496	200	52.3	2190	1590	313	104
Mg (mg/L)**	85.4	99.8	124	100	226	314	111	444	204	106	727	541	196	136
Sr (mg/L)**	2.28	2.14	3.76	3.23	3.86	4.42	3.6	4.61	6.66	3.86	3.2	4.1	3.03	3.07
Cl (mg/L)***	61	62	90	67	125	196	79	216	112	75	1010	1773	248	89
SO4 (mg/L)**	1895	1730	1972	1912	2635	3011	2171	3707	2588	2054	6297	4009	2315	1963
As (mg/L)***	1.031	0.845	0.94	1.103	1.856	1.797	1.58	2.057	2.305	2.302	1.762	1.379	0.905	1.338
Au (mg/L)***	0.163	0.0793	0.131	0.111	0.0731	0.0996	0.0985	0.127	0.157	0.0825	0.43	0.0729	0.263	0.243

Chapter 2: Hardpan formation in Egypt: Possibility and environmental risks

B (mg/L)***	0.196	0.116	0.123	0.139	0.135	0.115	0.217	0.137	0.157	0.229	0.054	0.052	0.086	0.145
Ba (mg/L)***	0.0187	0.0157	0.0321	0.0193	0.0286	0.0244	0.0262	0.0227	0.0229	0.0247	0.0266	0.0223	0.0266	0.0301
Cd (mg/L)***	0.000098	0.000092	0.000128	0.000099	0.000096	0.000111	0.000108	0.000115	0.000132	0.000197	0.000168	0.000151	0.000093	0.00007
Co (mg/L)***	0.00034	0.00034	0.00038	0.00036	0.0005	0.00049	0.00028	0.00038	0.00035	0.00187	0.0017	0.00272	0.00086	0.0029
Cu (mg/L)***	0.0329	0.0286	0.0274	0.0269	0.0313	0.0288	0.0319	0.0449	0.0416	0.0625	0.0406	0.0497	0.0394	0.0609
I (mg/L)***	0.0373	0.0312	0.0325	0.0253	0.0313	0.0375	0.0774	0.0774	0.108	0.0879	0.197	0.195	0.176	0.163
Li (mg/L)***	0.0154	0.0139	0.0188	0.0191	0.034	0.0296	0.0212	0.0471	0.044	0.0239	0.0375	0.0361	0.0137	0.0122
Mo (mg/L)***	0.0192	0.0155	0.0314	0.0386	0.0362	0.0226	0.0287	0.0452	0.0286	0.0197	0.044	0.0303	0.0163	0.0205
Ni (mg/L)***	0.00449	0.00353	0.00426	0.00424	0.00365	0.00381	0.0029	0.00375	0.00407	0.0204	0.0027	0.00959	0.00511	0.0204
Pb (mg/L)***	0.00059	0.00045	0.00086	0.00102	0.0004	0.00049	0.00066	0.00077	0.00083	0.00071	0.00062	0.0533	0.00049	0.00079
Rb (mg/L)***	0.0329	0.0205	0.0293	0.0297	0.0291	0.0275	0.0334	0.0276	0.0245	0.032	0.0344	0.0332	0.0395	0.0324
(Se) (mg/L)***	0.0103	0.0082	0.0118	0.0113	0.044	0.087	0.0121	0.117	0.0458	0.0076	0.308	0.257	0.0448	0.0111
C-carb (%)	2.44	2.57	2.65	2.46	2.19	2.01	2.29	2.31	2.4	2.5	2.46	2.13	2.46	2.53
S-sulfide (%)	0.336762	0.176524	0.312679	0.330913	0.226264	0.306695	0.427176	0.309194	0.04	0.163404	0.03	0.266146	0.36072	0.193854

Table.2.1. Geochemical data of the different samples in El Sid and Barramiya. *,** and *** refers to XRF, ICP-OES and ICP-MS analysis respectively.



**New columns design for the
investigation of ions accumulation in
the capillary head in unconsolidated
sands**

“This chapter is reprinted with permission from Soil
Science Society of America Journal”

3.1. Abstract

Electrical conductivity can easily be measured, but interpretation is ambiguous since saturation, fluid conductivity, and material properties are interacting parameters. This study aims to indirectly obtain fluid conductivity evolution in time and space in column experiments by repetitively applying two independent non-destructive multi-level methods. Water saturation, is derived from the difference in x-ray attenuation by dry, partially and fully saturated sand filled columns. Also, it is used to calculate fluid conductivity from the electrical conductivity in time intervals for each depth level in the column. The investigated columns show distinct patterns for water saturation, electrical conductivity, and calculated fluid conductivity for individual imbibition and drainage steps at distinct grain-size distributions. During imbibition, the unsaturated capillary fringe head shows a very unusual increase in electrical conductivity gaining with each step of capillary rise. During the drainage cycle, the electrical conductivity peak broadens and moves downward. The calculated fluid conductivities are much higher than expected, but correspond well to conductivity and ion strength of the extracted fluids. The strong increase in electrical conductivity was attributed to the fast rising capillary head fluids, which quickly accumulated all available ions around the particles and moved upward. The slow water was depleted, and showed even a different ion distribution pattern due to slowly reacting minerals. Monitoring of fluid conductivity in time and space by non-destructive methods provides access to enrichment–depletion processes in the critical zone, in the laboratory and in the field. This is essential for understanding the development of hardpans in natural and anthropogenic environments, causing eventually supergene economic enrichment of metals.

Abbreviations: C, coarse grain size, CM, coarse-medium grain size; CMF, coarse plus medium plus fine grain size; CT, computed tomography; EDXRF, energy dispersive x-ray fluorescence; F, fine; ICP, inductively coupled plasma; LREE, light rare earth elements; M, medium; MF, medium fine; MS, mass spectrometry; NMR, nuclear magnetic resonance; OES, optical emission spectrometry; PVC, polyvinyl chloride; REE, rare earth element.

3.2. Introduction

Monitoring changes related to water content and electrical conductivity are very important aspects in soil science. They are required for understanding transport, mobilization of ions, and precipitation mechanisms, especially in the unsaturated part of the soil.

Electrical conductivity measurements are used both in the field and in the laboratory to obtain information on rock, sediment, or soil conductivities. They are used either for estimating sulphide or graphite mineralized zones, zones of alteration, fresh water/salt water boundaries or for humidity levels in soils, sediments, and tailings (Katsube and Mareschal, 1993; Jones et al., 1997; Collins and Easley, 1999; Airo and Loukola-Ruskeeniemi, 2004; Logsdon and Laird, 2004; Hoffmann-Rothe et al., 2004; Harinarayana et al., 2006).

Electrical conductivity depends on a number of factors such as the electrical conductivity of the rock, sediment, or soil itself, as well as the conductivity of the fluid expressed by the salinity of the pore water and the level of water saturation (Archie, 1942; Chinh, 2000), and tortuosity of the current flow paths (Glover et al., 1996). Therefore, electrical conductivity measurements are not unambiguous for interpretation. Single profiles obtained by field measurements provide eventually nice anomalies, which can be hardly interpreted. A much more precise interpretation of the material characteristics is possible by monitoring changes in soil or mining residues before and after rain falls or active watering via repeated measurements (Furche et al., 2007; Rammlmair et al., 2008a, 2008b).

Changes in the electrical conductivity can be related to changes in the ion content of the fluid at steady hydrologic conditions. Furche et al. (2007) tested this method in a column filled with mine tailings material and found a good correlation between the measured pore water electrical conductivity and the conductivity calculated using geoelectrical measurements and geochemical modeling. For this column, the water content was quantified at the beginning of the experiment using the nuclear magnetic resonance (NMR) method at the Leibniz Institute of Applied Geophysics (LIAG; Rifai et al., 2006), and after finishing the experiment by weighing the amount of water lost due to drying of the individual horizons. Therefore, geophysical monitoring measurements will give valuable information about temporal changes in fluid conductivity caused by ion transport as long as one of the parameters water saturation or ion strength is quantified by an independent method.

To obtain information on water saturation in rocks and sediments is of major interest for the oil industry, and for environmental issues, too. Both NMR (e.g., Choi et al., 1997; Korb et al., 2003; Fleury et al., 2006; Rifai et al., 2006; Ohkubo et al., 2008) and x-ray absorption in computed tomography (CT) are used to obtain information on porosity, water saturation, and rock texture. While NMR applied in the field provides bulk information. The NMR, and CT measurement at the

laboratory scale offer detailed insight into cores, down to single pore and grain boundary levels at below micrometer-scale resolution. Computed tomography measurements have previously been used to get information on water saturation and bulk density (e.g., Petrovic et al., 1982; Brown et al., 1987; Anderson et al., 1988; Hopmans et al., 1992; Rogasik et al., 1999; Bayer et al., 2004), and further to estimate the porosity of sediments and rocks (e.g., Warner et al., 1989; Anderson et al., 1990; Akin and Kavscek, 2003; Van Geet et al., 2003) and to detect soils inner structure (Heijs et al., 1995; Ketcham and Carlson, 2001; Wildenschild et al., 2002). Roberts and Lin (1997b), using x-ray radiography visualized the flow of liquid in fractures and matrix in tuff and calculated the saturation within the matrix. Also, Mori et al. (1999) used soft x-ray radiography to visualize the drainage pattern and characterized the geometrical and hydraulic properties of structured soils.

In hydrogeology, many authors described the relationship between unsaturated hydraulic conductivity which governs liquid phase transport in soil and pressure head (the difference in wetting and non-wetting fluid potentials) as hysteretic (Haines, 1930; Stephens, 1996; Flynn et al., 2005). Where, at any given pressure head, there is a value of moisture content on the wetting curve and a slightly higher value on the drying curve. Therefore, at a specific pressure head, one can find two values for hydraulic conductivity, that the hydraulic conductivity during drainage will be higher than that during wetting. This may be attributed to several factors: changes in the moisture content during wetting and drying, air entrapment, non-uniform geometry of individual pores, different spatial connectivity of the pores during wetting and drying, and variations in liquid-solid contact angle.

Some of these factors are also concluded during the measurement of the geophysical properties of geologic substances (e.g., Longeron et al., 1989; Knight, 1991; Suman and Knight, 1997; Titov et al., 2004).

This study reveals that relationship between the electrical conductivity and the water saturation is not simple in the unsaturated part of the soil during imbibition (increase water saturation) and drainage (decrease water saturation). That, other factors should be included which have a very important effect on the changes in this environment.

The main objective of this paper is to make a continuous investigation of the changes in soil fluid conductivity and water saturation during imbibition and drainage, and trying to identify the mechanisms responsible for the increased fluid conductivity in the unsaturated part of the soil. This

will be achieved by simultaneous acquisition of electrical conductivity and water saturation by independent methods. The data will be obtained by repetitive multi-depth level monitoring at laboratory scale. Fluid conductivities can be derived for changing saturation conditions at each individual depth level. This is a new approach to obtain information on the dynamics of fluid conductivity in the critical zone without interrupting the experiment.

3.3. Methodology and Experimental Set-up

3.3.1. Theory of X-ray Absorption

The theory of x-ray absorption has been presented in many publications (e.g., Brooks and Di Chiro, 1975; Anderson et al., 1988; Heijs et al., 1995; Akin and Kovscek, 2003). However, we will give a brief discussion about it. When a monochromatic x-ray beam passes through a homogeneous sample, it is attenuated and the result of this attenuation can be expressed by Beer's law (e.g., Ingle and Crouch, 1988):

$$I = I_0 \exp[-\mu N] \quad [1]$$

where I_0 is the incident intensity, I is the transmitted intensity, N is the thickness of the homogeneous sample, and μ is the linear attenuation coefficient.

Because of using a polychromatic radiation beam, the energy dependent linear attenuation coefficient $\mu(E)$ must be taken into consideration, for corrections of the reconstructed images. Low energy photons are more absorbed than those of higher energies, when a polychromatic radiation beam penetrates the object, and this will introduce image artifacts (beam hardening which should be taken into account during image reconstruction). The attenuated intensity in this situation can be denoted by:

$$I = I_0 \exp\left[-\int_{E_{\min}}^{E_{\max}} \mu(E) dE\right] \quad [2]$$

When using cylindrical samples, the average transmission will not depend on the angle, because the path lengths of the photons through the sample are constant and the developed artifacts will be minimal (Heijs et al., 1995).

In an x-ray radiograph, as in our instrument, the absorption pattern of a three-dimensional (3D) body is projected to a two-dimensional (2D) image because all of the planes that are parallel to

the x-ray film are superimposed on top of each other. Hence, one of the dimensions is lost (Michael, 2001).

The volumetric water content can be calculated easily from the x-ray absorption measurements at different depth levels in the columns. This can be done by knowing the linear attenuation coefficients for the dry, partially wet and fully saturated samples.

3.3.2. Columns

For the experiments, a column was designed to allow simultaneous and continuous monitoring of position related changes in x-ray absorption as well as x-ray fluorescence and additionally electrical conductivity at 20 depth levels. A 50-cm long PVC (polyvinyl chloride) tube with an inner diameter of 70 mm, and 3 mm wall thickness was glued at the base to a 10-cm long, massive PVC rod of the same diameter. A cone, pointing downward was incised into the rod from top. The tip of the cone was connected to two horizontal pipes for feeding/releasing fluid. A filter plate with a 60-mm diameter and a 5-mm height was used to close the reservoir cone (42 mL) to prevent infiltration of soil particles from the sand-filled tube into it and to distribute the flow of water (Fig. 3.1). The tube itself was graded at four sides parallel to elongation to partially distress the column while cutting 2 cm by 45 cm windows at two opposing sides. These windows were closed sequentially with a 50- μ m PVC foil thin enough to minimize the effect of absorption by PVC, and to allow x-ray fluorescence to exit the sample for energy dispersive x-ray fluorescence (EDXRF) measurements (Fig. 3.1).

To monitor level dependent changes of electrical conductivity, a foil for electric conductivity measurements was fixed inside the column parallel to elongation at 90° to the open cuttings. This foil consisted of 20 depth levels, each level equipped with four electrodes each one attached to one of the 80 wires embedded in the foil. The two outermost electrodes were used for current injection, whereas the two innermost were potential electrodes displaying an azimuth angle of 33.2° between each other (Furche et al., 2007). This 20 depth levels are unevenly distributed from the base to the top of the column. The distance of these levels became narrower toward the top of the column (Fig. 3.1).

The column was further equipped with 15 ports to allow the emplacement of metal free Rhizon soil water samplers (ecoTech Environmental Measuring systems GmbH, Germany) of a 5-cm length to extract water from defined parts of the column even from unsaturated zones.

The column then was put on an aluminum holder, within a vertical EDXRF scanner (Fig. 3.1). Due to the opening of the two opposing sides of the column, it was deformed in x-ray transmission direction despite the applied grading at 90°. This deformation caused a slight change of the inner perimeter of the tube from a perfect circle to an elliptical transect, which gave different diameters along the vertical direction. Maximal changes of the diameter reached 70 ± 0.25 mm. The exact diameter of the x-ray absorption pathway was therefore calculated from the column filled only by water.

3.3.3. Materials Characterization

The material used in this study was almost pure quartz sand of $> 970 \text{ g kg}^{-1} \text{ SiO}_2$ with minor amounts of major and trace elements. The CIPW norm (acronym for Cross, Iddings, Pirsson and Washington; Cross et al., 1902) calculation (Hollocher, 1999) shows up to 950 g kg^{-1} in the coarse sand, and more than 990 g kg^{-1} quartz in the medium and fine sands, few minor phases such as plagioclase, orthoclase, corundum and hypersthene and accessory minerals such as apatite and ilmenite.

The grain sizes used were: coarse (C, particle size 0.50–1.00 mm); medium (M, 0.25- 0.50 mm); fine (F, 0.125–0.250 mm); coarse plus medium (CM), 1:1; medium plus fine (MF), 1:1; and coarse plus medium plus fine (CMF), 1:1:1. The average porosity was 0.36, 0.35, 0.37, 0.32, 0.35 and 0.315%, respectively. The porosity was estimated from the weight difference of each column for dry and saturated sands. These grain-size distributions were chosen to obtain information on the differences in shape of the capillary fringe. The six samples were filled by a rotating sample splitter (Sample Divider Type PK, Nr 2275, Retsch KG Germany) in a relatively homogeneous way into the PVC columns to avoid human based grain-size grading during the measurements. The columns were filled to a height ranging from 36 to 43.1 cm depending on the amount of available material.

3.3.4. Instrumentation

3.3.4.1. X-Ray Absorption

Absorption measurements were made using a unique, vertically operating EDXRF scanner (Geoscanner COX Analytical Systems AB, Sweden), which is an instrument based on a Rich. Seifert & Co. ISO-DEBEYEFLEX 3003 HV-Generator. The operated voltage for water content measurement was 60 kV and 45 mA with a yz-mobile long fine focus Philips XRD Mo tube Type PW 2275/20 (3 kW, 60 kV) generating a polychromatic x-ray beam (Fig. 3.1). This beam is focused by total reflection of part of the x-rays by a glass slit capillary to 250- μ m heights and a 20-mm width. Due to this beam guide, the low energy part up to about 6 keV is significantly reduced.

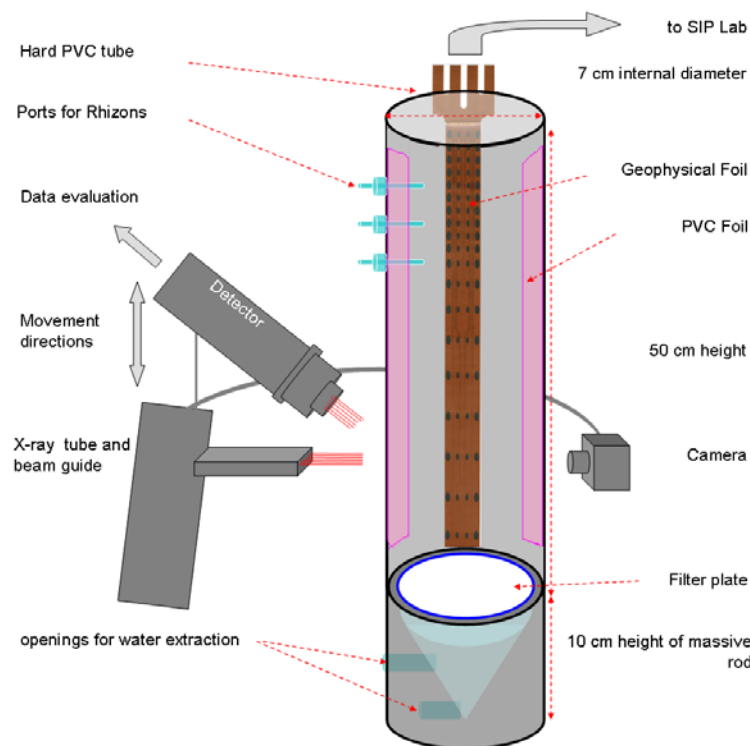


Fig. 3.1. Experimental setting showing the column with geophysical foil connected to the SIPLab unit, openings for x-ray absorption measurement, ports for Rhizon soil water samplers and position

of the y-z mobile x-ray source of the geoscanner with the attached EDXRF detector at 45° inclination and the camera for absorption on the opposite side.

A line camera for absorption measurements is mounted in a fixed position to the beam guide opposite to the column. A slit system controls the aperture for the incoming central beam, to reduce the influence of secondary scattered x-rays on the image. The image width is 6.6 mm which corresponds to 660 pixels of 10- μ m lateral resolution. The simultaneous vertical movement of beam and absorption camera ascertains a very high spatial resolution (down to 10- μ m steps). We applied 250- μ m steps without distortion in the vertical direction of upward movement and 2000-ms acquisition time.

The Geoscanner is further equipped with an EDXRF detector (Fig. 3.1) (Rammlmair et al., 2001, 2006).

3.3.4.2. Electrical Conductivity

Electrical conductivity measurements were made using a SIPLab (Spectral Induced Polarization, Radic Research, Berlin) system which was designed for frequency domain measurements on complex resistivity of sediments and rocks. The instrument is optimized for multi-electrode measurements in the laboratory, and the measurements can be automatically repeated at different time intervals.

The frequency range used by the instrument is between 1 mHz to 12 kHz, the voltage source is ± 10 V, ± 10 mA, the signal shape is sinusoidal, the buffer length is 8 k samples/channel. The instrument contains a digital power line filter (50/60Hz) and digital drift filter.

The frequency used for our experiments of electrical conductivity was at 11.72 Hz.

3.4. Measurement and Data Processing

3.4.1. X-Ray Absorption

3.4.1.1. Measurement

Absorption measurements followed the scheme below except for Step 6:

- 1) Each measurement was begun from the lower starting point about 2 cm in air (below the column), then 1 cm aluminum holder (as a base of the column), then the 60-cm entire

column (the 50-cm tube and its 10-cm massive base) and ending in 2 cm of air above the column. At each step, the attenuation of the x-ray beam by a sample volume of a 0.250-mm height, a 6.6-mm width, and a 70-mm length was recorded. The empty column (air only) was measured in four directions with an azimuth angle of 45° to obtain information of the PVC tube wall thickness (small changes) and the PVC foils at the two windows of the column.

- 2) Then the column was filled with water and measured in four directions as in Step 1 to obtain information on the deviation of the inner diameter. This was necessary to derive the exact volume of each measured water level as a control for the water input since the shape changed from ideal circle to ellipses.
- 3) Afterward a defined volume of the column was filled homogeneously with sand of defined grain size and specific weight and measured dry. The bulk porosity estimated from above parameters was used to calibrate the cumulative porosity of all 250- μm steps derived from x-ray absorption.
- 4) Then in a number of steps, defined amounts of water were added from the base by a pipe linked to a reservoir at about 5 cm above the sand filling limit in the column, to allow the pores to become slowly saturated by continuous air removal. At each step monitoring was done by x-ray absorption and electrical conductivity measurement. The measurements were performed after 30 min. relaxation time. The last measurement was done when saturation of the total sand volume was achieved with 1- to 2-cm water cover.
- 5) Finally the water was allowed to drain gravitatively in steps from the base of the column. Each step was measured again by both methods, till steady-state conditions were achieved.
- 6) In an additional setting for one extra column filled by fine sand, Rhizon soil water samplers were fixed at nine levels of it for water extraction. The water was analyzed for pH and fluid conductivity as well as for ions by inductively coupled plasma mass spectrometry (ICP–MS) and optical emission spectrometry (ICP–OES).

3.4.1.2. Data Processing

The 16 bit absorption images (660 by 2600 pixel) obtained from the absorption line-camera for each measurement, was then evaluated. This was done by taking the mean gray values for the central (approx. 0.5 mm wide) zone of the image, to obtain a data string which was imported to an

excel spreadsheet for further calculation. The starting points were optically adjusted and the intensity shifts were corrected on the basis of the air and the PVC rod.

In our experimental setting beam hardening effects were neglected, because of using a prehardened beam, homogeneous samples of cylindrical shapes (small variation of the path length), and by repeating the measurement at identical profiles. Also, according to Bayer et al. (2004), the differences that appeared due to beam hardening in the integral values are much smaller than those caused by water content changes. We used the following standard equation, derived from Eq. [1] to calculate the attenuation of the x-ray beam:

$$\ln \frac{I_0}{I} = \mu N \quad [3]$$

from the above equation we calculated the volumetric water content $\theta(x)$ at (x) height as shown in the following equation (Bayer et al., 2004):

$$\theta_{(x)} = \frac{\mu_{(x)} - \mu_d}{\mu_s - \mu_d} \phi \quad [4]$$

where μ_d is the calculated attenuation using Eq. [3] for the dry sample, μ_s for the fully saturated sample, $\mu_{(x)}$ for the sample at height (x) and ϕ is the porosity. The attenuations by the two 50- μm PVC foils of the windows were neglected as being of minor impact.

3.4.2. Electrical Conductivity

3.4.2.1. Measurements

Electrical conductivity measurements were performed in the columns as follows:

- 1) Measurement of the geometric factor at each depth (k-factor) for all the 20 levels in columns filled only with drinking water of conductivity ranging from 0.0501 to 0.05033 S m⁻¹.
- 2) After each step of saturation (120 mL, 30 min. relaxation time) from the base, to allow the pores to become slowly saturated by continuous air removal, until 1 to 2 cm water cover was achieved above the sand.
- 3) Direct fluid conductivity measurement of the 2-cm ponding water head by using a microprocessor conductivity meter type LF 323-B/set, model TetraCon 325 (Juergens & Co GmbH, Germany).

- 4) Then water was allowed in steps to leave the column gravitatively at the base, till steady-state conditions were achieved.
- 5) Fluid conductivity of the water which left the columns from below was also measured for each step.

3.4.2.2. Data Processing

The potential difference U (V) between the two potential electrodes was measured when an appropriate current I (max. 10 mA) was injected into the material at each depth level. The electrical conductivity σ (S m^{-1}) was calculated from the following formula:

$$\sigma = \frac{1}{U} K_n \quad [5]$$

where K_n is the geometric factor for the n -th depth level.

After that we applied Archie's law (Archie, 1942) which relates the electrical conductivity of the material to the conductivity of the conducting medium (fluid conductivity) in the pores using the following equation:

$$\sigma = \phi^m \sigma_w S_w^n \quad [6]$$

where ϕ denotes the porosity, σ_w is the fluid conductivity, S_w is the water saturation, n is the saturation exponent and m is the cementation exponent. The values of m range between 1.3 and 4. Higher values of m indicating lower electrical connectivities of the phase (Chinh, 2000; de Lima and Sharma, 1990) and it increases with increasing consolidation and compaction of the material. To be able to calculate the fluid conductivity at various depths we first determined the Archie parameters n , and m for each column experiment. This was done after full saturating each column and measuring the fluid conductivity for the overhead and the drained water.

The Archie parameters n and m were determined for each column after finishing the experiments using Eq. [6]. Parameter n is equal to 2 while parameter m shows small variations for C, M, F, CM, MF, and CMF sands equal to 1.37, 1.40, 1.44, 1.42, 1.44, and 1.40, respectively.

3.5. Results and Discussion

Due to the sequential measurements of x-ray absorption for empty, water-filled, and sand-filled columns at different water contents; the porosity of the sand at each level in each investigated

column was derived. Water saturation of the pore space at each investigated level was calculated for any step of imbibition and drainage down to levels of $\sim 1 \pm 0.05\%$. It has to be noted that the 660-pixel long x-ray absorption line image reflects the longest passage for x-rays through the column. It covers about 12% (115 mm^3) of the segment volume (961 mm^3). During evaluation, only the central half millimeter, $\sim 1\%$ of the segment volume as a maximum diameter was used, integrating all internal zones. The vertical distribution patterns of water saturation during each step of imbibition and drainage are shown in Fig. 3.2. As we said before, all our experiments were filled with water from below. Each step of imbibition showed a saturated lower part and a small capillary fringe till final saturation was achieved. The time required for filling the columns was much slower in the case of fine sand compared with coarse sand. This was due to the easier removal of air from the coarser communicating pores. In the finer fractions, film transport and capillary-force driven rise of water was enhanced, eventually hindering a continuous air removal by closing bottle necks. Nevertheless it was assumed that a minimum of air was locked up in the system. Air influenced the absorption measurement only in the capillary fringe zone and it almost quantitatively disappeared with continued slow imbibition.

The differences of the capillary fringes due to grain-size effects were significant for both, imbibition and drainage, respectively, even steady-state conditions were not achieved due to short relaxation times (Fig. 3.2).

The upper and lower edges of capillary fringes showed characteristic slopes and shapes of water saturation curves (Fig. 3.3a) during water saturation for individual grain sizes. The increase of the capillary fringe from CM, MF, to CMF sands was comparable with C, M, and F sands. While C, M, and F sands showed wider steps, the mixed types displayed more gradual changes.

The amount of water removed from the system by drainage generally decreases in the following sequence: $C > M > CM > CMF > MF > F$, which corresponds to grain-size changes toward smaller values and to lower pore sizes. This is shown in Fig. 3.3b, where the drainage curves of F and MF sands and to some extent the CMF sand are comparable in slope and shape.

Systematic electrical conductivity measurements were performed parallel to the x-ray absorption measurements for all columns during imbibition and drainage (Fig. 3.4). Archie's law was applied to derive fluid conductivities for saturation and drainage steps (Fig. 3.4) from water saturation (Fig. 3.2) and electrical conductivity (Fig. 3.4). The significant difference in shape of both electrical and

fluid conductivity curves for imbibition and drainage was due to missing electrical contact in the dry volume of sand above the capillary front during imbibition. After full saturation, all electrodes are wetted, and stay wet even after draining water. Therefore, the drainage curves show a tail, while imbibition curves show a sudden break in unsaturated parts due to missing contact to the electrodes

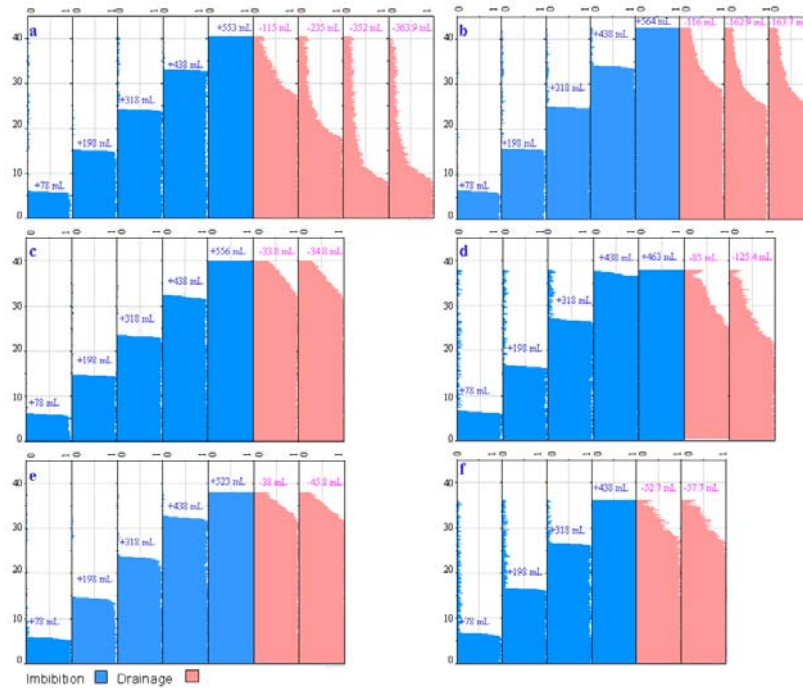


Fig. 3.2. Water saturation (S_w) of pores during imbibition and drainage defined by x-ray absorption measurement showing the level and shape of the capillary fringe for all grain sizes (a = coarse, b = medium, c = fine, d = coarse-medium, e = medium-fine and f = coarse-medium-fine). Vertical scale refers to sample height in centimeters and horizontal scale refers to water saturation (0–1, unsaturated to saturated, respectively).

In general, the electrical conductivity increases with the water content. In the case of fully saturated sands, electrical conductivity values are a function of the water/sand ratio and fluid conductivity. During drainage, the electrical conductivities of the drained parts of the sand columns are significantly lower than those of fully saturated parts (Fig. 3.4). This relates well to the decrease of the volume of water which is in contact with the pores, and also to the disappearance of surface conductance at the air–water interfaces (Knight, 1991).

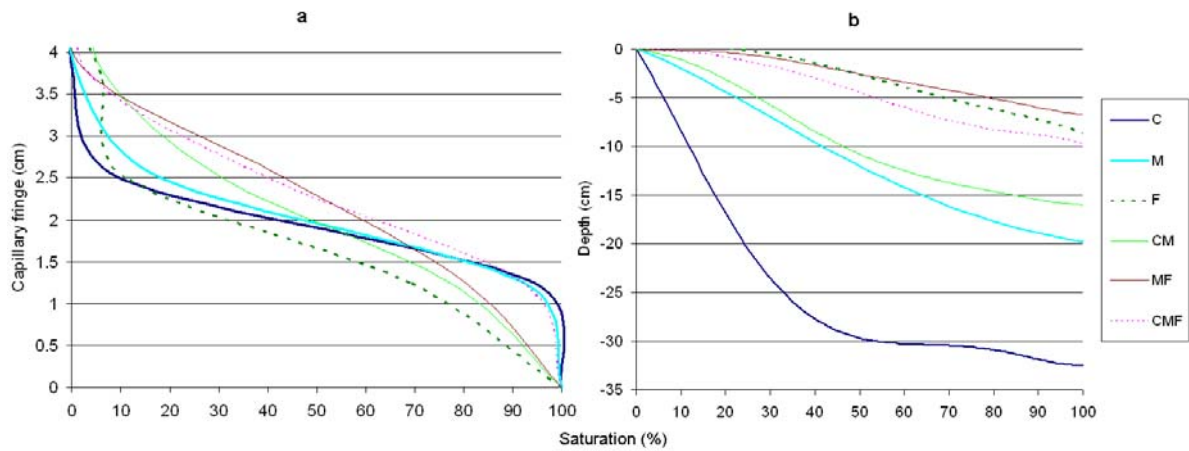


Fig. 3.3. Comparison of the shape of the capillary fringe curves for the different types of sand for (a) saturation without equilibration, and (b) for drainage when no water left the column gravitatively (C = coarse, M = medium, F = fine and mixtures; details in the above section of Methodology and Experimental Set-up Columns).

During water imbibition, the electrical conductivity was expected to decrease with decreasing water content at constant fluid conductivity in the capillary fringe above the water table. But we found the reverse situation during each saturation step. The electrical conductivity of the unsaturated and even saturated part of the capillary head measured during saturation was higher than the one measured for the fully saturated samples at deeper parts of the column (Fig. 3.4) and higher than the one measured during drainage, at comparable water saturation levels.

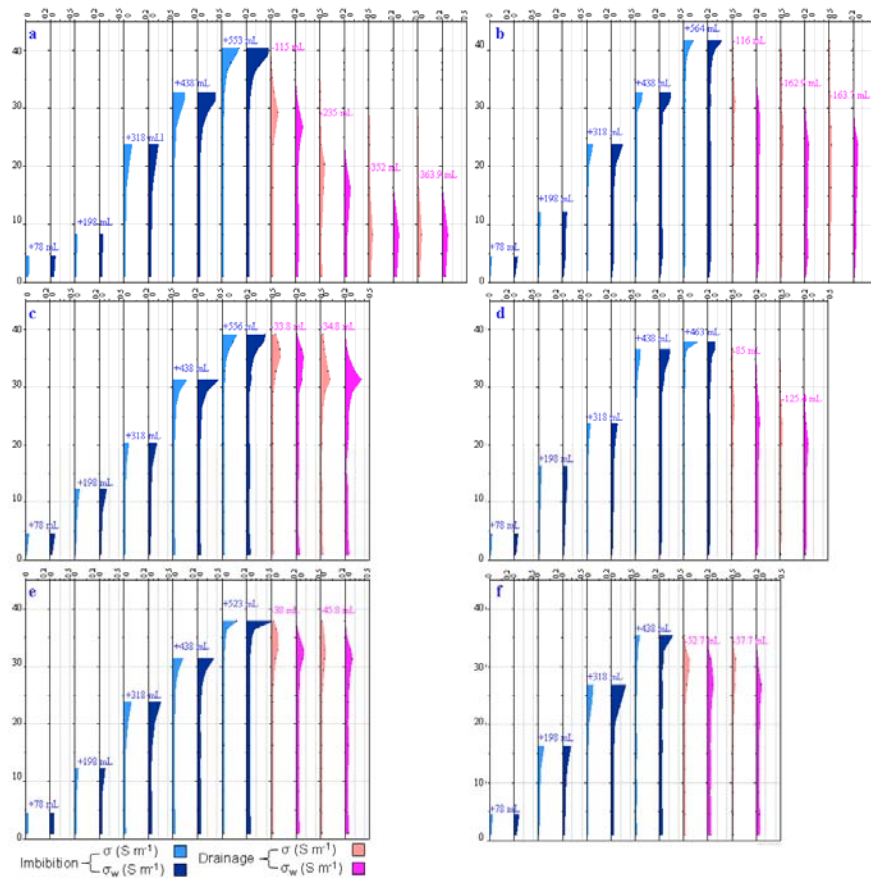


Fig. 3.4. Evolution of measured electrical conductivity and fluid conductivity during stepwise imbibition till saturation for individual grain sizes was achieved with 1- to 2-cm water cover and drainage (for key see Fig. 3.2). The numbers refer to the milliliters of water added or extracted from the system. Vertical scale refers to sample height in centimeters and horizontal scale refers to measured electrical (σ) and calculated fluid (σ_w) conductivities during imbibition and drainage.

This phenomenon was also observed by Knight (1991) during her measurement of the resistivity of partially saturated sandstones. She named this area, where the resistivity decreased, a hysteretic region. She attributed in her model the reasons for this hysteresis is due to the presence of a large continuous surface area of the air–water interface, larger than that found during drainage, that the water forms a thin coating around grains. With increasing imbibition (higher saturation level), a thick layer of water formed, separated by a thin central air phase, with rising saturation, the fluids rearrange and the air phase becomes disconnected and breaks down to a more stable geometry. Roberts and Lin (1997a) found the same hysteresis during wetting of Topopah spring Tuff which is

consistent with Knight's (1991) results. Also, Ulrich and Slater (2004) found consistent results with the model of Knight (1991) during their measurements of the induced polarization on unsaturated, unconsolidated sands (the polarization during saturation is greater than that during drainage below $S_w = 0.6$ for two samples and below $S_w = 0.5$ for one sample). Titov et al. (2004) considered during their measurements of the induced polarization of unsaturated sands, that during water filling the pores between grains are the zone of large current pathways and they defined areas of grain contact as the narrow pathways in saturated cells. However, in unsaturated cells, the areas of grain contact are the large pathways, and the thin water film on the surfaces of the grains are the narrow passageways, this would increase the polarization of unsaturated cells compared with saturated cells. With increased drying, water released from the surfaces of the grains causes a decrease in cell polarization due to the convergence of the effective radii of narrow and large current passageways. The pore size/water film ratio is controlled by surface area and the compaction of the material. This relationship basically explains the tendency toward elevated fluid conductivity with increase surface area/grain size ratio.

In all grain-size settings we observed changes toward higher electrical conductivities with decreasing saturation, but these are not consistent during stepwise imbibition (Fig. 3.4). Each additional step resulted in a stronger increase in electrical conductivity in both the saturated and unsaturated parts of the capillary head, at similar water saturation levels, derived from x-ray absorption measurement.

The measured electrical conductivity for the fine sand compared with the expected electrical conductivity on the base of the fluid conductivity of water (equal to 0.0571 S m^{-1}) before saturation showed significant differences. Figure 3.5 shows all saturation and drainage steps for fine sand. In the case of saturation measured and expected values fit quite well in the lower saturated part of the column, but the saturated part of the capillary head shows a distinct rise in amplitude of the measured values with each step of imbibition. This is explained by a strong rise of fluid conductivity (0.205 S m^{-1}), after total saturation with 2 cm of ponding water head, where the column maintained a high electrical conductivity in the uppermost level. In the drainage cycle the peak shape spreads out and moves down, showing in the final step a rise of electrical conductivity over the whole column length, higher than the expected values.

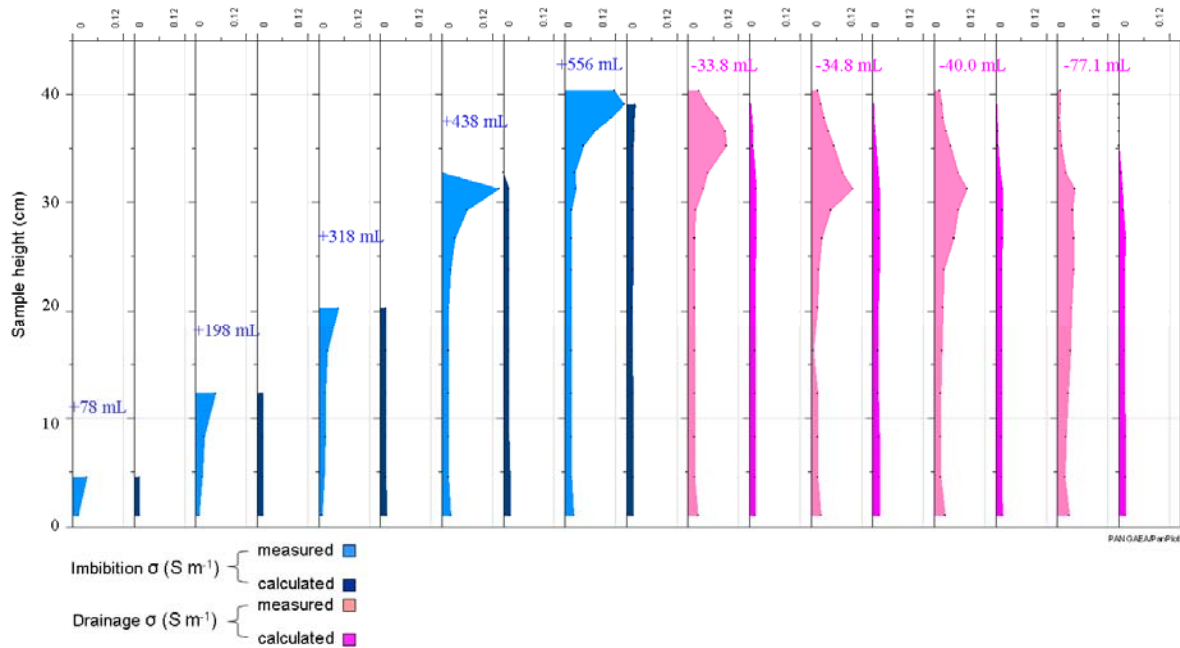


Fig. 3.5. Measured and calculated electrical conductivity for fine sand. Note the continuous gain in measured electrical conductivity during imbibition (+mL) and the smoothing due to drainage (-mL). This is in strong contrast to the expected electrical conductivity values based on fluid conductivity of 0.0571 S m^{-1} of the added water.

The hysteretic changes as described above cannot be solely responsible for the continuous increase within each column with each step of saturation (120 mL per step). Additionally, we observed a correlation of grain-size characteristics and hysteresis. Coarse grains show smaller hysteresis than finer grain sizes. To explain the continuous increase of electrical conductivity with each step of imbibition, we propose two additional mechanisms, namely, dissolution at grain boundaries and chromatographic effects. The first mechanism is due to small amounts of absorbed soluble salts that dissolve from the grain surfaces which will be brought in solution by the thin films coating the grains. Film and capillary transport are much faster (average velocities greater than 10 m yr^{-1} for average film thicknesses greater than $2 \text{ }\mu\text{m}$ and matrix potentials greater than $-10 \text{ cm H}_2\text{O}$, Tokunaga et al., 2000) than the rising saturated water table (e.g., Ghodrati et al., 1999; Tokunaga et al., 2000; Tokunaga and Wan, 2001; Tofteng et al., 2002; Nimmo, 2008). The film water therefore has to become more enriched in ions after each step of saturation than the slower rising water table. The width of the capillary fringe is a function of grain size, pore size, connectivity, surface area, and

wetting ability of each of the minerals. The finer the grain size, the larger the surface area and the more reactive surfaces and soluble salts absorbed on these surfaces. Additionally, the smaller the pores, the higher the capillary rise of water, and the larger the volume affected. Due to this effect and the non-homogeneous rising front, the hysteretic curve is not linear, but exponential.

To obtain a typical capillary fringe shape and saturation pattern for individual grain sizes, the time of the x-ray absorption measurement after imbibition was too short. In an experiment with medium-grained sand (washed five times with demineralized water), by adding 378 mL of demineralized water, the change of the capillary fringe after a step of imbibition at start (0.5 h relaxation time), after 19 and 44 h, shows within the first 19 h a strong smoothing of a quasi angular shaped starting curve (Fig. 3.6a). The lower portion shows a decline of saturation whereas the upper portion of the capillary fringe shows a rise in saturation providing contact to the next higher level electrodes. Conductivities are low at start, but rise fast within the first 19 h and getting slower after 44 h (Fig. 3.6b). The rise of electrical conductivity at the capillary fringe and within the saturated zone of the capillary head could be explained by two processes. First, by the advancing dissolution of the host material, explaining the overall increase; and second, by the suction power of the capillary head changing the shape of the curve with time and allowing water films to wet all available grains at each level.

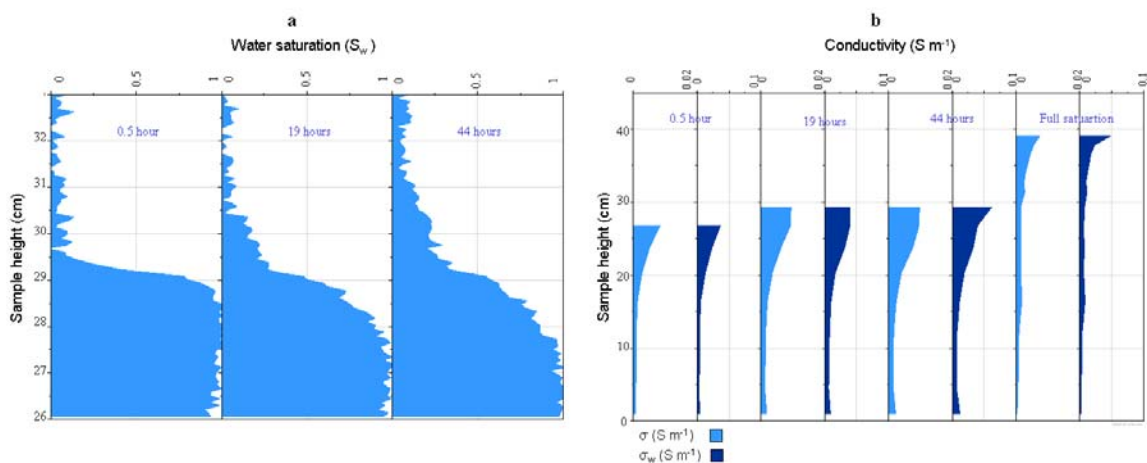


Fig. 3.6. Smoothing effect after imbibition with 378 mL of demineralized water into dry medium-grained sand after 0.5, 19, and 44 h on (a) the shape of the capillary fringe (enlarged scale), (b) the measured electrical conductivity, and the calculated fluid conductivity. For comparison, the fully saturated column (531 mL) is shown.

After saturation of the total volume the electrical conductivity curve at the previous capillary fringe level reaches again lower values. The change of fluid conductivity before saturation (demineralized water with 0.00025 S m^{-1}) and post saturation in the overhead (0.0685 S m^{-1}) and at the base after drainage (0.0242 S m^{-1}) shows significant differences, indicating fast reaction of mineral surfaces with the rising water and slow equilibration either by convection or diffusion within the column. The drained water on the other hand is a mixture of the fast draining enriched overhead water due to preferential flow by larger pores and the less enriched waters in the lower parts of the column. To show this particular feature of gaining electrical conductivity with column height all values were calculated as being saturated (Fig. 3.7). The continuous rise in electrical conductivity within the saturated zone reached 10 to 20 times more than the values at the base of the column, and this rise continued into the unsaturated zones with values up to more than 100 times. Much higher values should be expected for extremely low water contents where wetting of the electrodes did not occur, and no electrical conductivity could be measured. The graph shows that the fluid in the column after total saturation did not equilibrate during the experiment. Some remixing occurred during the drainage cycle, indicating gravity driven replacement of fast low conductivity bottom fluid by fast highly conductive capillary head fluids.

The mechanism of accumulating ions in the fast moving capillary head was proved in another experiment with a column of special design, where the water could be extracted from the base of the column to the top at different positions using metal free Rhizons. In this experiment we used fine sand $990 \text{ g kg}^{-1} \text{ SiO}_2$. The water was added in three steps. Sampling was performed after each step from top to bottom to avoid mixing. In the first step we added 408 mL of demineralized water. Then water was extracted in the first step from Positions 1.5 to 1.1, respectively, where 1.5 was located in the unsaturated zone (see Fig. 3.8a). In the second step, we added 200 mL more, then the water was extracted from positions 2.3 to 2.1 (Position 2.3 located in the unsaturated zone). In the final step the column was fully saturated with a 2-cm ponding water head. The excessive water was extracted (position 3.1). The extracted water samples were analyzed using ICP–MS and ICP–OES.

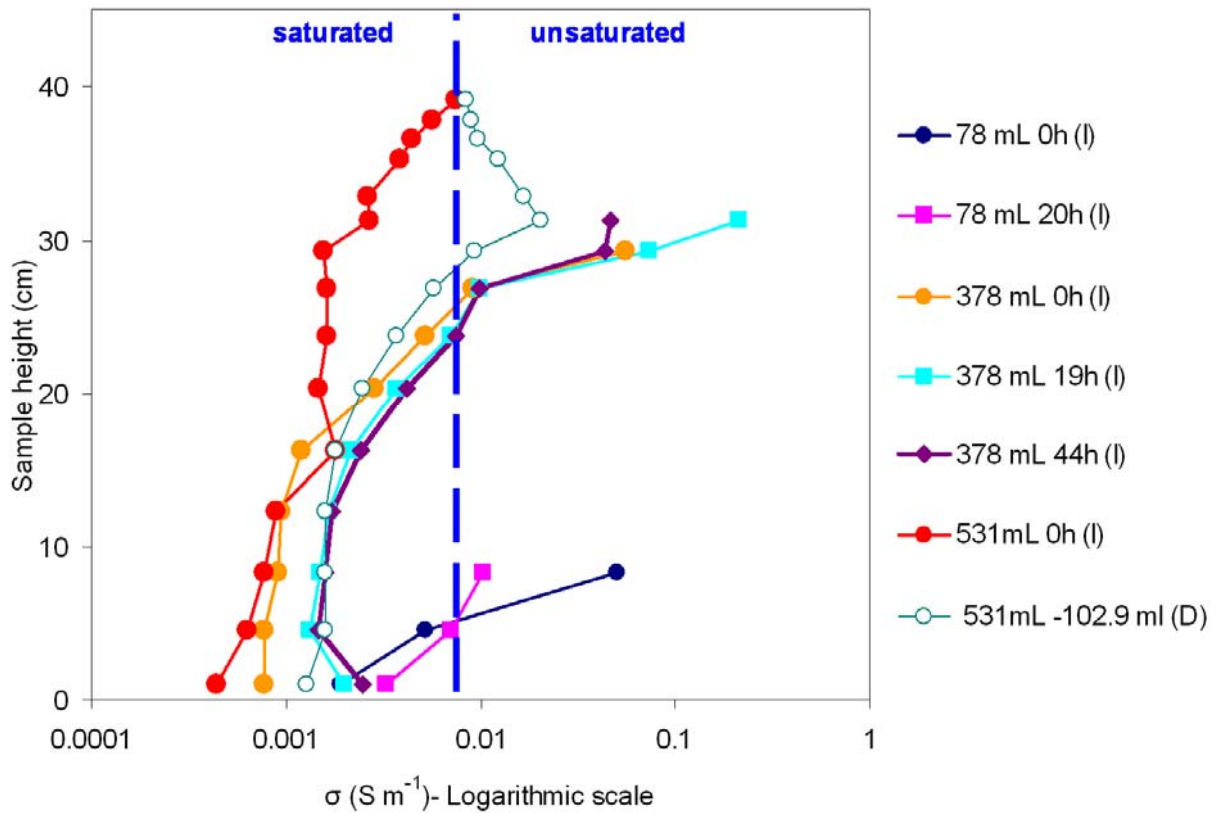


Fig. 3.7. For direct comparison of measured electrical conductivities at variable saturations, the measured values were calculated as being fully saturated (fully saturated $\sigma \text{ (S m}^{-1}\text{)} = \text{measured } \sigma \text{ (S m}^{-1}\text{)} \times 1/\text{measured water saturation } S_w^n$). The broken line marks the real saturated part of the column. The trend for imbibition (I) shows a gentle increase for the fully saturated column, but an extreme gain for the unsaturated parts.

Fluid conductivity as well as the sum of dissolved ions showed a significant increase with the rising capillary head, due to increasing ionic strength, rising with each step of saturation accompanied by a pH decrease (Fig. 3.8b; Sample 1.5, 2.3, and 3.1).

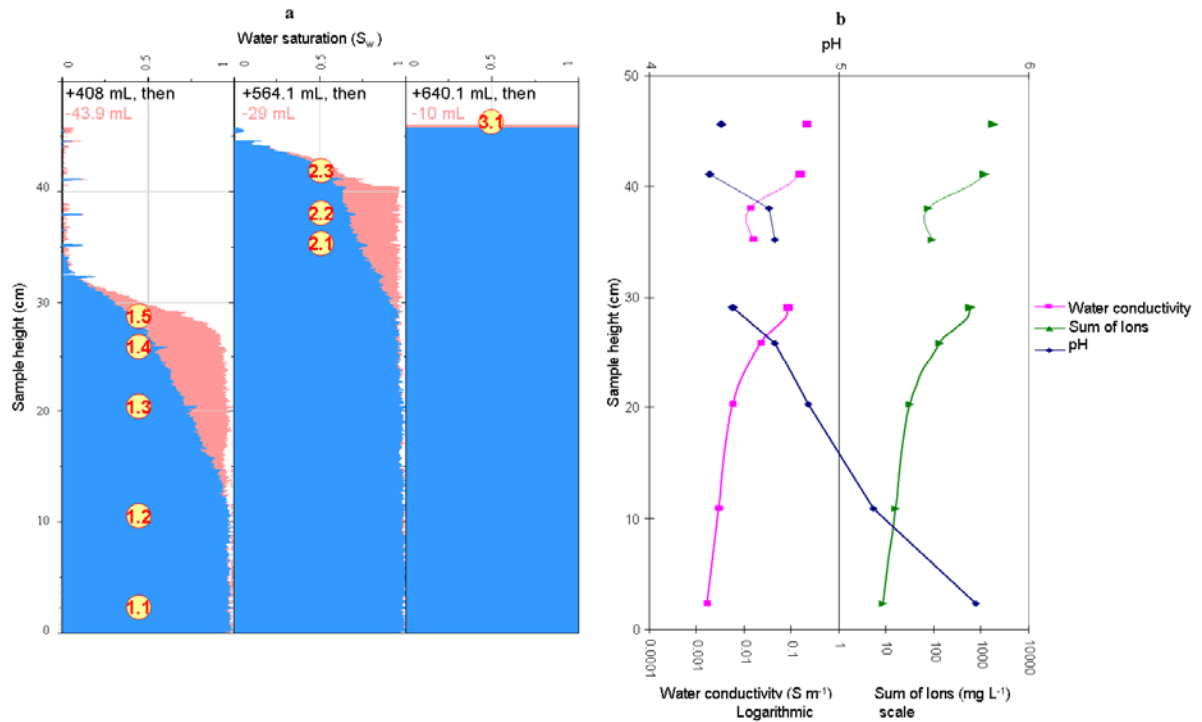


Fig. 3.8. Shows (a) the water saturation (S_w) of three filling steps, each prior (+mL) and after extraction by Rhizon soil water samplers (-mL) at different positions (1.1–3.1); (b) plot of water conductivity, pH, and sum of ions of extracted waters. (position of the Rhizons: 1.1–1.5 = Step 1, [thick line]; 2.1–2.3 = Step 2 [thin line]; and 3.1 = Step 3 [point]).

The observed pH values of 5.7 to 4.3 had little influence on fluid conductivities (max. 3.6%). The measured values were representative for Step 1, but for Step 2 and Step 3 the values were much below the expected due to Step 1 extraction and Step 1 and 2 sampling, respectively. The observed ion strength most probably related to surface reactions with each mineral and eventually small amount of soluble salts absorbed on the mineral surfaces. Calcium, Na, and K showed highest values in the solution. All analyzed elements exhibited a stepwise increase of the rising capillary head and a comparable element distribution pattern at different levels for the individual waters (Fig. 3.9).

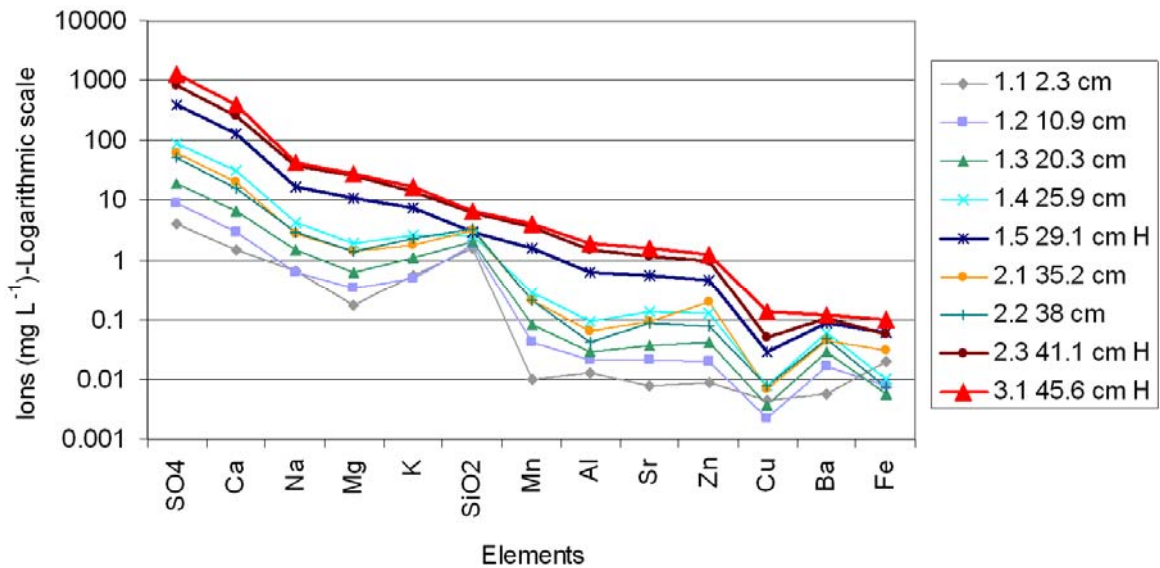


Fig. 3.9. Increase of major ions in the fast capillary head waters (H) with each step of imbibition showing an enrichment up to a factor >100 in relation to late waters (for key see Fig. 3.8).

Individual ions followed this trend, showing enrichment for the capillary head fluids of 10 to 100 times late fluids. Chondrite normalized REE (rare earth elements) pattern of the extracted water showed a smooth pattern with strong light rare earth elements (LREE) enrichment for the early rising water. Later water showed LREE depletion with a positive Eu anomaly (Fig. 3.10, Samples 1.1–1.4). This proved the mechanism of ion uptake by the rising capillary fringe right and explains the significant changes in electrical conductivity.

The second mechanism, a chromatographic effect could contribute to elevated conductivities due to preferential rise of some ions and retention of others. This has been observed in former long-term experiments showing both changes toward lower pH values and higher metal load (from mineral leaching) with reduced degree of water saturation (pH 3.5 at the bottom and pH 1.5 at the top of the column), but with an increase in fluid conductivity.

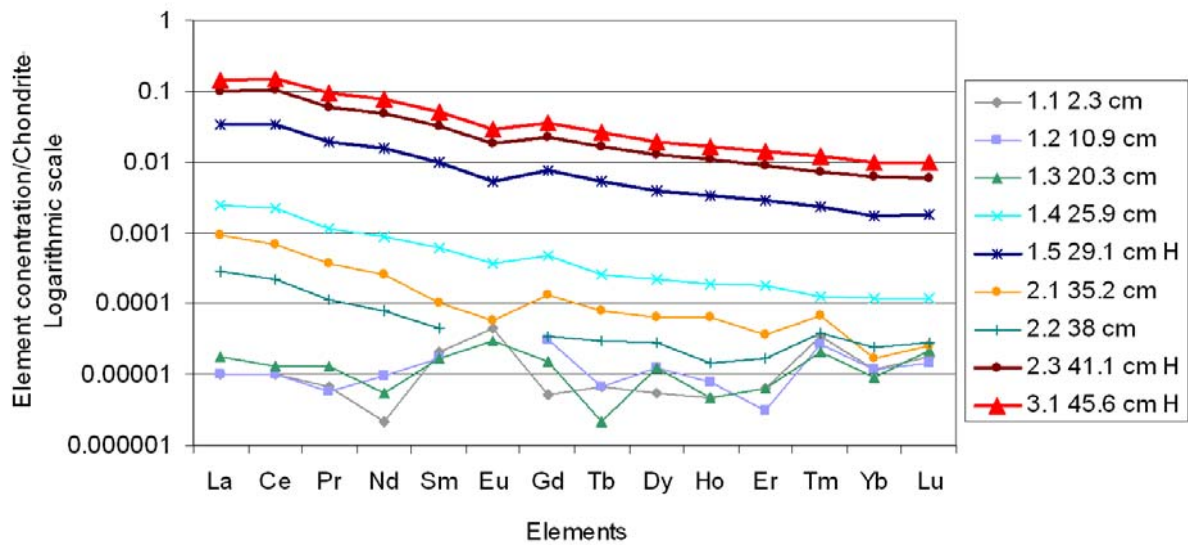


Fig. 3.10. Chondrite-normalized REE patterns of the fast capillary head (Chondrite data [from McDonough and Sun, 1995]) showing strong enrichment of capillary head waters in relation to late waters. Note the change of the pattern from LREE enrichment with negative Eu anomaly to flat patterns with positive Eu anomaly indicating sequential mineral dissolution (for key see Fig. 3.8).

Most probably all three mechanisms should be applied to explain the characteristic scheme of changes in electrical conductivity. The effect of both, the water/air ratio and the chromatographic impact were probably quite low, while the uptake of ions of the rising capillary head was the main control of the changes in fluid conductivity.

3.6. Conclusions

We experimentally investigated the transport and drainage of water in combination of electrical conductivity measurements in porous media of different grain sizes at various depths using nondestructive and non-invasive methods. These experiments allowed us to describe the shape of the capillary fringe, and to quantify the water content at distinct levels of the fringe. The capillary fringe is a critical zone, where dissolution, transport, and precipitation take place. It could be shown that an increased electrical conductivity level in the capillary head and fringe was not necessarily governed by the water/gas ratio of partially saturated pores, as described by a number of authors (Knight, 1991; Roberts and Lin, 1997a; Ulrich and Slater, 2004; Titov et al., 2004), since this mechanism could not explain the incremental rise of electrical conductivity of the capillary head

after each filling step. Another mechanism, namely increasing ion strength was invoked. Either surface reaction or soluble salts adsorbed on grain surfaces provide ions which accumulate in the capillaries and the grain boundary film transport system rising faster than the water table (Fig. 3.9). This mechanism is highly effective in the unsaturated part of the column where the water film/particle surface ratio was almost equal (Fig. 3.7). But even in the fully saturated part of the capillary head the rising fluid accumulated ions by interaction with these early films, leaving depleted grain boundaries behind. The effect is eventually supported by a chromatographic effect affecting ions and colloids individually but differently on grain boundary multi layer films or capillaries. This effect could be responsible for the observed decrease in pH due to H^+ rising faster in the column. The contribution of the decreasing pH to the fluid conductivity is small, but might on the other hand boost the mineral surface reactions at the capillary head.

This study opens up a distinct understanding of transport, enrichment, and precipitation processes of an oscillating capillary fringe in relationship to the underlying seasonally oscillating water table, and its retention capacity in cases where the water contains some mobilized, eventually toxic elements. These processes are essential for the formation of hardpan in soils and mining residues as well as for alteration and generation of supergene ore deposits in the critical zone. The interpretation of electrical conductivity data in the unsaturated zone has to pay attention to anomalously elevated fluid conductivities in the capillary fringe



**Effect of temperature and water
content on hardpan formation in mine
tailings: column experiments**

4.1. Introduction

The potential of acid mine drainage generation from sulfide-rich mine tailings is very high. Therefore, a detailed understanding of the interaction between the different components is a prerequisite for predicting the behaviour, and the potential for natural attenuation of these sites in the long term and for better remediation strategies.

As discussed before in detail, the different steps in a mine tailings life cycle such as deposition, oxidation and hardpan formations depend on the interaction of different factors regarding the material itself (grain size, amount of reactive phases e.g. sulfides/carbonates), its mode of deposition, the availability of water and oxygen in parts of the heap, and the climatic conditions. As Jung (2003) has shown, continuous rainfall may prevent hardpan formation due to slow wash out and downward movement of the water flow. Therefore, episodes of intense rain fall (e.g. winter times) followed by dry periods promoting evaporation (e.g. summer times) may be ideal for hardpans. Also, very dry climates will often not allow a storage of enough water for reaction times long enough to substantially promote the oxidation of sulfides.

The following experimental study focussed on the behaviour of the tailings material under variable surface temperatures and amounts of water added and its potential to develop hardpans as well as the effect on the oxygen infiltration within the columns.

4.2. Methodology and Experimental Set-up

This section is an extension to chapter 3, where water content, chemistry of the water extracted by Rhizon soil water samplers and electrical conductivity were measured. Additionally, oxygen content, temperature, pH were measured. The evaporation, forced by heating lamps was controlled by a series of 6 computerized balances.

4.2.1. Columns & Instrumentations

For the following experiment, we used the same type of column designed in the last chapter as a basis adding a few details (Fig. 4.1), and additional equipments.

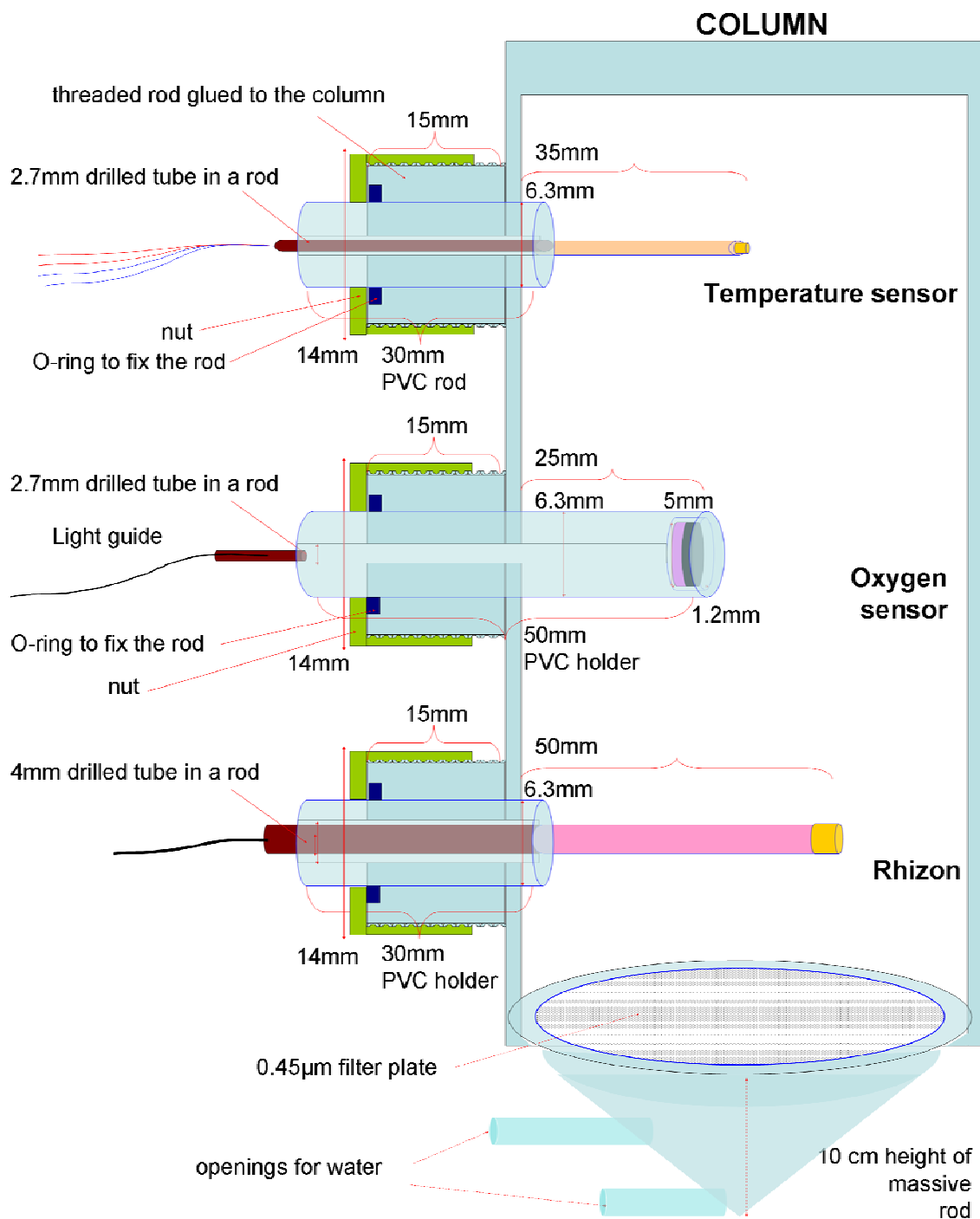


Fig. 4.1. Design of the column used in this study with the dimensions of ports and holders for temperature, oxygen, and Rhizon soil water sampler.

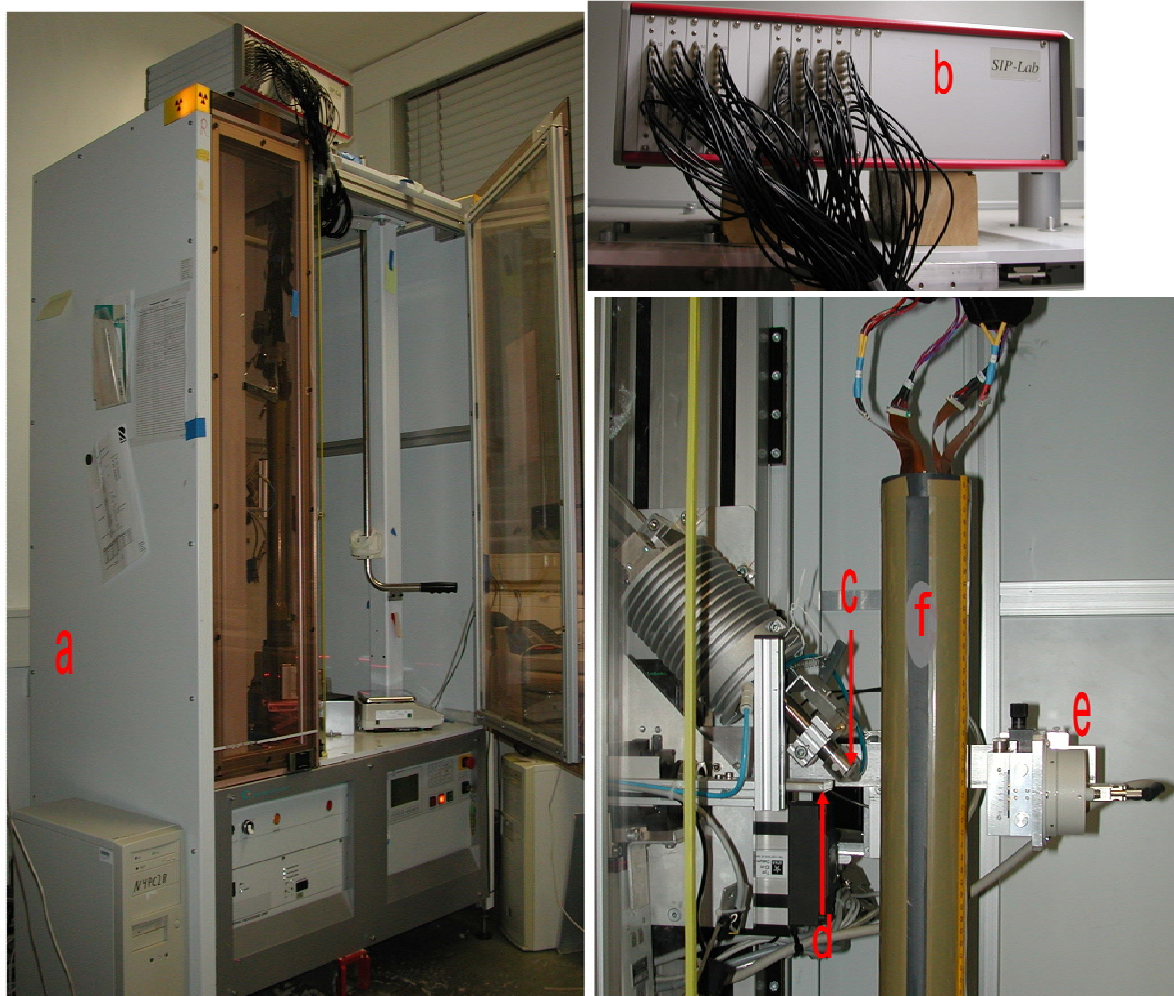


Fig. 4.2. Experimental set-up showing the EDXRF GeoScanner (a) and SIPLab (b) used for the measurements; EDXRF detector (c), X-ray source (d), absorption line detector (e) and the column (f).

Pore water was collected from the column using Rhizon soil moisture samplers (type Rhizon MOM 2.5mm in 5 cm length metal-free support, Eijkelkamp Agriresearch) which act as artificial root (Fig. 4.3A). They consisted of a hydrophilic porous PES (polyethersulfone), membrane tube, with a pore diameter of 0.1- 0.2 μm , extended with a polyvinyl chloride tube. Rhizon outer diameter is 2.5 mm, with filter section length of 5 cm. A wire is fixed to one end of the porous polymer to support it, this wire is made of PEEK fiber (polyether ether ketone), which used for metal measurements. Pore water samples from the sediment flows through the tiny space between the

porous tube and the supporting wire (Seeberg-Elverfeldt et al., 2005). The sampler is connected to a standard 10 mL syringe using luer-lock fittings and Tygon or PVC tubing. Evacuating the syringe by drawing the piston is enough to pull back filtered pore water from the soil (vacuum can be kept by using a piece of wood attached to the syringe piston).

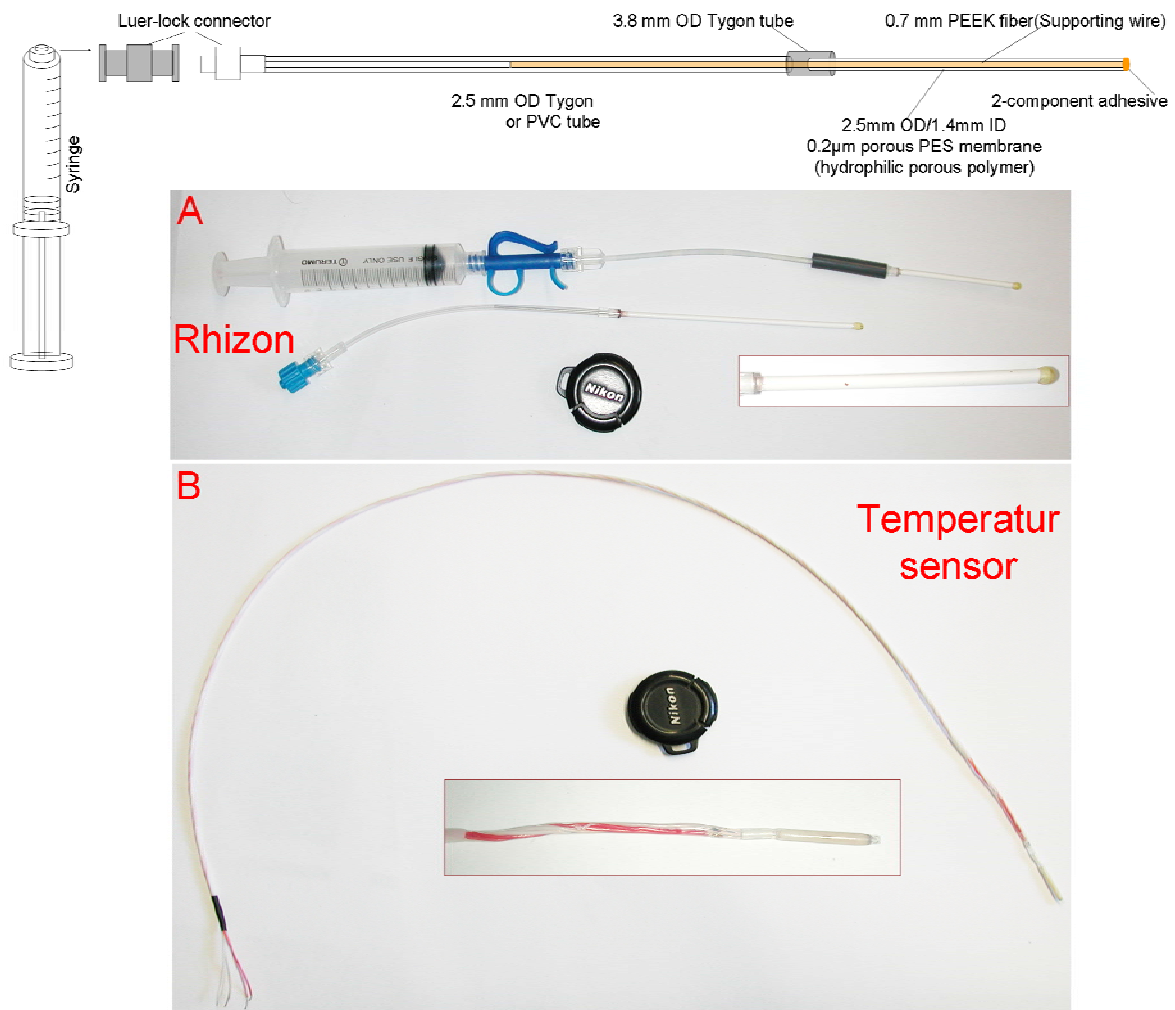


Fig. 4.3. Showing the Rhizon soil water samplers (A) with its components from Rhizosphere Research Products and the temperature sensor (B).

The sampling flow rate depends on the grain size of the soil material and its saturation degree. The temperature sensors (Fig. 4.3B) were extended by two meters cables, then connected to HP

3497 Hewlett Packard Data Acquisition/Control Unit and the temperature collected by program designed by Labview 7.0.

Non-invasive oxygen sensors (Fig. 4.4) measure the partial pressure of dissolved and gaseous oxygen. In order to measure the oxygen content, the sensor spots should be fixed on the inner surface of a transparent plastic material (in contact with the object). The oxygen concentration can be measured from outside, through the wall using an optical light guide generated using 4-channel fiber optic oxygen transmitters. The measurement ranges from 1ppb up to 45 ppm dissolved oxygen, signal independent on flow velocity with no consumption of the available oxygen. The measurement unit is % oxygen or air saturation. The light from the blue LED excites the sensor spot to emit fluorescence. If the sensor spot encounters an oxygen molecule, the excess energy is transferred in a non-radiative way, decreasing or quenching the fluorescence signal. The degree of quenching correlates to the partial pressure of oxygen in the matrix, which is in dynamic equilibrium with oxygen in the sample (Further details by [www. PreSens.de](http://www.PreSens.de)).

The pH values were collected using non bleeding pH indicator strips from Merck KGaA used for measurement in turbid solutions with colourless strips. In this method the pH indicator strips were glued to the side of the PVC foil in the column, that pictures can be taken from outside using digital microscope with fixed illumination values. The suggestion was done by Prof. Otto S. Wolfbeis, Institut für Analytische Chemie, Chemo- und Biosensoric, University of Regensburg.

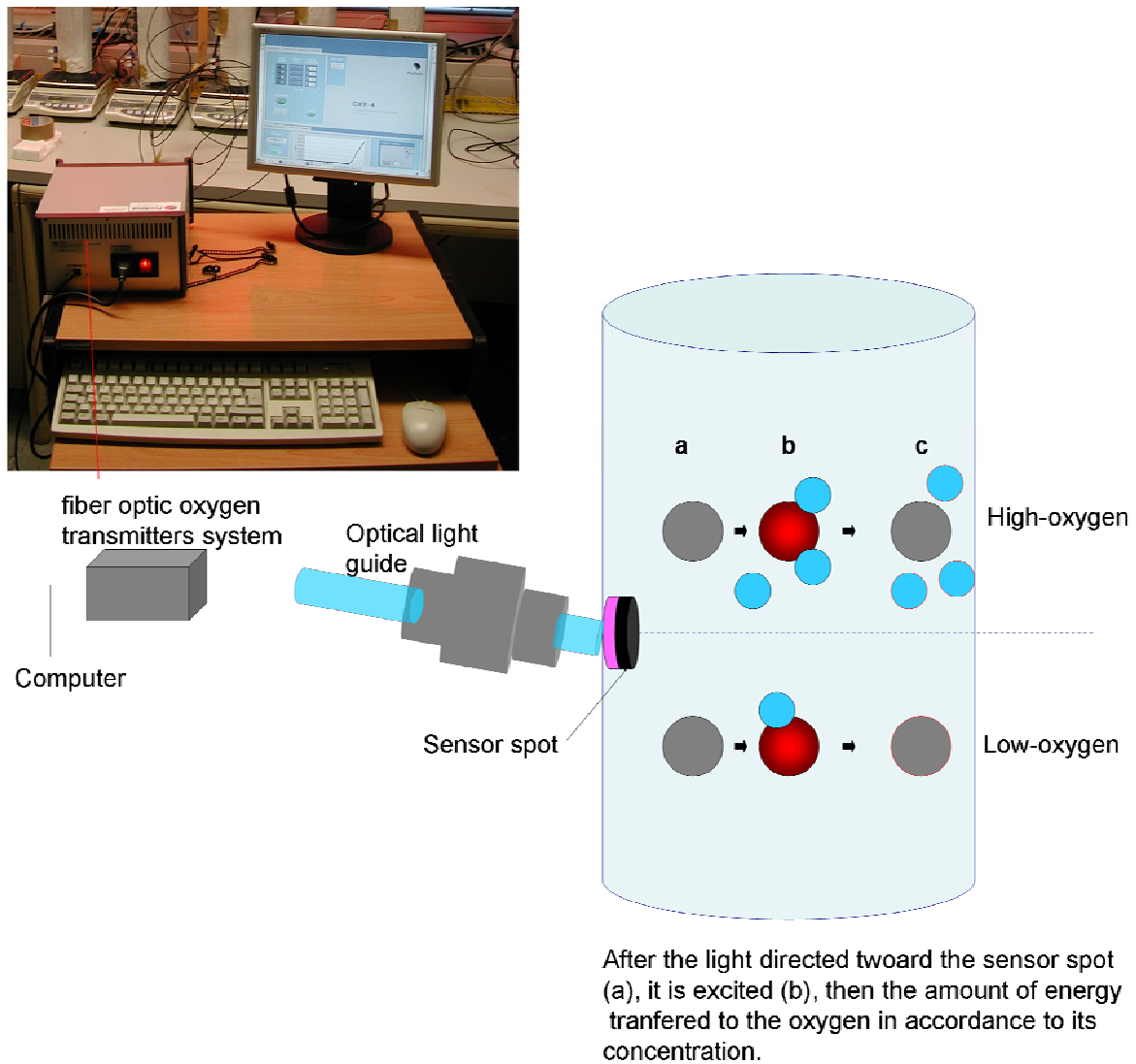


Fig. 4.4. Theoretical background and equipments used for oxygen measurement.

In order to prevent heat loss/or infiltration from the sides of the columns, a thermal insulation was applied using an isofelt mat with a thermal gradient of 0.0155 W/m.K , consisting of highly pure ceramic fibers with small quantities of organic bonding agents and one side aluminum foil was used (L.&F. PETERS GmbH) (Fig. 4.5B). Also, infrared lamps were used to obtain column top surface temperatures of 30 , 45 and 60°C with 50W , 75W and 100W , respectively, mounted at an adequate distance to the sample surface. Six balances (Kern type EW12000-1NM) were used to control the

evaporation rate for the columns through a data transmission unit (Moxa UPort 1650-16 device) and Collect 6.0 software (Labtronics Inc.).



Fig. 4.5. Showing the distribution of the sensors along the column (A), Isofelt used to prevent heat loss/ infiltration from the sides of the column, and the measurement environment around the columns (B-C).

The distribution of the temperature (3 for each column) and oxygen sensors (4 for each column), the Rhizon water samplers (4 for each column), and the pH paper at 12 positions are shown in Fig. 4.5A.

4.2.2. Materials Characterization

Six columns were constructed for this experiment. The filling material used in this study was unoxidized grey tailings from Davidschacht mine tailings (sample depth -6.97m; Fig. 1.1-a4, chapter 2 appendix). The material contained some moisture, which was removed by a freeze-drying system (model gamma 1-20, Christ Gefriertrocknungsanlagen GmbH) in order to decrease its oxidation using normal drying methods. According to XRD, the bulk minerals are quartz, chlorite, muscovite-illite, barite, siderite, pyrite, arsenopyrite, ankerite and gypsum. Also, one polished thin section was made for this material and measured using MLA (Fig. 4.6).

The main chemical analysis of the solid sample, paste-water extraction and LECO is summarized in table 1.

BET (m ² g ⁻¹) ^t	3.10	Cs (mg L ⁻¹) ^{fb}	0.0008	MnO (%) ^{tc}	0.486
pH ^f	6.35	Cu (mg L ⁻¹) ^{fb}	0.0229	MgO (%) ^{tc}	1.07
Conductivity (mS cm ⁻¹) ^f	2.75	Li (mg L ⁻¹) ^{fb}	0.023	CaO (%) ^{tc}	2.211
HCO ₃ titration (mg L ⁻¹) ^f	21	Mo (mg L ⁻¹) ^{fb}	0.011	Na ₂ O (%) ^{tc}	0.17
Al (mg L ⁻¹) ^{fa}	0.63	Ni (mg L ⁻¹) ^{fb}	0.0136	K ₂ O (%) ^{tc}	2.111
Ca (mg L ⁻¹) ^{fa}	581	Pb (mg L ⁻¹) ^{fb}	0.0026	P ₂ O ₅ (%) ^{tc}	0.189
Fe (mg L ⁻¹) ^{fa}	0.76	Rb (mg L ⁻¹) ^{fb}	0.0156	(SO ₃) (%) ^{tc}	1.61
K (mg L ⁻¹) ^{fa}	5.89	Sb (mg L ⁻¹) ^{fb}	0.003	(Cl) (%) ^{tc}	0.007
Mn (mg L ⁻¹) ^{fa}	0.011	Sc (mg L ⁻¹) ^{fb}	0.0001	LOI (%) ^{tc}	5.79
Na (mg L ⁻¹) ^{fa}	0.897	Se (mg L ⁻¹) ^{fb}	0.0019	(As) (mg kg ⁻¹) ^{tc}	11050
S (mg L ⁻¹) ^{fa}	649	Sn (mg L ⁻¹) ^{fb}	0.0053	Ba (mg kg ⁻¹) ^{tc}	19570
Mg (mg L ⁻¹) ^{af}	100	Sr (mg L ⁻¹) ^{fb}	0.182	Cu (mg kg ⁻¹) ^{tc}	205
Si (mg L ⁻¹) ^{af}	11	Tl (mg L ⁻¹) ^{fb}	0.0019	Pb (mg kg ⁻¹) ^{tc}	757
Zn (mg L ⁻¹) ^{fb}	1.82	U (mg L ⁻¹) ^{fb}	0.0003	Rb (mg kg ⁻¹) ^{tc}	161
As (mg L ⁻¹) ^{fb}	0.06	V (mg L ⁻¹) ^{fb}	0.0001	Sn (mg kg ⁻¹) ^{tc}	713
Ba (mg L ⁻¹) ^{fb}	0.012	W (mg L ⁻¹) ^{fb}	0.0001	Sr (mg kg ⁻¹) ^{tc}	364
Cd (mg L ⁻¹) ^{fb}	0.0256	SiO ₂ (%) ^{tc}	63.60	Zn (mg kg ⁻¹) ^{tc}	2113
Ce (mg L ⁻¹) ^{fb}	0.0001	TiO ₂ (%) ^{tc}	0.413	Zr (mg kg ⁻¹) ^{tc}	193
Co (mg L ⁻¹) ^{fb}	0.0002	Al ₂ O ₃ (%) ^{tc}	8.41	C-carb (%) ^{td}	2.12
Cr (mg L ⁻¹) ^{fb}	0.0015	Fe ₂ O ₃ (%) ^{tc}	9.66	S-sulfide (%) ^{td}	2.6

Table 4.1. Chemistry data of the solid tailings material (t) and the extracted fluid (f) used to fill the columns (a,b,c and d refers to ICP-OES, ICP-QMS, XRF and LECO methods, respectively).

The average porosity was 0.38-0.39% in all columns. The porosity was estimated from the weight difference of each column for dry and saturated tailings. Grain size is mainly medium to fine sands. The six columns were filled by a rotating sample splitter (Sample Divider Type PK, Nr 2275, Retsch KG Germany) in a homogeneous way into the PVC columns in order to avoid human based grain-size grading during the filling. The columns were filled to a height of 45 cm.

Chapter 4: Effect of temperature and water content on hardpan formation in mine tailings: column experiments

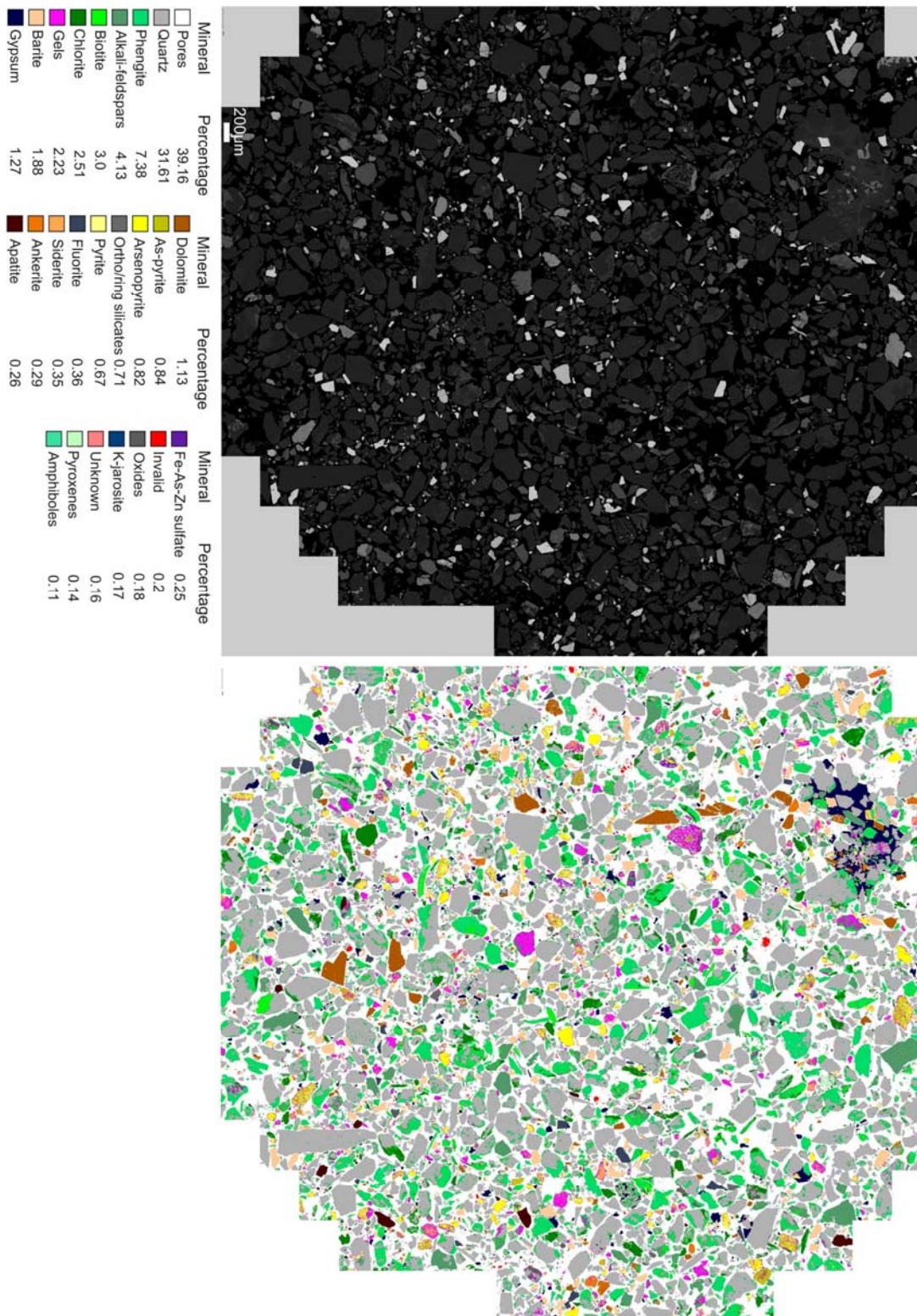


Fig. 4.6. BSE and Classified MLA images for the material used to fill the columns. Note that even the so-called unaltered material shows secondary phases such as gels, and gypsum agglutinating some particles.

4.3. Measurement and Data Processing

Absorption and electrical conductivity measurements followed the scheme below:

1) For the electrical conductivity measurement the geometric factor (k-factor) was estimated for each depth for all the 20 levels. To achieve this, the columns were filled only with drinking water of conductivity ranging from 0.0501 to 0.0504 S m⁻¹.

2) For x-ray absorption, each measurement started 2 cm below the column in air, then 1 cm aluminum holder (as a base of the column), then the 60-cm entire column (the 50-cm tube and its 10-cm massive base) and ending in 2 cm of air above the column.

3) Then the columns were filled homogeneously with tailings material and measured dry for absorption. The bulk porosity estimated from above parameters was used to calibrate the cumulative porosity of all 250- μ m steps derived from x-ray absorption.

4) Then the columns were filled until saturation (with 1- to 2-cm water cover) was achieved by adding water from the base by a pipe linked to a reservoir at about 5 cm above the tailings filling limit in the column, to allow the pores to become slowly saturated by continuous air removal. Then, absorption, and electrical conductivity were measured.

5) In the next step each column was put on a balance to monitor the evaporation progress. Date, time and values were recorded each 10min.

6) Water was added to the columns from the top in different amounts after three weeks based on the calculated evaporation rate for one week, for humid conditions in columns 1, 3, and 5. A reduced amount was applied to columns 2, 4, and 6 to simulate more arid conditions (Fig. 4.7). The amount of water added per filling stage was: 150ml for column 1, 100ml for column 2, 110ml for column 3, 70ml for column 4, 80ml for column 5 and 50 ml for column 6. Imbibition was done after 26 days drying period (stage 1) from the beginning of the experiment, after 33 days (stage 2), after 55 days (stage 3), after 69 days (stage 4), after 86 days (stage 5) and after 108 days (stage 6). Whereas x-ray

absorption and electrical conductivity measurements were done not for all stages, only for the dry, fully saturated, and stages 1, 3 and 6.

7) The temperature was adjusted to 60°C for columns 1 and 2; 45 °C for columns 3 and 4 and 30 °C for columns 5 and 6 and applied for approx. 8 hours/day. Temperature measurement data were collected at each 5 minutes (Fig. 4.7). The sensors were positioned at -1 (top of column), -19 and -31 cm.

8) The oxygen measurements were collected for column 4 continuously and two times a week for all the other columns (Fig. 4.4). The positions of the sensors were at -7 (top of column), -13, -25 and -37 cm.

9) Rhizon soil water samplers were fixed at 4 levels (-4, -10, -22 and -34) for each column for water extraction. The extracted water in two episodes (112 and 128 days), if sufficient in amount, it was analyzed for pH and fluid conductivity as well as for ions by inductively coupled plasma mass spectrometry (ICP–MS) and optical emission spectrometry (ICP–OES).

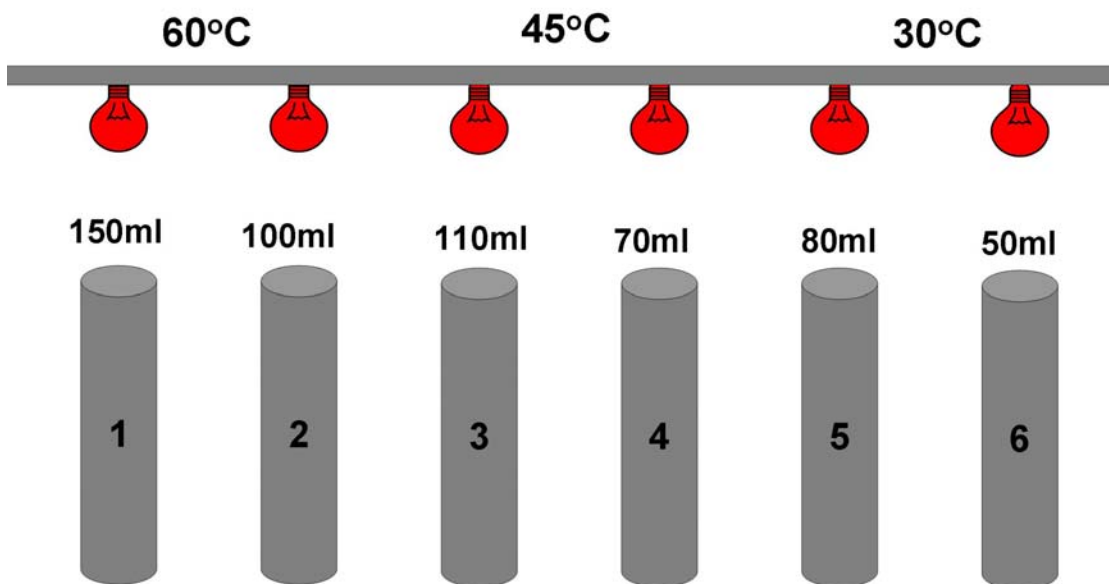


Fig. 4.7. Showing the different temperature and amount of water added to the columns.

10) At the inner side of the PVC foil sealing the longitudinal opening of the column, pH indicator strips was fixed at 12 positions. Monitoring of the colour changes was done by digital

microscope photography. Estimation of the pH was obtained by colour extraction of the RGB values of the middle square in the pH pictures (which influenced by pH from 6-7) and then extracted and compared to known pH. The measurements were done after saturation, and before and after adding water in the stages from S1 to S6.

11) At the end of the experiment (~155 days), the columns were cut for detailed chemical analysis of the solid samples and paste-water extractions.

After the acquisition, and processing of data for absorption and electrical conductivity the measurements were treated in the same way as described in the previous chapter. The Archie parameters n and m were determined for each column after full saturation stage. Parameter n is equal to 2 while parameter m shows small variations ranging from 2.3 to 2.5.

4.4. Results and discussion

After filling all columns with demineralised water from below until saturation, systematic electrical conductivity measurements were performed parallel to the x-ray absorption measurements for all columns (Figs. 4.11-4.16). From the amount of water added periodically to each column and the temperature applied during the experiment (Fig. 4.7), it can be visualized that the loss of water due to evaporation is more pronounced in columns 2, 4, and 6 compared to columns 1, 3, and 5 (Fig. 4.8). Archie's law (Archie, 1942) was applied to derive fluid conductivities for full saturation and drainage/raining events from water saturation and electrical conductivity. Generally, the electrical/fluid conductivities increases with water content, whereas during drainage, the electrical conductivities of the drained parts within the columns are significantly lower than those of fully saturated parts as a result of decreasing of the volume of water in contact with the pores, and also to lost surface conductance at the air–water interfaces (Knight, 1991).

4.4.1. Water loss.

During the raining events and the evaporation cycles, changes in the slopes of the balance-based (evaporation) curves can be recognized (Fig. 4.8). Each set of columns with the same temperature shows an identical slope of water loss in the first cycle of evaporation (water loss was calculated to 24 g/day in columns 1 & 2; 17 g/day in columns 3 & 4; 10 g/day in columns 5 & 6), but obviously differentiate after the second cycle due to variable water addition. At the last raining/evaporation

cycle, the loss of water was higher in columns 1, 3, and 5 during the first days of evaporation, due to the enrichment of the water at the upper surface layers directly after the raining event, compared to columns 2, 4, and 6 (Fig. 4.9). With continuous evaporation, the water loss becomes equal to or even lower than that in columns 2, 4, and 6.

4.4.2. Electrical/fluid conductivities.

Within the first step of the experiments, which involved water imbibition from the bottom, electrical and fluid conductivities were increased compared to the lower parts due to extreme ion accumulation in the rising capillary head with the effect of “first come, first serve” and a strong depletion of ions in the slower moving fluids in the deeper parts (Redwan and Rammlmair, 2010). With continuous drying and the following raining cycles, a correlation of electrical and fluid conductivities between columns 1 and 2, columns 3 and 4 and columns 5 and 6 can be extracted (Figs. 4.11-4.16). During the first two days of the experiment, the electrical/fluid conductivities decreased in column 1-4 and rised in column 5-6 due to the enrichment of water at the top surface at lower degrees of temperature. As evaporation proceeds, deeper parts of the columns are affected, and soluble salts will become concentrated in the lower portion. Decreased water contents in the upper parts of the columns correlate with reduced electrical/fluid conductivities values. Values of very low electrical/fluid conductivities were due to interrupted electrical contacts due to drying and/or sample shrinking at the foil contact (recognized before adding water in stages S1-S6, Figs. 4.11-4.16). During raining events, the upper parts get higher conductivities compared to the lower parts due to the solubility of the water-soluble efflorescent salts and water retention in this part. However, this depends on the speed of measurement after raining due to possible flashing of soluble sulfates to the lower parts in the columns. The fluid conductivities are related to the ion concentration in areas with low water content within the columns. In columns 1 and 3, spots of elevated fluid conductivities can be seen at some depths. These might be caused by ion accumulation in fluids due to a shifted evaporation/precipitation boundary, and/or eventually incipient cemented layer formation. In columns 2 and 4, the drying progrades smoothly from the top surface to the lower levels. In column 5 and 6, higher conductivities are recorded in the first days especially in the top parts, then slowly a turn over occurs, showing a decrease of conductivity at the top surface.

4.4.3. Oxygen and temperature measurements.

The main transport mechanisms of oxygen within tailings, due water contents often close to saturation, are considered to be through diffusion (Davis and Ritchie, 1987; Elberling et al., 1994) and advection (Wels et al., 2003). In the column tests, temperature, and oxygen saturation values were related to each other, showing that with increasing temperature oxygen infiltrated to deeper levels of the columns (columns 2 more than 1) until it stopped at the water table, due to the low rate of oxygen diffusion in water (Cussler, 1997). The infiltration decreased in medium temperature columns (3 and 4), and became very low in low temperature columns (5 and 6). The shape of the oxygen distribution is partly mirrored by the water saturation, indicating slow oxygen diffusion within the column by continuous loss of water due to evaporation. The oxygen concentration in the lower part of all columns shows a further decrease due to oxygen consumption probably in the course of mineral alteration. However, the consumption of oxygen by sulfide oxidation is considered to be very low due to the low sulfide contents (2.6%) of these tailings materials. The thermal gradient within the columns between heating and relaxing for the next heating time were variable. For example in the upper part of column one (Fig. 4.10), it takes about three hours to reach the maximum temperature of about 60°C, whereas it takes more than 14 hours to reach the room temperature at 20 °C, where temperature values are very low at deeper parts within the column. During heating, a heat loss due to evaporation might influence the gradient.

4.4.4. pH measurements.

Regarding the development of pH (Fig. 4.17) within the columns, a partial relationship of capillary transport related to the drying process can be seen showing a decrease in pH in these zones (the lower values ~6.2 at the lower depths of columns 5 and 6 are regarded to be small variations as the changes between the upper and lower parts are in the range of 0.2, or may be related to an error regarding the wide sampling rates). This is in concordance with the observations of Redwan and Rammlmair (2010), where the upward movement of ions in their experiments was accompanied by a slight decrease in pH. This relationship might be disturbed due to preferential flow or preferential retention of fluids at various raining steps. Local relationship is also found to electrical/fluid conductivity. Temperature and oxygen are not obviously influencing the pH. The pH of the extracted fluids using Rhizon soil water samplers was within the range of 5.9-7.03, whereas using the final paste-water extraction it was within the range of 6.2 - 6.7 corresponding quite well to the

pH optical monitoring (see Fig. 4.17). The reason for the difference in pH values for the paste-water extraction and extracted fluids using Rhizon soil water samplers, is that access to mobile water (about 40 to 50%) is achieved by means of Rhizon extraction, but all water is mobilized and mixed up during paste extraction. Paste extraction values better correspond to pH-optical monitoring. During raining, the pH equilibrated due to the high buffering capacity of the material and become higher to some extent at the top surface than samples at lower depths, probably due to flushing down low pH waters, whereas during drying the upper part get lower pH values (Table. 4.2). However, the small pH differences between the upper oxidized part and the lower reduced part are mainly due to the buffering capacity of the carbonates.

Taking all 6 columns into account, two trends namely for elevated (columns 1, 3, and 5) and reduced (columns 2, 4, and 6) water amounts for the different temperature levels 60°C, 45°C, and 30°C, for column pairs respectively, can be identified showing characteristic features in electrical and fluid conductivity, water content, level of oxygen infiltration as well as pH, showing remarkable changes of their overall conditions due to raining cycles.

4.4.5. Efflorescence sulfates composition.

In the first 10 days of running the experiments, on the top surface layer a well defined efflorescence of sulfates developed. These sulfates are rich in metals like Fe, Mg, As, Mn and Zn, as identified using SEM and XRD, due to sulfide oxidations (mainly As-pyrite, arsenopyrite and pyrite in these tailings). The growth of this efflorescence continued with increasing evaporation in the columns 1 and 2, was small in columns 3 and 4, but was not observed in columns 5 and 6. During the raining events, all the sulfates at the top surface dissolved and moved downwards. According to Fitzpatrick et al. (2005) sulfate minerals act as a storage for Fe, Mg, SO_4^{2-} , Pb, Zn, Cr and As, in addition to some rare earth elements like La and Ce and can easily release significant amounts of it to the draining water upon dissolution. During repeated raining/drying cycles, the efflorescence decreased in the columns 1 and 2, and increased in columns from 3 to 6. Crusts developed first in the columns 1 and 2, then followed by 3 and 4 and finally in 5 and 6 (Fig.4.18). The loss of efflorescence in columns 1 and 2 might be an indicator of that the first amount of water added during the raining event took the efflorescent sulfates downward followed by water almost free of soluble sulfates. This late water in the course of a rapid evaporation process evaporates first. Due to the very high temperatures (60°C) capillaries might disrupt leaving the efflorescence sulfates

dissolved in the early water to precipitate at some depths below the surface due to the downward movement of the evaporation head. However, the resistance against rapid dissolution of the crusts is different for all the columns. Columns with high temperature -high water had more stable crusts than columns with high temperature-low water. Furthermore, the crusts developed in low temperature columns are more easily soluble in water compared to high temperature columns (Figs. 4.18 and 4.19). It seems that the more soluble efflorescent sulfates become more resistant to dissolution with time. Possibly, they are replaced by more stable secondary phases or the advanced degree of agglutination reduced the accessibility to the more soluble phases. From investigations based on ESEM and XRD, the crusts are mainly composed of Mg-sulfates and gypsum showing variable crystal shapes and grain sizes. The first crusts accumulated on the top of columns one are mainly composed of hexahydrate ($\text{MgSO}_4 \cdot 6\text{H}_2\text{O}$) and bassanite ($\text{CaSO}_4 \cdot 0.5\text{H}_2\text{O}$). The first crusts accumulated on top of column 3 are composed of gypsum, starkeyite ($\text{MgSO}_4 \cdot 4\text{H}_2\text{O}$) and goethite ($\text{FeO}(\text{OH})$). Mg-sulfates showed a completely different appearance at different temperatures. For example, at 45°C it appeared as a sponge-like porous network, whereas at 60°C it looks more compact (Fig.4.19). Both the rounded-edges and sponge-like appearances are related either to continuing capillary transport re-dissolving the grains, or to dissolution due to the changing humidity in the room. The area percentage of gypsum crystals as well as its grain size increased in columns with lower water contents and decreasing temperatures. It showed different shapes ranging from very long laths, especially in column number 3 which almost filled the top surface of the column, to more compacted plates, especially in column 4 and to a lesser extent in column 6 (Fig.4.19). Looking to the lower surface of these crusts (Fig. 4.20), a nice crystallization of some secondary phases can be recognized. Columns 1 and 3 showed a more compact appearance with less pores compared to other columns. Secondary phases contain Fe, Zn and As in crystals. Columns 2-4 appeared to be more porous with agglutination mainly by gypsum and to a lesser amount in columns 5 (also Fe-hydroxide) and 6. The main source of Fe, Zn and As is from sulfide oxidation. Either in situ fixation within secondary precipitates at the source due to the high degree of oxidation or more likely capillary transport under reduced conditions as Fe^{2+} and As^{3+} or as colloids in the initial evaporation stage of the saturated columns and subsequent fixation in secondary phases at the evaporation front. Moreover, enrichment of Fe in the oxidation zone may be related to the formation of Fe(III) hydroxides which is stable under these conditions (Sima et al., 2011). Also, the mobility

of Fe under high pH can be increased in cases of formation of Fe-organometallic complexes (Boxma, 1976).

4.4.6. Pore-water extractions.

From the pore-water extractions during raining and drying events with Rhizon soil water samplers (Table 4.2), it was shown that during raining and drying events mainly Mn, Cu, Sr and As were enriched in the upper surface layer in all the columns. Fe showed enrichment during drying in the upper surface and at some depths below the surface during raining (Table 4.2). Mg and S showed the same trends of decreasing concentrations in columns 1, 3, and 6 during both events, and during drying in column 2, and enrichment in columns 4 and 5 in both events. Ca showed enrichment in both events in columns 1, 2, 3, 4 (except during drying in column 3) and decreased concentrations in columns 5 and 6 (Table 4.2). It has to be taken into account, that each extraction of a volume of water changes the overall distribution of saturation and chemistry. Additionally, the fluid extracted at a Rhizon position is not characteristic for the whole fluid of the zone, but for the mobilizable part only. The next extraction will take a fluid stripped by the amount extracted before and eventually much slower water of different ion affinity. Nevertheless a strong enrichment of most elements in all column settings was recorded.

4.4.7. Paste-water extractions and solid samples analysis.

From the water paste-extraction analysis, it is shown that the SO_4^{2-} and Mg were both higher in the upper surface layers in all columns and increased in the order from column one to six (except column 2) and showed a positive correlation with the fluid conductivity. Furthermore, most of the elements like Na, K, Mn (increasing in the order from column six to one), Br, Sr, Zn, As, Cu, Cd and Pb show enrichment in the top crusts. Fe showed enrichment at some depth below the surface (-5 to -12cm). The attenuation of elements in the crusts is possibly explained due to incorporation into the structure of secondary sulfate minerals (Hammarstrom et al., 2005; Carmona et al., 2009). Ca in the paste-extraction analysis on the other hand showed a decreased concentration on the top surface crusts compared to the lower parts (increasing in the order from column six to one). This may be due to the stability of Ca-sulfates (gypsum) during the normal extraction method (Fig. 4.21- 4.22, Table 4.3). Hot spots of concentrations of Fe and Pb can be recognized at -5 to -10 cm from the surface in columns 1 and 3, and to a lesser concentration in column two, which may enhance the possibility of incipient cemented layer formation. The XRF analysis (Fig. 4.21) showed a high enrichment of

Fe₂O₃, Ni, As, Zn, Co, and Cu at some depths below the oxidized surface (below -2.5cm) for columns 1, 3 and 5, in contrast to medium enrichments for columns 2, 4 and 6. Whereas SO₃, CaO, MgO and Na₂O showed enrichment in all the columns on the upper surface. This reflects the transport behaviour of mobile ions (e.g. SO₄²⁻, Ca²⁺, Na⁺, Mg²⁺), and relatively stationary compounds (e.g. colloids of Al, Si, Fe, As) in a fluid.

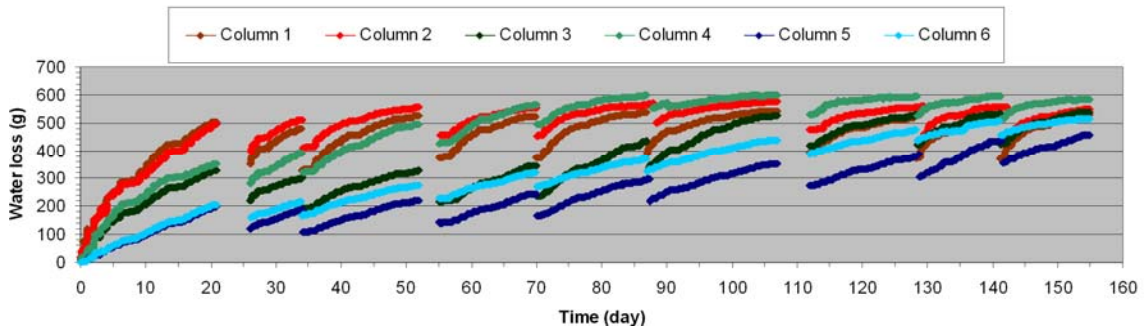


Fig. 4.8. Changes of water evaporation rate with time from the different columns during raining/evaporation cycles.

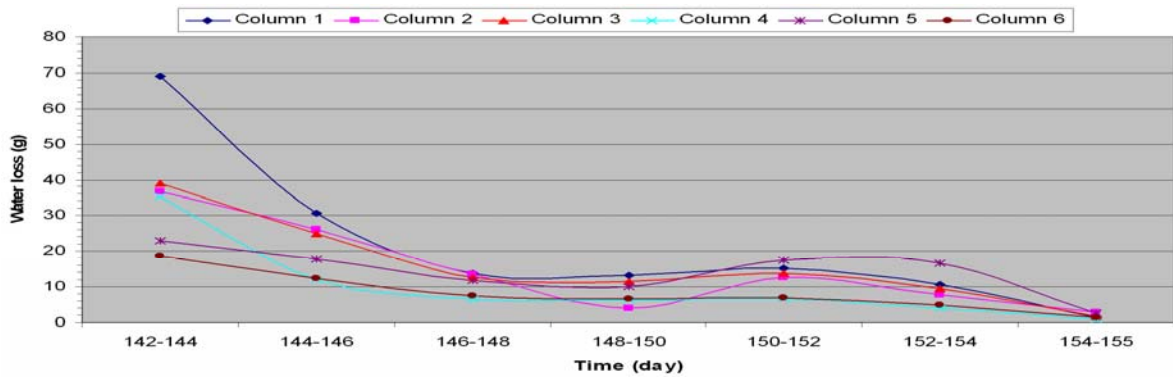


Fig. 4.9 . Changes of water evaporation rate during the last evaporation cycle.

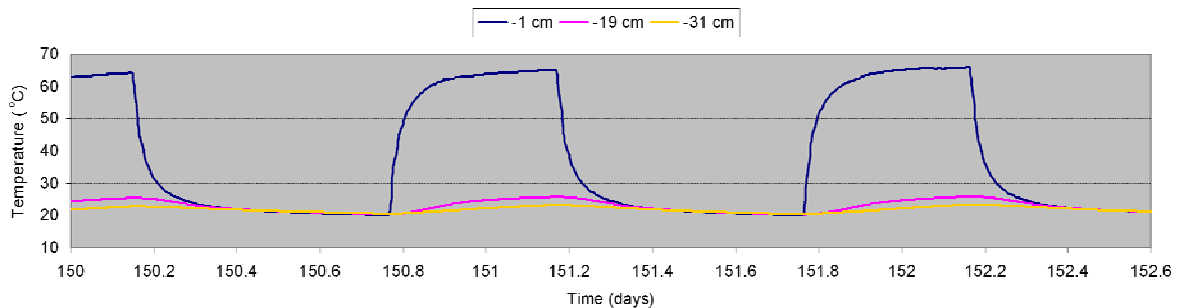


Fig. 4.10 . Thermal gradient of temperature within column 1 at different depth levels.

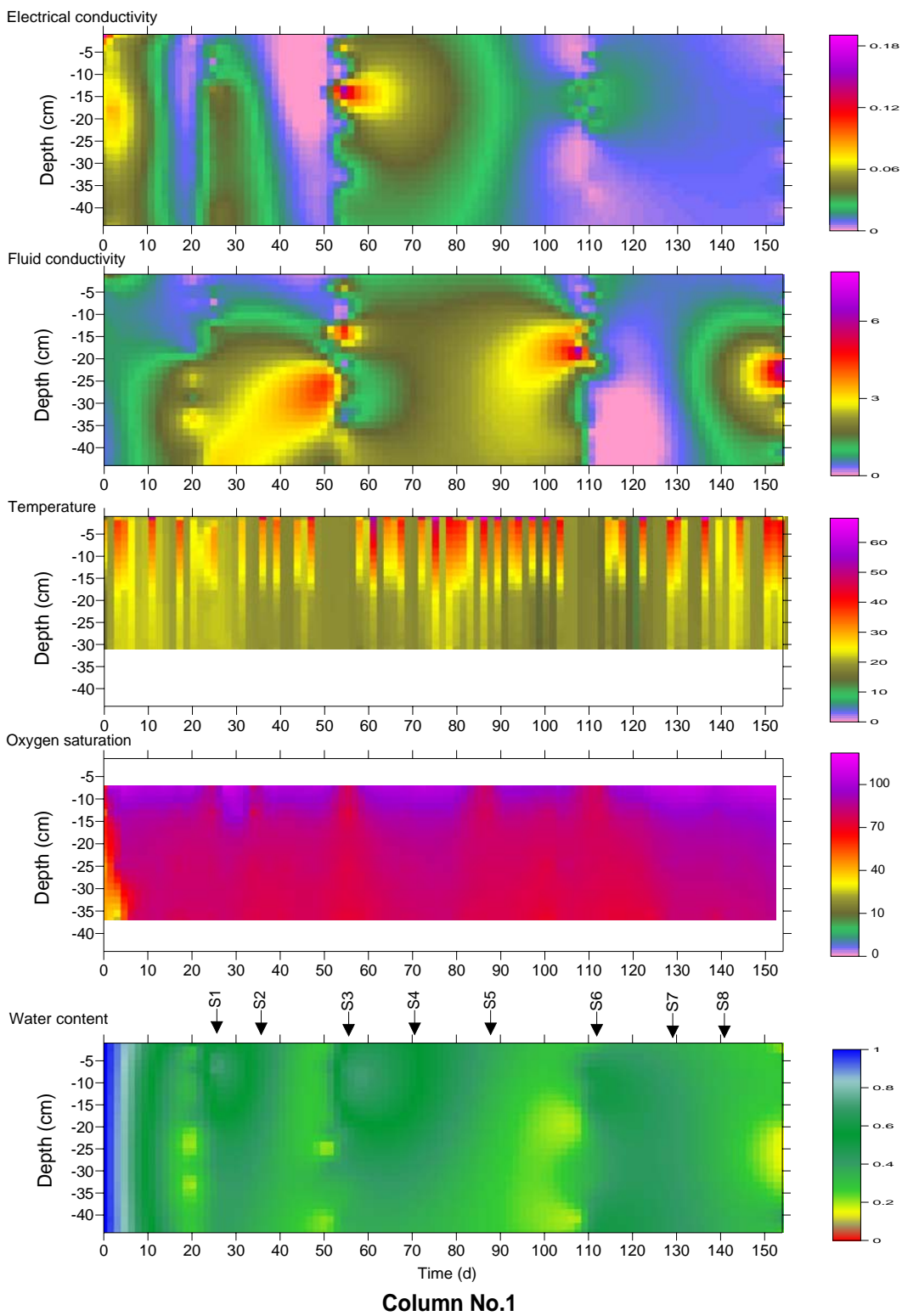


Fig. 4.11. Changes of Electrical and fluid conductivities (S m^{-1}), temperature ($^{\circ}\text{C}$), oxygen (%) and water (S_w) saturations with time in column 1.

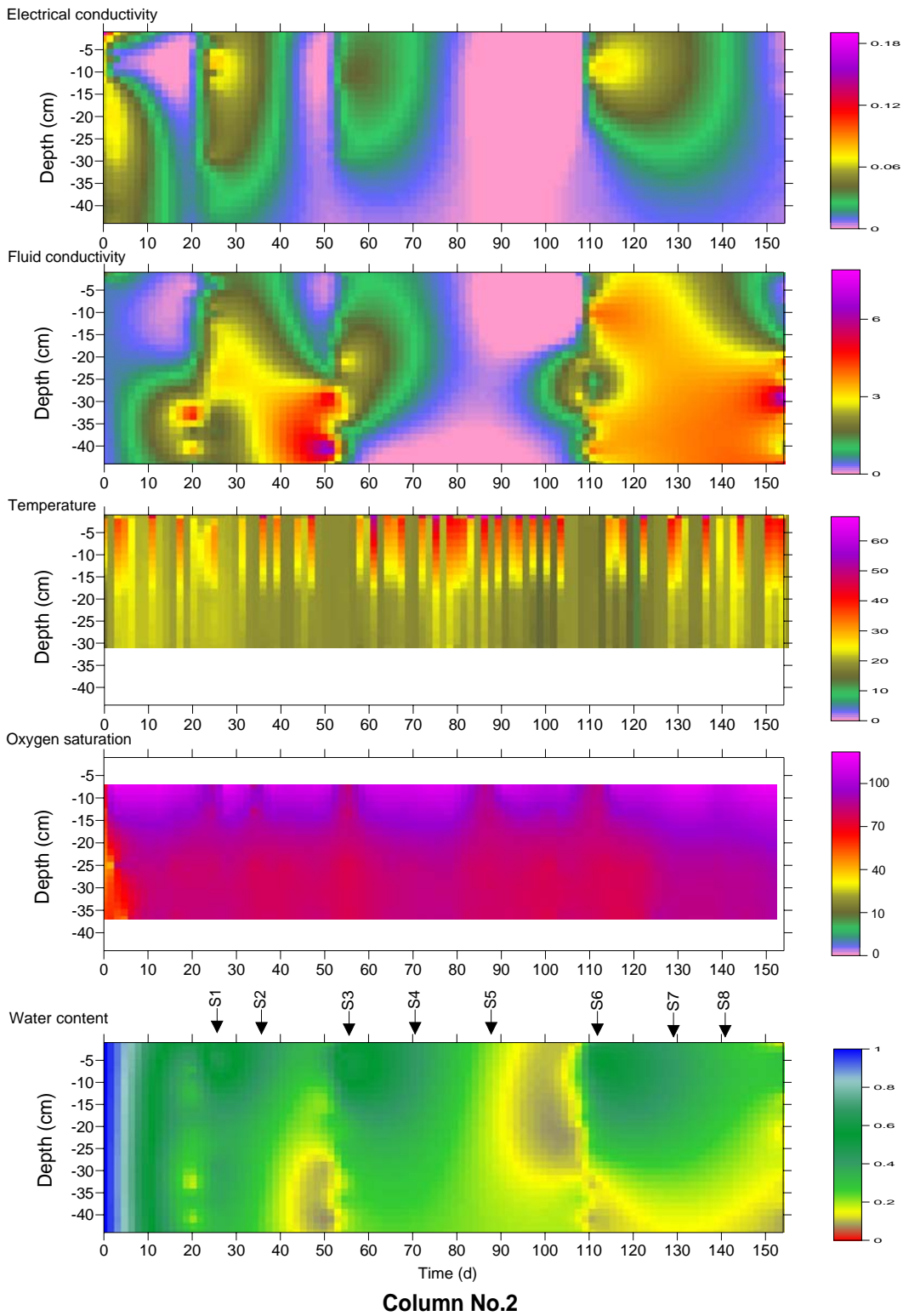


Fig. 4.12. Changes of Electrical and fluid conductivities (S m^{-1}), temperature ($^{\circ}\text{C}$), oxygen (%) and water (S_w) saturations with time in column 2.

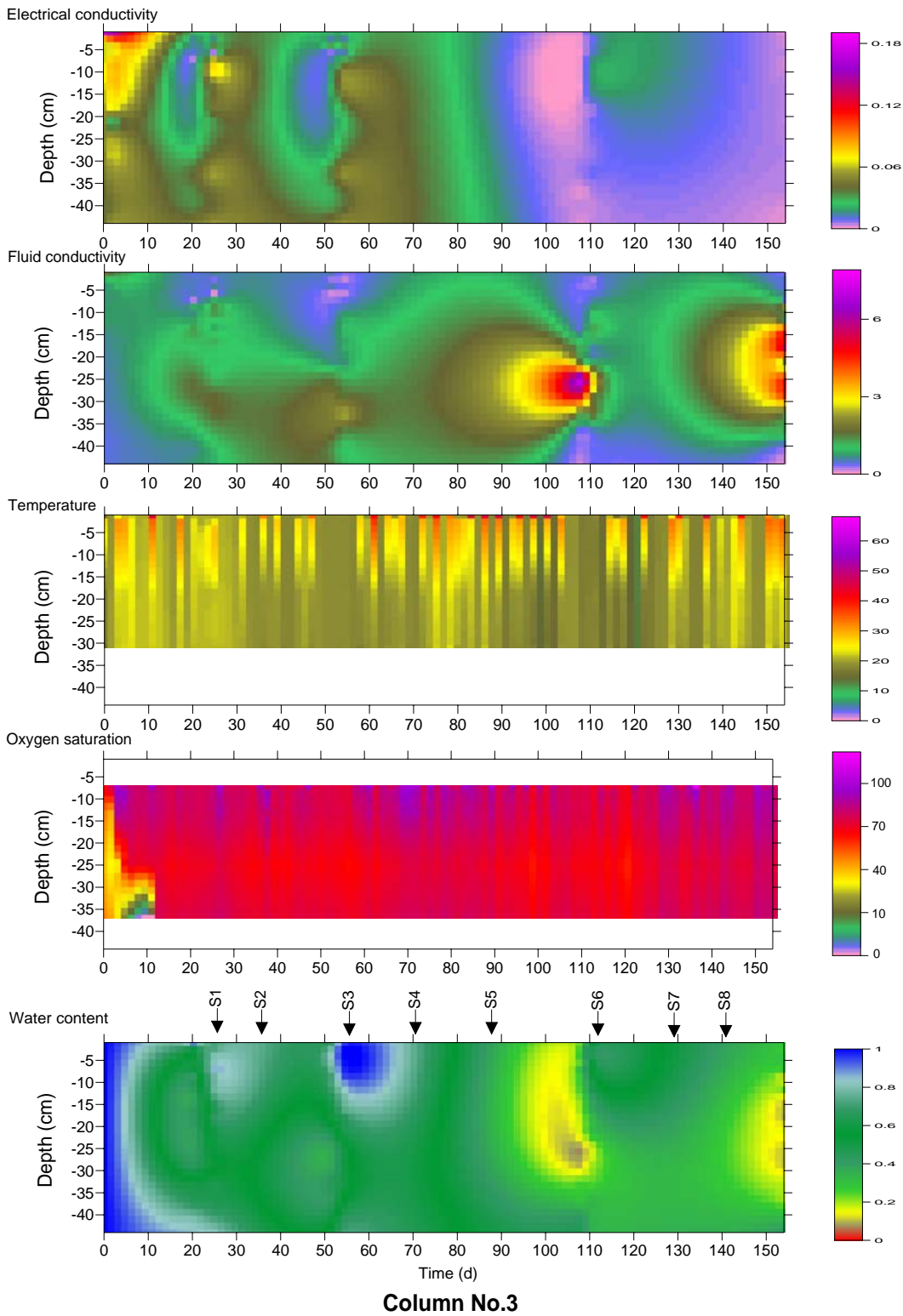


Fig. 4.13. Changes of Electrical and fluid conductivities (S m^{-1}), temperature ($^{\circ}\text{C}$), oxygen (%) and water (S_w) saturations with time in column 3.

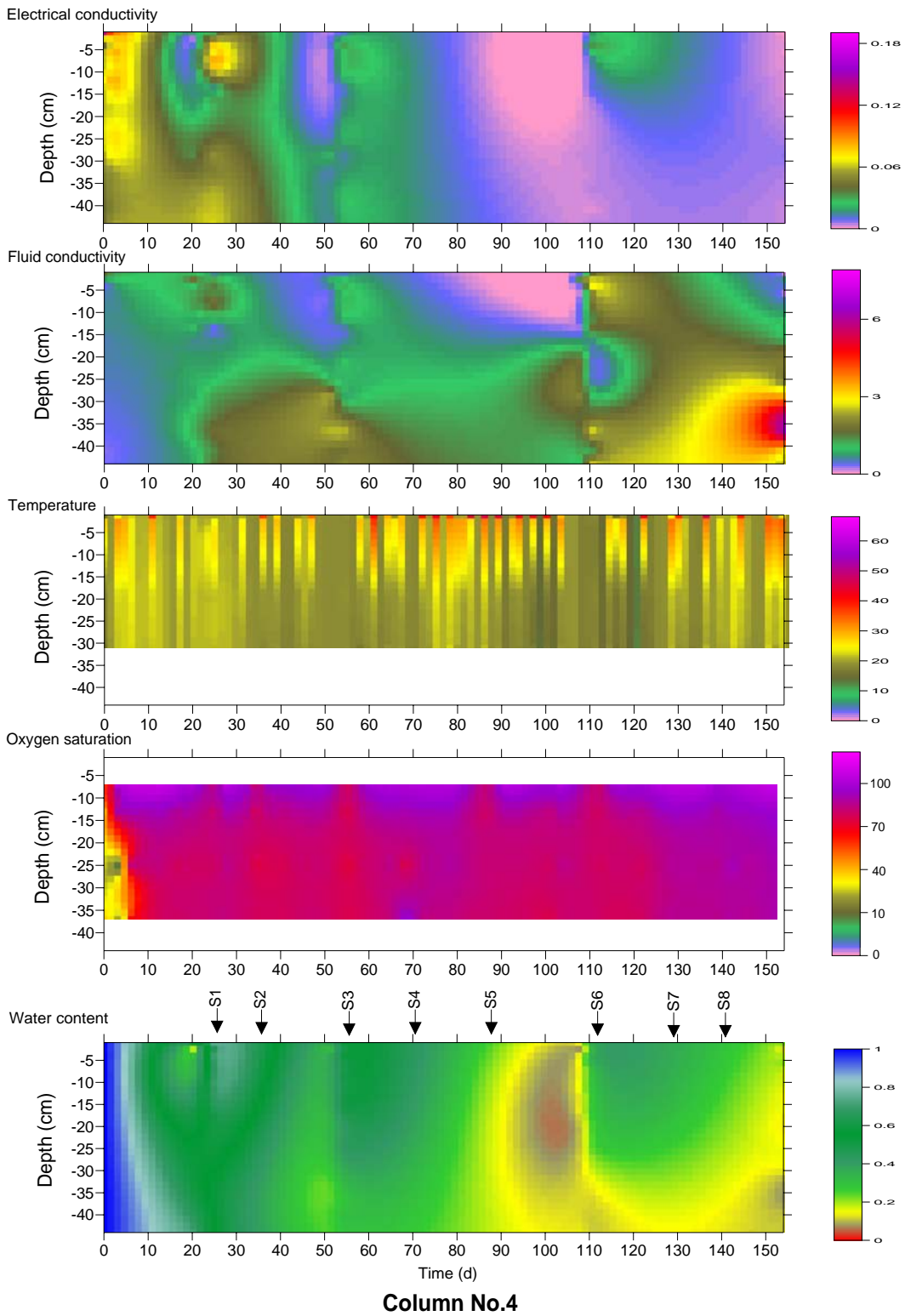


Fig. 4.14. Changes of Electrical and fluid conductivities (S m^{-1}), temperature ($^{\circ}\text{C}$), oxygen (%) and water (S_w) saturations with time in column 4.

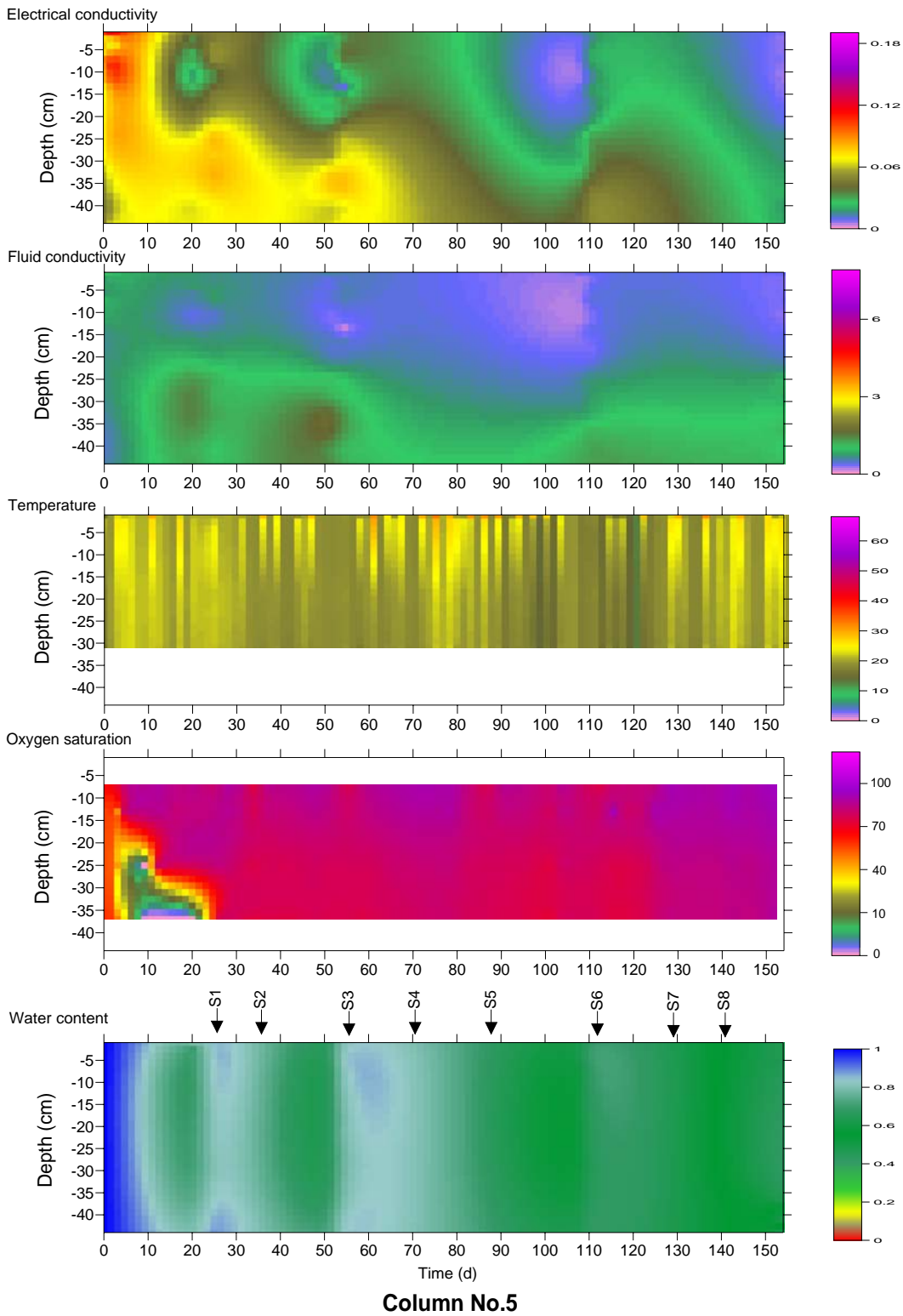


Fig. 4.15. Changes of Electrical and fluid conductivities (S m^{-1}), temperature ($^{\circ}\text{C}$), oxygen (%) and water (S_w) saturations with time in column 5.

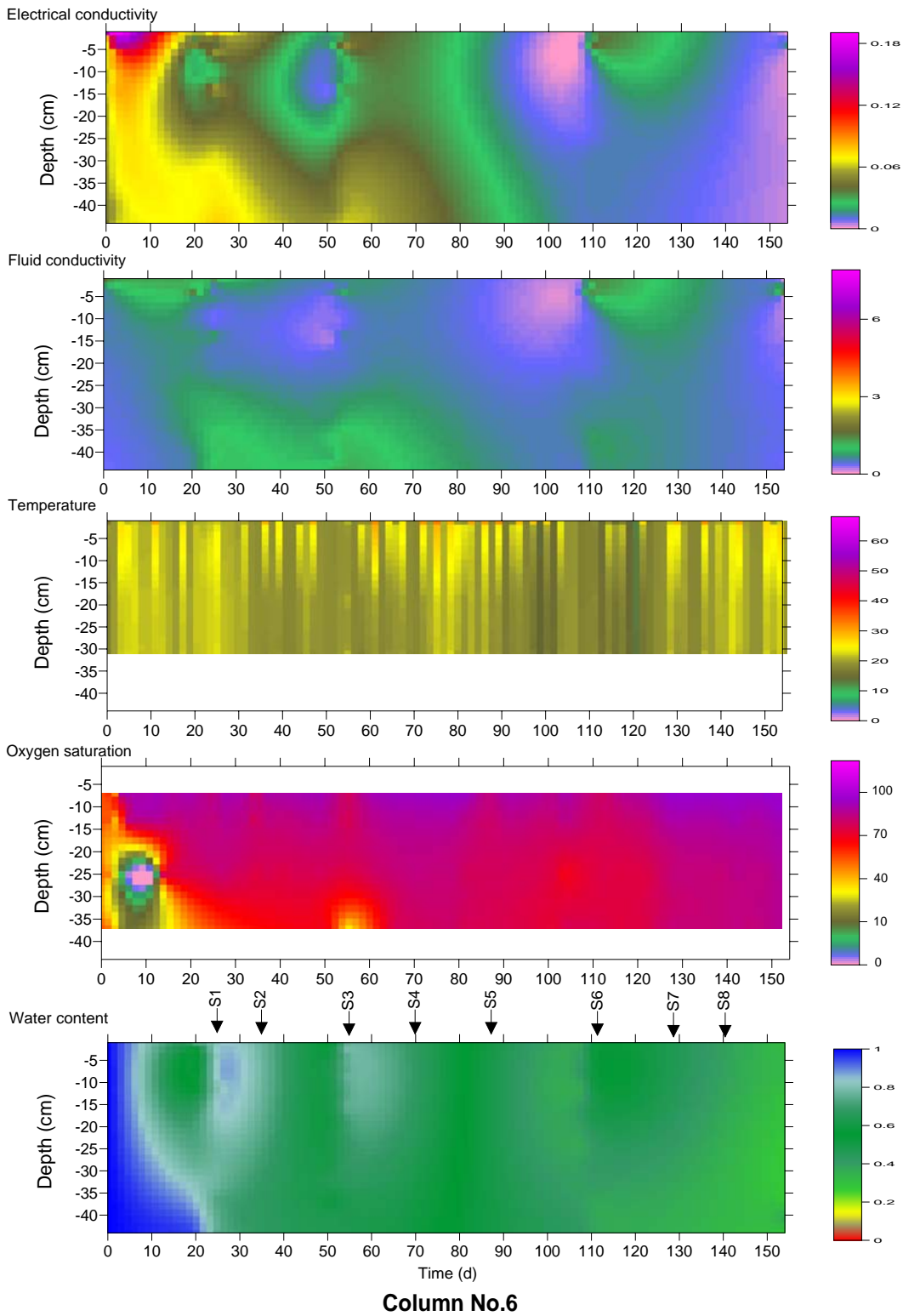


Fig. 4.16. Changes of Electrical and fluid conductivities (S m^{-1}), temperature ($^{\circ}\text{C}$), oxygen (%) and water (S_w) saturations with time in column 6.

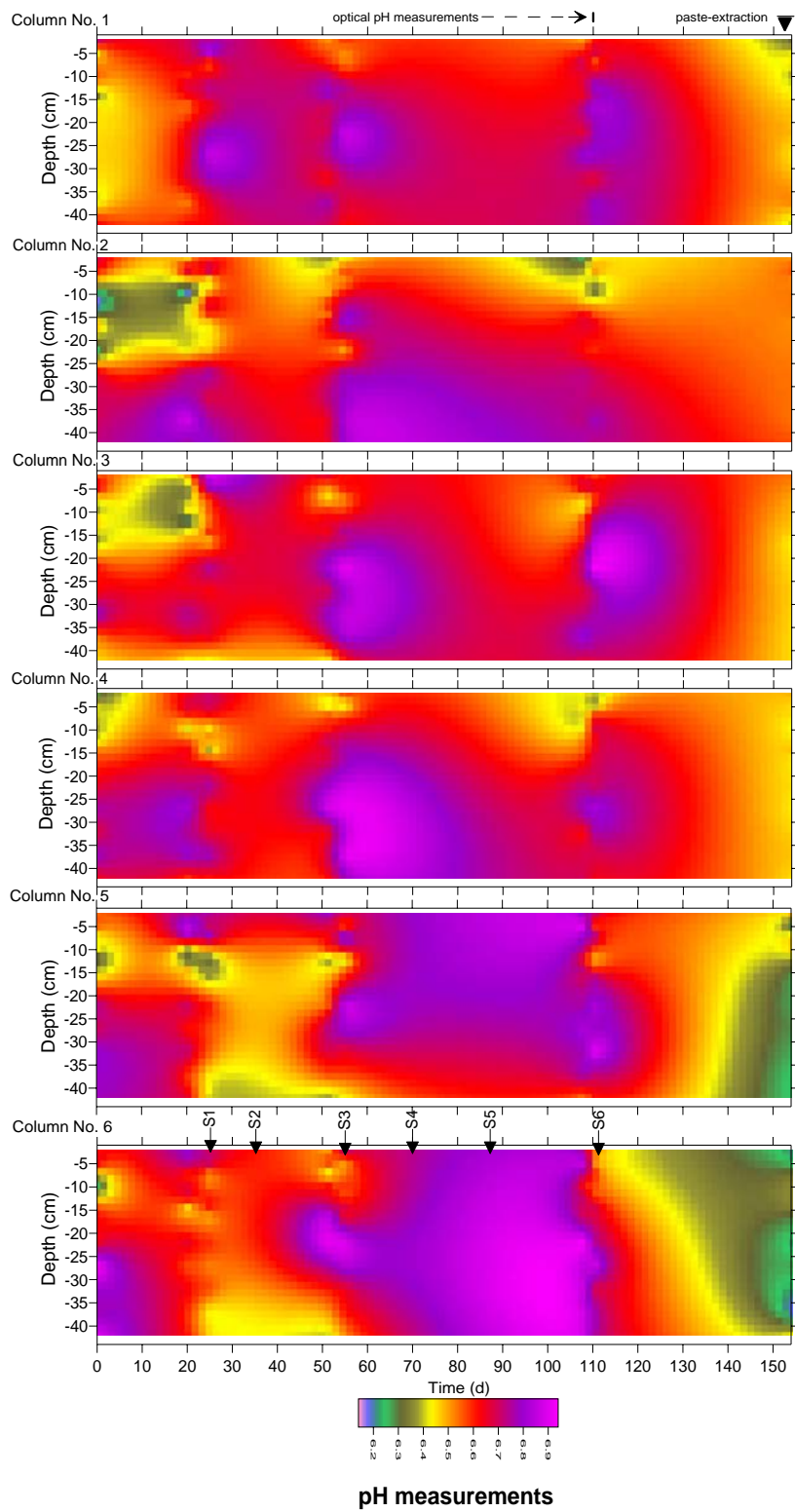


Fig. 4.17. Depth profiles showing variations of optical pH measurements with time.

Chapter 4: Effect of temperature and water content on hardpan formation in mine tailings: column experiments



Fig. 4.18. Time series of efflorescence on column tops.

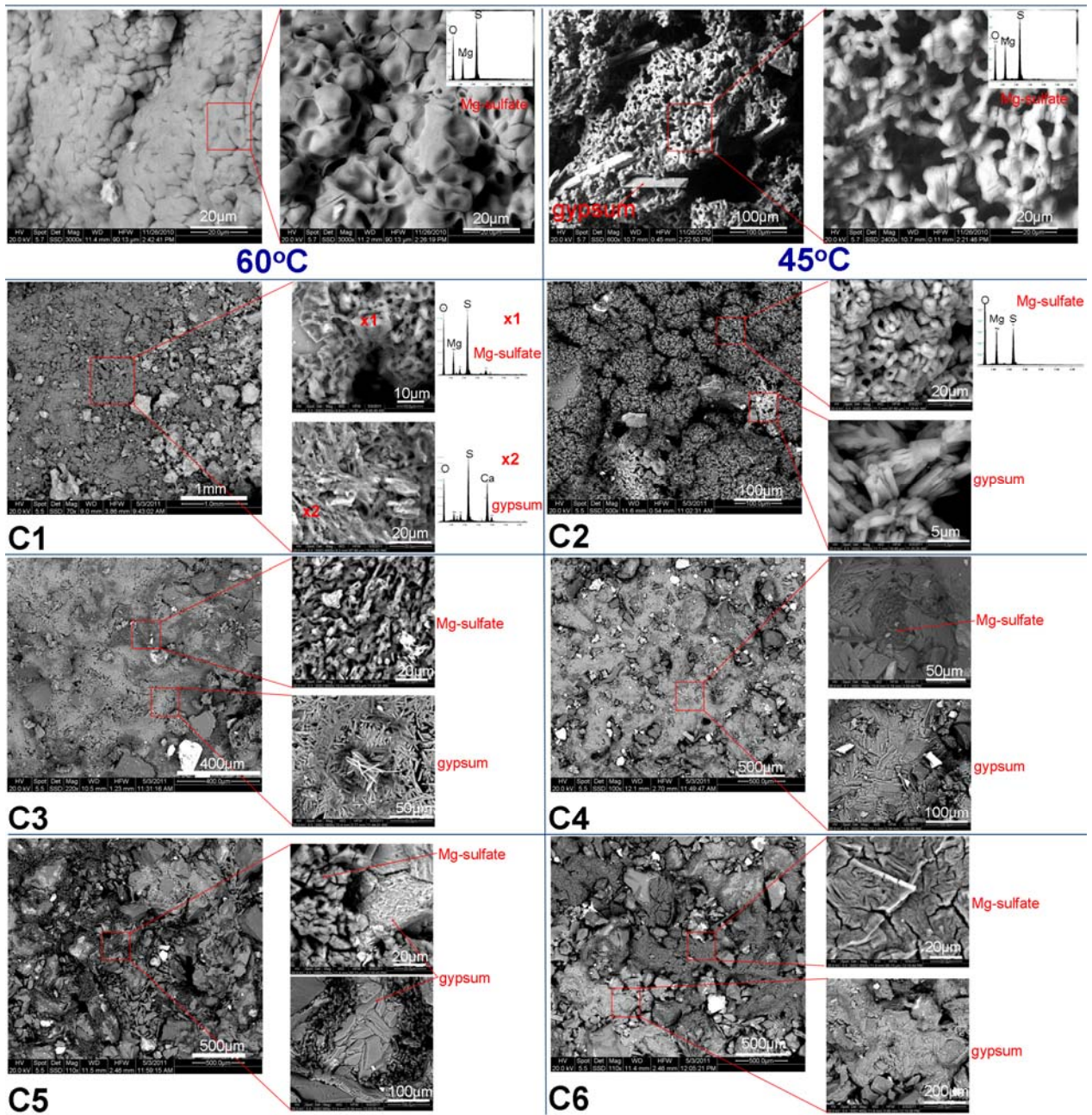


Fig. 4.19. Figure showing the composition of the crust developed on the first stage at 60 °C and 45 °C and at the last stage on columns from one (C1) to six (C6).

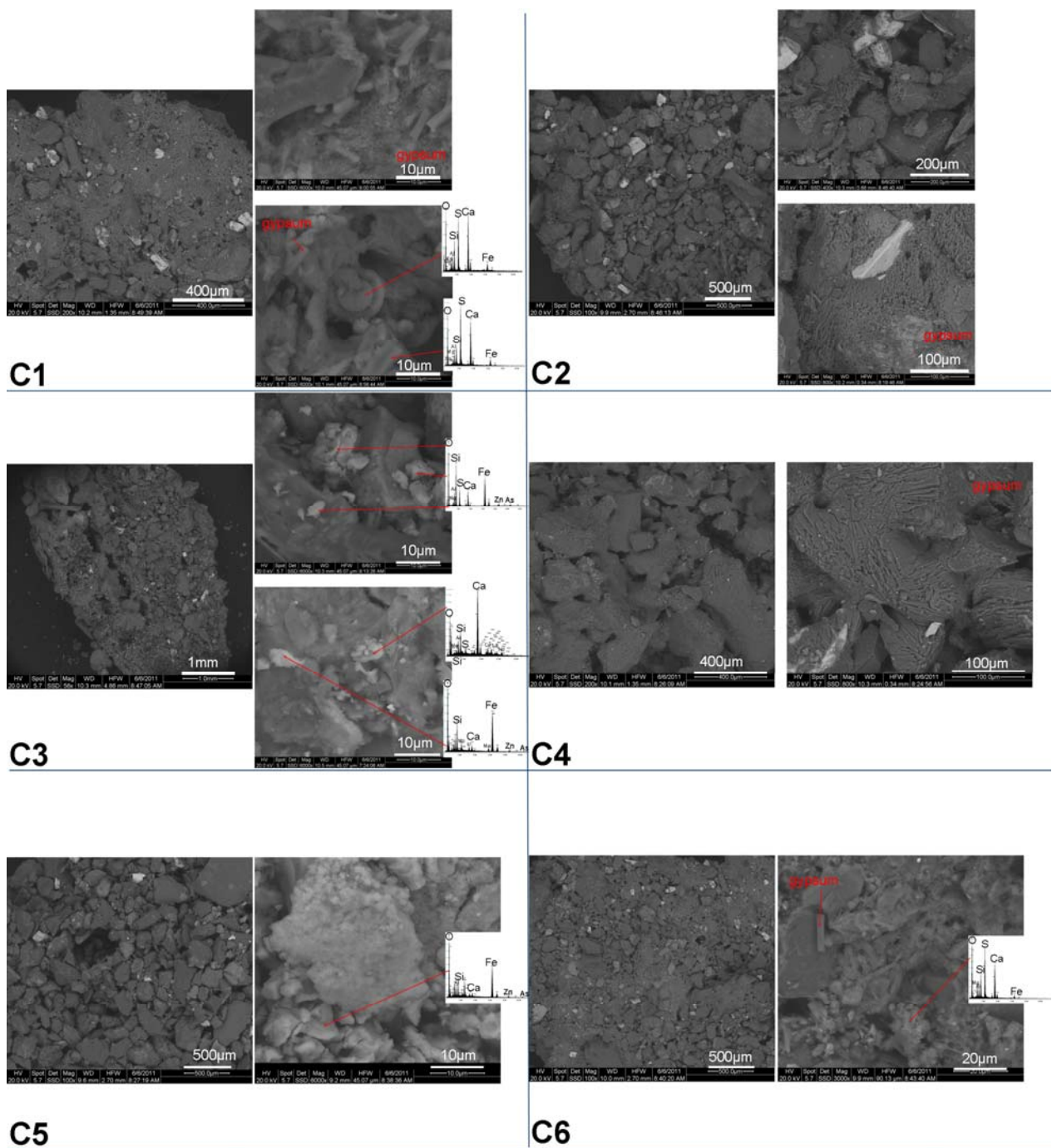


Fig. 4.20. Figure showing the composition of the crust developed on its lower surface at the last stage on columns from one (C1) to six (C6).

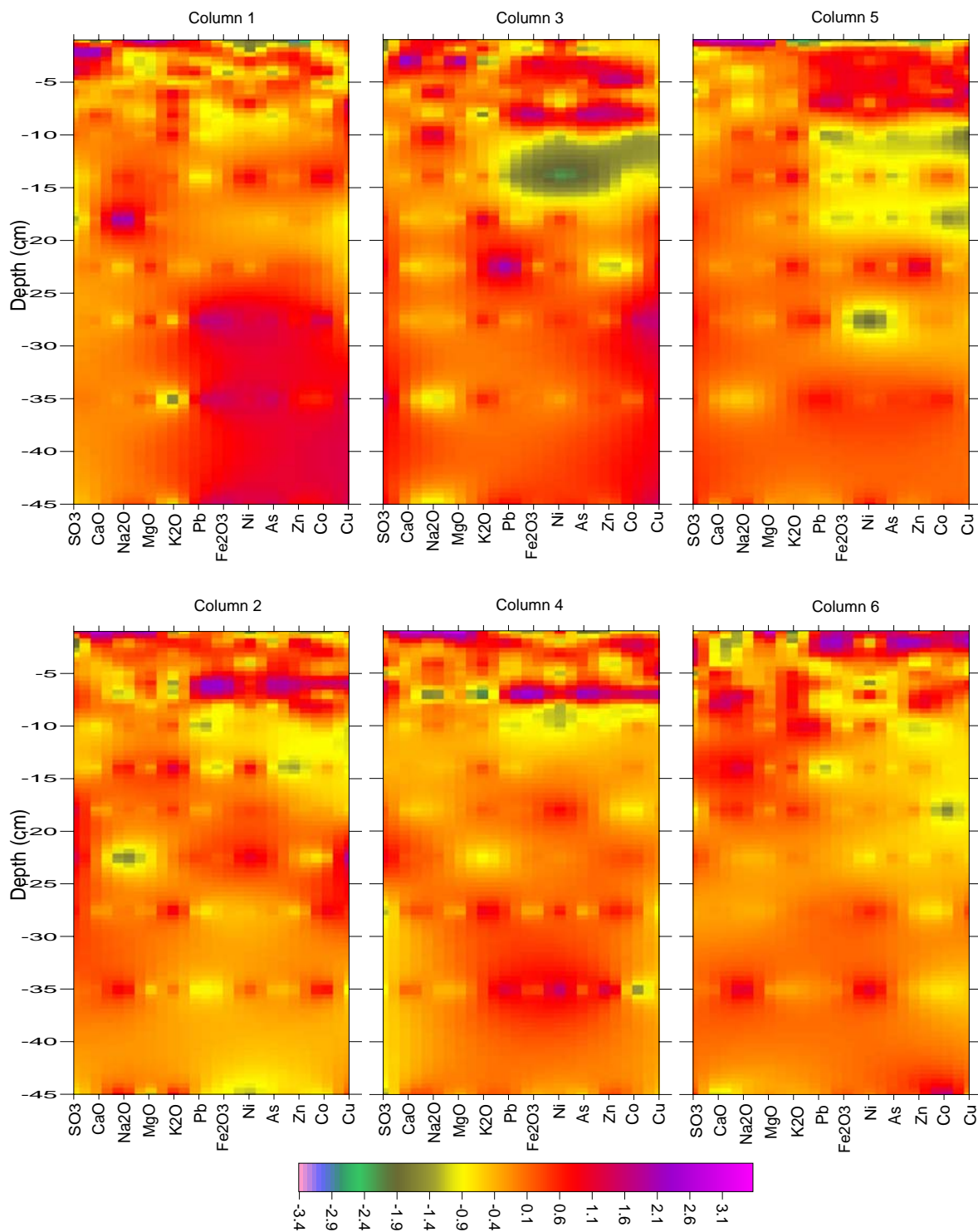


Fig. 4.21. Depth profiles showing the normalized (value-mean/standard deviation) chemical properties of the solid samples.

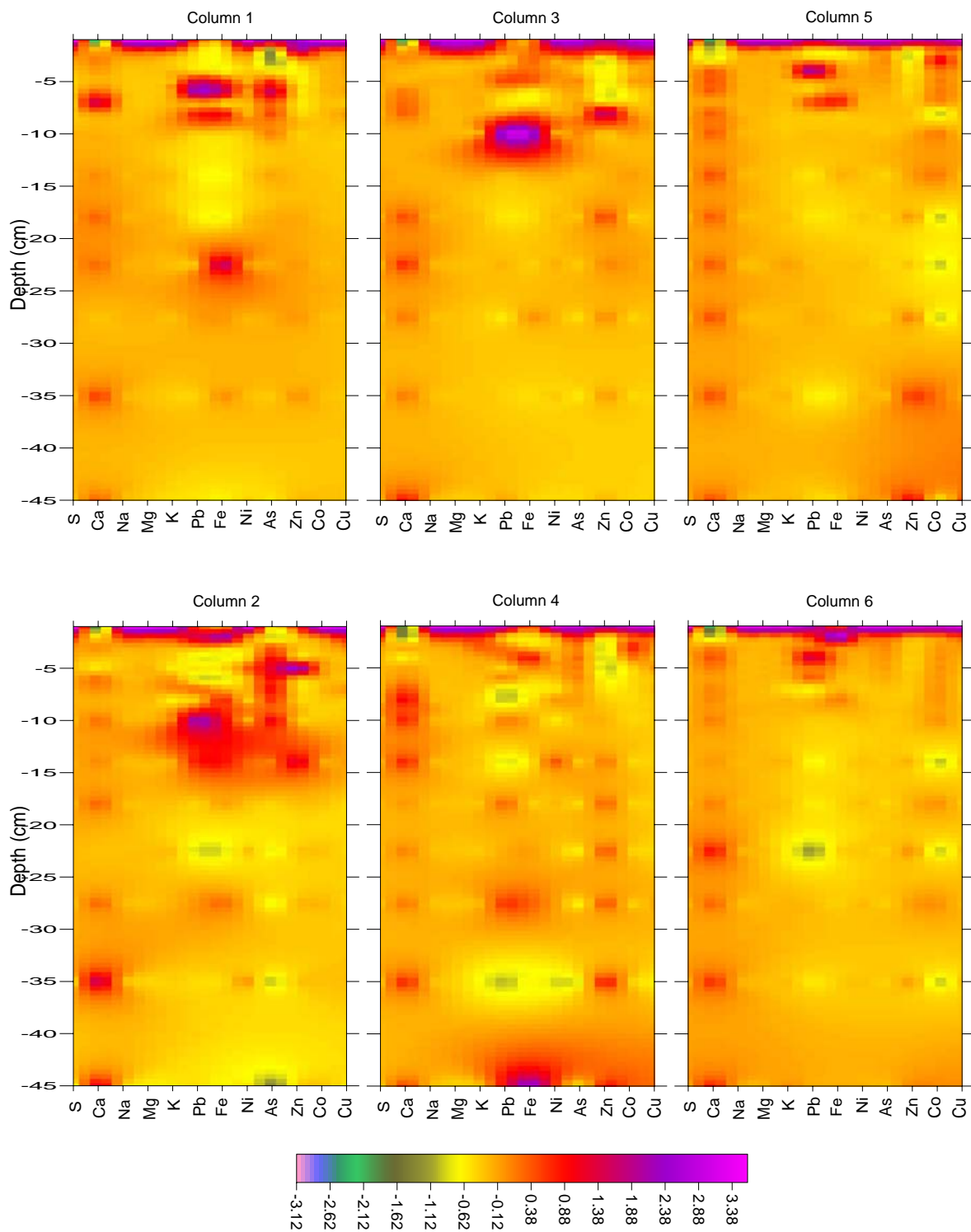


Fig. 4.22. Depth profiles showing the normalized (value-mean/standard deviation) chemical properties of the paste-water extraction.

4.5. Conclusions

A new multi parameter approach for simultaneous monitoring of the evolution of electrical/fluid conductivities, water saturation/evaporation, pH, temperature, and oxygen saturation, for column experiments was tested. Six columns filled with tailings material from Freiberg were monitored in order to investigate its behavior as a function of climatologic conditions. General similarities between columns with a high amount of raining and those with a low amount can be deduced. The oxygen concentration depends only on water saturation and the applied temperature. Infiltration was observed for columns with lower water content, and higher temperature. The electrical/fluid conductivity depends on the evaporation rate and the water contents within the columns. With continuous drying, the water at the upper surface layers evaporates and the measurements reach zero values, whereas the lower parts become enriched with ions and get higher conductivities. During raining, the efflorescent sulfates become soluble and result in higher conductivities compared to the lower parts. Only small pH changes of the water (6-7) were observed with time using optical monitoring and pore-water extractions. The duration of the experiments were probably too short to lead to a significant production of Acid Mine Drainage due to sulfide oxidation. As a result of continuous evaporation from the top surface of the columns, sulfates were brought to the column surface by capillary up-flow and mass transport processes which produced a crust. This crust showed an enrichment in the elements Mg, S, Na, K, Mn, Sr, Zn, As, Cu, Cd, and Pb. This crust also reduced the evaporation rate for the columns, but due to its instability, at the first contact with water, it was almost entirely redissolved. Therefore, removing or harvesting these sulfates crusts enriched in toxic elements during dry seasons, could be an important task in areas where tailings are located near the rivers to reduce the subsequent environmental impact. The predominance of Ca and Mg sulfate phases on the top surface relate to the elevated amount of carbonate minerals, especially dolomite, in the original tailings material used for filling the columns. The stability of the crusts with higher spreading of gypsum crystals combined with Fe-hydroxide may be due to its low solubility during raining events (Dold, 2003; Hammarstrom et al., 2005), and an enhanced grain size, due to slower growth at ambient temperatures. The development of hard crusts capable of reducing porosity, decreasing water infiltration and erosion requires that, reactive compounds such as water, oxygen, reactive phases, and eventually microbial assistance and enough time is available for reaction of these low sulfide tailings. This will lead to partly dissolve, transport, supersaturate the pregnant solution and finally to precipitate the secondary phases. Some of these phases will be

stable enough to partially survive raining events and eventually will grow and agglutinate larger zones. Continuous monitoring using this multidisciplinary experimental approach gave a good explanation of the element mobility during raining/drying cycles in combination to the amount of water added, changes of the electrical/fluid conductivities in relation to ion concentration with time, in addition to, oxygen and temperature infiltrations within the tailings which control the oxidation/precipitation reactions. It is recommended to monitor column experiments with tailings material of low sulfide content for a prolonged running time or to increase the sulfide content to enhance the oxidation process that way. It will further be necessary to run experiments on laminated tailings, containing carbonate-rich and sulfide-rich lamina for enhancement of in situ hardpan/cemented layers formation to better compare to field observations. Multi parameter monitoring is the key to understand processes of dissolution, transport and precipitation. Since strong gradients are the characteristics of the critical zone, a much more detailed continuous, densely spaced monitoring and evaluation concept is required to better understand the behavior and interaction of individual parameters in homogeneous or inhomogeneous, layered tailings system, and to highlight their contribution to the formation of hardpan layers and eventually contributing to Acid Rock Drainage.

Chapter 4: Effect of temperature and water content on hardpan formation in mine tailings: column experiments

sample name	C1-x1-1	C1-x1-2	C1-x1-3	C1-x1-4	C2-x1-1	C2-x1-2	C2-x1-3	C2-x1-4	C3-x1-1	C3-x1-2	C3-x1-3	C3-x1-4	C4-x1-1	C4-x1-2	C4-x1-3	C4-x1-4	C5-x1-1	C5-x1-2	C5-x1-3	C5-x1-4	C6-x1-1	C6-x1-2	C6-x1-3	C6-x1-4
pH	7.03	6.84	6.57	6.67	6.62	6.47	6.58	6.62	6.75	6.56	6.49	6.13	6.45	6.38	6.4	6.45	6.28	6.29	6.3	6.27	6.28	6.39	6.34	6.21
conductivity (S/m)	0.0661	0.238	0.276	0.25	0.238	0.818	0.0276	0.438	0.222	0.283	0.39	0.206	0.0001	0.0123	4E-05		1.557	0.431	0.303	0.33		0.272		0.298
redox (mv)	137	140	144	153	144	148	152	155	175	173	167	195	133	156	167	198	135	171	200	204	162	188	199	209
Al (mg L-1)**	0.63	0.63	0.63	0.63	0.63	0.63	0.63	0.63	0.63	0.63	0.63	0.63	0.63	0.63	0.63	0.63	0.63	0.63	0.63	0.63	0.63	0.63	0.63	0.63
Ca (mg L-1)**	604	568	583	549	530	519	480	556	561	503	544	575	514	506	504	534.24	508	545	538	560	492	522		564
Fe (mg L-1)**	0.175	0.033	0.312	0.093	0.008	0.042	0.038	0.023	0.031	0.01	0.006	0.006	0.026	0.014	0.022	0.0286	0.003	0.003	0.006	0.003	0.17	0.024		0.014
K (mg L-1)**	40	20.2	12	11.88	26.5	13.1	14.92	7.89	16.8	19.2	8.39	6.63	70.6	13.34	8.16	5.565	40.7	8.43	7.66	7.24	14.2	9.26		6.14
Mg (mg L-1)**	150	838	649	88.4	1720	1380	403	846	658	837	659	181	4350	928	387	57.3	3760	457	333	225	232	374		177
Na (mg L-1)**	29	64.2	38.7	6.81	74	43.7	13.1	26.2	57.1	57.7	28.7	6.17	100	26	10.7	1.15	129	12	5.53	5.06	4.76	5.26		2.31
S (mg L-1)**	695	1440	1180	278	2590	2150	684	1540	1360	1560	1320	728	5780	1460	7210	212	5150	1060	890	784	381	953		736
Zn(mg L-1)**	1.03	0.542	0.738	0.723	0.49	0.791	0.89	0.953	0.435	0.775	0.836	0.753	1.982	0.962	0.844	0.566	1.73	0.676	0.773	1.14	0.65	0.563		0.717
As(mg L-1)**	0.0671	0.106	0.101	0.0882	0.171	0.123	0.0962	0.0977	0.145	0.123	0.106	0.0767	0.464	0.127	0.084	0.0671	0.184	0.0854	0.079	0.0713	0.1125	0.068		0.0751
Ba(mg L-1)***	0.0146	0.053	0.0152	0.0215	0.0169	0.0143	0.0468	0.0133	0.0144	0.0126	0.0118	0.0117	0.024	0.0148	0.0138	0.0531	0.0138	0.0101	0.0106	0.0112	0.116	0.0123		0.0127
Cd(mg L-1)***	0.0293	0.0175	0.0201	0.02	0.016	0.018	0.0258	0.0199	0.0111	0.0152	0.0157	0.0133	0.0514	0.0176	0.0181	0.0131	0.0288	0.0124	0.0145	0.019	0.0168	0.0117		0.0157
Co(mg L-1)***	0.003	0.0001	0.0001	0.0003	0.0003	0.0001	0.0001	0.0002	0.0003	0.0002	0.0002	0.0001	0.0014	0.0001	0.0002	0.0002	0.0003	0.0001	0.0001	0.0001	0.0003	0.0001		0.0001
Cr(mg L-1)***	0.0003	0.0003	0.0005	0.0014	0.0002	0.0002	0.0007	0.0004	0.0002	0.0001	0.0002	0.0002	0.0006	0.0004	0.0005	0.0009	0.0002	0.0002	0.0002	0.0001	0.0014	0.0002		0.0001
Cs(mg L-1)***	0.0033	0.0078	0.0058	0.0065	0.0076	0.0069	0.0051	0.005	0.0038	0.0054	0.0054	0.0045	0.017	0.0049	0.0036	0.0033	0.0082	0.0034	0.0038	0.0037	0.0048	0.0031		0.0034
Cu(mg L-1)***	0.0377	0.0358	0.0288	0.1113	0.0561	0.034	0.128	0.0252	0.0426	0.0412	0.0247	0.0321	0.132	0.04	0.0446	0.0706	0.0795	0.0189	0.0183	0.0303	0.141	0.0132		0.017
Li(mg L-1)***	0.0839	0.144	0.0944	0.0876	0.149	0.0598	0.1122	0.13	0.0574	0.0613	0.0699	0.0537	0.266	0.0526	0.166	0.0811	0.124	0.0326	0.0481	0.0527	0.0795	0.0411		0.0722
Mn(mg L-1)***	6.687	0.119	0.129	0.219	0.426	0.128	0.268	0.325	0.298	0.084	0.048	0.095	1.046	0.112	0.296	0.2258	0.322	0.101	0.118	0.267	0.165	0.126		0.188
Mo(mg L-1)***	0.0191	0.0339	0.0292	0.0286	0.0645	0.0401	0.0326	0.0347	0.0619	0.037	0.0339	0.0229	0.1644	0.0386	0.041	0.0279	0.0886	0.0231	0.0217	0.0221	0.033	0.0216		0.024
Ni(mg L-1)***	0.0141	0.004	0.0049	0.0717	0.0054	0.005	0.0448	0.0099	0.0089	0.0111	0.0083	0.0063	0.046	0.027	0.0336	0.0646	0.017	0.0042	0.0039	0.0053	0.1135	0.0029		0.0037
Pb(mg L-1)***	0.0008	0.0021	0.0007	0.0047	0.0007	0.0007	0.0022	0.0015	0.0012	0.0015	0.001	0.0015	0.0025	0.0014	0.0024	0.0029	0.0014	0.0007	0.0009	0.0006	0.0055	0.0015		0.0009
Rb(mg L-1)***	0.0416	0.087	0.0676	0.0696	0.0891	0.0751	0.0614	0.0578	0.0621	0.0688	0.0633	0.0509	0.216	0.057	0.0464	0.0391	0.111	0.0412	0.0476	0.0446	0.063	0.0401		0.0424
Sb(mg L-1)***	0.0071	0.0043	0.004	0.0105	0.0018	0.0029	0.005	0.0044	0.0035	0.0036	0.0033	0.0029	0.0144	0.007	0.0067	0.0073	0.0034	0.0025	0.0025	0.0025	0.0082	0.0045		0.0028
Sc(mg L-1)***	0.0001	0.0001	0.0001	0	0.0001	0.0001	0.0001	0.0001	0.0001	0	0.0001	0.0001	0.0001	0	0.0001	0.0001	0.0001	0.0001	0.0001	0.0001	0.0001	0.0001		0
Sn(mg L-1)***	0.0002	0.0014	0.0003	0.0073	0.0005	0.0002	0.0038	0.0003	0.0005	0.0002	0.0002	0.0002	0.0038	0.0029	0.0031	0.0068	0.0003	0.0001	0.0001	0.0001	0.0131	0.0002		0.0001
Sr(mg L-1)***	0.357	0.303	0.315	0.285	0.326	0.265	0.282	0.26	0.289	0.28	0.295	0.255	0.518	0.27	0.266	0.229	0.315	0.249	0.264	0.254	0.295	0.238		0.255
Ti(mg L-1)***	0.0003	0.0002	0.0006	0.0019	0.0004	0.0004	0.0007	0.0004	0.0002	0.0003	0	0.0006	0.001	0.0001	0.0005	0.0012	0.0006	0.0002	0.0001	0.0001	0.0026	0.0006		0.0004
Tl(mg L-1)***	0.0012	0.0015	0.0012	0.0129	0.0019	0.0013	0.0032	0.001	0.0013	0.0013	0.001	0.0008	0.0056	0.0021	0.157	0.0052	0.0023	0.0009	0.0009	0.0009	0.006	0.0007		0.0009
U(mg L-1)***	0.0012	0.0014	0.0014	0.0016	0.0032	0.0014	0.0009	0.0018	0.0032	0.0017	0.0018	0.0019	0.0058	0.0011	0.0015	0.0017	0.0035	0.0019	0.0023	0.0022	0.0007	0.0014		0.0022

Table 4.2. Geochemical data of the pore-water extracted using Rhizon soil water samplers in columns from one (C1) to six (C6). ** and *** refers to ICP-OES and ICP-MS analysis respectively. X1 refers to the first sampling cycle during raining and x2 refers to the second sampling cycle during draying , also, -1, -2, -3 and -4, refer to the Rhizon soil water samplers depths at -4, -10, -22 and -34 cm, respectively.

Chapter 4: Effect of temperature and water content on hardpan formation in mine tailings: column experiments

sample name	C1-x2-2	C1-x2-3	C1-x2-4	C2-x2-1	C2-x2-2	C2-x2-3	C2-x2-4	C3-x2-1	C3-x2-2	C3-x2-3	C3-x2-4	C4-x2-1	C4-x2-2	C4-x2-3	C4-x2-4	C5-x2-1	C5-x2-2	C5-x2-3	C5-x2-4	C6-x2-1	C6-x2-3	C6-x2-4
pH	6.11	6.26	6.31	6.31	5.93	6.11	6.21	6.24	6.04	6.28	6.29	6.35	6.37	6.49	6.41	6.17	6.33	6.5	6.46	6.38	6.28	6.37
conductivity (S/m)	0.063	0.596	0.53		0.0062		0.517		0.205	0.355	0.305			0.0146		0.603	0.397	0.367	0.328			0.204
redox (mv)	129	131	132	147	137	137	142	139	144	156	167	143	149	153	156	152	167	178	188	145	186	197
Al (mg L-1)**	0.63	0.63	0.63	0.63	0.63	0.63	0.63	0.63	0.63	0.63	0.63	0.63	0.63	0.63	0.63	0.63	0.63	0.63	0.63		0.63	0.63
Ca (mg L-1)**	530	518	548	478.2	468	480	521	395.2	492	506	542	477.4	465.6	464	498	481	505	532	544		0	0
Fe (mg L-1)**	0.069	0.234	0.059	0.876	0.072	0.588	0.096	1.148	0.072	0.5305	0.062	0.396	0.714	0.072	0.138	0.123	0.216	0.043	0.012		0.179	0.07
K (mg L-1)**	12	8.05	6.03	39.24	26.4	15.96	6.19	19.92	12.7	4.95	5.13	46.64	10.32	6.7	-0.47	12.8	5.14	6.2	5.14		0	0
Mg (mg L-1)**	606	726	565	154	456	123	630	98.3	344	525	229	194	136	367	40.1	848	389	335	214		89.4	96
Na (mg L-1)**	52.5	48.4	40.8	9.97	21.1	5.03	28	10.4	24.7	27.9	10.2	8.82	5.38	13	2.85	43.6	13	7.63	4.81		1.04	1.04
S (mg L-1)**	1160	1290	1100	265	772	213	1210	286	654	1110	761	308	251	671	271	1580	950	866	751		261	365
Zn(mg L-1)**	0.312	0.764	0.794	0.252	0.598	1.17	0.887	0.432	0.536	0.68	0.685	17.16	7.56	0.89	0.33	0.59	0.563	0.644	0.876		0	0
As(mg L-1)***	0.0983	0.0888	0.0865	0.1386	0.1072	0.09	0.0896	0.1124	0.0914	0.0954	0.0712	0.1683	0.0948	0.07	0.0747	0.131	0.0861	0.081	0.0711		0.0249	0.0327
Ba(mg L-1)***	0.0148	0.0277	0.0172	0.0678	0.034	0.1452	0.0391	0.2128	0.0228	0.0386	0.0436	0.1441	0.4254	0.0253	0.0624	0.0202	0.0266	0.0104	0.0102		0.0226	0.0102
Cd(mg L-1)***	0.0116	0.0127	0.0153	0.0138	0.0117	0.0184	0.0151	0.0089	0.0096	0.0117	0.0093	0.0226	0.0133	0.0129	0.0147	0.0136	0.0092	0.0108	0.0128		0.0046	0.0061
Co(mg L-1)***	0.0001	0.001	0.0002	0.0007	0.0001	0.0023	0.0001	0.0006	0.0001	0.0004	0.0001	0.002	0.0014	0.0001	0.0002	0.0001	0.0002	0.0001	0		0.0002	0.0002
Cr(mg L-1)***	0.0023	0.0017	0.0058	0.0051	0.0023	0.0109	0.0025	0.0176	0.0076	0.0067	0.0011	0.03	0.0139	0.0011	0.0147	0.0026	0.0014	0.0006	0.0002		0.0043	0.0039
Cs(mg L-1)***	0.0052	0.0036	0.0048	0.0098	0.0055	0.0049	0.0044	0.0038	0.0031	0.0045	0.0035	0.0083	0.004	0.0028	0.0037	0.0036	0.0023	0.0035	0.0032		0.001	0.0013
Cu(mg L-1)***	0.0163	0.0205	0.0192	0.1596	0.05	0.1566	0.0166	0.09	0.0346	0.0203	0.0215	0.2321	0.1296	0.0986	0.0795	0.0371	0.0224	0.0215	0.0266		0.0337	0.0227
Li(mg L-1)***	0.072	0.0521	0.0413	0.153	0.0448	0.0942	0.0817	0.0596	0.0448	0.0528	0.0363	0.1584	0.0479	0.1074	0.0906	0.0648	0.0315	0.0415	0.0499		0.018	0.035
Mn(mg L-1)***	0.093	0.07	0.07	0.48	0.07	0.234	0.207	0.284	0.016	0.068	0.021	0.407	0.12	0.182	0.207	0.078	0.017	0.021	0.053		0.047	0.022
Mo(mg L-1)***	0.0294	0.0223	0.0228	0.072	0.0284	0.029	0.0251	0.058	0.0292	0.0312	0.0206	0.0725	0.031	0.0276	0.0303	0.0577	0.0221	0.0207	0.0189		0.0072	0.0093
Ni(mg L-1)***	0.0038	0.0312	0.0105	0.1512	0.0298	0.147	0.0055	0.1676	0.028	0.0074	0.0058	0.2453	0.1236	0.0278	0.0597	0.008	0.0044	0.0038	0.0047		0.0216	0.0148
Pb(mg L-1)***	0.0022	0.0038	0.0021	0.0107	0.0111	0.0206	0.0051	0.0267	0.0024	0.0216	0.0019	0.0168	0.0293	0.0028	0.0303	0.0026	0.0076	0.0011	0.0009		0.008	0.002
Rb(mg L-1)***	0.0592	0.0459	0.0544	0.099	0.0624	0.0612	0.0504	0.0588	0.0422	0.0519	0.0412	0.0988	0.0496	0.0382	0.0456	0.0473	0.031	0.0454	0.0399		0.0133	0.0168
Sb(mg L-1)***	0.0037	0.0029	0.0028	0.0618	0.0062	0.0144	0.003	0.019	0.0042	0.0035	0.0027	0.0134	0.0117	0.0055	0.0054	0.003	0.0023	0.0035	0.0028		0.0019	0.0018
Sc(mg L-1)***	0.0001	0	0.0001	0.0002	0.0002	0.0005	0	0.0002	0.0001	0	0.0001	0.0007	0.0002	0.0002	0.0002	0.0001	0.0001	0.0001	0.0001		0.0001	0.0001
Sn(mg L-1)***	0.0007	0.0004	0.0003	0.0188	0.0031	0.0174	0.0005	0.0114	0.0032	0.0007	0.0003	0.026	0.0152	0.0031	0.008	0.0003	0.0003	0.0002	0.0002		0.0023	0.0016
Sr(mg L-1)***	0.268	0.261	0.262	0.336	0.236	0.276	0.243	0.316	0.256	0.27	0.23	0.297	0.252	0.228	0.249	0.286	0.26	0.26	0.238		0.083	0.108
Ti(mg L-1)***	0.0023	0.0017	0.0014	0.051	0.0022	0.0115	0.0022	0.0071	0.0012	0.0017	0.0007	0.0018	0.019	0.0006	0.0016	0.0003	0.0029	0.0002	0.0001		0.0013	0.0016
Tl(mg L-1)***	0.001	0.0008	0.0008	0.0033	0.0023	0.0019	0.0008	0.002	0.0033	0.0008	0.0006	0.7975	0.0208	0.001	0.0048	0.0012	0.0006	0.0007	0.0006		0.0005	0.0004
U(mg L-1)***	0.0014	0.0016	0.0021	0.0008	0.0011	0.0009	0.0018	0.0012	0.0011	0.0018	0.002	0.0004	0.0009	0.0009	0.0016	0.0009	0.0015	0.0021	0.0021		0.0005	0.0009

Table 4.2. Continued

Chapter 4: Effect of temperature and water content on hardpan formation in mine tailings: column experiments

sample name	C1(0-1)	C1(-1-2)	C1(-2-3)	C1(-3-4)	C1(-4-5)	C1(-5-6)	C1(-6-7)	C1(-7-8)	C1(-8-12)	C1(-12-16)	C1(-16-20)	C1(-20-25)	C1(-25-30)	C1(-30-40)	C1(-40-50)	C2(0-1)	C2(-1-2)	C2(-2-3)
pH	6.43	6.31	6.41	6.40	6.41	6.43	6.44	6.44	6.38	6.44	6.46	6.48	6.44	6.52	6.40	6.48	6.50	6.55
conductivity (S/m)	0.718	0.359	0.275	0.266	0.261	0.268	0.267	0.273	0.274	0.276	0.281	0.281	0.277	0.271	0.265	0.57	0.349	0.289
redox (mv)	133.00	160.00	191.00	196.00	207.00	214.00	208.00	211.00	211.00	206.00	206.00	207.00	208.00	207.00	204.00	147.00	165.00	195.00
SiO2(%)*	65.45	61.86	63.61	64.82	63.84	64.03	64.44	64.31	64.39	64.07	64.01	63.48	62.61	62.80	62.79	60.52	63.10	62.92
TiO2(%)*	0.410	0.409	0.402	0.401	0.407	0.410	0.410	0.406	0.406	0.409	0.407	0.411	0.419	0.411	0.416	0.392	0.416	0.424
Al2O3(%)*	8.47	8.24	8.31	8.34	8.33	8.41	8.42	8.45	8.52	8.41	8.37	8.36	8.31	8.30	8.31	7.93	8.39	8.38
Fe2O3(%)*	8.77	9.40	9.14	8.58	9.42	9.35	9.09	8.81	9.00	9.19	9.08	9.43	9.93	9.87	9.94	9.32	9.13	9.82
MnO(%)*	0.398	0.462	0.490	0.493	0.503	0.491	0.482	0.479	0.475	0.477	0.478	0.485	0.484	0.487	0.487	0.449	0.494	0.498
MgO(%)*	1.21	1.00	0.97	0.97	1.02	1.02	1.01	0.99	1.02	1.04	1.02	1.07	1.07	1.05	1.04	1.20	1.08	1.09
CaO(%)*	1.893	2.973	2.530	2.487	2.270	2.233	2.232	2.471	2.300	2.278	2.362	2.357	2.303	2.323	2.263	3.307	2.736	2.297
Na2O(%)*	0.20	0.15	0.15	0.17	0.15	0.17	0.16	0.16	0.17	0.18	0.22	0.15	0.15	0.16	0.17	0.17	0.15	0.16
K2O(%)*	2.142	2.071	2.087	2.126	2.066	2.124	2.104	2.111	2.122	2.095	2.082	2.078	2.053	2.033	2.052	1.962	2.070	2.048
P2O5(%)*	0.182	0.180	0.182	0.177	0.191	0.186	0.181	0.178	0.179	0.183	0.184	0.186	0.195	0.191	0.193	0.182	0.173	0.187
(SO3)(%)*	0.71	1.48	0.93	1.29	0.64	0.77	0.57	0.63	0.79	0.52	0.37	0.69	0.67	0.74	0.59	0.71	0.36	0.50
LOI(%)*	6.44	7.53	6.95	6.35	6.79	6.59	6.84	7.17	6.66	6.96	7.33	6.99	7.15	6.97	7.09	9.58	8.07	7.17
(As)(mg kg-1)*	9517	11020	11000	9556	11200	10900	10490	9807	10310	10680	10330	11000	11930	12050	11980	11180	9530	11580
Ba(mg kg-1)*	16640	19000	18910	16890	19550	19190	18130	17320	17910	18670	18080	19370	21230	20850	21060	18840	16750	20530
Co(mg kg-1)*	19	16	18	22	16	19	16	18	18	22	18	19	23	20	21	16	18	20
Cr(mg kg-1)*	21	21	22	19	23	22	24	21	18	21	23	23	24	21	18	23	21	21
Cu(mg kg-1)*	191	189	178	180	180	185	200	196	192	186	180	182	182	200	199	188	180	189
Mo(mg kg-1)*	12	11	9	7	11	9	9	14	9	8	9	11	7	9	8	13	9	8
Nb(mg kg-1)*	12	10	12	10	13	13	11	10	10	13	10	13	12	12	12	10	11	12
Ni(mg kg-1)*	15	15	17	16	16	16	17	16	16	17	16	16	17	17	17	14	18	17
Pb(mg kg-1)*	747	747	691	757	698	718	692	698	691	687	719	713	783	774	765	736	747	744
Rb(mg kg-1)*	164	155	159	163	155	166	161	157	159	157	155	155	154	147	155	145	155	149
Sn(mg kg-1)*	585	661	673	622	680	670	682	630	639	628	630	681	728	740	760	680	625	714
Sr(mg kg-1)*	315	353	359	315	366	359	336	325	336	349	335	359	387	388	389	359	315	375
Zn(mg kg-1)*	1539	2099	2131	2045	2092	2021	2009	2012	1995	2006	1993	2050	2082	2100	2115	1951	2172	2076
Zr(mg kg-1)*	167	183	184	171	191	182	178	175	177	186	187	197	212	218	223	195	190	212
Al (mg L-1)**	0.63	0.63	0.63	0.63	0.63	0.63	0.63	0.63	0.63	0.63	0.63	0.63	0.63	0.63	0.63	0.63	0.63	0.63
Ca (mg L-1)**	522	569	574	570	567	577	602	570	568	572	577	576	565	582	578	511	563	579
Fe (mg L-1)**	0.047	0.021	0.022	0.011	0.124	0.196	0.017	0.141	0.033	0.014	0.011	0.201	0.063	0.068	0.015	0.02	0.14	0.025
K (mg L-1)**	29.9	10.2	5.74	6.43	6.26	6.87	6.54	7.47	6.82	6.29	6.41	6	5.86	5.43	4.81	20.1	9.8	6.58
Mg (mg L-1)**	973	242	99.7	77.3	66.9	71	72.1	79.1	87.7	94	104	104	99.4	78.4	52.9	676	227	124
Na (mg L-1)**	114	22.5	5.44	2.79	2.63	3.44	3.12	3.83	4.23	4.58	5.28	5.22	5.07	3.77	2.63	56.3	17.4	4.7
S (mg L-1)**	1580	788	629	590	574	589	551	583	622	628	646	655	626	584	570	1330	803	682
Zn(mg L-1)**	1.26	1.16	0.286	0.119	0.132	0.162	0.146	0.189	0.212	0.261	0.324	0.367	0.37	0.379	0.29	0.91	0.284	0.328
As(mg L-1)***	0.118	0.0479	0.0557	0.0698	0.0965	0.119	0.089	0.0934	0.0848	0.0791	0.0777	0.0779	0.0776	0.073	0.0688	0.0714	0.0696	0.0882
Ba(mg L-1)***	0.0212	0.0152	0.0145	0.0148	0.023	0.0274	0.0134	0.0144	0.0135	0.0146	0.0131	0.0171	0.0137	0.0139	0.0135	0.0139	0.0167	0.0135
Cd(mg L-1)***	0.0369	0.0307	0.0112	0.007	0.0065	0.0069	0.0067	0.0064	0.0061	0.0068	0.0073	0.0082	0.0079	0.0079	0.0073	0.0248	0.0105	0.0052
Co(mg L-1)***	0.0154	0.0026	0.0007	0.0005	0.0004	0.0004	0.0002	0.0002	0.0001	0.0001	0.0001	0.0001	0.0001	0.0001	0.0001	0.0043	0.0005	0.0002
Cr(mg L-1)***	0.0003	0.0003	0.0005	0.0002	0.0003	0.0003	0.0002	0.0002	0.0003	0.0002	0.0002	0.0005	0.0002	0.0003	0.0002	0.0002	0.0002	0.0006
Cs(mg L-1)***	0.0038	0.0025	0.0015	0.0008	0.0007	0.0008	0.0008	0.0008	0.0008	0.0006	0.0006	0.0006	0.0008	0.0008	0.0009	0.0034	0.0022	0.0014
Cu(mg L-1)***	0.1	0.0252	0.0176	0.0169	0.0145	0.0168	0.0105	0.0183	0.0105	0.0111	0.0124	0.0151	0.0133	0.0115	0.0122	0.0408	0.0211	0.0137
Li(mg L-1)***	0.0971	0.0402	0.0293	0.0248	0.0243	0.0289	0.0304	0.0314	0.0288	0.026	0.0237	0.0289	0.0323	0.0231	0.0124	0.164	0.0609	0.0387
Mn(mg L-1)***	8.813	3.072	0.896	0.478	0.331	0.267	0.135	0.037	0.021	0.007	0.008	0.032	0.013	0.012	0.01	2.769	0.399	0.167
Mo(mg L-1)***	0.171	0.0211	0.0216	0.0436	0.0594	0.0666	0.0643	0.0481	0.0456	0.0429	0.0459	0.0443	0.0428	0.0428	0.0418	0.0835	0.0375	0.0444
Ni(mg L-1)***	0.0474	0.0161	0.0068	0.0044	0.0052	0.0055	0.0042	0.0041	0.0037	0.0038	0.0053	0.0062	0.0053	0.0049	0.0039	0.0163	0.005	0.0032
Pb(mg L-1)***	0.0046	0.0016	0.0014	0.0013	0.0089	0.0132	0.0016	0.0065	0.0017	0.0009	0.001	0.0018	0.0031	0.0016	0.0014	0.0024	0.0043	0.0019
Rb(mg L-1)***	0.137	0.0509	0.0275	0.0155	0.015	0.0161	0.0163	0.0165	0.0165	0.0128	0.0128	0.0137	0.016	0.0172	0.0186	0.0972	0.0432	0.0243
Sb(mg L-1)***	0.0035	0.0035	0.0038	0.0039	0.0036	0.0048	0.0028	0.004	0.0033	0.0037	0.0046	0.0039	0.0041	0.0041	0.004	0.0027	0.0031	0.0031
Sc(mg L-1)***	0.0001	0.0001	0.0001	0.0001	0.0001	0.0001	0.0001	0.0001	0.0001	0	0.0001	0.0001	0.0001	0.0001	0.0001	0.0001	0.0001	0.0001
Sn(mg L-1)***	0.0049	0.0032	0.0039	0.0052	0.006	0.0072	0.0062	0.006	0.0054	0.0052	0.005	0.0049	0.0049	0.0048	0.0048	0.0044	0.0043	0.0059
Sr(mg L-1)***	0.497	0.416	0.325	0.284	0.256	0.25	0.232	0.219	0.2	0.196	0.203	0.207	0.196	0.186	0.173	0.472	0.342	0.272

Chapter 4: Effect of temperature and water content on hardpan formation in mine tailings: column experiments

Ti(mg L-1)***	0.0008	0.0005	0.0009	0.0004	0.0005	0.0004	0.0003	0	0.0007	0.0002	0.0003	0.0006	0.0006	0.0003	0.0006	0.0005	0.0004	0.0002
Tl(mg L-1)***	0.006	0.0025	0.0017	0.0013	0.0016	0.0014	0.0021	0.0011	0.001	0.001	0.001	0.0023	0.0013	0.0011	0.0016	0.0049	0.003	0.0017
U(mg L-1)***	0.0017	0.0001	0.0002	0.0005	0.0008	0.0009	0.0009	0.0009	0.0007	0.0007	0.0006	0.0008	0.0007	0.0008	0.0008	0.0005	0.0002	0.0005

Table. 4.3. Geochemical data of the different samples in columns from one (C1) to six (C6) for the final stage. *,** and *** refers to XRF, ICP-OES and ICP-MS analysis respectively.

sample name	C2(-3-4)	C2(-4-5)	C2(-5-6)	C2(-6-7)	C2(-7-8)	C2(-8-12)	C2(-12-16)	C2(-16-20)	C2(-20-25)	C2(-25-30)	C2(-30-40)	C2(-40-50)	C3(0-0)	C3(1-2)	C3(0-2)	C3(-2-4)	C3(-4-5)	C3(-5-6)
pH	6.55	6.56	6.51	6.51	6.53	6.53	6.52	6.51	6.52	6.53	6.53	6.56			6.53	6.48	6.51	6.56
conductivity (S/m)	0.278	0.277	0.281	0.281	0.275	0.276	0.279	0.275	0.275	0.275	0.265	0.252			0.82	0.287	0.281	0.273
redox (mv)	205.00	208.00	209.00	206.00	215.00	207.00	215.00	213.00	209.00	212.00	215.00	233.00			149.00	200.00	211.00	217.00
SiO2(%)*	63.53	62.99	61.29	61.94	64.60	64.95	65.32	63.70	63.57	64.21	64.12	64.73	63.83	65.15	60.45	63.91	64.01	63.61
TiO2(%)*	0.419	0.424	0.431	0.422	0.410	0.417	0.409	0.416	0.417	0.414	0.412	0.404	0.399	0.401	0.410	0.419	0.419	0.418
Al2O3(%)*	8.45	8.35	8.22	8.24	8.49	8.57	8.57	8.47	8.42	8.49	8.44	8.43	8.30	8.58	8.06	8.46	8.49	8.47
Fe2O3(%)*	9.82	10.12	10.97	10.48	8.98	9.25	8.91	9.67	9.64	9.36	9.16	9.09	8.91	9.07	8.50	10.04	9.62	9.70
MnO(%)*	0.495	0.495	0.504	0.499	0.480	0.482	0.479	0.485	0.483	0.480	0.483	0.477	0.473	0.471	0.473	0.493	0.485	0.492
MgO(%)*	1.07	1.08	1.10	1.08	1.03	1.06	1.05	1.06	1.02	1.05	1.02	0.99	1.15	0.99	1.29	1.08	1.06	1.07
CaO(%)*	2.059	2.066	2.103	2.209	2.252	1.965	2.049	2.092	2.173	2.129	2.306	2.183	2.235	2.378	2.749	2.116	1.992	2.086
Na2O(%)*	0.16	0.15	0.15	0.14	0.16	0.16	0.17	0.16	0.14	0.16	0.17	0.17	0.17	0.17	0.15	0.16	0.18	0.16
K2O(%)*	2.064	2.038	1.995	2.004	2.081	2.095	2.130	2.084	2.067	2.107	2.074	2.105	2.065	2.128	1.974	2.091	2.100	2.098
P2O5(%)*	0.192	0.194	0.207	0.202	0.182	0.183	0.177	0.184	0.197	0.185	0.186	0.188	0.185	0.171	0.196	0.182	0.188	0.188
(SO3)(%)*	0.60	0.58	0.62	0.65	0.66	0.57	0.56	0.74	0.75	0.69	0.61	0.53	0.39	0.41	0.72	0.95	0.74	0.81
LOI(%)*	6.53	6.69	7.10	7.10	6.65	6.22	6.29	6.48	6.61	6.46	6.86	6.62	7.53	7.05	8.71	6.19	6.23	6.38
(As)(mg kg-1)*	12070	12410	13790	12960	10130	10400	9875	11380	11720	11030	10570	10450	10850	8954	12580	11000	11390	11360
Ba(mg kg-1)*	20690	21730	24310	23010	17980	18050	17240	20040	20250	19060	18360	18340	18530	15710	21670	19070	19950	20060
Co(mg kg-1)*	18	18	21	17	20	18	18	18	17	20	20	17	17	17	18	21	17	18
Cr(mg kg-1)*	23	18	23	21	22	23	23	20	23	25	22	21	24	21	23	24	18	25
Cu(mg kg-1)*	187	189	207	191	188	178	179	182	208	192	178	191	192	186	185	185	193	189
Mo(mg kg-1)*	7	9	5	9	9	9	10	10	11	7	9	8	10	12	9	10	9	7
Nb(mg kg-1)*	11	12	14	13	11	12	11	13	10	10	10	10	13	11	9	12	14	11
Ni(mg kg-1)*	15	17	17	17	17	16	18	17	18	16	17	15	18	17	17	17	16	15
Pb(mg kg-1)*	722	732	796	771	724	680	705	712	740	698	692	704	695	680	718	755	705	739
Rb(mg kg-1)*	150	151	150	148	157	152	157	157	150	158	155	158	157	156	144	156	158	155
Sn(mg kg-1)*	722	732	855	773	634	615	588	685	699	670	652	649	682	547	743	681	683	686
Sr(mg kg-1)*	384	405	449	424	332	337	326	374	376	352	342	342	348	294	397	355	373	371
Zn(mg kg-1)*	2083	2081	2176	2105	2137	2000	1964	2032	2031	2006	2035	2013	1993	1977	2031	2119	2007	2068
Zr(mg kg-1)*	193	210	231	204	178	172	172	191	192	181	189	181	178	157	207	201	182	188
Al (mg L-1)**	0.63	0.63	0.63	0.63	0.63	0.63	0.63	0.63	0.63	0.63	0.63	0.63			0.63	0.63	0.63	0.63
Ca (mg L-1)**	568	561	584	578	571	583	578	585	568	585	626	612			459	596	579	601
Fe (mg L-1)**	0.014	0.026	0.009	0.037	0.073	0.083	0.075	0.039	0.009	0.052	0.022	0.015			0.024	0.055	0.058	0.011
K (mg L-1)**	6.07	5.27	7.44	7.84	4.9	7.56	6.4	6.32	6.46	6.57	6.04	5.32			31.8	5.38	5.46	4.84
Mg (mg L-1)**	105	113	112	117	112	112	105	98	97.2	95	74	42.4			1420	126	108	90.2
Na (mg L-1)**	3.14	3.35	3.42	4.22	3.68	3.93	3.5	3.1	3.19	3.12	2.17	0.919			107	6.45	5.73	3.79
S (mg L-1)**	662	645	670	663	656	654	662	655	652	639	589	566			2380	662	666	624
Zn(mg L-1)**	0.08	2.25	0.155	0.172	0.197	0.22	1.32	0.302	0.303	0.346	0.323	0.289			0.799	0.097	0.146	0.151
As(mg L-1)***	0.0929	0.0972	0.0926	0.0946	0.0902	0.0964	0.0822	0.0761	0.0715	0.0718	0.0684	0.0638			0.229	0.0912	0.0907	0.0834
Ba(mg L-1)***	0.014	0.0137	0.0136	0.0136	0.0118	0.0186	0.0117	0.0117	0.0129	0.0127	0.0154	0.0131			0.0117	0.0103	0.0128	0.0099
Cd(mg L-1)***	0.0047	0.0066	0.0065	0.0064	0.0058	0.0061	0.0068	0.0065	0.0065	0.0069	0.0069	0.0065			0.01	0.0047	0.0055	0.0049
Co(mg L-1)***	0.0002	0.0004	0.0002	0.0002	0.0001	0.0001	0.0002	0.0001	0.0001	0.0002	0.0001	0.0001			0.0009	0.0002	0.0001	0
Cr(mg L-1)***	0.0002	0.0035	0.0002	0.0002	0.0002	0.0002	0.0017	0.0002	0.0002	0.0003	0.0003	0.0002			0.0007	0.0002	0.0002	0.0002
Cs(mg L-1)***	0.0009	0.0014	0.001	0.001	0.0016	0.001	0.0011	0.001	0.001	0.0009	0.0009	0.0007			0.0037	0.001	0.0009	0.0009
Cu(mg L-1)***	0.0106	0.0112	0.01	0.0134	0.0101	0.0107	0.0126	0.0093	0.0095	0.0095	0.011	0.0086			0.0623	0.0136	0.014	0.011
Li(mg L-1)***	0.0334	0.0359	0.0328	0.0294	0.0233	0.0254	0.0263	0.0321	0.0279	0.0197	0.0242	0.0142			0.128	0.0316	0.0411	0.0346
Mn(mg L-1)***	0.165	0.149	0.155	0.081	0.025	0.023	0.019	0.013	0.008	0.012	0.01	0.011			0.341	0.123	0.068	0.017
Mo(mg L-1)***	0.0572	0.0484	0.0584	0.048	0.0316	0.0383	0.0382	0.0367	0.0372	0.0367	0.037	0.0335			0.256	0.052	0.046	0.037
Ni(mg L-1)***	0.003	0.006	0.0037	0.0038	0.003	0.0036	0.0057	0.0037	0.0041	0.0041	0.0051	0.0033			0.05	0.0065	0.0087	0.0054

Chapter 4: Effect of temperature and water content on hardpan formation in mine tailings: column experiments

Pb(mg L-1)***	0.001	0.0015	0.0008	0.0027	0.0014	0.0056	0.0033	0.0015	0.0009	0.0021	0.0015	0.0015			0.0028	0.0012	0.0033	0.0015
Rb(mg L-1)***	0.0166	0.0201	0.0183	0.019	0.0232	0.0198	0.0204	0.0203	0.0201	0.0193	0.0188	0.0138			0.0843	0.0176	0.0173	0.0164
Sb(mg L-1)***	0.0027	0.0034	0.0029	0.0029	0.0023	0.0036	0.0026	0.0029	0.0029	0.0028	0.0034	0.0036			0.0063	0.0023	0.0026	0.0028
Sc(mg L-1)***	0.0001	0	0	0.0001	0.0001	0.0001	0.0001	0	0.0001	0.0001	0.0001	0.0001			0.0001	0.0001	0.0001	0.0001
Sn(mg L-1)***	0.0061	0.006	0.0062	0.0059	0.0056	0.0054	0.0054	0.0055	0.0052	0.005	0.005	0.005			0.0066	0.0056	0.0063	0.0053
Sr(mg L-1)***	0.213	0.197	0.189	0.183	0.177	0.18	0.184	0.185	0.183	0.18	0.173	0.16			0.4	0.226	0.205	0.186
Ti(mg L-1)***	0.0004	0.0011	0	0.0006	0.0002	0.0003	0.0012	0.0002	0.0001	0.0011	0.0007	0.0002			0.0008	0.0007	0.0005	0.0007
Tl(mg L-1)***	0.0015	0.0016	0.0013	0.0013	0.0026	0.0013	0.0011	0.0009	0.0012	0.0011	0.0012	0.0012			0.0072	0.0092	0.0041	0.0061
U(mg L-1)***	0.0008	0.0007	0.0008	0.0007	0.0007	0.0007	0.0007	0.0007	0.0007	0.0008	0.001	0.0012			0.0016	0.0009	0.0009	0.0008

Table 4.3. Continued

sample name	C3(-6-7)	C3(-7-8)	C3(-8-12)	C3(-12-16)	C3(-16-20)	C3(-20-25)	C3(-25-30)	C3(-30-40)	C3(-40-50)	C4(0-1)	C4(1-2)	C4(2-3)	C4(-3-4)	C4(-4-5)	C4(-5-6)	C4(-6-7)	C4(-7-8)	C4(-8-12)
pH	6.49	6.48	6.48	6.46	6.43	6.45	6.46	6.45	6.45	6.45	6.48	6.47	6.49	6.45	6.46	6.45	6.46	6.42
conductivity (S/m)	0.277	0.272	0.273	0.277	0.277	0.27	0.263	0.257	0.252	0.891	0.442	0.301	0.288	0.281	0.28	0.275	0.28	0.279
redox (mv)	220.00	225.00	217.00	223.00	223.00	222.00	225.00	235.00	220.00	153.00	180.00	207.00	211.00	215.00	215.00	219.00	216.00	216.00
SiO2(%)*	61.83	64.46	66.30	65.07	65.02	64.24	64.10	63.93	64.06	61.53	62.33	63.29	63.65	63.70	62.83	60.77	64.02	64.43
TiO2(%)*	0.425	0.416	0.406	0.413	0.417	0.416	0.417	0.416	0.413	0.399	0.423	0.420	0.421	0.417	0.423	0.432	0.419	0.413
Al2O3(%)*	8.28	8.50	8.63	8.51	8.53	8.49	8.49	8.48	8.49	8.09	8.31	8.36	8.44	8.39	8.35	8.14	8.47	8.48
Fe2O3(%)*	10.68	9.21	8.36	9.09	9.18	9.51	9.52	9.61	9.43	8.66	9.75	9.85	9.83	9.66	10.21	11.24	9.63	9.44
MnO(%)*	0.496	0.481	0.470	0.481	0.473	0.483	0.484	0.486	0.490	0.449	0.487	0.493	0.481	0.484	0.494	0.505	0.486	0.482
MgO(%)*	1.08	1.05	1.02	1.03	1.05	1.04	1.05	1.05	1.04	1.41	1.23	1.08	1.07	1.06	1.08	1.11	1.07	1.06
CaO(%)*	2.116	2.112	2.075	2.035	1.992	2.065	2.114	2.080	2.191	3.068	2.402	2.127	2.022	2.111	2.092	2.130	2.048	2.022
Na2O(%)*	0.15	0.18	0.17	0.16	0.16	0.16	0.15	0.15	0.16	0.19	0.15	0.15	0.17	0.16	0.16	0.12	0.16	0.16
K2O(%)*	2.018	2.090	2.130	2.162	2.152	2.132	2.137	2.116	2.129	2.050	2.075	2.092	2.109	2.086	2.075	2.007	2.094	2.097
P2O5(%)*	0.209	0.182	0.167	0.185	0.187	0.188	0.188	0.193	0.186	0.169	0.183	0.185	0.191	0.188	0.197	0.213	0.188	0.189
(SO3)(%)*	0.83	0.67	0.80	1.01	1.18	1.01	1.35	1.15	1.08	0.79	0.54	0.69	0.86	0.41	0.97	0.85	0.75	0.62
LOI(%)*	6.72	6.46	6.00	5.83	5.60	6.00	5.75	5.97	6.16	9.65	7.76	6.69	6.24	6.93	6.35	6.99	6.29	6.40
(As)(mg kg-1)*	13530	10740	8523	10450	10700	11370	11220	11650	10790	9205	11610	12190	12220	12000	12710	14940	11550	11040
Ba(mg kg-1)*	23590	18610	15430	18100	18350	19310	19240	20080	18880	15700	19540	20610	20680	20110	21880	25980	19480	18890
Co(mg kg-1)*	21	16	17	18	17	21	18	20	19	17	22	21	18	18	17	23	16	18
Cr(mg kg-1)*	26	20	24	25	24	23	21	21	20	20	21	21	21	22	22	23	21	22
Cu(mg kg-1)*	199	174	175	222	232	243	234	240	201	185	218	206	221	232	197	247	193	193
Mo(mg kg-1)*	7	7	9	11	9	9	12	9	7	10	9	9	7	9	7	9	8	8
Nb(mg kg-1)*	10	11	10	13	10	12	13	13	8	11	11	13	10	10	12	13	12	13
Ni(mg kg-1)*	17	15	14	17	17	17	16	17	15	17	15	17	16	15	16	17	15	15
Pb(mg kg-1)*	780	695	647	689	853	708	718	769	753	708	785	735	719	718	744	800	731	706
Rb(mg kg-1)*	152	149	155	167	163	162	164	160	163	156	156	160	160	157	160	154	159	156
Sn(mg kg-1)*	761	635	541	632	643	665	697	700	661	547	682	692	684	707	770	872	681	656
Sr(mg kg-1)*	436	345	290	340	342	359	359	371	353	298	364	385	386	374	407	479	364	352
Zn(mg kg-1)*	2102	1977	1933	1984	1939	2004	2039	2017	2077	1987	2111	2032	1980	2029	2074	2143	2021	1999
Zr(mg kg-1)*	214	180	150	168	170	181	187	187	184	161	200	187	179	200	205	224	184	178
Al (mg L-1)**	0.63	0.63	0.63	0.63	0.63	0.63	0.63	0.63	0.63	0.63	0.63	0.63	0.63	0.63	0.63	0.63	0.63	0.63
Ca (mg L-1)**	605	611	583	581	616	629	602	601	644	453	492	556	529	552	556	577	602	591
Fe (mg L-1)**	0.012	0.046	0.164	0.031	0.018	0.02	0.04	0.017	0.019	0.039	0.011	0.017	0.088	0.043	0.019	0.01	0.011	0.031
K (mg L-1)**	5.37	4.58	4.2	5.52	4.06	3.86	3.8	3.94	3.22	34.5	15.2	12	7.87	7.23	6.26	6.37	5.51	5.39
Mg (mg L-1)**	99.7	88.2	96.1	101	99.8	79.8	62.5	46.9	38.8	1630	529	164	129	105	107	99.7	104	105
Na (mg L-1)**	4.31	3.58	4.08	4.03	3.84	2.89	1.84	0.953	0.64	92.5	24.7	5.96	3.75	2.92	3.03	3.01	3.01	3.07
S (mg L-1)**	647	606	627	655	621	579	582	567	543	2660	1160	721	660	666	659	659	656	670
Zn(mg L-1)**	0.162	0.879	0.251	0.312	0.515	0.382	0.389	0.359	0.31	0.451	0.139	0.105	0.107	0.113	0.134	0.153	0.171	0.192
As(mg L-1)***	0.084	0.0826	0.0928	0.0738	0.0708	0.0685	0.063	0.0602	0.0646	0.177	0.123	0.0974	0.101	0.0962	0.0955	0.0898	0.0892	0.0855
Ba(mg L-1)***	0.0097	0.0098	0.018	0.0103	0.0097	0.0105	0.0101	0.0124	0.0106	0.0102	0.009	0.0122	0.0118	0.0119	0.0111	0.0112	0.0109	0.0113
Cd(mg L-1)***	0.0049	0.0052	0.0057	0.0063	0.0063	0.0068	0.0065	0.0064	0.0066	0.0145	0.0064	0.0055	0.0054	0.0052	0.0053	0.0053	0.0055	0.0058
Co(mg L-1)***	0	0.0001	0.0001	0.0001	0	0.0001	0	0	0	0.0006	0.0002	0.0003	0.0002	0.0001	0.0001	0.0001	0.0001	0.0001
Cr(mg L-1)***	0.0001	0.0007	0.0002	0.0004	0.0004	0.0001	0.0002	0.0001	0.0002	0.0002	0.0002	0.0002	0.0004	0.0004	0.0002	0.0002	0.0002	0.0002
Cs(mg L-1)***	0.0009	0.0007	0.0008	0.0007	0.001	0.001	0.0012	0.0011	0.001	0.0041	0.002	0.001	0.0009	0.0009	0.0009	0.0009	0.0009	0.001

Chapter 4: Effect of temperature and water content on hardpan formation in mine tailings: column experiments

Cu(mg L-1)***	0.0111	0.0106	0.0112	0.0114	0.0104	0.0113	0.0107	0.0087	0.0084	0.033	0.0133	0.0108	0.0098	0.0111	0.0091	0.0098	0.0091	0.0091
Li(mg L-1)***	0.035	0.0285	0.0258	0.0293	0.026	0.0228	0.02	0.0194	0.0183	0.197	0.073	0.047	0.0361	0.0288	0.0245	0.0199	0.0211	0.0248
Mn(mg L-1)***	0.006	0.008	0.024	0.013	0.005	0.007	0.009	0.006	0.008	0.403	0.137	0.124	0.091	0.035	0.02	0.01	0.008	0.011
Mo(mg L-1)***	0.037	0.0362	0.0324	0.038	0.0344	0.0349	0.0321	0.0301	0.029	0.183	0.0659	0.0585	0.0518	0.0433	0.0387	0.0391	0.0383	0.038
Ni(mg L-1)***	0.0054	0.0066	0.0055	0.0073	0.0065	0.0074	0.0064	0.0053	0.0039	0.01	0.0046	0.0042	0.0043	0.0045	0.0043	0.0038	0.0047	0.0038
Pb(mg L-1)***	0.0009	0.0017	0.0084	0.0014	0.0009	0.0017	0.0008	0.0013	0.002	0.0031	0.0012	0.0016	0.0016	0.0012	0.0016	0.001	0.0009	0.0016
Rb(mg L-1)***	0.0161	0.0127	0.0122	0.0137	0.0174	0.0171	0.0193	0.0179	0.0164	0.119	0.0448	0.021	0.0168	0.0162	0.0166	0.0174	0.0174	0.0187
Sb(mg L-1)***	0.0023	0.0023	0.0025	0.0027	0.0024	0.0022	0.0024	0.0025	0.0024	0.0044	0.0032	0.0034	0.0034	0.0043	0.0032	0.0031	0.0033	0.0034
Sc(mg L-1)***	0	0.0001	0.0001	0.0001	0	0.0001	0.0001	0	0.0001	0	0.0001	0.0001	0	0.0001	0	0.0001	0.0001	0.0001
Sn(mg L-1)***	0.0051	0.0055	0.0046	0.0045	0.0044	0.0043	0.0042	0.0042	0.0041	0.006	0.0057	0.0057	0.0055	0.0053	0.0051	0.0052	0.0052	0.0048
Sr(mg L-1)***	0.185	0.169	0.171	0.17	0.172	0.172	0.166	0.157	0.148	0.37	0.267	0.267	0.185	0.174	0.175	0.179	0.175	0.185
Ti(mg L-1)***	0.0002	0.0001	0.0004	0.0002	0.0001	0.0003	0.0002	0.0002	0	0.0004	0.0003	0.0008	0.0006	0.0004	0.0002	0.0003	0.0002	0.0002
Tl(mg L-1)***	0.002	0.0009	0.001	0.0024	0.0013	0.0015	0.0016	0.0363	0.003	0.251	0.0077	0.0025	0.0011	0.0072	0.0037	0.044	0.0029	0.0011
U(mg L-1)***	0.0008	0.0007	0.0008	0.0008	0.0007	0.0009	0.0009	0.001	0.0011	0.0003	0.0003	0.0007	0.0008	0.0007	0.0008	0.0008	0.0007	0.0007

Table 4.3. Continued

sample name	C4(-12-16)	C4(-16-20)	C4(-20-25)	C4(-25-30)	C4(-30-40)	C4(-40-50)	C5(0-1)	C5(-1-2)	C5(-2-3)	C5(-3-4)	C5(-4-5)	C5(-5-6)	C5(-6-7)	C5(-7-8)	C5(-8-12)	C5(-12-16)	C5(-16-20)	C5(-20-25)
pH	6.47	6.44	6.45	6.44	6.47	6.45	6.52	6.48	6.38	6.38	6.26	6.46	6.46	6.30	6.46	6.29	6.27	6.27
conductivity (S/m)	0.277	0.275	0.271	0.269	0.259	0.252	1.168	0.341	0.29	0.286	0.28	0.283	0.276	0.27	0.264	0.262	0.261	0.261
redox (mv)	217.00	220.00	221.00	221.00	217.00	223.00	150.00	174.00	210.00	216.00	217.00	219.00	219.00	220.00	219.00	222.00	227.00	225.00
SiO2(%)*	63.84	63.57	63.15	63.68	63.19	63.68	58.11	63.62	62.73	62.76	62.62	62.34	61.78	63.56	65.82	65.29	65.01	64.33
TiO2(%)*	0.417	0.422	0.418	0.414	0.414	0.407	0.363	0.421	0.431	0.423	0.422	0.422	0.425	0.417	0.415	0.402	0.404	0.416
Al2O3(%)*	8.46	8.46	8.38	8.43	8.36	8.35	7.39	8.42	8.43	8.34	8.31	8.26	8.21	8.33	8.55	8.54	8.47	8.52
Fe2O3(%)*	9.57	9.82	9.72	9.37	9.64	9.46	8.00	9.94	10.12	10.21	10.15	10.13	10.45	9.73	8.67	8.71	8.72	9.34
MnO(%)*	0.487	0.487	0.490	0.490	0.491	0.491	0.414	0.484	0.502	0.495	0.499	0.494	0.501	0.483	0.474	0.477	0.475	0.485
MgO(%)*	1.06	1.08	1.06	1.04	1.05	1.05	1.89	1.10	1.11	1.08	1.07	1.08	1.07	1.04	1.02	1.02	1.00	1.03
CaO(%)*	2.141	2.055	2.263	2.308	2.316	2.303	3.792	1.936	2.128	2.104	2.150	2.308	2.288	2.141	2.056	2.228	2.332	2.124
Na2O(%)*	0.15	0.15	0.16	0.16	0.15	0.16	0.19	0.16	0.16	0.14	0.15	0.15	0.14	0.15	0.17	0.17	0.16	0.16
K2O(%)*	2.095	2.094	2.068	2.100	2.080	2.082	1.851	2.098	2.074	2.075	2.074	2.050	2.038	2.078	2.159	2.157	2.113	2.134
P2O5(%)*	0.190	0.190	0.195	0.188	0.187	0.186	0.163	0.191	0.199	0.198	0.201	0.198	0.205	0.195	0.178	0.177	0.176	0.188
(SO3)(%)*	0.57	0.71	0.86	0.40	0.46	0.39	1.31	0.49	0.64	0.77	0.60	0.46	0.73	0.64	0.64	0.77	0.92	0.86
LOI(%)*	6.68	6.46	6.70	7.21	7.26	7.20	13.00	6.60	6.78	6.58	6.85	7.40	7.13	6.67	6.12	6.34	6.41	6.23
(As)(mg kg-1)*	11360	11930	11710	10890	11440	10900	9449	12120	12380	12930	13170	12610	13400	12140	9558	9439	9571	10910
Ba(mg kg-1)*	19400	20140	20520	18820	19530	18880	15170	20720	21380	21950	22380	21490	23130	20590	16620	16670	16850	19000
Co(mg kg-1)*	18	16	19	19	14	18	16	17	18	21	21	18	23	18	16	19	15	17
Cr(mg kg-1)*	23	25	23	23	23	22	16	20	24	20	19	22	25	19	23	25	23	23
Cu(mg kg-1)*	195	199	201	185	197	193	183	203	208	192	202	213	197	197	171	185	179	190
Mo(mg kg-1)*	7	11	10	10	8	11	10	9	7	7	7	9	8	8	9	11	9	12
Nb(mg kg-1)*	13	13	11	13	13	12	11	12	12	13	10	11	12	11	11	13	10	13
Ni(mg kg-1)*	16	17	16	17	18	16	13	17	16	17	17	17	15	17	15	16	15	17
Pb(mg kg-1)*	721	739	728	750	782	745	613	739	787	764	753	774	819	734	650	679	681	716
Rb(mg kg-1)*	153	157	155	155	155	155	140	158	155	159	156	152	150	157	165	164	156	159
Sn(mg kg-1)*	664	693	710	673	705	674	569	707	770	779	758	744	841	706	594	598	570	641
Sr(mg kg-1)*	341	377	378	349	361	353	295	379	397	403	416	393	423	383	311	311	320	348
Zn(mg kg-1)*	2036	2029	2067	2095	2156	2077	1729	2082	2162	2069	2058	2098	2132	2021	1924	1984	1974	2235
Zr(mg kg-1)*	178	197	194	201	204	199	144	205	236	215	215	221	224	189	164	159	167	173
Al (mg L-1)**	0.63	0.63	0.63	0.63	0.63	0.63	0.63	0.63	0.63	0.63	0.63	0.63	0.63	0.63	0.63	0.63	0.63	0.63
Ca (mg L-1)**	590	555	561	564	592	584	450	544	553	609	609	608	581	608	609	613	609	610
Fe (mg L-1)**	0.009	0.017	0.035	0.052	0.011	0.187	0.145	0.005	0.011	0.026	0.021	0.027	0.061	0.012	0.013	0.018	0.006	0.013
K (mg L-1)**	6.19	5.81	5.79	6.3	3.46	5.36	44.1	8.14	5.48	5.66	4.65	4.65	3.97	3.48	3.58	3.84	4.33	6.58
Mg (mg L-1)**	101	99.5	89.5	83.4	62	42	2470	232	141	129	117	120	109	88.7	71.5	63.5	59.5	54.6
Na (mg L-1)**	2.87	2.38	1.97	1.94	1.1	0.843	174	18.1	4.63	3.92	3.43	3.74	3.08	2.45	1.75	1.61	1.36	0.7
S (mg L-1)**	660	660	646	629	594	556	3850	823	619	677	664	650	661	625	590	592	587	581
Zn(mg L-1)**	0.235	0.253	0.265	0.268	0.321	0.32	0.82	0.19	0.186	0.237	0.261	0.262	0.282	0.301	0.318	0.339	0.349	0.3
As(mg L-1)***	0.0784	0.0779	0.0728	0.0709	0.0663	0.0663	0.338	0.113	0.107	0.0954	0.0904	0.0851	0.0802	0.077	0.0704	0.0638	0.062	0.0612

Chapter 4: Effect of temperature and water content on hardpan formation in mine tailings: column experiments

Ba(mg L-1)***	0.0122	0.0113	0.0142	0.0128	0.0102	0.0132	0.0124	0.0091	0.0117	0.0105	0.0102	0.01	0.0104	0.0109	0.0104	0.0105	0.0096	0.0124
Cd(mg L-1)***	0.0059	0.0064	0.0065	0.0065	0.0063	0.0072	0.0144	0.0053	0.0051	0.0056	0.0058	0.0059	0.0059	0.0061	0.0062	0.0063	0.0065	0.006
Co(mg L-1)***	0.0001	0.0001	0.0001	0.0001	0.0001	0.0002	0.0003	0.0001	0.0002	0.0001	0.0001	0.0001	0.0001	0	0.0001	0.0001	0	0
Cr(mg L-1)***	0.0004	0.0002	0.0002	0.0002	0.0002	0.0005	0.0002	0.0001	0.0002	0.0002	0.0001	0.0002	0.0002	0.0001	0.0001	0.0001	0.0002	0.0002
Cs(mg L-1)***	0.0008	0.0008	0.0008	0.0008	0.001	0.0007	0.0054	0.0011	0.0008	0.0007	0.0007	0.0007	0.0006	0.0005	0.0005	0.0006	0.0008	0.0007
Cu(mg L-1)***	0.0089	0.009	0.0086	0.0105	0.0075	0.0129	0.0848	0.015	0.015	0.0148	0.0141	0.0143	0.0128	0.013	0.0121	0.0121	0.0107	0.0091
Li(mg L-1)***	0.0273	0.0504	0.0281	0.0352	0.0355	0.0265	0.276	0.039	0.0351	0.0336	0.0282	0.0245	0.021	0.0191	0.0202	0.0204	0.0257	0.023
Mn(mg L-1)***	0.008	0.011	0.012	0.013	0.006	0.029	0.06	0.007	0.008	0.009	0.007	0.008	0.019	0.004	0.008	0.005	0.005	0.008
Mo(mg L-1)***	0.0374	0.0382	0.0348	0.0348	0.0279	0.0336	0.366	0.0531	0.0485	0.0476	0.0407	0.0386	0.0345	0.0351	0.0348	0.0316	0.0299	0.0328
Ni(mg L-1)***	0.0055	0.0044	0.0043	0.0047	0.0034	0.0055	0.045	0.0064	0.0044	0.0058	0.0057	0.0049	0.0041	0.0043	0.0044	0.0042	0.0038	0.0044
Pb(mg L-1)***	0.001	0.0017	0.0014	0.0019	0.0009	0.002	0.0044	0.0009	0.0012	0.0056	0.0014	0.001	0.0025	0.0013	0.0013	0.0008	0.0008	0.0012
Rb(mg L-1)***	0.0175	0.0168	0.0169	0.0168	0.0177	0.0142	0.168	0.0215	0.0147	0.0123	0.0107	0.0106	0.0098	0.0089	0.0086	0.0107	0.0143	0.0148
Sb(mg L-1)***	0.0032	0.003	0.0034	0.0039	0.0027	0.0034	0.007	0.0029	0.0031	0.0026	0.0024	0.0033	0.0029	0.0028	0.0024	0.0032	0.0035	
Sc(mg L-1)***	0.0001	0.0001	0.0001	0.0001	0.0001	0.0001	0.0001	0.0001	0	0.0001	0	0.0001	0	0	0.0001	0.0001	0	0.0001
Sn(mg L-1)***	0.0048	0.0046	0.0046	0.0046	0.0043	0.0046	0.004	0.0027	0.0026	0.0026	0.0024	0.0024	0.0023	0.0022	0.0023	0.0023	0.0022	0.0045
Sr(mg L-1)***	0.181	0.181	0.178	0.175	0.162	0.156	0.433	0.186	0.18	0.172	0.168	0.17	0.174	0.176	0.173	0.165	0.163	0.162
Ti(mg L-1)***	0.0006	0.0004	0.0002	0.0001	0.0001	0.0234	0.0005	0.0001	0.001	0.0004	0.0003	0.0003	0.0002	0.0001	0.0001	0.0002	0.0001	0.0002
Tl(mg L-1)***	0.0016	0.0056	0.0459	0.01	0.0007	0.0009	0.0044	0.0064	0.0016	0.0012	0.0024	0.0015	0.0038	0.0009	0.0014	0.0011	0.01	0.0009
U(mg L-1)***	0.0007	0.0007	0.0008	0.0009	0.0008	0.0011	0.0028	0.001	0.0009	0.0009	0.0008	0.0008	0.0008	0.0008	0.0009	0.0009	0.0009	0.0009

Table 4.3. Continued

sample name	C5(-25-30)	C5(-30-40)	C5(-40-50)	C6(0-1)	C6(-1-2)	C6(-2-3)	C6(-3-4)	C6(-4-5)	C6(-5-6)	C6(-6-7)	C6(-7-8)	C6(-8-12)	C6(-12-16)	C6(-16-20)	C6(-20-25)	C6(-25-30)	C6(-30-40)	C6(-40-50)
pH	6.28	6.24	6.24	6.21	6.21	6.29	6.26	6.23	6.26	6.33	6.35	6.35	6.35	6.29	6.22	5.81	5.92	5.67
conductivity (S/m)	0.261	0.258	0.254	1.395	0.34	0.281	0.272	0.27	0.27	0.266	0.266	0.261	0.261	0.259	0.261	0.258	0.255	0.253
redox (mv)	220.00	225.00	221.00	151.00	197.00	217.00	213.00	217.00	218.00	227.00	217.00	226.00	227.00	224.00	231.00	225	222	224
SiO2(%)*	64.73	63.52	64.35	60.31	61.78	63.26	64.86	64.52	64.60	64.75	64.36	65.48	64.97	64.71	64.79	64.38	64.40	64.60
TiO2(%)*	0.404	0.420	0.412	0.404	0.419	0.416	0.401	0.403	0.403	0.400	0.400	0.395	0.399	0.394	0.399	0.398	0.403	0.403
Al2O3(%)*	8.44	8.43	8.38	7.98	8.17	8.32	8.44	8.41	8.48	8.47	8.47	8.49	8.48	8.38	8.44	8.39	8.41	8.41
Fe2O3(%)*	8.93	9.87	9.44	9.91	10.60	9.88	9.04	8.52	8.71	8.41	8.41	8.29	8.44	8.66	8.75	9.02	8.94	9.22
MnO(%)*	0.476	0.489	0.485	0.467	0.499	0.486	0.472	0.476	0.480	0.477	0.486	0.470	0.475	0.475	0.469	0.474	0.474	0.475
MgO(%)*	1.02	1.08	1.03	1.54	1.14	1.05	1.00	1.00	0.99	0.99	0.99	0.99	0.99	0.99	0.98	0.99	1.00	1.01
CaO(%)*	2.289	2.072	2.065	2.378	2.072	2.103	2.123	2.573	2.445	2.556	2.686	2.402	2.469	2.439	2.349	2.319	2.362	2.114
Na2O(%)*	0.16	0.15	0.17	0.14	0.15	0.16	0.16	0.16	0.16	0.18	0.17	0.17	0.18	0.17	0.16	0.16	0.18	0.16
K2O(%)*	2.122	2.103	2.098	1.965	2.031	2.085	2.109	2.123	2.138	2.137	2.133	2.151	2.136	2.125	2.114	2.106	2.099	2.104
P2O5(%)*	0.179	0.193	0.189	0.192	0.209	0.193	0.188	0.170	0.175	0.170	0.172	0.171	0.173	0.177	0.179	0.182	0.178	0.184
(SO3)(%)*	1.00	0.90	0.99	0.42	0.73	0.81	0.78	0.35	0.60	0.37	0.47	0.50	0.65	0.42	0.62	0.51	0.56	0.63
LOI(%)*	6.33	6.21	6.01	9.54	6.95	6.50	6.31	7.66	7.12	7.55	7.68	7.02	6.31	7.34	6.87	7.02	7.01	6.50
(As)(mg kg-1)*	10090	12100	11300	12810	14270	12730	10660	9068	9372	8896	8814	8720	8926	9477	9943	10460	10190	10940
Ba(mg kg-1)*	17570	20830	19740	21460	24350	21280	18360	16170	16460	15680	16040	15420	16040	16780	17370	18200	17700	18880
Co(mg kg-1)*	18	20	19	20	20	18	18	17	18	19	18	16	16	14	17	16	16	22
Cr(mg kg-1)*	27	22	23	18	21	24	23	22	18	24	22	23	22	24	21	22	21	21
Cu(mg kg-1)*	186	190	193	209	223	195	179	176	200	188	181	183	179	180	179	194	181	183
Mo(mg kg-1)*	11	10	10	6	9	12	9	10	9	10	11	10	10	13	10	8	9	9
Nb(mg kg-1)*	15	11	13	11	13	11	11	10	13	11	13	13	12	14	11	12	13	11
Ni(mg kg-1)*	13	16	17	17	13	16	15	15	13	17	14	16	15	15	14	16	17	15
Pb(mg kg-1)*	770	776	712	734	757	742	682	691	718	688	684	737	675	709	702	712	706	702
Rb(mg kg-1)*	162	160	159	147	156	162	159	162	163	157	160	162	160	161	158	159	157	159
Sn(mg kg-1)*	641	713	690	775	818	715	630	562	595	573	577	567	580	604	639	646	647	651
Sr(mg kg-1)*	330	385	365	401	449	396	344	303	311	293	304	288	301	316	324	337	331	355
Zn(mg kg-1)*	2001	2073	2014	1993	2078	2002	1949	2007	1985	2022	2033	1955	1987	1991	1966	1971	1976	2000
Zr(mg kg-1)*	177	204	192	201	224	193	164	158	161	158	170	155	163	170	167	181	177	182
Al (mg L-1)**	0.63	0.63	0.63	0.63	0.63	0.63	0.63	0.63	0.63	0.63	0.63	0.63	0.63	0.63	0.63	0.63	0.63	0.63
Ca (mg L-1)**	614	614	618	445	528	580	596	582	571	579	578	581	574	581	618	590	609	616
Fe (mg L-1)**	0.014	0.004	0.006	0.021	0.148	0.023	0.026	0.02	0.014	0.015	0.03	0.01	0.007	0.008	0.01	0.008	0.01	0.018

Chapter 4: Effect of temperature and water content on hardpan formation in mine tailings: column experiments

K (mg L-1)**	4.31	4.98	5.03	42.6	9.39	8.82	7.67	7.3	7.3	4.14	6.96	6.46	7.11	6.43	3.69	7.22	6.69	9.81
Mg (mg L-1)**	56.6	47.9	40.6	3520	273	116	88.1	82.7	81.3	74.8	67.3	61.4	60.7	55.5	58.5	50	41.1	36.4
Na (mg L-1)**	1.21	1.16	1.27	92.9	7.54	2.31	1.47	1.49	1.28	1.11	1.02	0.846	0.704	0.7	1.19	-0.7	0.7	0.7
S (mg L-1)**	592	581	576	4750	820	658	628	611	617	583	579	572	561	561	571	566	573	567
Zn(mg L-1)**	0.382	0.462	0.577	1.4	0.269	0.208	0.18	0.185	0.208	0.204	0.22	0.236	0.275	0.27	0.354	0.31	0.326	0.357
As(mg L-1)***	0.0653	0.0713	0.0819	0.258	0.109	0.0903	0.0844	0.0792	0.0759	0.0697	0.0664	0.0646	0.0628	0.0599	0.061	0.0621	0.0609	0.0675
Ba(mg L-1)***	0.0105	0.0095	0.0095	0.0095	0.0174	0.0129	0.0112	0.0124	0.0124	0.0109	0.0122	0.0123	0.0111	0.0116	0.0091	0.0116	0.0126	0.0117
Cd(mg L-1)***	0.007	0.008	0.0095	0.0214	0.0061	0.0053	0.0052	0.0053	0.0054	0.0049	0.0054	0.0057	0.0057	0.006	0.0065	0.0064	0.0066	0.0084
Co(mg L-1)***	0	0.0001	0	0.0004	0.0001	0.0001	0.0001	0.0001	0.0001	0.0001	0.0001	0.0001	0	0.0001	0	0.0001	0	0.0001
Cr(mg L-1)***	0.0001	0.0001	0.0001	0.0002	0.0004	0.0002	0.0002	0.0002	0.0002	0.0002	0.0002	0.0002	0.0002	0.0002	0.0001	0.0002	0.0001	0.0001
Cs(mg L-1)***	0.0011	0.001	0.0009	0.0046	0.0018	0.0008	0.0008	0.0008	0.0008	0.0012	0.0007	0.0007	0.0007	0.0007	0.0009	0.0007	0.0007	0.0006
Cu(mg L-1)***	0.0107	0.0141	0.0266	0.0941	0.0263	0.0158	0.0126	0.0111	0.0099	0.0089	0.01	0.0101	0.0093	0.009	0.0104	0.0106	0.0102	0.0172
Li(mg L-1)***	0.0196	0.0204	0.0145	0.179	0.0411	0.0291	0.025	0.0234	0.0206	0.0219	0.0239	0.0316	0.0205	0.0382	0.0202	0.0192	0.0256	0.0159
Mn(mg L-1)***	0.006	0.007	0.012	0.102	0.036	0.015	0.011	0.012	0.01	0.006	0.009	0.007	0.006	0.008	0.004	0.008	0.009	0.042
Mo(mg L-1)***	0.0282	0.027	0.0268	0.186	0.0516	0.0525	0.0452	0.0413	0.0405	0.0308	0.0359	0.0358	0.0354	0.033	0.0279	0.0332	0.0314	0.0307
Ni(mg L-1)***	0.0034	0.0052	0.0077	0.0535	0.0108	0.0069	0.0051	0.0044	0.004	0.0028	0.0039	0.004	0.0041	0.0043	0.0036	0.0047	0.0043	0.0052
Pb(mg L-1)***	0.0014	0.0007	0.001	0.0036	0.0022	0.0016	0.0031	0.0017	0.002	0.001	0.0014	0.0013	0.001	0.0011	0.0006	0.0014	0.0011	0.0014
Rb(mg L-1)***	0.0181	0.0172	0.0161	0.13	0.0289	0.0173	0.0167	0.0164	0.0167	0.0198	0.0149	0.0143	0.0145	0.0141	0.0152	0.0147	0.0139	0.0124
Sb(mg L-1)***	0.0026	0.0033	0.0034	0.0057	0.0063	0.0041	0.0039	0.0034	0.0042	0.0035	0.0038	0.0035	0.0037	0.0032	0.0022	0.0044	0.0051	0.0062
Sc(mg L-1)***	0.0001	0.0001	0.0001	0.0001	0.0001	0.0001	0.0001	0	0.0001	0.0001	0.0001	0.0001	0	0.0001	0	0	0.0001	0
Sn(mg L-1)***	0.0021	0.002	0.002	0.0071	0.0058	0.0058	0.0051	0.0051	0.0048	0.0047	0.0047	0.0046	0.0045	0.0045	0.0021	0.0044	0.0043	0.0045
Sr(mg L-1)***	0.166	0.159	0.148	0.358	0.184	0.164	0.164	0.169	0.176	0.169	0.168	0.169	0.166	0.163	0.165	0.159	0.153	0.147
Ti(mg L-1)***	0.0002	0.0002	0.0002	0.0009	0.0004	0.0002	0.0002	0.0003	0.0002	0.0005	0.0001	0.0003	0.0001	0.0001	0.0004	0.0001	0.0001	0.0002
Tl(mg L-1)***	0.0007	0.0009	0.0009	0.0026	0.0012	0.001	0.0011	0.0009	0.0009	0.0063	0.0008	0.0021	0.0015	0.0009	0.0007	0.0011	0.0008	0.0009
U(mg L-1)***	0.0009	0.0009	0.0008	0.0006	0.0006	0.0008	0.0008	0.0007	0.0008	0.0006	0.0008	0.0008	0.0008	0.0008	0.0009	0.0009	0.0009	0.0008

Table. 4.3. Continued



Summary and Conclusions

5.1. Synthesis of the results

Weathering of sulfide minerals within mine tailings impoundments, produce acid mine waters rich in SO_4^{2-} , Fe^{2+} and some toxic metals. The environmental risk of these mine waters mainly depends on the type of sulfide minerals, the presence and percentage of acid-neutralizing minerals and the predominating climate in the area. Hardpans and cemented layers might be formed in the vadose zone at the top surface of the tailings or at the boundary between the oxidized and unoxidized or rather unsaturated and saturated layers, respectively, based on the availability of reacting compounds. They might act as physical and/or chemical barriers against water and oxygen infiltration, decreasing transport of loose material and fines on the top surface of the heap and eventually for dissolved metals in the migrating fluids. These natural attenuation effects are very important for reducing the environmental impacts of mine tailings products to the surrounding environment.

The following study was carried out to investigate the role of climate on hardpan formation in mine tailings, the influence of the geochemical-mineralogical characteristics on its formation, and its effect on the attenuation of the mobilisation of toxic elements through co-precipitation/adsorption processes. In this study MLA was applied as a new method for quantification of the textural, mineralogical and chemical changes in a μm - and mm scale for a better understanding of processes relevant for mineral alteration, precipitation of secondary phases and gels guiding to the formation of hardpans. The results have lead to the following main conclusions.

5.1.1. General conclusions

Conclusion 1: Tailings sedimentology.

The investigated tailings in Germany and Egypt were subject to two different depositional methods. In Germany, the tailings were pumped to the impoundment as a sediment-water slurry and disposed by using several discharge (spigot) points. This method allowed the solid particles to settle according to the grain sizes and density leading to different sedimentary structures with vertically upward and laterally distal fining individual sequences. The heavy minerals, reactive sulfides and

carbonates were enriched in the coarser parts of the graded silicate lamina, whereas quartz, silicates and sheet silicates are quite homogeneously distributed along the profile with local accumulation of mica preferentially in the finest top layer within an individual sequence. This local enrichment of reactive phases in a grain size graded system is very effective in promoting the formation of hardpans. In contrast, Egypt tailings were disposed using a thickened discharge method, which involved recovery of a significant percentage of water in the thickening process and subsequent deposition by lorry. Due to this method, each sample within the profile is homogeneous, no grain size or mineralogical fractionations happen within individual depositional layers. Therefore hardpan formation possibility is very low because no critical amounts of reactive materials are achieved.

Conclusion 2: Tailings composition.

The relationships between the reactive acid producing and acid buffering phases, or simplified the carbonates and sulfides within the tailings is very important as it determines the alteration path of the material after mine closure. If the tailings have high amounts of reactive carbonates and low ones of reactive sulfides, the ARD potential is expected to be very low and in respect to climatic premises eventually even seldom, whereas if the reactive sulfides are higher than reactive carbonates, the formation of ARD will be potentially high. Tailings from Davidschacht, Germany, are characterized by low sulfides (1.66% for the unoxidized layers) and carbonates (0.61%). Due to the depositional mineralogical fractionation unusual mineralogical coincidence favours chemically extreme compositions, providing and linking unexpected micro-environments together in individual lamina packages. The contrasting reaction condition in each lamina is responsible for the formation of cemented layers and hardpans in the long run.

In Egypt, the carbonates content in the two tailings were very high compared to sulfides (2.39%:0.25% for Barramiya and 1.21%:0.72% for El Sid). Even so, the critical enrichment in layers was never achieved. However, El Sid has higher potential for hardpan formation than Barramiya, as it contains little higher sulfide and lower carbonate contents. This can be happen only through spigot discharge of its material and in abundance of water for the reaction.

Conclusion 3: Tailings alterations.

In the investigated μm -lamina within the different thin sections from the samples from Germany, the alteration processes appeared to be quite inhomogeneous. Different alteration stages can be observed within the same lamina. Precipitation of amorphous gels and secondary phases within the pores were localized at the contact zone of graded layers. In which very fine grained mica and chlorite fragments, store water. This overlain by coarse grained particles with high content of primary reactive sulfides and coarse open pores, providing access to oxygen and rain water to stimulate reactions. Due to the high temperatures and low water in Egypt, the tailings undergo rapid desiccation process accompanied by desiccation cracks on the top surface and limited alterations products around the sulfide grains. The possibility of hardpan formation is very low within these types of tailings, since time for reaction is quite low and the extreme evaporative conditions of the pre-thickened slimes hindered the accessibility of water on its surface during short, but heavy rain fall events.

Conclusion 4: Ions mobility and enrichments.

From column experiments it was shown that during imbibition (rising of water table), the unsaturated capillary fringe head shows a very unusual increase in electrical/fluid conductivity gaining with each step of capillary rise. On the other hand, during the drainage cycle, the electrical conductivity peak broadens and moves downward. The strong increase during imbibitions was attributed to the fast rising capillary head fluids, which quickly accumulated all available ions around the particles and moved upward. In contrast, the water in the lower part of the column became depleted in most of the ions, and showed even a different ion distribution pattern due to slowly reacting minerals and on site precipitation. These processes are very important in the precipitation at the contact between the saturated/unsaturated zones and responsible for hardpan formation. But, it has to be taken into account that only small part of the precipitating phases will be stable on the long term and may contribute to hardpan formation. The bulk of the efflorescence will re-dissolve and re-precipitate, if not flushed away.

Conclusion 5: Climate.

Climate is considered to be one important parameter affecting hardpan formation as it controls in major part the fluid mobility direction, water table fluctuations, and therefore oxidation/precipitation reactions. In column tests homogeneously filled with unoxidized material from Davidschacht, Germany, the influence of temperature and amount of water input was monitored. Soluble efflorescent sulfates were the first secondary phases produced during column experiments, especially in columns with higher temperature. These sulfates completely dissolved during the first raining event. Efflorescence from columns of lower temperatures formed later. With continuous drying and raining cycles, these soluble efflorescent sulfates disappeared and substituted by more stable phases like gypsum filling the pores on the top surface. From the mineralogical point of view, phases favouring high temperature ranges like bassanite were found in high temperature columns and phases stables in low to medium temperature range like gypsum were detected in low-medium temperature columns. Also, the shape, distribution of gypsum and Mg-sulfates were found to be different within columns of different water and temperature. Elevated temperatures in the columns caused after some imbibition/evaporation cycles a washout of the top layer accompanied with a shift in evaporation to slightly deeper levels and therefore displacement of the precipitation zone.

Conclusion 6: Elements attenuation.

Amorphous gels and secondary crystalline phases which precipitated within the hardpans played an important role in attenuating some of the toxic elements as a result of adsorption/co-precipitation processes. Amorphous gels showed the possibility to store large percentage of As reaching 39.4% in Davidschacht mine tailings in addition to other elements like Pb (6.8%) and Zn (6.2%). Whereas jarosite contains 15.6% As, 1.8% Zn and 1.5% Pb and gypsum contain As of about 1.4%. In column experiments, As, Pb and other elements showed higher concentrations in the upper surface layers due to the co-precipitation within the efflorescent sulfates. The physical and chemical stability, and also future accessibility of these toxic element attenuating phases under changing environmental conditions are key points for the long term retention capacity of a tailings impoundment.

5.1.2. Specific conclusions

The understanding of the development of hardpans from the bulk analysis of samples from mine tailings impoundments only is not possible, but requires a detailed knowledge of the sedimentation induced micro-environmental structure controlling the alteration progress at the rim and the core of the impoundment. Furthermore, it is difficult to obtain a definite measure of the status of an impoundment concerning the alteration lifetime, or rather to predict the ARD potential.

In this thesis, detailed investigations on the textural relationships between the different lamina elucidate the real interactions between the different phases. It was shown that the oxidation surface is irregular, depending on the grain size layering and the distribution of the reactive phases which showed rhythmic repetition of heavy -minerals-rich and sulfides-rich lamina, silicate-rich lamina, and carbonate-rich lamina in case of spigot tailings discharge (Germany case). On the other hand the homogeneous distribution of all the phases in thickened tailings discharge (Egypt case) shows only incipient alteration due to rapid desiccation in the area. Porosity changes, from relatively homogeneous distribution in the unaltered material to its reduction at certain horizons within hardpans are obvious. The effect of sandwich structures in the laminated tailings is responsible for enhanced hardpan formation within a thin boundary layer through the precipitation of secondary phases. The availability of different reactive materials in the immediate vicinity to each other cannot be detected without the help of micro -analytical instrumentation, nor quantified without MLA or adequate methods, providing the sound basis for more accurate modelling.

Column experiments, performed in the laboratory over long periods, are the best way to get insight into processes controlling the progress of different interactions of minerals, water, oxygen, temperature, element mobility, conductivity changes with time. These detailed investigations can only be done by using different techniques and sensors to monitor changes during the whole process. This information cannot be unravelled in the field due to the difficulty of its application on large-scale over long terms. From our column experiments, it can be deduced that within the first few months of tailings deposition, the reactions run slowly.

In dry climate areas, availability of oxygen is in general provided, so water is the principal rate determining factor for oxidation of reactive sulfides which takes place within the upper part of the columns or tailings, being accompanied by upward migration of ions related to this process. In humid climate areas, the accessibility for oxygen is controlled by the water content, therefore both,

water and oxygen are the rate determining factors, in addition to other basic factors like the presence of bacteria, grain surface area, etc. Within the column test, the oxygen infiltration progress relates to the temperature applied to the surface, and therefore the enhancement of evaporation. In case of high temperature columns, the oxygen infiltrated quickly, already after a few days to very deep levels of the column following the moving water table, whereas at lower temperatures deep levels were reached much later. The ion transport direction up-/down-ward depend on the imbibition and drying events, driven by gravity and capillary transport, respectively. This controls water table fluctuations and offers therefore different precipitations positions. The long term fixation of mobilized ions as freshly precipitated secondary phases such as sulfates, hydroxides, and gels, is related to their stability and/or accessibility in the newly formed crusts.

5.2. Outlook

Micro-scale identifications, measurements and quantifications become essential parameters rather than the traditionally normal bulk analyzing methods. With the new adaptation of MLA techniques to the tailings environment, a more realistic prediction of the tailings behaviour can be achieved. Acid-base accounting test can be applied easily on MLA results for different lamina and it will be more effective than usual methods based on bulk chemical/mineralogical analysis. Combined methods like MLA and micro-XRD, micro-Raman and micro-LIBS will be useful especially for mineral identification and for following chemical changes of amorphous phases with time. Pore-scale modelling, applying reactive transport models such as FLOTRAN and TOUGHREACT, are required to follow the alterations/porosity changes with time. With the new developments of tools used in ESEM, like heating system, in-situ information on stability of amorphous gels as sinks for large proportions of toxic elements, and information on the crystallization of more stable phases out of complex gels under defined temperature conditions can be gained. These new approaches will be very useful for future remediation strategies.

REFERENCES CITED

- Ahn JS, Park YS, Kim J-Y, Kim K-W. Mineralogical and geochemical characterization of arsenic in an abandoned mine tailings of Korea. *Environ Geochem and Health* 2005; 27:147-157.
- Airo M-L, Loukola-Ruskeeniemi K. Characterization of sulfide deposits by airborne magnetic and gamma-ray responses in eastern Finland. *Ore Geol Rev* 2004;24:67–84.
- Akin S, Kovscek AR. Computed tomography in petroleum engineering research. In: Mees F et al., editors. *Application of x-ray computed tomography in the geosciences*. Spec. Publ. 215. Geological Society, London 2003: 231–238.
- Akpokodje EG. The occurrence of bassanite in some Australian arid-zone soils. *Chem Geol* 1984;47:361-364.
- Al TA, Blowes DW. The hydrogeology of a tailings impoundment formed by central discharge of thickened tailings: implications for tailings management *J Contam Hydrol* 1999;38:489-505.
- Alakangas L, Öhlander B. Formation and composition of cemented layers in low-sulphide mine tailings, Laver, northern Sweden. *Environ Geol* 2006;50: 809-819.
- Alderton DHM, Pearce JA, Potts PJ. Rare earth element mobility during granite alteration: Evidence from southwest England. *Earth and Planetary Science Letters* 1980; 49: 149-165.
- Allen RD, Kramer H. Occurrence of bassanite in two desert basins in southeastern California. *Amer Mineral* 1953;38:1266–1268.
- Allison JD, Brown DS, Novo-Gradac KJ. MINTEQA2/PRODEFA2, a geochemical assessment model for environmental systems-version 3.0 user's manual: Environmental Research Laboratory, Office of Research and Development, U.S. Environmental Protection Agency, Athens, Georgia; 1990, 106 p.
- Anderson SH, Gantzer CJ, Boone JM, Tully RJ. Rapid nondestructive bulk density and soil-water content determination by computed tomography. *Soil Sci Soc Am J* 1988;52:35–40.
- Anderson SH, Peyton RL, Gantzer CJ. Evaluation of constructed and natural soil macropores using x-ray computed tomography. *Geoderma* 1990;46:13–29.

References Cited

- Archie GE. The electrical resistivity log as an aid in determining some reservoir characteristics. *Trans. Am. Inst. Mining Metallurgic. Petrol Eng.* 1942;146:54–62.
- Attia MI. Geology of the Barramiya mining district. Geological Survey of Egypt, Cairo, 1948;76p.
- Banwart SA, Malmström ME. Hydrochemical modelling for preliminary assessment of minewater pollution. *J Geochem Explor* 2001;74:73–97.
- Basilio CI, Kartio IJ, Yoon R-H. Lead activation of sphalerite during galena flotation. *Min. Eng* 1996;9:869–879.
- Bau M. Scavenging of dissolved yttrium and rare earths by precipitating iron hydroxide: experimental evidence for Ce oxidation, Y–Ho fractionation, and lanthanide tetrad effect. *Geochim Cosmochim Acta* 1999;63:67–77.
- Baumann L, Kuschka E, Seifert T. *Die Lagerstätten des Erzgebirges*. Enke im Georg Thieme Verlag, Stuttgart, New York; 2000.
- Bayer A, Vogel H-J, Roth K. Direct measurement of the soil water retention curve using x-ray absorption. *Hydrol Earth Syst Sci* 2004;8:2–7.
- Behre Dolbear international limited. NI43-101 technical report on the Fawakhir/El Sid 2009;1-53.
- Bigham JM, Schwertmann U, Pfab G. Influence of pH on mineral speciation in a bioreactor simulating acid mine drainage. *Appl Geochem* 1996;11:845-849.
- Blowes DW, Jambor JL. The pore-water chemistry and the mineralogy of the vadose zone of sulfide tailings, Waite Amulet, Quebec. *Appl Geochem* 1990;5:327–346.
- Blowes DW, Reardon EJ, Jambor JL, Cherry JA. The formation and potential importance of cemented layers in inactive sulfide mine tailings. *Geochim Cosmochim Acta* 1991;55:965-978.
- Blowes DW, Ptacek CJ, Jambor JL. Remediation and prevention of low-quality drainage from Tailings impoundments. In: Jambor JL, Blowes DW, editors. *Short Course Handbook on Environmental Geochemistry of Sulfide Mine-Wastes*. Mineral Assoc Canada 1994;22:365–379.

References Cited

- Blowes DW, Al T, Lortie L, Gould WD, Jambor JL. Microbiological, chemical and mineralogical characterization of the Kidd Creek mine tailings impoundment, Timmins area, Ontario. *Geomicrobiol J* 1995;13:13–31.
- Blowes DW, Jambor JL, Hanton-Fong CJ. Geochemical, mineralogical and microbiological characterization of a sulphide-bearing carbonate-rich gold-mine tailings impoundment, Joutel, Québec. *Appl Geochem* 1998;13:687-705.
- Botros NS. A new classification of the gold deposits of Egypt. *Ore Geology Reviews* 2004;25:1-37.
- Boxma R. Mobility of iron in the estuaries of the Rhine and the EMS relevant to plant-availability problems. *Plant and Soil* 1976;44:407-422.
- Brunauer S, Emmett P H, Teller E. Adsorption of gases in multimolecular layers. *J Am Chem Soc* 1938;60:309-319.
- Brooks RA, Di Chiro G. Theory of image reconstruction in computed tomography. *Radiology* 1975;117:561–572.
- Broughton LM, Robertson AM. Acid Rock Drainage from Mines - Where We Are Now. IMM Minerals, Metals and Environment Conference, February 4-6, Manchester, UK 1992.
- Brown JM, Fonteno WC, Cassel DK, Johnson GA. Computed tomographic analyses of water distribution in three porous foam media. *Soil Sci Soc Am J* 1987;51:1121–1125.
- Carmona DM, Faz Cano Á, Arocena JM. Cadmium, copper, lead, and zinc in secondary sulfate minerals in soils of mined areas in Southeast Spain. *Geoderma* 2009;150:150-157.
- Chinh PD. Electrical properties of sedimentary rocks having interconnected water-saturated pore spaces. *Geophysics* 2000;65:1093–1097.</jrn>
- Choi C, Bharatam J, Frola I, Dusseault MB, Geilikman MB, Chatzis J, Pintar MM. Monitoring of gravity drainage of water and light oil through a sand column by proton nuclear magnetic resonance. *Appl. Phys. Lett.* 1997;71:3436–3438.
- Collins WH, Easley DH. Fresh-water lens formation in an unconfined Barrier-Island aquifer. *J. Am Water Resour Assoc* 1999;35:1–21. Cross W, Iddings JP, Pirsson LV, Washington HS. A quantitative chemico-mineralogical classification and nomenclature of igneous rocks. *J Geol* 1902;10:555–590.

References Cited

- Courtin-Nomade A, Brila H, C. Neela, Lenain J-F. Arsenic in iron cements developed within tailings of a former metalliferous mine—Enguialès, Aveyron, France. *Applied Geochemistry* 2003;18:395–408.
- Courtin-Nomade A, Grosbois C, Marcus MA, Fakra SC, Beny J-M, Foster AL. The weathering of a sulfide orebody: speciation and fate of some potential contaminants. *The Canadian Mineralogist* 2009;47:493-508.
- Cussler EL. *Diffusion - Mass Transfer in Fluid Systems*, 2nd Ed., Cambridge University Press, 1997.
- Davies MP, Martin TE. Upstream constructed tailings dams- a review of the basics. In: *Proceedings of the Seventh International Conference on Tailings and Mine Waste'00*. Fort Collins, Colorado, USA, 23-26 January 2000, Balkema, Rotterdam, pp3-15.
- Davis GB, Ritchie AIM. A model of oxidation in pyritic mine waste: part 3: import of particle size distribution. *Appl Math Modelling*, 1987;11: 417-422.
- de Lima OAL, Sharma MM. A grain conductivity approach to shaly sandstones. *Geophysics* 1990;55:1347–1356.
- DeSisto SL. *Dynamic Arsenic Cycling in Scorodite-Bearing Hardpan Cements, Montague Gold Mines, Nova Scotia*. Msc Thesis, Queen's University, Kingston, Ontario, Canada 2008, 222p.
- Dill HG, Pöllmann H, Bosecker K, Hahn L, Mwiya S. Supergene mineralization in mining residues of the Matchless cupreous pyrite deposit (Namibia)—a clue to the origin of modern and fossil duricrusts in semiarid climates. *Journal of Geochemical Exploration* 2002;72:43-70.
- Dobbe R, Gottlieb P, Gu Y, Butcher AR, Fandrich R, Lemmens H. Scanning Electron Beam-Based Automated Mineralogy—Outline of Technology and selected applications in the Natural Resources Industry. *EMAS 2009*. 11th European Workshop on Modern Development and Applications in Microbeam Analysis, Gdynia/Rumia, Gdansk, Poland; 10-14 May 2009. p.169-189.
- Dold B. *Basic Concepts of Environmental Geochemistry of Sulfide Mine-Waste*. Decimo Noveno Curso Internacional De Postgrado En Metalogenia"UNESCO Society of Economic Geologists (SEG), 12th – 20th June 2000, QUITO-ECUADOR.

References Cited

- Dold B. Speciation of the most soluble phases in a sequential extraction procedure adapted for geochemical studies of copper sulfide mine waste. *J Geochem Explor* 2003;80:55–68.
- Dold B, Fontboté L. Element cycling and secondary mineralogy in porphyry copper tailings as a function of climate, primary mineralogy, and mineral processing. *J Geochem Explor* 2001;74:3 – 55.
- Dold B, Fontboté L. A mineralogical and geochemical study of element mobility in sulfide mine tailings of Fe oxide Cu–Au deposits from the Punta del Cobre belt, northern Chile. *Chemical Geol* 2002;189:135– 163.
- Dove PM, Rimstidt JD. The solubility and stability of scorodite, $\text{FeAsO}_4 \cdot 2\text{H}_2\text{O}$. *American Mineralogist* 1985;70:838-844.
- Dutrizac JE, Jambor JL. Jarosites and their application in hydrometallurgy. In: Alpers CN, Jambor JL, Nordstrom DK, editors. *Sulfate Minerals: Crystallography, Geochemistry, and Environmental Significance*, *Rev Mineral Geochem* 2000;40:405–452.
- Dutrizac JE, MacDonald RJC. The effect of some impurities on the rate of chalcopyrite dissolution. *Can Metall Quart* 1973;12:409–420.
- Elbaz-Poulichet F, Dupuy C. Behaviour of rare earth elements at the freshwater- seawater interface of two acid mine rivers: the Tinto and Odiel (Andalucia, Spain). *Appl Geochem* 1999;14:1063-1072.
- Elberling B, Nicholson RV, Scharer JM. A combined kinetic and diffusion model for pyrite oxidation in tailings: a change in controls with time. *J Hydrol*, 1994;157: 47-60.
- EI-Bouseily AM, EI-Dahhar MA, Arslan AI. Ore-microscopic and geochemical characteristics of gold-bearing sulfide minerals, El Sid Gold Mine, Eastern Desert, Egypt. *Mineralium Deposita* 1985;20: 194-200.
- El Ramly MF, Ivanov SS, Kochin GC, Bassyouni FA, Abdel Aziz AT, Shalaby IM, El Hammady MY. The occurrence of gold in the Eastern Desert of Egypt. In: Moharram O, Gachechiladze DZ, El Ramly MF, Ivanov SS, Amer AF, editors. *Studies on some mineral deposits of Egypt. Part I, Sec. A, Metallic Minerals*, *Geol Surv Egypt* 1970;21:53-64.

References Cited

- Evangelou VP, Zhang YL. A Review: Pyrite oxidation mechanisms and acid mine drainage prevention. *Crit Rev Environ Sci Technol* 1995;25:141-199.
- Fandrich R, Gu Y, Burrows D, Moeller K. Modern SEM-based mineral liberation analysis. *Int J Miner Process* 2007;84:310–320.
- Fernández-Caliani JC, Barba-Brioso C, DelaRosa JD. Mobility and speciation of rare earth elements in acid minesoils and geochemical implications for river waters in the southwestern Iberian margin. *Geoderma* 2009; 149:393-401.
- Ferreira da Silva E, Bobos I, Xavier Matos J, Patinha C, Reis AP, Cardoso Fonseca E. Mineralogy and geochemistry of trace metals and REE in volcanic massive sulfide host rocks, stream sediments, stream waters and acid mine drainage from the Lousal mine area (Iberian Pyrite Belt, Portugal). *Appl Geochem* 2009;24:383–401.
- Fitzpatrick RW, Baker AKM, Raven M, Rogers S, Degens B, George R, Kirby J. Mineralogy, biogeochemistry, hydro-pedology and risks of sediments, salt efflorescences and soils in open drains in the wheatbelt of western australia . In: Roach IC, editor. *Regolith 2005 – Ten Years of CRC LEME*, pp. 97-101.
- Fleury M, Boyd D, Al-Nayadi K. Water Saturation from NMR, Resistivity and oil-base core in a heterogeneous middle-east carbonate reservoir. *Petrophysics* 2006;47:60–73.
- Flynn D, Mcnamara H, O’Kane P, Pokrovskü A. Application of the Preisach model to soil-moisture hysteresis. In: Bertotti G, Mayergoyz I, editors. *The Science of Hysteresis*. Academic Press, New York 2006;689–744.
- Folk RL, Ward WC. Brazos River bar, a study in the significance of grain-size parameters. *J Sedimentary Petrology* 1957;27: 3-27.
- Furche M, Meima JA, Graupner T, Grisse mann C, Rammlmair D. Transport in mine tailings: Geophysical monitoring and reactive transport modelling. In: Andrew CJ et al., editors. *Digging deeper: Proc. of the Ninth Biennial SGA Meeting, 2007, Dublin, Ireland. SGA, Switzerland* 2007;1295–1298.

References Cited

- Garnier P, Angulo-Jaramillo R, DiCarlo D A, Bauters TWJ, Darnault CJG, Steenhuis TS, Parlange J-Y, Baveye P. Dual-energy synchrotron X ray measurements of rapid soil density and water content changes in swelling soils during infiltration, *Water Resour Res* 1998;34:2837-2842.
- G.E.O.S. Freiberg Ingenieuresellschaft mbH. Kurzbericht zur Gefährdungsabschätzung der Davidschicht-Spülhalde, Freiberg, März 1993.
- Ghodrati M, Chendorain M, Chang YJ. Characterization of macropore flow mechanisms in soil by means of a split macropore column. *Soil Sci Soc Am J* 1999;63:1093–1101.
- Ghoneim EM, Arnell NW, Foody GM. Characterizing the flash flood hazards potential along the Red Sea coast of Egypt. *The Extremes of the Extremes: Extraordinary Floods. IAHS Publ* 2002;271: 211- 216.
- Gimeno MJ, Auqué LF, Nordstrom DK. REE speciation in low-temperature acidic waters and the competitive effects of aluminum. *Chem Geol* 2000;165:167-180.
- Glover PWJ, Gome JB, Meredith PG, Boon SA, Sammonds PR, Murrell SAF. Modelling the stress-strain behaviour of saturated rocks undergoing triaxial deformation using complex electrical conductivity measurements. *Surv Geophys* 1996;17:307–330.
- González RC, González-Chávez MC. Metal accumulation in wild plants surrounding mining wastes. *Environ Pollut.* 2006;144:84-92.
- Gorbach LP, Suprychev VA, Shekhotin VV. Jarosite pseudomorphs of iron sulfides from Maikop formations of mountainous Crimea. *Dokl Akad Nauk SSR* 1967;173:413-416.
- Graupner T, Kassahun A, Rammlmair D, Meima JA, Kock D, Furche M, Fiege A, Schippers A, Melcher F. Formation of sequences of cemented layers and hardpans within sulfide-bearing mine tailings (mine district Freiberg, Germany). *Appl Geochem* 2007;22:2486–2508.
- Greenbaum N, Margalit A, Schick AB, Backer, VR. A high magnitude storm and flood in a hyperarid catchment, Nahal Zin, Negev Desert, Israel. *Hydrol Processes* 1998;12: 1-23.
- Gu Y. Automated Scanning Electron Microscope Based Mineral Liberation Analysis: An Introduction to JKMRC/FEI Mineral Liberation Analyser. *Journal of Minerals & Materials Characterization & Engineering* 2003;2:33-41.

References Cited

- Gunsinger MR, Ptacek CJ, Blowes DW, Jambor JL, Moncur MC. Mechanisms controlling acid neutralization and metal mobility within a Ni-rich tailings impoundment. *Appl Geochem* 2006;21:1301-1321.
- Hänsel S, Matschullat J. Drought in a Changing Climate, Saxon Dry Periods. *Bioclimatology and water in the land*. International scientific conference, Strecno, Slovakia;11–14 September 2006.
- Haffert L, Craw D. Mineralogical controls on environmental mobility of arsenic from historic mine processing residues, New Zealand. *Appl Geochem* 2008;23:1467–1483.
- Haines WB. Studies on the physical properties of soils: V. The hysteresis effect in capillary properties, and the modes of moisture distribution associated therewith. *J Agric Sci.* 1930;20:97–116.
- Hammarstrom JM, Seal II RR, Meier AL, Kornfeld JM. Secondary sulfate minerals associated with acid drainage in the eastern US: recycling of metals and acidity in surficial environments. *Chemical Geology* 2005; 215 407- 431.
- Harinarayana T, Naganjaneyulu K, Patro BPK. Detection of a collision zone in south Indian shield region from magnetotelluric studies. *Gondwana Res* 2006;10:48–56.
- Heijs AWJ, de Lange J, Schoute JFT, Bouma J. Computed tomography as a tool for non-destructive analysis of flow patterns in macroporous clay soils. *Geoderma* 1995;64:183–196.
- Henke KR. Arsenic in natural environments. In: Henke KR, editor. *Arsenic environmental chemistry, health threats and waste treatment*. John Wiley & Sons Publications 2009;69-235.
- Hoffmann-Rothe A, Ritter O, Janssen C. Correlation of electrical conductivity and structural damage at a major strike-slip fault in northern Chile. *J Geophys Res* 2004;109:B10101.
- Hollocher K. CIPW norm program. Geology Dep., Union College, Schenectady, NY. Available at http://minerva.union.edu/hollochk/c_petrology/programs/norm4.xls (verified 19 July 2010) 1999.
- Hopmans JW, Vogel T, Koblík PO. X-ray tomography of soil water distribution in one-step outflow experiments. *Soil Sci Soc Am J* 1992;56:355–362.

References Cited

- Hussein AA. Mineral deposits. In: Said R (Ed.), *The Geology of Egypt*. Balkema, Rotterdam 1990;511– 566.
- Ingle JD, Crouch SR. *Spectrochemical analysis*. Prentice Hall, Englewood Cliffs, NJ 1988.
- Jambor JL. Mine-waste mineralogy and mineralogical perspectives of acid-base accounting. In: Jambor JL, Blowes DW, Ritchie AIM, editors. *Environ Aspects of Mine Wastes*. Mineral Assoc Can Short Course 2003;31:117-145.
- Jambor JL, Blowes DW. Mineralogical study of low-sulfide, high-carbonate, arsenic bearing tailings from the Delnite minesite, Timmins area, Ontario. In *Second International Conference on the Abatement of Acidic Drainage 4*. CANMET, Natural Resources Canada, Ottawa, Ontario 1991;173-198.
- Jambor JL, Dutrizac JE, Groat LA, Raudsepp M. Static tests of neutralization potentials of silicate and aluminosilicate minerals. *Environ Geol* 2002; 43: 1-17.
- Johnson RH, Blowes DW, Robertson WD, Jambor JL. The hydrogeochemistry of the Nickel Rim mine tailings impoundment, Sudbury, Ontario. *J Contam Hydrol* 2000;41:49–80.
- Jones AG, Katsube TJ, Schwann P. The longest conductivity anomaly in the world explained: Sulphides in fold hinges causing very high electrical anisotropy *J Geomagn Geoelectric* 1997;49:1619–1629.
- Jung HG. *Secondary Processes in Mine Dumps and Tailings Impoundments-Control of Metal Mobility and Hardpan Formation*. Unpublished PhD thesis, Marburg University, Germany 2003.
- Katsube TJ, Mareschal M. Petrophysical Model of deep electrical conductors: Graphite lining as a source and its disconnection due to uplift. *J Geophys Res* 1993;98:8019–8030.
- Ketcham RA, Carlson WD. Acquisition, optimization and interpretation of x-ray computed tomographic imagery: Applications to the geosciences. *Comput Geosci* 2001;27:381–400.
- Klemm D, Klemm R, Murr A. Gold of the Pharaohs – 6000 years of gold mining in Egypt and Nubia. *African Earth Sciences* 2001;33:643–659.
- Knight R. Hysteresis in the electrical resistivity of partially saturated sandstones. *Geophysics* 1991;56:2139–2147.

References Cited

- Kochin GG, Bassyuni FA. Mineral resources of the UAR. Report on the generalisation of geologic data on mineral resources in the UAR, carried out under contract 1247 (1966 to 1968), part I: Metallic minerals. Internal Report 18/68, Geol Surv Egypt 1968.
- Korb JP, Godefroy S, Fleury M. Surface nuclear magnetic relaxation and dynamics of water and oil in granular packings and rocks. *Magn Reson Imaging* 2003;21:193–199.
- Kunov A, Mandova E. Supergene minerals in the Obichnik Au-Ag deposit (Eastern Rhodopes). *Spis Bulg Geol Druzh* 1997;58:19-24.
- Landmesser L. Liesegang ring and the problem of self-organization in agates. In: Johann Wolfgang Goethe Universität Frankfurt/M. (Hrsg). Book of abstracts of the 2nd International Symposium on Fractals and Dynamic system in Geoscience (April 4-7), 1995, Gelnhausen, Frankfurt am Main: 40-43.
- Langmuir D, Mahoney J, Rowson J. Solubility products of amorphous ferric arsenate and crystalline scorodite ($\text{FeAsO}_4 \cdot 2\text{H}_2\text{O}$) and their application to arsenic behaviour in buried mine tailings, *Geochim Cosmochim Acta* 2006;70: 2942–2956.
- Lasaga AC, Berner RA. Fundamental aspects of quantitative models for geochemical cycles. *Chem Geol* 1998;145:161-175.
- Lee SY, Gilkes RJ. Groundwater geochemistry and composition of hardpans in southwestern Australian regolith. *Geoderma* 2005;126:59–84.
- Logsdon SD, Laird DA. Electrical conductivity spectra of smectites as influenced by saturating cation and humidity. *Clays Clay Miner* 2004;52:411–420.
- Longeron DG, Argaud MJ, Feraud JP. Effect of overburden pressure and the nature and microscopic distribution of fluids on electrical properties of rock samples. *SPE Format Eval* 1989;4:194–202.
- Lottermoser, B.G. 2003. *Mine Wastes: Characterization, Treatment and Environmental Impacts*. Springer-Verlag Berlin Heidelberg, 277p.
- Lottermoser BG, Ashley PM. Mobility and retention of trace elements in hardpan-cemented cassiterite tailings, north Queensland, Australia. *Environ Geol* 2006;50:835–846.
- McDonough WF, Sun S-S. The composition of the Earth. *Chem. Geol.* 1995;120:223–253.

References Cited

- McGregor RG, Blowes DW. The physical, chemical and mineralogical properties of three cemented layers within sulfide-bearing mine tailings. *J Geochem Explor* 2002;76:195–207.
- McGregor RG, Blowes DW, Jambor JL, Robertson WD. The solid-phase controls on the mobility of heavy metals at the Copper Cliff tailings area, Sudbury, Ontario, Canada. *J Contam Hydrol* 1998;33:247–271.
- McGregor RG, Blowes DW. The physical, chemical and mineralogical properties of three cemented layers within sulfide-bearing mine tailings. *J Geochem Expl* 2002; 76:195–207.
- Michael G. X-ray computed tomography. *J Phys Educ*2001;36:442–451.
- Meima JA, Graupner T, Rammlmair D. Modeling the effect of stratification on cemented layer formation in sulfide-bearing mine tailings. Submitted to *Appl Geochem*.
- Mendez MO, and Maier RM. Phytostabilization of mine tailings in arid and semiarid environments - An emerging remediation technology. *Environ. Health Perspect.* 2008;116: 278–283.
- Moncur MC, Ptacek CJ, Blowes DW, Jambor JL. Release, transport and attenuation of metals from an old tailings impoundment. *Appl Geochem* 2005; 20: 639–659.
- Mori Y, Maruyama T, Mitsuno T. Soft x-ray radiography of drainage patterns of structured soils. *Soil Sci Soc Am J* 1999;63:733–740.
- Morin G, Calas G. Arsenic in soils, mine tailings, and former industrial sites. *Elements* 2006;2:97–101.
- Nesbitt HW. Mobility and fractionation of rare elements during weathering of a granodiorite. *Nature* 1979;279:206–210.
- Nesbitt HW, Muir IJ, Pratt AR. Oxidation of arsenopyrite by air and air-saturated, distilled water, and implications for mechanism of oxidation. *Geochim Cosmochim Acta* 1995;59: 1773 – 1786.
- Nieto JM, Sarmiento AM, Olías M, Canovas CR, Riba I, Kalman J, Delvalls TA. Acid mine drainage pollution in the Tinto and Odiel rivers (Iberian Pyrite Belt, SW Spain) and bioavailability of the transported metals to the Huelva Estuary. *Environment International* 2007;33:445–455.

References Cited

- Nimmo JR. Film flow in macro- and micropores: How much unsaturated-zone hydrology can it explain? *Eos Trans. Am Geophys Union*. Fall Meeting Supplement 89(53), Abstract H51I-0984 2008.
- Nordstrom DK. Aqueous pyrite oxidation and the consequent formation of secondary iron minerals. In: Kittrick JA, Fanning DS, Hossner LR, Kral DM, Hawkins S, editors. *Acid sulfate weathering*. *Soil Sci Soc Am* 1982:37-56.
- Nordstrom DK, Jenne EA, Ball JW. Redox equilibria of iron in acid mine waters. In: Jenne EA, editor. *Chemical modeling in aqueous systems*. *Am Chem Soc Symp Washington, D.C.* 1979;93:51-79.
- Nordstrom DK, Alpers CN. Geochemistry of acid mine waste. In: Plumlee GS, Logsdon MJ, editors. *Reviews in Economic Geology: the environmental geochemistry of ore deposits. Part A: Processes, techniques and health issues* 1996;6A:133-160.
- Ohkubo T, Kikuchia H, Yamaguchi M. An approach of NMR relaxometry for understanding water in saturated compacted bentonite. *Phys Chem Earth* 2008;33:S169–S176.
- Olanipekun EO. Kinetics of sphalerite leaching in acidic ferric chloride solutions. *Trans Indian Inst Metall* 1999;52:81–86.
- Paktunc D, Foster A, Heald S, Laflamme G. Speciation and characterization of arsenic in gold ores and cyanation tailings using X-ray absorption spectroscopy. *Geochim Cosmochim Acta* 2004;68:969–983.
- Parkhurst DL, Appelo CAJ. *User's Guide to PHREEQC (Version 2)-A Computer Program for Speciation, Batch-Reaction, One-Dimensional Transport, and Inverse Geochemical Calculations*. *Water Resources investigations report 99-4259*;1999, 312p.
- Petrovic AM, Siebert JE, Rieke PE. Soil bulk density analysis in three dimensions by computed tomographic scanning. *Soil Sci Soc Am J* 1982;46:445–450.
- Plumlee GS. The environmental geology of mineral deposits. In: Plumlee GS, Logsdon MJ, editors. *Reviews in Economic Geology, the Environmental Geochemistry of Mineral Deposits, Part A. Processes, Techniques and Health Issues* 1999;6A:71-116.

References Cited

- Pring A, Tarantino SC, Tenailleau C, Etschmann B, Carpenter MA, Zhang M, Liu Y, Withers RL. The crystal chemistry of Fe-bearing sphalerites: an infrared spectroscopic study. *Am Mineral* 2008;93:591–597.
- Rammlmair, D. The role of gels in self organisation of slagheaps from the arsenic production site Muldenhütten, Freiberg, Saxony, FRG. In: *Proceedings of Fifth International Congress Applied Mineralogy in the Minerals Industry*, Warsaw, Subdan-Druk, Warszawa, Poland, 1996;378–382.
- Rammlmair D. Hard pan formation on mining residuals. In: Merkel B, Planer-Friedrich B, Wolkersdorfer C, editors. *Uranium in the Aquatic Environment*. In: *Proceedings of International Conference Uranium Mining and Hydrogeology III and International Mine Water Association Symposium*. TU Bergakademie Freiberg, Germany 2002:173–182.
- Rammlmair D, Meyer L. Crust Formation: via Column Experiments to mathematical Modelling. In: Rammlmair D, Mederer J, Oberthür Th, Heimann RB, Pentinghaus H, editors. *Applied mineralogy in research, economy, technology, ecology and culture*. Proc.6th International Congress on Applied Mineralogy, ICAM 2000, Göttingen, Germany, 17-19 July 2000;2:641-644.
- Rammlmair D, Grisseemann Ch. Natural Attenuation in slag heaps versus remediation. In: Rammlmair D, Mederer J, Oberthür Th, Heimann RB, Pentinghaus H, editors. *Applied mineralogy in research, economy, technology, ecology and culture*. Proc.6th International Congress on Applied Mineralogy, ICAM 2000, Göttingen, Germany, 17-19 July 2000;2:645-648.
- Rammlmair D, Tacke K-D, Jung H. Application of new XRF-scanning techniques to monitor column experiments. In *Proc of the Int Conf. on Mining and the Environment: Securing the Future*. vol. 6a. Skellefteå. 25 June–1 July 2001. The Swedish Mining Association, Sweden 2001;683–692.
- Rammlmair D, Wilke M, Rickers K, Schwarzer RA, Möller A, Wittenberg A. Geology, mining, metallurgy. In: Beckhoff B et al., editors. *Handbook of practical x-ray fluorescence analysis*. Springer, Heidelberg 2006;640–687.

References Cited

- Rammlmair D, Grisseemann C, Furche M, Noell U, Graupner T, Meima JA, Romero-Baena A. Evidence of reduced water infiltration by microhardpans-electrical resistivity measurements at Peña de Hierro, Rio Tinto, Spain. In Proc. of the 9th Int. Congress for Applied Mineralogy, ICAM 2008, Brisbane, 8–10 Sep. 2008. The Australasian Institute of Mining and Metallurgy, Pub. Series No 8/2008. The Australasian Institute of Mining and Metallurgy, Australia 2008a; 349–356.
- Rammlmair D, Grisseemann C, Graupner T, JA Meima, Romero-Baena A. Acid mine drainage remediation starts at the source. In: González Díez I, Romero Baena A, invited editors. Post mining problems related to polymetallic sulfide mining. Macla 10, 17–19 Nov. 2008, Spanish Society of Mineralogy, Sevilla, Spain 2008b;29–33.
- Raper RL, Schwab EB, Dabney SM. Measurement and variation of site specific hardpans for silty upland soils in the Southeastern United States. Soil and Tillage Research 2005;84:7-17.
- Redwan M, Rammlmair D. Simultaneous Monitoring of Water Saturation and Fluid Conductivity in Unconsolidated Sand Columns. SSSAJ 2010;74:1457-1468.
- Rifai H, Kappes R, Kischkies S, Furche M, Schmerler J, Rammlmair D, Wonik T. NMR—Investigations on with electrodes equipped liners to determine transport processes (In German). In Abstracts, Annu Meet, German Geophysical Society, 6-9 Mar. 2006, p. 502, Bremen, Germany 2006.
- Rimstidt JD, Chermak JA, Gagen PM. Rates of reaction of galena, sphalerite, chalcopyrite, and arsenopyrite. In: Alpers CN, Blowes DW, editors. Environmental Geochemistry of Sulfide Oxidation. American Chemical Society, Washington, DC 1994;550:2–13.
- Ripley EA, Redmann RE, Crowder AA. Environmental effects of mining. St lucie Press, Delray Beach 1996; 356 p.
- Roberts JJ, Lin W. Electrical properties of partially saturated topopah spring tuff: Water distribution as a function of saturation. Water Resour Res 1997a ;33:577–587.
- Roberts JJ, Lin W. X-ray radiography of fracture flow and matrix imbibition in topopah spring tuff under a thermal gradient. Int J of Rock Mechanics & Mining Sci 1997b;34: 259.e1 - 259.e12.

References Cited

- Robertson WD. The physical hydrogeology of mill-tailings impoundments. In: Jambor JL, Blowes DW, editors. Short Course Handbook on Environmental Geochemistry of Sulfide Mine-wastes, Mineralogical Association of Canada, 1994;1-17.
- Robinsky EI. Tailings disposal by thickened discharge method for improved economy and environmental control. Tailings disposal today, Proceedings of the 2nd international tailings symp, 1978:75-95.
- Robinsky EI, Barbour SL, Wilson GW, Bordin D, Fredlund DG. Thickened slope tailings discharge. Proceedings of the 2nd international conference on the abatement of acidic drainage, invited lecture, September 16-18, Montreal, Quebec, 1991:1-20.
- Rogasik H, Crawford JW, Wendroth O, Young IM, Joschko M, Ritz K. Discrimination of soil phases by dual energy x-ray tomography. Soil Sci Soc Am J 1999;63:741-751.
- Romero FM, Prol-Ledesma RM, Canet C, Alvares LN, Pérez-Vázquez R. Acid drainage at the inactive Santa Lucia mine, western Cuba: Natural attenuation of arsenic, barium and lead, and geochemical behavior of rare earth elements. Appl Geochem 2010;25:716-727.
- Roussel C, Néel C, Bril H. Minerals controlling arsenic and lead solubility in an abandoned gold mine tailings. Science of the Total Environment 2000;263:209-219
- Sánchez-España J, Pamo EL, Santofimia E, Aduvire O, Reyes J, Baretino D. Acid mine drainage in the Iberian Pyrite Belt (Odiel river watershed, Huelva, SW Spain): Geochemistry, mineralogy and environmental implications Appl Geochem 2005;20:1320-1356.
- Sánchez España JS, Pamo EL, Pastor ES. The oxidation of ferrous iron in acidic mine effluents from the Iberian Pyrite Belt (Odiel Basin, Huelva, Spain): Field and laboratory rates. J Geochem Explor 2007;92:120-132.
- Seeberg-Elverfeldt J, Schlüter M, Feseker T, Kölling M. Rhizon sampling of porewaters near the sediment-water interface of aquatic systems. Limnol. Oceanogr: Methods 2005; 3: 361-371.
- Seifert T, Sandmann D. Mineralogy and geochemistry of indium-bearing polymetallic vein-type deposits: Implications for host minerals from the Freiberg district, Eastern Erzgebirge, Germany. Ore Geol Rev 2006;28:1-31.

References Cited

- Shapter JG, Brooker MH, Skinner WM. Observation of oxidation of galena using Raman spectroscopy. *Int J Min Process* 2000;60:199–211.
- Sholkovitz ER. The aquatic geochemistry of rare earth elements in rivers and estuaries. *Aquat. Geochem* 1995;1:1-43.
- Sidenko NV, Sherriff BL. The attenuation of Ni, Zn and Cu, by secondary Fe phases of different crystallinity from surface and ground water of two sulfide mine tailings in Manitoba, Canada *Appl Geochem* 2005;20:1180–1194.
- Sima M, Dold B, Frei L, Senila M, Balteanu D, Zobrist J. Sulfide oxidation and acid mine drainage formation within two active tailings impoundments in the Golden Quadrangle of the Apuseni Mountains, Romania *J Hazardous Materials* 2011;189: 624-639.
- Singer PC, Stumm W. Acid mine drainage-rate determining step. *Science* 1970;167:1121–1123.
- Smyth JR, McCormick TC. Crystallographic data for minerals. In: Ahrens TJ, editor. *Mineral physics & crystallography: a handbook of physical constants*. Am Geophy U 1995;1-14.
- Stephens DB. *Vadose zone hydrology*. Lewis Publishers, Boca Raton, FL 1996.
- Stumm W, Morgan JJ. *Aquatic Chemistry Aquatic Chemistry*, 2nd ed. Wiley, New York; 1981;632 p.
- Suman RJ, Knight RJ. Effects of pore structure and wettability on the electrical resistivity of partially saturated rocks—A network study. *Geophysics* 1997;62:1151–1162.
- Thornber MR, Bettenay E, Russell WGR. A mechanism of aluminosilicate cementation to form a hardpan. *Geochim Cosmochm Acta* 1987;51:2303-2310.
- Tichomirowa M, Pelkner S, Junghans M, Haubrich F. Sulfide oxidation at the polymetallic sulfide deposit Freiberg (Germany) and consequences for heavy metal mobilization. In: Schulz HD, Haderer A, editors. *Geochemical processes in soil and groundwater measurement –Modelling – Upscaling*, GeoProc 2002. Wiley–VCH; 2002.p.356–379.
- Titov K, Kemna A, Tarasov A, Vereecken H.. Induced polarization of unsaturated sands determined through time domain measurements. *Vadose Zone J* 2004;3:1–9.

References Cited

- Tofteng C, Hansen S, Jensen HE. Film and pulse flow in artificial macropores. *Nord. Hydrol* 2002;33:263–274.
- Tokunaga TK, Wan J, Sutton SR. Transient film flow on rough fracture surface. *Water Resour Res* 2000;36:1737–1746.
- Tokunaga TK, Wan JM. Surface-zone flow along unsaturated rock fractures. *Water Resour Res* 2001;37:287–296.
- Tossell JA, Vaughan DJ. Electronic structure and the chemical reactivity of the surface of galena. *Can Min* 1987;25:381–392.
- Tuovinen OH, Bhatti TM, Bigham JM, Hallberg KB, Garcia Jr O., Lindström, E.B. Oxidative dissolution of arsenopyrite by mesophilic and moderately thermophilic acidophiles. *Appl Environ Microbiol* 1994;60:3268–3274.
- Ulrich C, Slater LD. Induced polarization measurements on unsaturated, unconsolidated sands. *Geophysics* 2004;69:762–771.
- Valente T, Leal Gomes C. Occurrence, properties and pollution potential of environmental minerals in acid mine drainage. *Science of the Total Environ* 2009;407:1135–1 152.
- Van Geet M, Lagrou D, Swennen R. Porosity measurements of sedimentary rocks by means of microfocus x-ray computed tomography (μ CT). In: Mees F et al., editors. *Application of x-ray computed tomography in the geosciences*. Spec. Publ. 215. Geological Society, London 2003;51–61.
- Verplanck PL, Nordstrom DK, Taylor HE, Kimball BA. Rare earth element partitioning between hydrous ferric oxides and acid mine water during iron oxidation. *Appl Geochem* 2004;19:1339–1354.
- Vink BW. Stability of antimony and arsenic compounds in the light of revised and extended Eh-pH diagrams. *Chemical Geol* 1996;130:21–30.
- Walder I, Schuster P. Acid Rock Drainage. In: SARB Consulting, Inc. *Environmental geochemistry of ore deposits and mining activities*. Short course Notes, Albuquerque, New Mexico; 1998.
- Wang S, Mulligan CN. Natural attenuation processes for remediation of arsenic contaminated soils and groundwater. *J Hazardous Materials* 2006;B138:459–470.

References Cited

- Warner GS, Nieber JL, Moore ID, Geise RA. Characterizing macropores in soil by computed tomography. *Soil Sci Soc Am J* 1989;53:653–660.
- Wels C, Lefebvre R, Robertson AM. An overview of prediction and control of air flow in acid-generating waste rock dumps. 6th ICARD Cairns, QLD, 12 - 18 July 2003.
- Wiersma CL, Rimstidt JD. Rates of reaction of pyrite and marcasite with ferric iron at pH 2. *Geochim Cosmochim Acta* 1984;48:85–92.
- Wildenschild D, Hopmans JW, Vaz CMP, Rivers ML, Rikard D, Christensen BSB.. Using x-ray computed tomography in hydrology: Systems, resolutions, and limitations. *J Hydrol* 2002;267:285–297.
- Wilkin RT. Metal Attenuation Processes at Mining Sites. U.S. Environmental Protection Agency, EPA/600/R-07/092 , 2007.
- Williams MPA, Seddon KD. Thickened tailings discharge: A review of Australian experience. In: *Tailings and mine waste' 99*. Balkema, Rotterdam 1999;125-135.
- Worrall F, Pearson DG. The development of acidic groundwaters in coal-bearing strata: Part I. Rare earth element fingerprinting. *Appl Geochem* 2001;16:1465-1480.
- Zänker H, Moll H, Richter W, Brendler V, Hennig C, Reich T, Kluge A, Huttig G. The colloid chemistry of acid rock drainage solution from an abandoned Zn-Pb-Ag mine. *Appl Geochem* 2002;17:633–648.
- Zuoping Z, Chuanxian L. The behaviour of Rare-Earth Elements (REE) during weathering of granites in southern Guangxi, China. *Chinese J Geochem* 1996;15:344-35.
- Zuddas P. Water-Rock Interaction Processes Seen through Thermodynamics. *Elements* 2010;6: 305-308.

ACKNOWLEDGEMENTS

Here I should thank a large number of people who gave positive support in any way or form during my work on my PhD.

First, I would like to express my deepest thanks to Prof. Dr A. El-Shater, head of Geology Department, Sohag University and all the staff members in the department for giving me the chance to get this scholarship and for their encouragements and providing the logistic supports during our field trip in the Eastern Desert of Egypt. Also, the Egyptian government, Cultural Affairs & Missions Sector for the immense support during my stay as a scholarship-holder in Hannover to complete my PhD work.

Also, I am very much indebted to Prof. Dr. Francois Holtz, Leibniz University of Hannover, Institute of Mineralogy, my PhD supervisor, for accepting me as a PhD candidate as well as for the most possible freedom within the framework of my project, for the encouragement and fruitful discussions during the progress of the present work.

A special word of thanks should go to Dr. Dieter Rammlmair, Bundesanstalt für Geowissenschaften und Rohstoffe (BGR) in Hannover, for his close supervision, useful guidance in the field and laboratory works, providing very valuable feedback, helpful comments and interesting discussions throughout the work.

My profound gratitudes are dedicated to Dr. Jeannet Meima (BGR), for her valuable discussions and comments during the different stages of the present work.

I would not forget Dr. Antje Wittenberg (BGR & European Commission), I send to her my deepest thanks, for her guideness during my first stay in BGR, introducing me to the staff, and to facilitate the problems which I faced.

Also, I would like to thank BGR institute and his president Prof. Dr. Hans-Joachim Kümpel and the heads of B1, and B1.2 for accepting me to do my work during that time.

Aknowledgements

Furthermore, I would like to express my deepest gratitudes to Prof. Dr. Lee Slater from Rutgers University, Dept of Earth & Environmental Sciences and Dr. Burkhard Beckhoff from the section of x-ray Spectrometry at PTB, the Physikalisch-Technische Bundesanstalt in Berlin, Héctor Conesa (Institute of Terrestrial Ecosystems, Switzerland), Dr. Torsten Graupner (BGR), Dr. Gregorio Garcia (Dep. of Agricultural Science and Technology, Technical University of Cartagena, Spain) and Dr. Izabella Farkas (Dep. of Mineralogy, Eötvös L. University, Hungary) for their useful comments and suggestions. Also very special thanks to Sharon Mateo from FEI Australia for the valuable advices during MLA measurements.

Finally, I want to thank all the BGR members in Hannover and Berlin who helped me during my research, including, A. Scheibner, Prof. Dr. A. Schippers, A. Goldmann, B. Burkhart, B. Harazim, C. Kamphuis, C. Czora, Dr. C. Grisseemann, D. Requard, D. Klosa, D. Weck, E. Adick, F. Korte, Dr. F. Melcher, Dr. Ch. Gaedicke, G. Ehlers, H. Lorenz, Dr. H.-W. Müller, Dr. H. Gäbler, D. Henry, I. Bitz, J. Lodziak, Dr. J. Stummeyer, K. Kuhn, K. Tacke, L. Kaste, M. Sack, Dr. M. Sitnikova, Dr. M. Furche, M. Hein, P. Rendschmidt, R. Seibold, R. Koch, Dr. S. Kaufhold, T. Koch, Dr. T. Oberthür, Dr. T. Pletsch, Dr. U. Noell, Dr. U. Schwarz-Schampera and W. Glatte. I apologize if I forgot to mention other people who have helped me during my PhD work.

Lebenslauf

Name	<i>Mostafa Gamal Eldeen Taha Redwan</i>
geboren am	<i>07.12.1978 in Sohag, Ägypten</i>
Schulbildung	
<i>1984-1989</i>	<i>Grundschule</i>
<i>1989-1992</i>	<i>Mittelschule</i>
<i>1992-1995</i>	<i>Oberschule</i>
Hochschulbildung	
<i>1995-1999</i>	<i>Studium der Geologie an der Universität Sohag- Ägypten, mit dem Abschluss Bachelor (Note: Mit Auszeichnung, hors.)</i>
<i>2000/2002</i>	<i>Aufbaustudium (Vorbereitungsphase) im Fachbereich Geologie an der Universität Sohag, Ägypten</i>
<i>2002-2005</i>	<i>Studium mit Erlangung des M.Sc. im Fachbereich Geologie an der Universität Sohag, Ägypten</i>
<i>2005-2007</i>	<i>Wissenschaftlicher Angestellter an der Universität Sohag, Ägypten im Fachbereich Geologie, Universität Sohag, Ägypten</i>
<i>2007-2011</i>	<i>Doktorand am Institut für Mineralogie der Gottfried Wilhelm Leibniz Universität Hannover und an der Bundesanstalt für Geowissenschaften und Rohstoffe (BGR)</i>
Berufstätigkeit	
<i>2000-2007</i>	<i>Wissenschaftlicher Angestellter im Fachbereich Geologie der Universität Sohag, Ägypten</i>
<i>2007 bis heute</i>	<i>Gastwissenschaftler an der BGR, B1.2 AB Mineralische Reststoffe. Stipendium der Kulturabteilung und Studienmission der Botschaft der Arabischen Republik Ägypten</i>